# Collective motion in reactive suspensions

Francisco Rojas Perez

INSTITUT POLYTECHNIQUE DE PARIS

NNT : 2022IPPAX076

Thèse de doctorat

# Collective motion in reactive suspensions

Thèse de doctorat de l'Institut Polytechnique de Paris
préparée à l'École polytechnique

École doctorale n°626 École doctorale de l'Institut Polytechnique de Paris (EDIPP)
Spécialité de doctorat: Mécanique des fluides et des solides, acoustique

Thèse présentée et soutenue à Palaiseau, le 27 Septembre 2022, par

**FRANCISCO ROJAS PÉREZ**

Composition du Jury :

| | |
|---|---|
| Cecile Cottin-Bizonne<br>Directrice de recherche, Université Lyon 1 (Institut Lumière Matière) | Président |
| Marisol Ripoll<br>Directrice de recherche, Institute of Biological Information Processing (Theoretical Physics of Living Matter) | Rapporteur |
| Fernando Peruani<br>Professeur des universités, Cergy Paris Université (Laboratoire de Pysique Théorique et Modélisation) | Rapporteur |
| Eric Keaveny<br>Associate Professor, Imperial College London (Department of Mathematics) | Examinateur |
| Sébastien Michelin<br>Professeur, Ecole Polytechnique (LadHyX) | Directeur de thèse |
| Blaise Delmotte<br>Chargé de recherche, Ecole Polytechnique (LadHyX) | Co-directeur de thèse |

## Abstract

Collective motion of active systems spans many physical scales from macroscopic flocks of birds and nice whirlpools of fish schools, to microscopic turbulent patterns of swimming bacteria and group strategies of spermatozoa to be more efficient. In these systems, the presence of a large number of active elements, that are able to move autonomously by converting biochemical energy into motion, induces collective patterns that emerge spontaneously that are unexpected just by looking at one of them isolated.

In the last decades, synthetic self-propelled microscopic particles have been developed to mimic and study their natural counterparts but also to explore different applications like microsurgery, water purification, or the development of new materials with tunable properties. Reactive suspensions are one of them and consist of large numbers of chemically-active colloids suspended in a fluid, which modify the concentration of chemical solutes surrounding them in order to self-propel. By doing so, they generate long-ranged hydrodynamic flows and chemical gradients that perturb the trajectories of other particles. These hydrodynamic and chemical interactions induce the formation of coherent structures and the development of collective motion.

Given the scale of these phoretic particles, the problem is governed by the Laplace equation for the concentration field and the Stokes equations for the velocity field, both coupled by the boundary conditions on the particles' surfaces. The numerical modeling of such suspensions remains particularly challenging given the coupled nature of the hydro-chemical interactions and the rapid increase in the required computational resources for large numbers of particles.

In this thesis, a new framework called Diffusiophoretic Force Coupling Method (DFCM) is proposed which is able to handle both the chemical diffusion and Stokes flow problems for a large number of particles. It is based on the core ideas of the Force Coupling Method, which is a regularized multipole expansion for hydrodynamics problems used in the study of colloidal particles. Instead of relying on Green's functions of the Laplace and Stokes operators to obtain the particle signatures in the far-field, DFCM relies on grid-based volume averages of the concentration field to calculate the particle surface concentration moments. These moments define the chemical multipoles of the modified Laplace problem and provide the swimming forcing of the Stokes problem.

The precision of DFCM is evaluated against exact and accurate numerical solutions for a few canonical cases using particle pairs. Its improvements over far-field approximations for a wide range of inter-particle distances are quantified, obtaining better results for distances larger than half a radius, which is relevant for dilute and semi-dilute suspensions. Another advantage of the method lies in its linear scalability with the number of particles.

In the second part of this thesis, a highly scalable implementation of the new DFCM is performed to study collective motion within semi-dilute reactive suspensions. Depending on the particles' individual properties, a wide range of coherent structures is observed including small clusters of short-lived existence and persistent clusters of small or big size. Chaotic motion is observed in the population of free particles and small clusters, while collective ballistic motion is in the case of big clusters.

The resulting suspension patterns were classified into five regimes considering their microstructure and collective motion. An analysis of these results brings new insights on how the individual properties of the particles and their interactions, as well as the volume fraction of the suspension condition the emerging regimes and the transitions between them.



**Key-words**: Reactive suspensions, active matter, phoretic particles, collective motion, computational fluid dynamics.

**Résumé**

Les mouvements collectifs dans les systèmes actifs s'étendent sur de nombreuses échelles physiques, allant des essaims macroscopiques d'oiseaux ou des tourbillons au sein de bancs de poissons, aux motifs turbulents microscopiques des suspensions bactériennes ou aux stratégies de groupe des spermatozoïdes leur permettant d'être plus efficaces. Dans ces systèmes, la présence d'un grand nombre d'éléments actifs, chacun capable de se déplacer de manière autonome en convertissant une énergie bio-chimique en mouvement, induit des motifs collectifs spontanés inattendus de l'observation d'un élément isolé.

Au cours des dernières décennies, des particules microscopiques synthétiques auto-propulsées ont été développées pour imiter et étudier leurs homologues naturels, mais aussi pour explorer différentes applications telles que la microchirurgie, la purification de l'eau ou le développement de nouveaux matériaux aux propriétés contrôlables. Les suspensions réactives en font partie et sont constituées de nombreux de colloïdes chimiquement actifs en suspension dans un fluide, qui modifient la concentration des solutés chimiques qui les entourent pour s'auto-propulser. De cette manière, ils génèrent des écoulements et des gradients chimiques à longue portée qui perturbent les trajectoires d'autres particules. Ces interactions hydrodynamiques et chimiques induisent la formation de structures cohérentes et le développement des mouvements collectifs.

Compte tenu de l'échelle de ces particules phorétiques, le problème est régi par l'équation de Laplace pour le champ de concentration et les équations de Stokes pour le champ de vitesse, couplées par les conditions aux limites physico-chimiques à la surface des particules. La modélisation numérique de telles suspensions reste particulièrement difficile compte tenu de la nature couplée des interactions hydro-chimiques et de l'augmentation rapide des ressources de calcul nécessaires pour de grands ensembles de particules.

Dans cette thèse, un nouveau cadre appelé Diffusiophoretic Force Coupling Method (DFCM) est proposé, capable de gérer à la fois les problèmes de diffusion chimique et de écoulements de Stokes pour un grand nombre de particules. Il est basé sur les idées fondamentales de la Force Coupling Method, qui est une expansion multipolaire régularisée pour les problèmes d'hydrodynamique utilisés dans l'étude des particules colloïdales. Au lieu de s'appuyer sur les fonctions de Green des opérateurs de Laplace et de Stokes pour obtenir les signatures de particules en le champ lointain, la DFCM s'appuie sur des moyennes de volume basées sur la grille du champ de concentration pour calculer les moments de concentration de surface des particules. Ces moments définissent les multipôles chimiques du problème de Laplace modifié fournissent le forçage de nage du problème de Stokes.

La précision de la DFCM est évaluée par rapport à des solutions numériques exactes et précises pour quelques cas canoniques d'interaction de paires de particules. Ses améliorations par rapport aux approximations en champ lointain pour une large gamme de distances inter-particules sont quantifiées, obtenant de meilleurs résultats pour des distances supérieures à un demi-rayon, pertinentes pour les suspensions diluées et semi-diluées. Un autre avantage de la méthode réside dans sa scalabilité linéaire avec le nombre de particules.

Dans la deuxième partie de cette thèse, une implémentation hautement scalable de la nouvelle DFCM est réalisée pour modéliser des suspensions réactives semi-diluées. En fonction des propriétés individuelles des particules, un large spectre de structures cohérentes est observé, y compris de petits agrégats d'existence éphémère, aussi bien que des agrégats persistants de taille petite ou grande. Un mouvement chaotique est observé dans les populations de particules libres et de petits ensembles, tandis qu'un mouvement balistique dans le cas de gros agrégats.

Ces motifs ont été classés en cinq régimes sur la base de leur micro-structure et des caractéristiques du mouvement collectif. Une analyse des résultats de cette thèse apportent de

nouvelles informations sur la façon dont les propriétés individuelles des particules et leurs interactions, ainsi que la fraction volumique de la suspension conditionnent les régimes émergents et les transitions entre eux.

**Mots-clés**: Suspensions réactives, matière active, particules phorétiques, mouvement collectif, dynamique des fluides computationnelle.

**Acknowledgements / Agradecimientos**

Part of the journey is the end, although each end does not mean anything other than the beginning of a new one. The most important thing is what we learn along the way, but above all, those who are by our side in the process. Along these lines, I take the opportunity to thank them now.

Después de estos 3 años de estudios doctorales deseo agradecerle en primer lugar a Dios y a toda mi familia por su apoyo constante. A mi esposa Adriana por ser la compañera incondicional en toda esta aventura en Francia y por apoyarme siempre, tanto en las buenas como en las malas, por recordarme las cosas importantes en esta vida y siempre poner alegría en ella. A mis padres Elizabeth y José Alberto por siempre haberme dado la mejor educación posible en el amplio sentido de la palabra, por siempre creer en mi así como apoyarme en todo y por ser ejemplos a seguir para mí. A mis hermanos Marcela y Esteban por bridarme siempre su apoyo y amistad, además de la alegría de dos sobrinos hermosos. De igual forma le agradezco a mi suegros Rudy y Angelina por todo su apoyo, y especialmente a esta última por haber cruzado un océano entero por venir a verme en mi defensa. Gracias doña Marielos y don François por habernos recibido en esta ciudad como familiares de toda la vida y por haberse convertido efectivamente en parte de ella en este tiempo. Al resto de mi familia cercana que ha estado en contacto durante estos años en el extranjero y me ha brindado su apoyo de una u otra forma, muchísimas gracias por todo. ¡Sin ustedes nada de esto habría sido posible y espero el momento para reunirme de nuevo con ustedes y darles las gracias personalmente!

Once again, thanks to both my supervisors, Sebastien and Blaise, for all your professionalism and respect for me, for the continuous commitment to my job, and for the support you provided me during all this time in France. Because during this journey, I have learned valuable things from you, including how to perform high-level research, how to be critical with my job to improve its quality, good practices to become an excellent academic mentor, as well as technical aspects, including physics, mechanics, and computing. Thanks to all the staff in LadHyX (including researchers, professors, administrators, and technicians) because the lab's scientific culture is very high and the atmosphere was always welcoming, something precious for all the people on this journey. Also, thanks to my lab-mates for all the time together, for making the lab even a better place to work, and for all your help; special thank goes to Nikhil, Tulio, Francesco, Akhil, Daniel, Prathmesh, Benjamin, Pierre, Ursy and to all those who attended my defense and subsequent cocktail party.

I also would like to thank Marisol and Fernando for accepting to be rapporteurs of this thesis manuscript, for your positive feedback about my work, and especially for your detailed review as well the indication of some improvement possibilities in your reports and during my defense with your relevant questions. Thanks to Cecile and Eric for being accepted as my examinateurs, for all your contributions, and for your important and enriching questions during my defense. All this together has allowed me to obtain a broader vision of my work and to put it into perspective.

Finalmente quiero agradecerle al Instituto Tecnológico de Costa Rica por todo su apoyo en esta iniciativa, en particular a mis compañeros de la Escuela de Física y de la oficina de Recursos Humanos por confiar en mi propuesta y en mi capacidad para llevarla a cabo. Además, quiero darle las gracias a don Julio por su gran apoyo para esta aventura y por su confianza en mí. De igual forma a Juan José (Pineda) por su relevante influencia académica cuando era muy joven, así como por su amistad y apoyo desde entonces. También a mis compañeros y amigos en este viaje transatlántico de la investigación Juan José (Montero), Carlos y Ana Yancy por las experiencias compartidas y el apoyo mutuo.

# Contents

# List of Figures

# Chapter 1

# Introduction to Active Matter and reactive suspensions

Active matter is an area of physics that studies systems with large sets of constituent elements, each one of them consumes stored energy to self-propel, leading to collective motions unexpected only from the individual element properties. In this chapter, I will introduce the reader to this field of study, starting with macroscopic systems to gain familiarity with them. Then we will move to the microscopic scale in which many systems of interest consider both natural and synthetic examples. With the last ones, we will look into some of the technological applications explored in recent years. I will also describe the most relevant interactions between these elements of the system and some of their emerging patterns of interest.

## 1.1 Macroscopic active matter

After three years of working on my thesis, I arrived at the previous definition of what active matter is in a broad sense. Initially, I didn't know how vast this subject was, but this seemed intriguing given the large set of scales that the topic could study and its potential universality and applicability. Sometimes the best way to introduce someone to a new topic is by bringing them some familiar examples. For this purpose, I call attention to the images in figure 1.1.

In the first place, flocks of several hundreds of starlings can fly as a uniformly moving group adopting lovely shapes (figure 1.1.a)) to produce chaotic aerial patterns suddenly. There are a lot of videos on the internet showing these kinds of collective motions, and they have called the attention of researchers that have been trying to understand what factor rules the dynamics of these systems [20, 21]. I ask myself, for example: how do they effectively communicate to fly like this and how do these wave patterns emerge? Or what are the relevant interactions between birds to produce them? But maybe the first question should be, why do they fly this way? It seems that migration and protection from predators are some of the causes [22, 23].

Similarly, schools of fish can swim very orderly and abruptly change direction rising the interest on their physical study [24, 25]. Because of the influence of a nearby predator, the same fish can swirl like a stirred fluid (figure 1.1.b)). In this case, some interesting questions are: is there some "alpha fish" that guides the rest of the flock? Or instead, is it more like a democracy? In which the majority decides how to move collectively. But again, why do they move in these intricate patterns? Regarding the first question, it seems that the fish make decisions based on consensus, and as the group size increases, they make them more accurately [26]. Regarding the second one, some causes are foraging and protection from predators [23, 27].

The presence of these collective motions in the animal kingdom is not limited to flock of birds or schools of fish, but also includes swarms of insects that can move by walking, swimming or flying, including locusts [23], ants [28] or midges [29, 30]. Also land animals exhibits this collective behaviours being very popular the case of the sheep herds [31, 32].

Moving to more daily examples in our daily routines, anyone who has attended a massive event such as a music concert (or a sports game of their favorite team or simply commuting in a very crowded day) will have experienced the feeling of being in the middle of a vast crowd, and perhaps even with a bit of trepidation, will have worried about their safety at the time entering and leaving the place in some bottleneck. This concern is not badly-posed since many fatal accidents have occurred in these kinds of events, and their prevention is an important issue, for example, in the design of emergency routes. Recently, some researchers have shown how the flow and density of people vary in bottlenecks with variables like the width and properties of the entrances, the motivation of the persons in the event, etc [1]. They provided as well evidence of how to pressure other persons to move faster, could effectively induce the opposite result [33] (figure 1.1.c)).

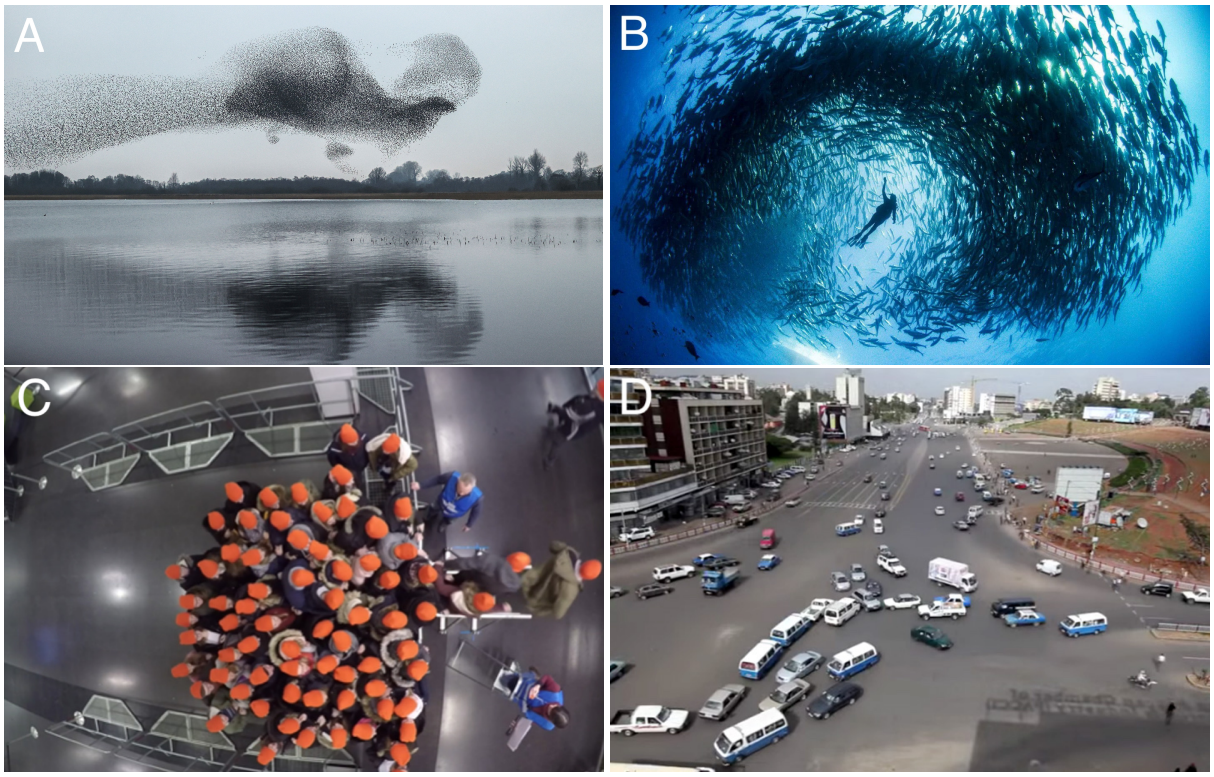


Figure 1.1: Active matter and collective motion examples at macroscopical scale: a) aerial flock of birds with a very particular shape, https://euronewssource.com, b) school of fish in a swirl pattern, https://medium.com, c) pedestrian bottleneck experiment following heads trajectories (in orange) [1], d) traffic intersection without traffic lights in Meskel Square, Ethiopia, https://thekidshouldseethis.com.

Finally, in the case of the flow of vehicles on the roads, we know that this is governed by a series of signs and rules that allow its correct flow. In this system, we see well-aligned patterns with high speeds on highways, but there are also congestions before a toll or when an accident occurs. Another example is the case of intersections, where many roads cross and vehicles are forced to stop and alternate their turns to travel in the desired direction; all this is regulated through some computing control system. Could you imagine the chaos generated in a large intersection at rush hour if this system were to fail? A traffic light system failure or a power outage, for example. The truth is that this occurs permanently in some intersections around the world. It works relatively well (figure 1.1.d)) since drivers spontaneously regulate themselves in chaotic patterns, in a process that balances request and demand in each direction, without the number of accidents or total blocks one might expect. Two interesting questions are: What mechanisms allow these intersections to function effectively? Which are the emerging patterns in this system, and how efficient are they? The need to avoid collisions, entering the intersection in groups of cars, and the widespread use of horns are some aspects related to these questions.

Maybe the central common aspect between these intriguing examples is the presence of the collective motion that emerges unexpectedly in each system, revealing well-coordinated regimes between its elements. Although, of course, there is an external constraint in each system like the number of lanes and the possible senses for the road, the water-air surface for birds and fish while the walls and doors width for the people flow, the internal constraints (excluded volume of the entities for example) and the interactions between them are crucial to understand and explain

the collective dynamics.

Another similar characteristic between these systems is the presence of self-propelled constitutive elements able to move autonomously, converting local energy into motion. This converts them into out-of-thermodynamic-equilibrium systems in which the second law of thermodynamics does not apply. So they could increase their order spontaneously (decreasing the entropy). For these particular systems, the constitutive elements use previously stored energy on them, but in general, they could extract instantaneous energy from their environment as well.

The last shared characteristic that I would like to remark in these cases is the presence of a large number of entities. If only two or three entities existed, they would probably follow simpler trajectories (straight lines towards their objectives) almost without relation between them. So the critical point here is that a large number of entities in the system enforces continuous interactions, and this changes the evolution of the system dramatically.

Although the previously selected examples were deliberately in the macroscopic scale to illustrate the reader with familiar systems, similar dynamics exist in the microscopic world, for instance, among micro-organisms such as bacteria or micro-algae. At this scale, cognitive systems are absent (lack of vision/sensory systems), and the movement of individuals occurs without inertia. So one might wonder if these collective movements can be explained by physical, chemical, or biological interactions. Understanding the behavior of microscopic systems is essential from the point of view of fundamental physics and biology, but it is also of interest for developing new technologies.

In recent decades, the study and development of the synthetic counterpart of these biological micro-organisms have become a very active interdisciplinary research area known as (microscopic) active matter [34, 35]. In this thesis, I study the essential characteristics of active matter and collective motion that emerge from the interaction of many synthetic self-propelled particles suspended in a liquid. More specifically, in the study of particles that swim autonomously by performing chemical reactions on their surface called reactive suspensions.

## 1.2 Microscopic active matter

Although we can't see them, maybe fortunately for our peace of mind, nature is filled with swimming micro-organisms: the bacteria that inhabit our intestines or the protozoa in our lakes and the algae in the ocean. Some bacteria, such as Escherichia coli, detect nutrient gradients and move to regions of higher concentration (chemotaxis) [36, 37]. Human spermatozoa develop group strategies while swimming to the oocytes in challenging environments such as cervical mucus [4, 38].

However, the physics governing swimming at the micrometer scale drastically differs from its analog at the macroscopic scale (our human scale). The reality in which micro-organisms live is sometimes called the world of low "Reynolds number", a regime where viscous damping rules over inertial effects. As we introduce below, the Reynolds number Re is an important dimensionless number that quantifies the relative importance between inertial and viscous forces in fluids. Swimming strategies employed by macroscopic organisms that operate at high Reynolds numbers (such as the birds, fish, or humans) are ineffective at the microscopic scale [39] making micro-organisms evolve and develop useful propulsion strategies that overcome and exploit the dominant drag at its scale. By propelling, they generate hydrodynamic flows that perturb the trajectories of other organisms [40, 41]. Large-scale collective behavior can emerge from the resulting long-ranged interactions between individual agents [42, 43], but also modifications of the effective macroscopic rheological and transport properties of such active suspensions [44, 45]. This is true for biological micro-organisms and active colloids, as seen in the following sections.

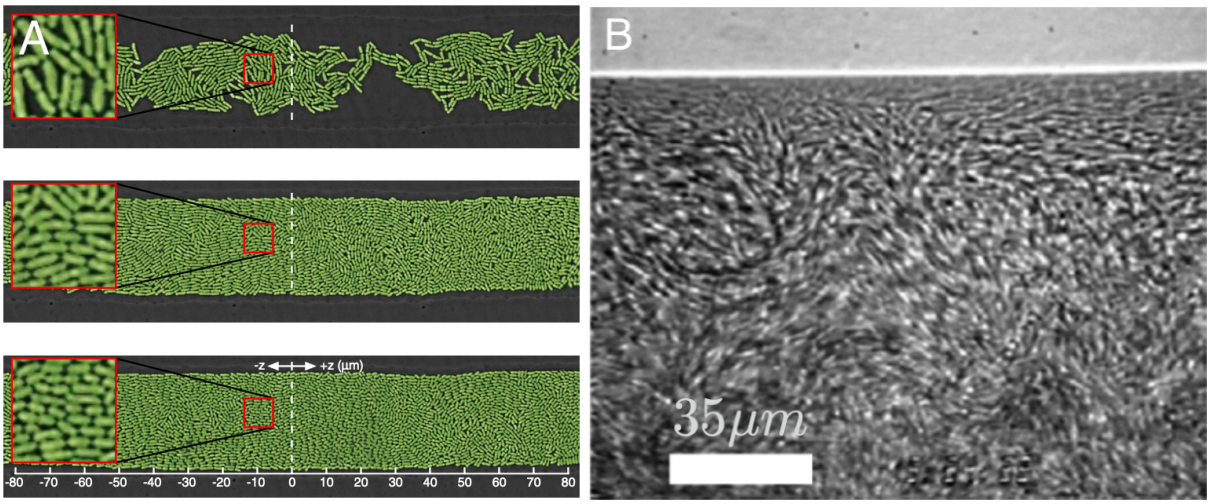


Figure 1.2: Active matter and collective motion examples at micron-size scale: a) The growth and ordering of the bacteria Escherichia coli in a quasi 2D open microfluidic cavity. Starting from a random configuration, three snapshots at 60, 90 and 138 minutes are presented (from top to bottom) showing the transition from a disordered phase to a highly ordered one. Figures adapted from [2]. b) Turbulence in a sitting drop of Bacillus subtilis at zero Reynolds number. Figure reproduced from [3].

### 1.2.1 Biological microswimmers

Figure 1.2 presents some examples of biological active matter in the microscopical world of low Reynolds numbers. In figure 1.2.a), Volfson et al. addressed the effects of the biomechanical interactions (coming from the growth and division of the bacteria cells in a suspension) on the colony formation through observation and simulation of the structure and dynamics of a growing two-dimensional colony of non-motile bacteria (Escherichia coli) [2]. They found that the growth of the bacterias and its division in a dense colony led to a dynamic transition from a completely disordered phase to a highly ordered one, mainly characterized by the orientational alignment of the rod-shaped bacterias (from top to bottom images).

In figure 1.2.b), Dombrowski et al. studied suspensions of aerobic bacteria, which develop flows from the interactions of chemotaxis and buoyancy in sessile drops [3]. They found notable collective motions with transient, high-speed jets, and strong vortices in these regions in a turbulent-like motion at small Re. They proposed a mechanism for large-scale coherence, considering hydrodynamic interactions between swimming cells. These turbulent patterns appear to be very common among (microscopic) active matter systems. Similar active turbulence has been reported in other active systems, including molecular motors, microtubule suspensions, and vortices in active nematics [35]. As can be seen, the interaction of large sets of microscopical agents triggers different coherent structures inducing order in the first case and chaos in the second one.

Another interesting collective behavior appears in the study of the spermatozoa of different species, in which diverse group strategies are found [4]. The sperm is made up of 3 parts, the head with the genetic material, the midpiece, which contains the mitochondria for the energy production, and the flagellum in charge of its propulsion, reaching sizes ranging from 30 $\mu m$ to 300 $\mu m$ depending on the species. In general, the flagellum motion occurs in a twisting movement, and the beat can either be planar for sperm swimming near surfaces or be three-dimensional with a conical envelope.

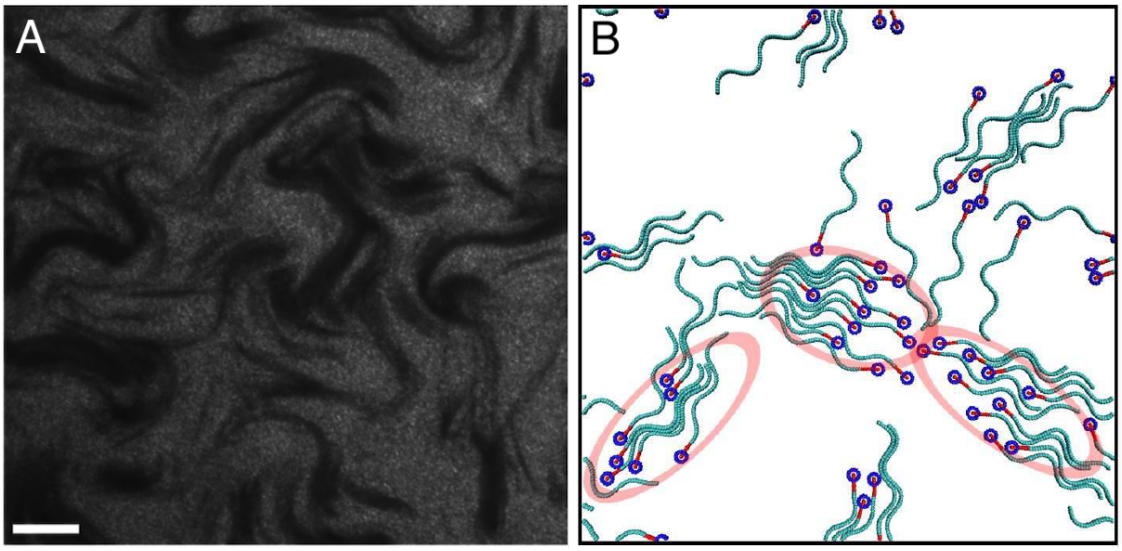


Figure 1.3: Collective motion observed in sperm samples: a) Massal motility observed in ram semen. Figure reproduced from [4]. b) Sperm trains in a simulation of 50 sperms, where the red ellipses indicate the trains. Figure reproduced from [5].

The first collective movement observed in large concentrations is called massal motility, which consists of a macroscopic wavy movement observable at low microscope magnifications. Its scale is much larger than the size of the sperm by a factor of $\approx 20$. This large-scale undulating pattern resembles the turbulent patterns mentioned earlier (figure 1.3.a). Another notable pattern is a cooperative structure known as sperm trains (or swarms) observed at low concentrations. In this case, small groups of spermatozoa cooperate by swimming in parallel first, synchronizing their beating pace, and finally reducing slowly the space between them [5], and by doing this there is an increase in the group speed (figure 1.3.b)).

Figure 1.4 shows three representative micro-swimmers in the biological context. Starting with Escherichia Coli, which is bacteria with many flagella (helical filaments for their propulsion), where each flagellum rotates connected to a motor by a hook (figure 1.4.a)), other bacteria such as Salmonella typhimurium also share these characteristics. They swim in a characteristic "run-and-tumble" motion [37]: in the "run" phase, the flagella form a bundle behind the bacteria, and it moves forward. Then in the "tumble" phase, some flagella reverse their direction of rotation and leave the bundle. This induces a tumbling motion that randomly changes the bacteria's orientation, eventually starting the cycle again. Its purpose is to detect gradients in chemical concentration or temperature. This is performed by extending the "run" phase in case of improving conditions and shortening it in case of worsening conditions. Note that this swimmer has its impulsion system behind its body, pushing the fluid behind it and propelling the swimmer forward.

Paramecium is an example of a ciliated micro-organism (figure 1.4.b)) with a size ranging between 50 $\mu m$ to 350 $\mu m$. Its surface is covered by thousands of cilia that beat in a coordinated manner known as metachronal waves, propelling the cell at speeds of 500 $\mu m/s$ to 1000 $\mu m/s$. The beat of the cilia has two different phases (power stroke and recovery stroke): during the first movement, the cilium is stretched straight and moves quite fast in one direction, while during the second movement, it slowly bends and retracts [40]. Opalina is another ciliated micro-organism that shares many of the Paramecium characteristics.

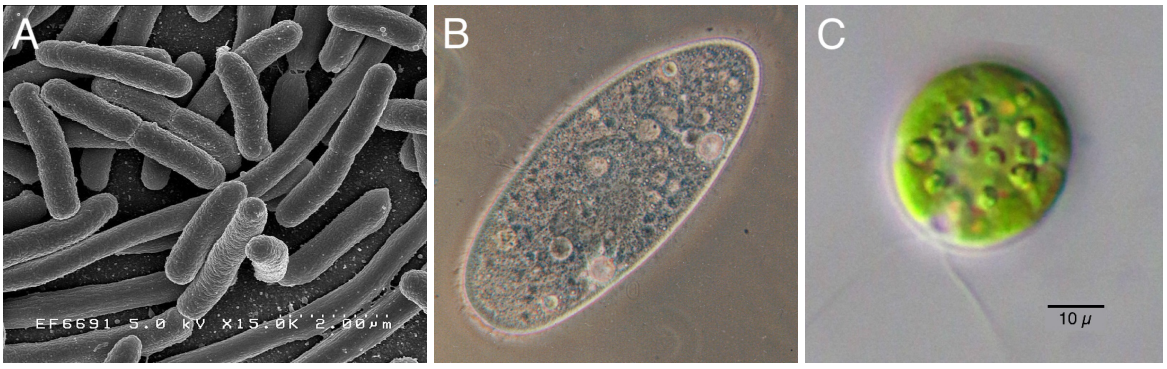


Figure 1.4: Biological micro-swimmers in the microscope: a) group of Escherichia Coli, https://en.wikipedia.org/wiki/Escherichia_coli, b) single Paramecium, https://en.wikipedia.org/wiki/Paramecium, c) single Chlamydomonas reinhardtii, https://en.wikipedia.org/wiki/Chlamydomonas.

Chlamydomonas reinhardtii is a green algae of about 10 $\mu m$ in diameter, which swims with two flagella in its front (figure 1.4.c)). The swimming motion of Chlamydomonas is as follows; the flagella are pulled back almost straight from their base, then bent and pushed forward again, reducing the drag, in direct analogy to the human stroke. When it is exposed to bright light, it swims in reverse, with its two flagella extended as in the case of sperms described previously [40].

As described in the previous lines, biological swimmers propel themselves through the action of flagella or cilia and the deformation of their surfaces [40, 46, 47]. Such cell motility in viscous fluids plays a critical role in diverse biological processes, including mammal fertility [4, 48] or the balance of marine life ecosystems [49]. Inspired by these natural examples, many promising applications in diverse fields such as biomedicine and engineering have been explored. Researchers and engineers across disciplines have focused on the design of microscopic self-propelled systems [50]. The following section considers the efforts in the development of the synthetic analog of the biological swimmers and beyond from them.

### 1.2.2 Synthetic microswimmers

#### Biomimetic swimmers

Many earlier designs were directly inspired by the rotation of the helical flagella of bacteria or the bending of flexible cilia [51, 52, 53]. For example, in the first case [51], the flagellum is built from a chain of magnetic colloidal particles and is attached to a red blood cell, which imitates the sperm head. This swimmer is set in motion by an alternating magnetic field, which generates a lateral oscillatory deflection of the flagellum. However, the swimming motion is the opposite of the one of a real sperm; the observed motion is more wagging than a traveling sine wave and generates a swimming motion towards the end of the tail (and not towards the head).

More recently, another swimmer that mimics sperm movement has been developed [54]. In this case, the microswimmer consists of a polydimethylsiloxane filament with a short, stiff head and a long, thin tail in which contractile heart muscle cells are grown. They periodically contract and deform the filament to propel the swimmer, reaching speeds of 5-10 um/s. This is a true biohybrid microswimmer because it requires no external force fields as its biological counterpart. These two examples of biomimetic microswimmers bring a vital differentiation

that must be made. It is about how the microswimmers obtain their energy, introducing the distinction between externally powered and autonomous active particles.

### Externally driven active particles

From the energy perspective, active particles harvest energy from their environment to power their movement and organization. One way to do this is by using external fields that provide the required energy. Using external fields to power active particles provides some significant advantages: the energy can be supplied remotely and controlled with precision, it is not time decaying, and the particles can be guided through the field lines. The external fields could also be used after their specific use in the separating and collecting process. Electric, magnetic, acoustic, and optical fields [55] are some of the most important external fields used. We could be more precise in the system guided by electric fields and mention specific mechanisms like electro-hydrodynamic flows, induced-charge electrophoresis, and field rectification.

An exciting demonstration of the use of external electrical fields to reconfigure active matter into different phases was performed numerically and experimentally by [6]. They used a phenomenon known as induced-charge electrophoresis [56] to modify the microstructure and the collective motion states of the active suspended particles, as can be seen in figure 1.5. They consider systems of Janus particles [57] with different electrical properties in each hemisphere in two different approaches. First, they considered molecular dynamics simulations in the numerical part in 3D. By modifying the charge and relative magnitude of the Janus particle's hemispheres, they predicted the states reported in figures 1.5-(a-d) as follows. They predicted a gas phase for particles with similar charges of the same sign (a), for equal charges with an opposite sign, they predicted active chains (b). When the charge magnitude is imbalanced, an alignment torque rises, inducing swarms (c) and clusters (d). Second, on the experimental side, they considered spherical Janus particles made of silica (of 3 $\mu m$ diameter) with a titanium and silicon dioxide coating on the half particle, settled in water in a 2D array between two electrodes. Then they applied electrical fields perpendicular to the moving plane inducing self-propulsion induced by ionic flows. By changing the field frequency (from $kHz$ to $MHz$), they recover several matter phases, including particles in gas-like phase, swarms, chains, and clusters (see figures 1.5-(e-h)). Beyond the predicted states, they also observed traveling waves in the swarm states that eventually evolved into large vortices or small vortices depending on the particle density in their experiments.

The usage of magnetic fields is one of the most explored, efficient, and target-specific ways of generating forces in this context. The most common active particles that convert energy from global magnetic fields to create localized hydrodynamic forces for self-propulsion are particles with flexible magnetic tails, rotary particles, and axially symmetric particle spinners [55]. The latter comprises particles that rotate about a single axis and propel colinearly in the direction of the same axis. The one shown in figure 1.6.a) consists of a helical structure with a uniform magnetic coating that propels in a weak rotating magnetic field. Depending on the design and the assembly of the particle, it could swim in one or both axis directions [7].

A hybrid design is shown in figure 1.6.b), which consists of two halves: one that is helical and magnetically driven and the other that is acoustically powered. This design allows the particle to swim in both directions according to its energy source [8]. The application of mechanical waves (sound) has appeared very recently [55]; in general, it works by a concave geometry of the tip of the rods in which the localized scattering of sound provides thrust along the axis of the

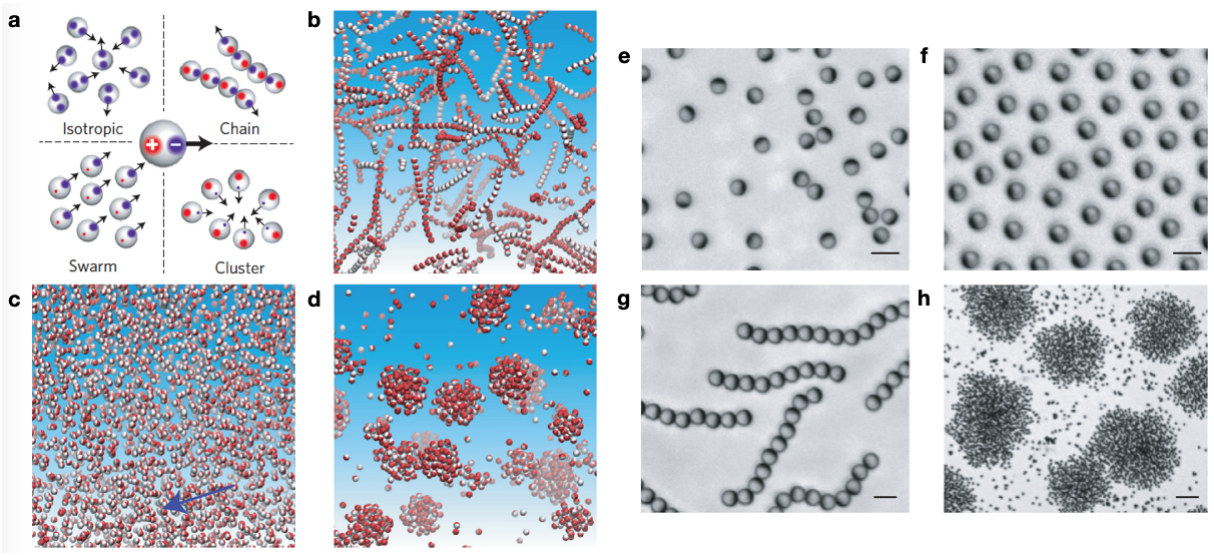


Figure 1.5: Observed states of synthetic micro-swimmers externally powered by induce-charge electrophoresis including computational (a-d) and experimental results (e-h). *In the numerics*, a) schematics of the particles showing the charge sign in color code, the charge magnitude in the dot size and the black arrow indicating the swimming direction. Four phases are expected depending in the combinations of parameters. The results of three of them are shown in the 3D model, in detail: b) chains, c) swarms, and d) clusters. *In the 2D experiments*, some of the observed phases are presented including e) gas, f) swarms, g) chains and h) clusters of particles. Figures adapted from [6].

rod. Depending on the input fields, these particles could exhibit collective behavior, including aggregation, swarming motion, and swarming vortex patterns.

### Autonomous active particles

Synthetic autonomous swimmers take energy from their immediate surroundings and convert it into movement. Since they swim at low Reynolds numbers, their inertia is irrelevant, and they must continually transform this energy to maintain their propulsion. One way to do this is through a very different strategy to the mechanisms discussed above, in which biological or biomimetic autonomous swimmers move their flagella or cilia, always carrying their energy (molecular ATP). This strategy is through the local generation of gradients (chemical, thermal, acoustic, electrical) and their use to generate hydrodynamic fluxes at the surface of the swimmers [58, 59].

The most famous and commonly-used design is that of Janus phoretic nano- or micro-particles with two different catalytic properties [57, 60]. These colloids exhibit short-term ballistic behavior in dilute suspensions, but their long-time dynamics are more diffusive due to thermal fluctuations [61]. In contrast, complex collective behavior is observed in denser suspensions with the coexistence of cluster and gas-like phases [13, 18]. Understanding the emergence of such phase-separation is currently a leading challenge in active matter physics [62].

To generate autonomous propulsion, these chemically-active colloids exploit a combination of two different physicochemical properties [59, 63]. The first one is a *phoretic mobility*, namely the ability to generate slip flow along the boundary of a colloidal particle in response to gradients of a solute (diffusiophoresis), temperature (thermophoresis), or electric potential

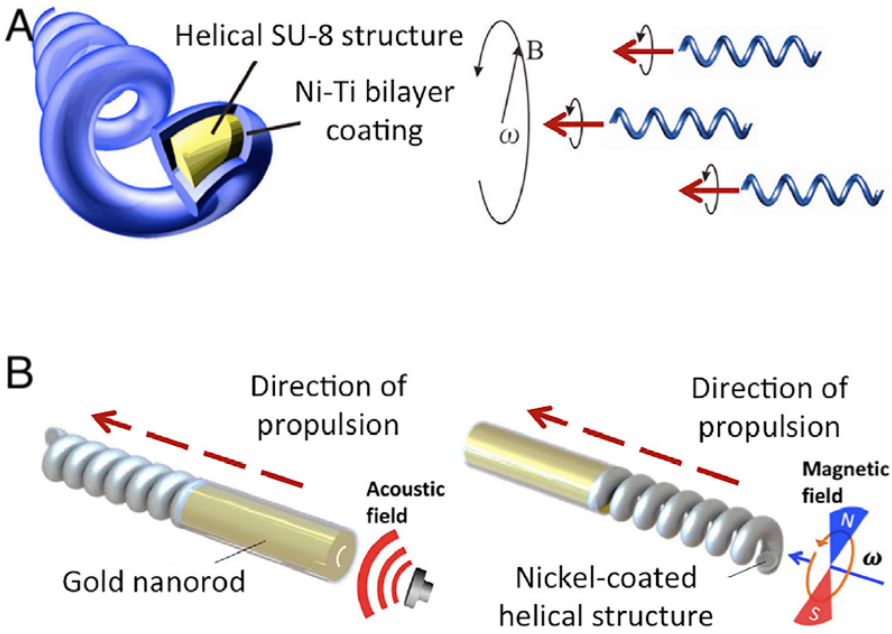


Figure 1.6: Examples of synthetic micro-swimmers externally powered by: a) rotating magnetic field, with a helical shape (Figure adapted from [7]), b) acoustic and magnetic fields, in an hybrid configuration to propel in both directions depending on the stimulation (Figure adapted from [8]).

(electrophoresis) [64], resulting in a net drift of this particle. The second one is the ability of the particle itself to generate the local gradients through a *surface activity*, e.g., surface-catalysis of chemical reactions [65] or heat release [66]. The combination of these two generic properties, or *self-phoresis*, provides the colloid with the ability to swim [63]. Other self-propulsion mechanisms also share significant similarities with self-phoresis, including the propulsion of active droplets [67] or light-illuminated colloids in binary mixtures [68]. For simplicity, we focus on self-diffusiophoresis of particles absorbing or releasing neutral chemical solutes [69, 70], keeping in mind that the approach and framework presented here can be applied or generalized to account for more generic self-phoretic systems.

Symmetry-breaking is an intrinsic requirement for directed motion in viscous flows (to generate local gradients and then fluid slip velocity); for self-phoretic colloids, this requires creating or sustaining a chemical surface polarity. As a result, strictly isotropic colloids can not self-propel individually, although they may do so by self-assembling into geometrically- or chemically-asymmetric structures [17, 71, 72, 73]. In practice, most chemically-active colloids thus exhibit an intrinsic chemical asymmetry, where the two sides of a Janus colloid capture or release solutes of different natures or at different rates [59]. Geometrically-asymmetric colloids also break the symmetry of their chemical environment and may thus self-propel [74, 75]. Based on instability, a third route to symmetry-breaking arises for isotropic colloids when the chemical solutes diffuse sufficiently slowly for the nonlinear convective coupling of phoretic flows and chemical transport to become significant [76, 77].

Like all microswimmers, Janus phoretic particles self-propel by stirring the fluid around them, thus modifying their neighbors' trajectory and speed. Due to their chemical activity, they also alter their chemical environment, thus also drive an additional phoretic motion of the surrounding particles. In most experiments on chemically active particles, the diffusing solutes

are small (e.g., dissolved gas), and chemical transport is dominated by diffusion. Such micron-size colloids typically propel in fluids of kinematic viscosity $\nu \approx 10^6\ \mu m^2 s^{-1}$ with velocities $U \approx 1 - 10\ \mu m s^{-1}$ and consume or release solutes of diffusivity $D \approx 10^3\ \mu m^2 s^{-1}$, so that the relevant Reynolds Re and Péclet number Pe (which measures the relative intensity of the advection vs diffusion of some chemical solute in the fluid formally introduced latter) are always small ($\mathrm{Re} \approx 10^{-6} - 10^{-5}$, $\mathrm{Pe} \approx 10^{-3} - 10^{-2}$) [13, 60, 61, 78].

## 1.3 Applications of microscopic phoretic particles

Beyond their fundamental interest and the puzzling details of their individual and collective self-propulsions, these active colloids are already considered for different applications, including biomedical, engineering, and environmental fields. Some of the most interesting are summarized now, including some detailed applications.

### 1.3.1 Biomedical applications

The use of nano and micron size technology for biomedical applications has experienced great development in recent decades. Particularly, Janus particles have recently received considerable interest as one of the next generation technologies due to their flexibility in the structures they can form and functionalities they can develop [79]. This includes a wide range of potential applications such as microsurgery [9], drug delivery [80], imaging [81], bio-sensing [82], intelligent cargo delivery [83] and chemical analysis [84].

For example, recently, operating Janus particles able to ablate thrombus have been developed [9]; they have biocompatible characteristics and were tested in vitro experiments. In this case, the particles are propelled by self-thermophoresis under the irradiation of near-infrared lasers, which generate temperature gradients due to the asymmetric distribution of gold on the particle (figure 1.7.a)). The particles are made biocompatible (but also biodegradable and non-immunogenic) through the coverage of their surfaces with erythrocytes (red blood cells) membrane, which also gives them higher velocities in comparison to noncovered particles in different biological fluids. The particles' velocities (figure 1.7.b)), as well as their mean square displacement (figure 1.7.c)), could be modulated based on the laser intensity providing a control parameter for the thrombolysis process. In this case, the presence of many free particles with high velocity and random motion around the thrombi enhances the efficiency of the process.

### 1.3.2 Engineering applications

One of the goals of material science and engineering is the assembly of complex structures that mimic their natural counterparts to perform useful tasks, creating new kinds of materials in the process. This is the case of active materials, a new class of soft matter that has turned into an active research area in the last decade [34]. In this process, active particles have been used to create nano- and microscale motors propelled by self-generated gradients [60]. While some applications are focused on autonomous motion [85], others instead focus on externally powered particle systems that act more like transducers gaining direct control of the particle's motion [55].

In one interesting application inspired by biological self-healing capacity [10], researchers have designed and characterized a repair system in which self-propelled Janus particles detect and repair microscopic cracks restoring the electrical conductivity of broken electronic pathways (figure 1.8). They used gold-platinum particles produced by depositing a hemispheric platinum

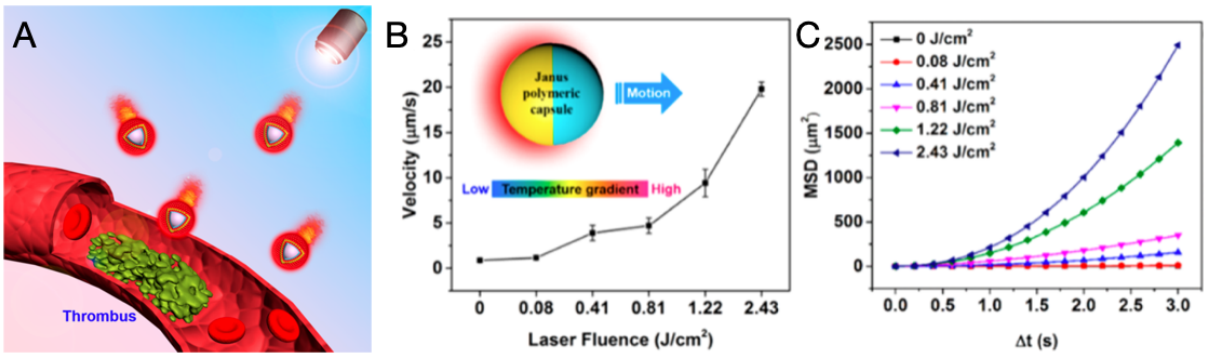


Figure 1.7: Biomedical application: micro-surgery where a local thrombus is ablated, a) application schematic, b) particle velocity as function of the laser intensity, c) mean square displacement evolution. Figures adapted from [9].

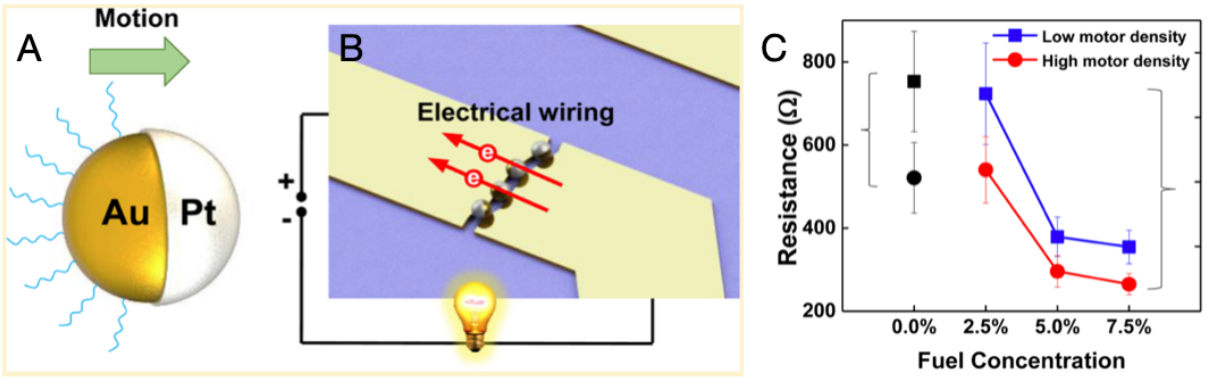


Figure 1.8: Engineering application: self-healing microchip, a) schematic of the Janus particle, b) schematic of the application, c) pathway electrical resistance as function of the particle density and fuel concentration. Figures adapted from [10].

film on the gold spheres and self-propel efficiently in the presence of hydrogen peroxide fuel. Both elements on the particle are stable metals with high electrical conductivity making them appropriate for this application. The repair is carried out by transporting and clustering the particles into the cracks (figure 1.8.b)). In this case, the hydrogen peroxide concentration determines the particles' velocity, and together with the particle density, they determine the healing efficiency (figure 1.8.c)).

In this case, higher velocities are useful to extend the search area and accelerate the repair. The creation of particle clusters is desirable if their nucleations start in the crack because of the addition of conductive materials in this zone. However, it is undesirable if the clustering happens in the suspensions because the clusters move slower than single particles. Although the clusters eventually could reach the cracks, it only decelerates the healing process.

### 1.3.3 Environmental applications

Water contamination in rivers and oceans with non-biodegradable and dangerous organic compounds is a major global environmental problem. Organic contaminants are often found in industrial wastewater and cannot be efficiently processed with conventional chemical or biological treatments. Recently, the rapid and recent advances in nanotechnology have increased

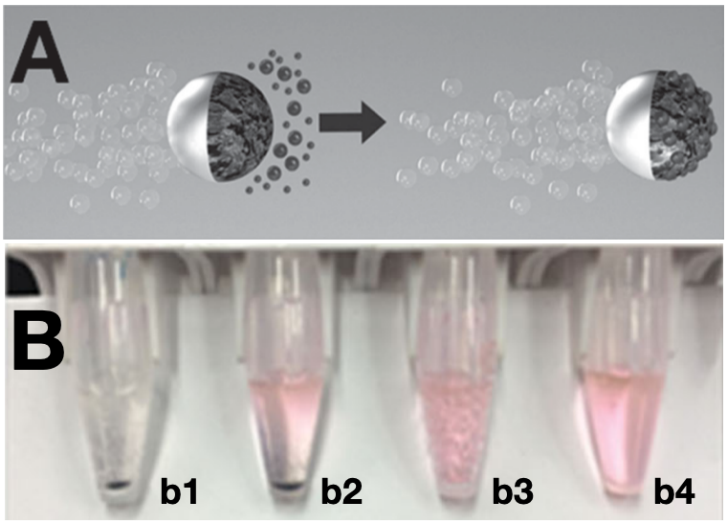


Figure 1.9: Environmental application: water purification, a) schematic of the Janus Particle (JP) and the application, b) water sample *b1*-cleaned with activated carbon platinum JP, *b2*-cleaned with activated carbon particles, *b3*-cleaned with polystyrene platinum JP, *b4*-in its initial conditions (polluted). The pink color is an indicative of the pollutant concentration. Figures adapted from [11].

the interest in finding useful nanomaterials for environmental applications, including cleaning polluted water. Some solutions rely on microjet particles immersed in hydrogen peroxide to perform the task [86, 87], which are hollow cylinders with an internal surface covered with platinum and an external surface in charge of performing the capturing of the water pollutants. Another possibility is the use of Janus particles, as described below.

While evaluating new possibilities for water purification [11], researchers have developed and tested the use of self-propelled activated carbon Janus particles that show efficient performance in removing pollutants like heavy metals or nitroaromatic explosives. The particle is constructed based on active carbon spheres, partially covered with a platinum sheet and propelled using hydrogen peroxide as a fuel (figure 1.9). Its efficiency was contrasted against two control microparticles used for this purification purposes: a polystyrene sphere analogously covered with a platinum sheet and activated carbon particles without any coating. The activated carbon Janus particles always present higher efficiencies than the other control particles (figure 1.9.b)). Their relative advantage comes from the combination of two fundamental properties: the adsorption capacity of the activated carbon and the enhanced mixing in the fluid produced by the dynamical movement of all the Janus particles in suspension. The technology can operate efficiently in raw viscous real-life environments. In this case, the random motion of the free particles enhances the effectivity of the purification process, and no clustering is reported.

The previous examples are experimental realizations of proof of concept applications. Their combination with theory and computational models research is ideal for improving these technologies, given their ability to access scenarios that are currently hard to perform experimentally. On the one hand, the theory could predict a viable propulsion mechanism before its experimental testing [88]. On the other hand, models and theory can predict collective behaviors that could emerge for a large number of active colloids above those that can be observed owing to experimental constraints [89].

As indicated in each case, sometimes the suspension of particles should remain as free

particles with random motion enhancing the mixing in the fluid. In contrast, in others, the formation of clusters is desirable in specific conditions and the directed movement of particles towards some well-defined objective. Understanding how individual particle properties and their interactions cause each state is crucial to performing these applications efficiently.

## 1.4 Interactions in reactive suspensions & collective dynamics

These phoretic self-propelled particles continually draw the researchers' attention for their enormous potential to self-organize into dynamic nonequilibrium structures such as living clusters [13] or self-propelling molecules featuring a complexity that is rarely found in the biological world. In particular, besides showing comparatively short-ranged interactions (well known from passive colloids), active particles show novel hydrodynamic interactions as well as phoretic and substrate-mediated osmotic cross-interactions (all of them long-ranged), which hinge on the action of the phoretic field gradients which are induced by the colloids on other colloids in the system. Given this system's large number of particles, its dynamics become very complex. Three origins of the interactions between particles are listed:

- Hydrodynamic: they arise from the perturbation that one swimming particle induces on their neighboring fluid (and particles). These perturbations could come from the body's surface deformation in biological swimmers or the induced slip velocity in the interfacial layer on the phoretic swimmer (because of a field gradient). This flow perturbation decays slowly in space (typically scales as $r^{-2}$ where $r$ is the interparticle distance) and advects other colloids in the system, leading to hydrodynamic cross-interactions among the microswimmers. Additionally, they can experience hydrodynamic interactions because of the influence of surfaces or walls when the perturbation they create bounces back to them.

- Phoretic: autophoretic self-propulsion is based on the action of a phoretic field gradient in the vicinity of the particle which induces this gradient. These gradients usually decay slowly in space (ideally as $r^{-1}$). This generates a phoretic motion of one colloid towards or away from a second one (attraction or repulsion), and this strength typically scales as $r^{-2}$. In this case, the presence of surfaces or external potentials deforming the phoretic field due to an active colloid generates additional phoretic self-interactions.

- Osmotic: when the external walls or other confinement are not far enough from the particles, the gradients of the phoretic field due to active particles also create forces in the interfacial layers of the walls, leading to an osmotic flow along these walls. These flows can advect other particles in the system leading to wall-induced cross-interactions. These interactions could be significant in experiments [90, 91, 92], but for this thesis in which the studies are performed in bulk, they will no longer be relevant to us.

The combination of these interactions triggers the emergence of collective motion as the well-known dynamic clustering observed in experiments [12, 13, 14]. Other collective motions mentioned previously could arise as well, including the turbulent patterns like in concentrated suspensions of swimming bacteria [3], the swarms and vortices observed in suspensions of sperms [4] or the gas-phase, chains, swarms, and clusters when the induce-charge electrophoresis is present [6]. Populations of swimmin bacteria are able to phase-separate [93, 94] or form active crystals [95].

Motility-induced phase separation (MIPS) consists of the phase separation (from a gas-like phase only to a dominant clustered phase with gaslike) that happens at sufficiently high density

and swimming velocity in active suspensions [62]. A well-known experimental setup [12] shows MIPS, where carbon-coated Janus particles propelled due to diffusiophoresis are studied. At low densities, small dynamical clusters are observed in which the mean cluster size increases linearly with the particles' velocities (figure 1.10.(Top-left)). At higher densities, phase separation into large clusters and a dilute gas phase occurs in the suspension (figure 1.10.(Top-right)).

Dynamic particle clusters were reported [13] in experiments, including self-phoretic spherical colloids half coated with platinum, which become active when adding hydrogen peroxide (figure 1.10.(Center)). Effective attractive and repulsive interactions exist, producing pronounced dynamic clustering even at very low area fractions. These forces arise from diffusiophoresis, which the colloids experience in non-uniform chemical fields produced by their neighbors while consuming the fuel. So, such artificial systems can imitate chemotactic processes found in biological systems.

The collective motion of colloidal surfers on a substrate formed by a hematite cube attached to a polymer sphere is reported [14]. The combination of self-propulsion, chemical, and steric interactions triggers the formation of clusters with a well-defined crystalline structure. These living crystals are highly dynamic: they form, rearrange, and break up continuously (figure 1.10.(Bottom)).

Various collective motion and coherent structures have been described in the preceding lines due to the interaction of many active micro-swimmers. Their experimental, numerical, and theoretical study is an active research area in which a lot of work still needs to be done to fully understand the underlying physics and be used in diverse applications.

## 1.5 Conclusions and outline of the thesis

Recently, active matter has become an active research area that studies systems with large sets of active agents, where macroscopic properties arise from the interactions between the parts, such as collective motion and coherent structures. The current chapter intends to provide the reader with a concise knowledge of the field, including the typical studied systems, their constitutive active agents, the kind of interactions that rules their physics, and some of the current efforts to provide useful applications to these systems.

In the process, we have seen the common aspects between the macroscopic and microscopic active systems (*large set* of *self-propelled elements* that induce *collective patterns*), but also the differences between them (the relative magnitude of inertial and drag forces and its implication on the way the elements move, the differences in which the elements interacts between them). Some of the most representative biological and synthetic micro-swimmers were introduced, but also their emerging collective patterns, including clustering, swarming, phase separation, and turbulence. We also see in the applications section how some properties of these systems could lead to real solutions in medicine, environment, and engineering and how the different active matter phases could be useful in each case.

From a broad perspective, the objective of my thesis is to study the collective motion and coherent structures that emerge in reactive suspensions by modeling as accurately as possible the physics in these systems for large sets of auto-phoretic particles using a particle approach. To do so, I have developed a new numerical framework called the Difusiophoretic Force Coupling Method (DFCM) that aims to be a comprehensive tool for modeling these systems today.

The rest of the manuscript is organized as follows. In Chapter 2, the physical principles and the governing equations for the collective motion of phoretic particles are first reminded. This includes the description of the hydrodynamic problem (Stokes equations) as well as the details of living in the world of 'Low Reynolds numbers'. The chemical problem is also presented

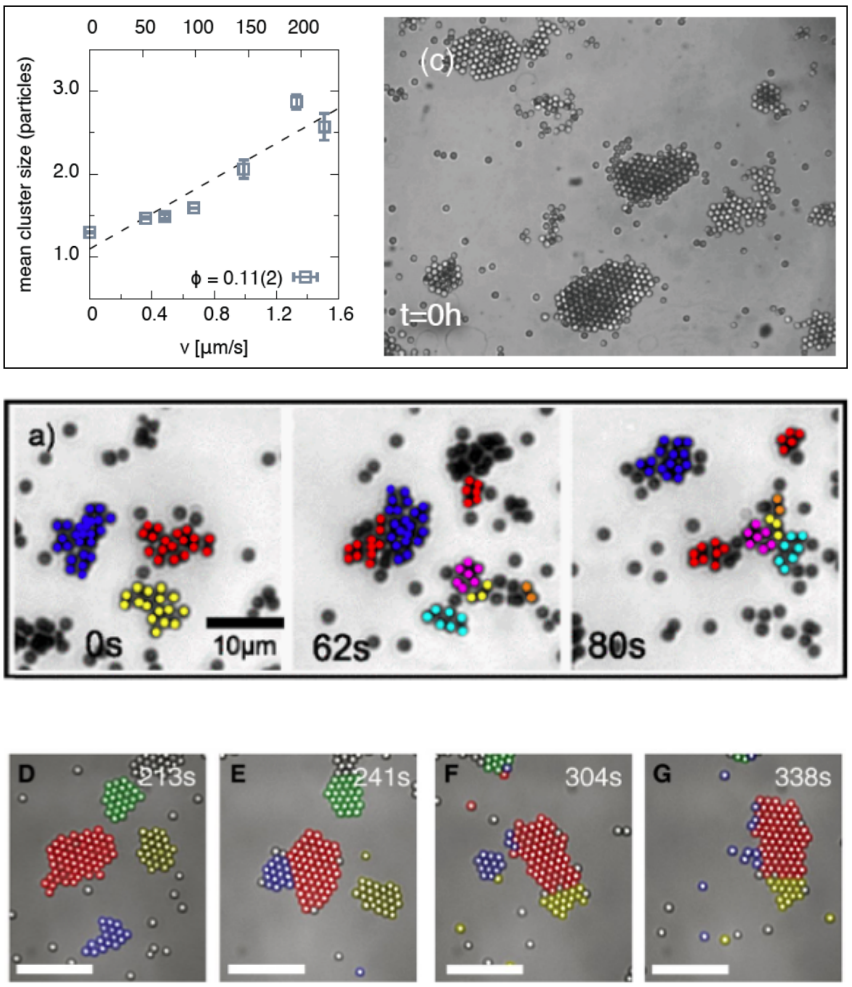


Figure 1.10: Collective dynamics of self-propelled particles showing: (Top) dynamic clustering mean cluster size variation (left) and phase separation of self-diffusiophoretic particles (right), (Center) dynamic clusters of self-phoretic active colloids interacting via chemotaxis, (Bottom) living crystals by light-activated colloidal surfers. Adapted from [12, 13, 14] respectively.

(Laplace equation) and how both problems are coupled (diffusiophoresis phenomena). Finally, a review of the current numerical methods to approach the problem is also presented.

The new Diffusiophoretic Force Coupling Method (DFCM) is presented in detail in Chapter 3. More specifically, the new solution framework for the Laplace problem is first presented. Then the main elements of the classical hydrodynamic FCM method and its extension to active particles are summarized. Afterward, the details about how the two steps are conveniently coupled to solve successively the chemical and hydrodynamic problems are presented. Finally, a validation considering particle-pairs configurations is presented, providing critical information for future use in larger suspension simulations, including the range of distances where the method provides improvements in the numerical results.

Later in Chapter 4, a scalable code in parallel is developed, presented, and validated against the results in Chapter 3. The dimensionless parameters and their ranges are determined, a parametric study is proposed, and their results for large suspensions are presented and analyzed. Additional statistical tools were used to get information about the microstructure of the reactive suspensions, the emerging regimes (or phases) depending on the system's physical parameters, and the transitions between them. Chapter 5 summarizes the main findings during the thesis and presents some possible research lines in which the current work could be used and extended.

# Chapter 2

# Fundamentals and modeling of reactive suspensions

Reactive suspensions are one of the efforts to mimic biological active matter to study it and explore applications at the micron scale. In this chapter, I will present the theoretical foundations required to study them and some of the current numerical methods used in their modeling.

## 2.1 Relevant physics for suspensions

### 2.1.1 Hydrodynamics

In the framework of classical mechanics, the dynamics of a fluid of density $\rho$ can be obtained considering the conservation of two quantities: momentum and mass, which locally can be written as:

$$\rho\Big(\frac{\partial \boldsymbol{u'}}{\partial t'} + \boldsymbol{u'} \cdot \nabla' \boldsymbol{u'}\Big) = \nabla' \cdot \boldsymbol{\sigma'} + \boldsymbol{f'}, \tag{2.1}$$

$$\frac{\partial \rho}{\partial t'} + \nabla' \cdot (\rho \boldsymbol{u'}) = 0, \tag{2.2}$$

where $\boldsymbol{u'}$ is the Eulerian fluid velocity field, $\boldsymbol{f'}$ is an external volumetric force, and $\boldsymbol{\sigma'}$ is the Cauchy stress tensor. In the common case of an incompressible Newtonian fluid of viscosity $\mu$, $\boldsymbol{\sigma'}$ becomes:

$$\boldsymbol{\sigma'} = -p'\boldsymbol{I} + 2\mu \boldsymbol{E'}, \tag{2.3}$$

where $p'$ is the pressure field, $\boldsymbol{I}$ is the identity tensor and $\boldsymbol{E'}$ is the strain rate tensor

$$\boldsymbol{E'} = \frac{1}{2}\Big(\nabla' \boldsymbol{u'} + (\nabla' \boldsymbol{u'})^T\Big). \tag{2.4}$$

Then the conservation equations are reduced to the well known Navier-Stokes and continuity equations:

$$\rho\Big(\frac{\partial \boldsymbol{u'}}{\partial t'} + \boldsymbol{u'} \cdot \nabla' \boldsymbol{u'}\Big) = -\nabla' p' + \mu \nabla'^2 \boldsymbol{u'} + \boldsymbol{f'}, \tag{2.5}$$

$$\nabla' \cdot \boldsymbol{u'} = 0. \tag{2.6}$$

These equations are made dimensionless by introducing the characteristic length scale $L^*$, time scale $T^*$, velocity scale $U^*$ of the flow, which depends on the particular system and could be defined later. These quantities are used to define the dimensionless variables $\boldsymbol{r} = \boldsymbol{r'}/L^*$, $t = t'/T^*$, $\boldsymbol{u} = \boldsymbol{u'}/U^*$, $p = p'/(\mu U^*/L^*)$, $\boldsymbol{f} = \boldsymbol{f'}/(\mu U^*/L^{*2})$ and $\nabla = L^* \nabla'$ as follow

$$\mathrm{Re}\Big(\mathrm{St}\frac{\partial \boldsymbol{u}}{\partial t} + \boldsymbol{u} \cdot \nabla \boldsymbol{u}\Big) = -\nabla p + \nabla^2 \boldsymbol{u} + \boldsymbol{f}, \tag{2.7}$$

$$\nabla \cdot \boldsymbol{u} = 0, \tag{2.8}$$

where the dimensionless Reynolds number is introduced as the ratio between the inertial and the viscous forces in the system

$$\mathrm{Re} = \frac{|\rho \boldsymbol{u'} \cdot \nabla' \boldsymbol{u'}|}{|\mu \nabla'^2 \boldsymbol{u'}|} = \frac{\rho U^* L^*}{\mu}, \tag{2.9}$$

and the dimensionless Strouhal number is the ratio between the convective time $L^*/U^*$ and the characteristic time scale $T^*$

$$\mathrm{St} = \frac{L^*}{U^* T^*}. \tag{2.10}$$

Together with the boundary conditions on the objects' surface and the force and torque balances, the previous equations govern the motion of objects immersed in a fluid. Depending on their size and velocity (as well as the fluid properties), one or another term in the equations will be dominant. For example, for a human swimming in water $\mathrm{Re} \approx 10^4$, the full Navier-Stokes equations will be the applicable ones. On the other hand, for tiny swimmers in water like bacteria (or suspension of micron-size particles) $\mathrm{Re} \approx 10^{-4}$ and so a reduced version of these equations (called Stokes equations) will be the relevant ones. In fact, for the particular systems of interest in this thesis (i.e., suspensions in micro-scale flows), typically, the viscous forces are much greater than the inertial ones, resulting in small Reynolds numbers ($\mathrm{Re} \ll 1$) and making in principle the left-hand side of equation 2.7 negligible.

However if the product ReSt is of order 1, this leads to the dimensionless unsteady Stokes equations in cases in which the importance of the local acceleration can't be neglected

$$\frac{\partial \boldsymbol{u}}{\partial t} = -\nabla p + \nabla^2 \boldsymbol{u} + \boldsymbol{f}. \tag{2.11}$$

In the absence of an intrinsic time scale differing from $L^*/U^*$, we could take $T^* = L^*/U^*$ making $\mathrm{St} = 1$, which in general will be the case for the study of reactive suspensions in this thesis. Consequently, the right hand side terms in 2.7 will be the only relevant in the system, leading to the dimensionless Stokes equations

$$\nabla p - \nabla^2 \boldsymbol{u} = \boldsymbol{f}. \tag{2.12}$$

By comparing the Stokes equations against the Navier-Stokes equations, we note the loss of the time-dependent term and the non-linear term, something that drastically changes the physics of the system and the characteristic of these flows. In particular, some important properties of the Stokes equations are [96]:

- Linearity: from a mathematical point of view, it means that we could apply the superposition principle, and so by adding different solutions of the Stokes equations, we get new solutions of them. It also means that one physical solution does not affect the others and that they should be coupled only by the boundary conditions. Physically, because of this property, a change in the magnitude of the forcing is linearly reflected in the velocity and vice-versa.

- Reversibility: once we have a solution to the Stokes equations $(p, \boldsymbol{u}, \boldsymbol{f})$, we could take its reverse flow $(-p, -\boldsymbol{u})$, and it will also be a solution of the equations (obtaining an inversed force $(-\boldsymbol{f})$). By reversing the driving force, the streamlines remain the same, but the flow direction is reversed. The application of this property helps to explain easily why a sphere settling adjacent to a vertical plane wall remains at the same distance of it [15], or why a sphere in a Poiseuille flow does not cross streamlines [96].

- Instantaneity: pressure, velocity, and body forces balance each other always no matter if the flow is unsteady, this means that the instantaneous flow only depends on the boundary geometry and the boundary conditions at that specific time, not in the history of the system, and so the boundary motion is communicated to the entire fluid instantly.

The (dimensionless) hydrodynamic force $\boldsymbol{F}$ and torque $\boldsymbol{T}$ that act on a body immersed in a fluid are calculated by integrating the stress tensor along the body surface,

$$\boldsymbol{F} = \int_S \boldsymbol{\sigma} \cdot \boldsymbol{n} \, \mathrm{d}S, \qquad \boldsymbol{T} = \int_S \boldsymbol{r} \times (\boldsymbol{\sigma} \cdot \boldsymbol{n}) \, \mathrm{d}S, \tag{2.13}$$

where $\boldsymbol{n}$ is the normal vector to the object surface and $\boldsymbol{\sigma}$ is the dimensionless stress tensor which following the previous scaling applied to the pressure $\boldsymbol{\sigma} = \boldsymbol{\sigma}'/(\mu U/L)$ becomes:

$$\boldsymbol{\sigma} = -p\boldsymbol{I} + 2\boldsymbol{E} = -p\boldsymbol{I} + \left(\nabla\boldsymbol{u} + (\nabla\boldsymbol{u})^T\right). \tag{2.14}$$

Given the linearity of the Stokes equations it is possible to solve the velocity $\boldsymbol{u}$ and the pressure $p$ fields using the Green's function over the external force $\boldsymbol{f}$ leading to the general solution:

$$\boldsymbol{u}(\boldsymbol{r}) = \int \boldsymbol{O}(\boldsymbol{r} - \boldsymbol{r}^*) \cdot \boldsymbol{f}(\boldsymbol{r}^*)\, \mathrm{d}V^*, \tag{2.15}$$

$$p(\boldsymbol{r}) = \int \boldsymbol{o}(\boldsymbol{r} - \boldsymbol{r}^*) \cdot \boldsymbol{f}(\boldsymbol{r}^*)\, \mathrm{d}V^*, \tag{2.16}$$

where $\boldsymbol{O}(\boldsymbol{r})$ and $\boldsymbol{o}(\boldsymbol{r})$ are the Oseen tensor and the pressure vector respectively given by

$$\boldsymbol{O}(\boldsymbol{r}) = \frac{1}{8\pi}\left(\frac{\boldsymbol{I}}{r} + \frac{\boldsymbol{r}\boldsymbol{r}}{r^3}\right), \tag{2.17}$$

$$\boldsymbol{o}(\boldsymbol{r}) = \frac{1}{4\pi}\frac{\boldsymbol{r}}{r^3}. \tag{2.18}$$

The most basic solution is the case of the force monopole (also called point force) $\boldsymbol{f} = f_0\boldsymbol{e}\delta(\boldsymbol{r} - \boldsymbol{Y}_0)$, located at $\boldsymbol{Y}_0$ and oriented along $\boldsymbol{e}$ in an unbounded fluid where $\delta(\boldsymbol{r})$ is the Dirac $\delta$ function. The solution for this case, is the fundamental solution to the Stokes equation called *Stokeslet*

$$\boldsymbol{u}_{STO}(\boldsymbol{r}_0) = \frac{f_0}{8\pi r_0}\left(\boldsymbol{I} + \frac{\boldsymbol{r}_0\boldsymbol{r}_0}{r_0^2}\right) \cdot \boldsymbol{e}, \tag{2.19}$$

where $\boldsymbol{r}_0 = \boldsymbol{r} - \boldsymbol{Y}_0$ and $r_0 = |\boldsymbol{r}_0|$. The Stokeslet decays slowly as $r_0^{-1}$ and it describes the flow far from the object when it is forced externally, like with gravity in a settling problem. One can also construct higher order solutions using a singular multipole expansion of the flow field [97, 98, 99]. The next contributions decay faster and are called force dipole $r_0^{-2}$, force quadrupole $r_0^{-3}$, force octupole $r_0^{-4}$ and so on.

As in electrostatics or gravitation, the force dipole consist of two opposite points forces separated by a distance $l$: if the two forces are aligned along the body axis ($\boldsymbol{f}_1 = f_0\boldsymbol{e}\delta(\boldsymbol{r} - (\boldsymbol{Y}_0 + (l/2)\boldsymbol{e}))$ and $\boldsymbol{f}_2 = -f_0\boldsymbol{e}\delta(\boldsymbol{r} - (\boldsymbol{Y}_0 - (l/2)\boldsymbol{e}))$), we will get a symmetric solution (along the the body axis). In the limit $l \to 0$ (or when $r_0 \gg l$), but keeping the strength of the symmetric dipole $f_d = f_0 l$ finite (also known as *Stresslet*), the flow dipole becomes

$$\boldsymbol{u}_{STR}(\boldsymbol{r}_0) = \frac{f_d}{8\pi r_0^2}\left(-\frac{\boldsymbol{r}_0\boldsymbol{I}}{r_0} + \frac{3\boldsymbol{r}_0\boldsymbol{r}_0\boldsymbol{r}_0}{r_0^3}\right) : \left(\boldsymbol{e}\boldsymbol{e} - \frac{\boldsymbol{I}}{3}\right), \tag{2.20}$$

when $f_0 > 0$ the two forces point outwards and the flow field is called extensile, while if $f_0 < 0$ the two forces point inwards and the flow field is called contractile. The force dipole decays faster than the force monopole as $r_0^{-2}$ and it describes the dominant flow field of micro-swimmers. In this context, the micro-swimmers with extensile flows are called *pushers*, since they push fluid along their body axes, while contractile flows are called *pullers*, since they pull fluid along it. In contrast, if the two forces are not aligned along the body axes, some torque is induced and so some rotational flow is induced as well,

$$\boldsymbol{u}_{ROT}(\boldsymbol{r}_0) = -\frac{\boldsymbol{T}_h \times \boldsymbol{r}_0}{8\pi r_0^3} \tag{2.21}$$

where the strength of the anti-symmetric dipole (called *Rotlet*) could be calculated using the hydrodynamical torque $\boldsymbol{T}_h$.

Independent of the previous solutions and the higher order terms, there are other kind of solutions called source singularities. They solves the Stokes equations for constant pressure fields, obtaining the Laplace equation for the velocity which implies potential flow solutions. By combining sources and sinks in the fluid, one can obtain source monopoles, dipoles, quadrupoles and so on. The *Source Dipole* for microswimmers is given by

$$\boldsymbol{u}_{SD}(\boldsymbol{r}_0) = \frac{\boldsymbol{D}}{8\pi r_0^3} \cdot \Big( -\boldsymbol{I} + \frac{3\boldsymbol{r}_0\boldsymbol{r}_0}{r_0^2} \Big) \tag{2.22}$$

where $\boldsymbol{D}$ is the source dipole strength.

Given the linearity of the Stokes equations, any flow field can be expressed as the sum of all the relevant force and source singularities. For instance, the exact solution for the case of a *passive sphere* of radius $a$ settling at velocity $\boldsymbol{U}$ by the effect of an external force $\boldsymbol{F}$ is the combination of the Stokeslet and source dipole flow field and in the laboratory frame of reference is

$$\boldsymbol{u}_{PS}(\boldsymbol{r}_0) = \frac{\boldsymbol{F}}{8\pi r_0} \cdot \Big( \boldsymbol{I} + \frac{\boldsymbol{r}_0\boldsymbol{r}_0}{r_0^2} \Big) + \frac{a^2\boldsymbol{F}}{24\pi r_0^3} \cdot \Big( \boldsymbol{I} - \frac{3\boldsymbol{r}_0\boldsymbol{r}_0}{r_0^2} \Big) \tag{2.23}$$

in which the no-slip boundary condition applies on the sphere surface $\boldsymbol{u}(r_0 = a) = \boldsymbol{U}$. This is a typical example of passive particle that is moved externally, in this case by an external body force, but it could happen through surfaces forces by a pressure gradient. Another way to induce directed motion is through phoretic transport [64], using temperature, chemical or electric potential gradients, processes called thermophoresis, diffusiophoresis and electrophoresis. On the other hand, active swimmers are able to swim through surface deformations or generating their own phoretic gradients in which they could drift.

An important property of Stokes flows is called the Reciprocal theorem, and it is a principle of virtual work which takes a particularly simple form thanks to the linearity of Stokes equations 2.12. Alternatively, it could be seen as the application of Green's second identity to the viscous equations of motion. Considering a volume of fluid $V$, bounded by a surface $S$ with outward normal $\boldsymbol{n}$, the reciprocal theorem states that the mixed virtual works of two solutions to the Stokes equations ($\boldsymbol{u}_1, \boldsymbol{\sigma}_1$ and $\boldsymbol{u}_2, \boldsymbol{\sigma}_2$, with the same boundary conditions at infinity) are equal:

$$\int_S \boldsymbol{u}_1 \cdot \boldsymbol{\sigma}_2 \cdot \boldsymbol{n} \mathrm{d}S = \int_S \boldsymbol{u}_2 \cdot \boldsymbol{\sigma}_1 \cdot \boldsymbol{n} \mathrm{d}S, \tag{2.24}$$

The usefulness of this theorem is that it allows one to determine some results for one unknown solution of the Stokes equations $\boldsymbol{u}_1$, based upon another known solution $\boldsymbol{u}_2$ in the same geometry that shares the exact boundaries but with different boundary conditions.

### 2.1.2 Swimming at low Reynolds numbers

In the case of low Reynolds numbers, the hydrodynamics poses major challenges for swimming if we compare it to our knowledge in the macroscopic scales where the inertia dominates over the fluid's dissipative friction force. The time independence on Stokes equation (2.12), means that only an asymmetric swimming stroke can lead to net motion [100, 101]. The reversibility property of the Stokes equations leads to an interesting result regarding swimming at low Reynolds numbers called Scallop theorem [39], by which a swimmer that exhibits time-symmetric motion cannot achieve net displacement. This swimmer deforms its body into a

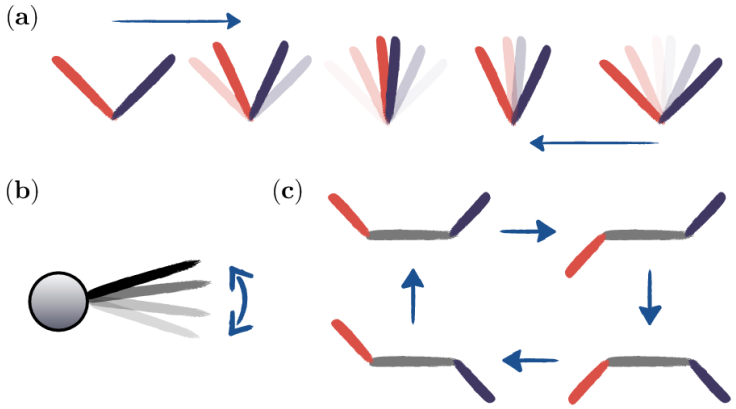


Figure 2.1: Scallop theorem examples of a) one degree of freedom motion of a scallop without net motion, the sequence of shapes is indistinguishable viewed forward or backward in time (reciprocal motion), b) another one degree of freedom organism which flaps its straight, rigid tail (reciprocal motion) without effective swimming as well, c) Purcell's two degrees of freedom swimmer undergoing non-reciprocal deformation and swimming. Figures reproduced from [15].

particular shape through a sequence of motions (moving it from its original position to a new one) followed by the reversed sequence reaching the original shape (and returning it to its original position) as sketched in figure 2.1.a). It is named considering the one degree of freedom motion of a scallop opening and closing. Bodies with a single degree of freedom deform reciprocally, and subsequently, they do not achieve locomotion in low Reynolds number environments.

Consequently, it is needed to introduce some symmetry-breaking to produce propulsion in this context. The simplest example is a Purcell type swimmer [39], which possesses two degrees of freedom of motion: a two-hinged body composed of three rigid links rotating out-of-phase with each other achieving locomotion as sketched in figure 2.1.c). Biological swimmers, like sperm or Escherichia coli bacteria, have a rotating helical tail whose chirality allows for symmetry-breaking under continuous rotation. Metachronal waves along Paramecia and Opalina lead to effective propulsion generating a net directional slip velocity on its surface [102]. Autophoretic swimmers produce local concentration gradients on their surface, which provides them the necessary phoretic forcing to induce self-propulsion [63].

Considering the general problem of self-propelled motion at low Reynolds number, we will call 'swimmer' any body that deforms its surface to sustain movement through fluid without external forces and torques. The lack of inertia for our regime implies the force-free and torque-free condition

$$\boldsymbol{F} = \int_S \boldsymbol{\sigma} \cdot \boldsymbol{n} \, \mathrm{d}S = \boldsymbol{0}, \qquad \boldsymbol{T} = \int_S \boldsymbol{r}_0 \times (\boldsymbol{\sigma} \cdot \boldsymbol{n}) \, \mathrm{d}S = \boldsymbol{0}, \tag{2.25}$$

where $\boldsymbol{r}_0 = \boldsymbol{r} - \boldsymbol{Y}_0$ is the generic position of some point in the body surface with respect to its centroid $\boldsymbol{Y}_0$.

Consider a body submerged in a viscous fluid: using a fixed frame of reference on its body, the swimmer deforms its surface in a prescribed time-dependent pattern given by a velocity field on its surface $\boldsymbol{u}^s(t)$. The swimmer could be seen instantaneously as a solid body with unknown velocity $\boldsymbol{U}(t)$ and rotation rate $\boldsymbol{\Omega}(t)$. The instantaneous velocity on the swimmer's surface is then given by

$$\boldsymbol{u} = \boldsymbol{U} + \boldsymbol{\Omega} \times \boldsymbol{r}_0 + \boldsymbol{u}^s, \tag{2.26}$$

which provides the boundary conditions needed to solve Stokes equations. The unknown values of the swimmer velocities are determined by satisfying the force-free and torque-free condition 2.25. A significant simplification to the swimming problem was derived [103] applying the reciprocal theorem 2.24. Let $\boldsymbol{u}$ and $\boldsymbol{\sigma}$ be the velocity and stress fields we are looking for in the swimming problem and suppose that $\boldsymbol{u}_2$ and $\boldsymbol{\sigma}_2$ are the velocity and stress fields for the auxiliary problem of instantaneous solid body motion of the swimmer with velocity $\boldsymbol{U}_2$ and rotation rate $\boldsymbol{\Omega}_2$ (correspondingly force $\boldsymbol{F}_2$ and torque $\boldsymbol{T}_2$). Applying the reciprocal theorem, we obtain [103]

$$\boldsymbol{U} \cdot \boldsymbol{F}_2 + \boldsymbol{\Omega} \cdot \boldsymbol{T}_2 = -\int_S \boldsymbol{u}^s \cdot \boldsymbol{\sigma}_2 \cdot \boldsymbol{n} \mathrm{d}S, \tag{2.27}$$

that shows explicitly how the $\boldsymbol{U}$ and $\boldsymbol{\Omega}$ may be found instantaneously in terms of the surface velocity $\boldsymbol{u}^s$, given the solution to the auxiliary problem of the flow induced by the motion of the rigid body with instantaneous shape $S$, subject to $\boldsymbol{F}_2$ and $\boldsymbol{T}_2$. Note that in 2.27, the variables $\boldsymbol{U}$, $\boldsymbol{\Omega}$, $\boldsymbol{F}_2$ and $\boldsymbol{T}_2$ are implicitly time dependent through the time-dependence of the shape $S$. In the specific case when the shape of the swimmer surface remains constant in the normal direction and all deformations are tangential to the surface ($\boldsymbol{u}^s \cdot \boldsymbol{n} = 0$), the previous equation simplifies even more. For a spherical swimmer of radius $a$ with these properties, we got explicitly [103]

$$\boldsymbol{U} = -\frac{1}{4\pi a^2}\int_S \boldsymbol{u}^s \mathrm{d}S = -\langle \boldsymbol{u}^s \rangle, \tag{2.28}$$

$$\boldsymbol{\Omega} = -\frac{3}{8\pi a^3}\int_S \boldsymbol{n} \times \boldsymbol{u}^s \mathrm{d}S = -\frac{3}{2a}\langle \boldsymbol{n} \times \boldsymbol{u}^s \rangle, \tag{2.29}$$

in which the notation $\langle . \rangle$ simply means the averaging on the surface of the particle. For our particular case of interest of reactive suspensions and phoretic particles, the slip velocity $\boldsymbol{u}^s$ is known and it is provided from the coupling between chemistry and hydrodynamics. Its explicit form will be presented later.

### 2.1.3 Squirmer model

The active motion of self-propelled particles is essentially determined by the surface velocity $\boldsymbol{u}^s$, which can be assumed prescribed. One model used frequently today for micro-swimmers is the one called the squirmer model [104, 105], which consists of a spherical self-propelled particle that moves through a fluid with velocity $\boldsymbol{U} = U\boldsymbol{e}$, by using axisymmetric surface distortions along the swimming direction $\boldsymbol{e}$. When the amplitude of the distortions is small compared to the particle radius $a$, the surface velocity $\boldsymbol{u}^s(\boldsymbol{r}_s = a\boldsymbol{n})$ could become described in general by its radial $u_r^s$ and azimuthal $u_\theta^s$ components using the Legendre polynomials $L_n$:

$$u_r^s = \sum_{n=0}^{\infty} A_n(t) L_n(x), \tag{2.30}$$

$$u_\theta^s = \sum_{n=1}^{\infty} B_n(t) V_n(\theta), \tag{2.31}$$

$$V_n(\theta) = \frac{2\sin\theta}{n(n+1)} \frac{\mathrm{d}L_n(x)}{\mathrm{dx}}, \tag{2.32}$$

where $x = \cos(\theta)$ and the angle $\theta$ is measured from the direction $\boldsymbol{e}$. The coefficients $A_n(t)$ and $B_n(t)$ are called surface velocity modes.

For most of the micro-swimmers, only the polar component $u^s_\theta$ is relevant, and so we take $A_n = 0$ for all $n$. Typically only the first two terms of $u^s$ are used ($B_n = 0$ for $n >= 3$), since $B_1$ and $B_2$ captures well the basic features of the polar velocity [106]. It can be demonstrated that while $B_1$ is linearly related to the source dipole strength (that decays as $r^{-3}$ as in 2.22) and related to the particle velocity: $U = 2B_1/3$, the coefficient $B_2$ is linearly related to the force dipole strength (that decays as $r^{-2}$ as in 2.20) and is proportional to the particle stresslet.

The squirmer parameter $\beta = B_2/B_1$, which describes the relative intensities between the second and first modes, is used to distinguish between types of swimmers (figure 2.2): in particular if $\beta < 0$ it is called "pusher" bringing fluid laterally and expelling it along $\boldsymbol{e}$, while if $\beta > 0$ it is called "puller" bringing fluid along $\boldsymbol{e}$ and expelling it laterally. Finally, in the transition between pushers and pullers ($\beta = 0$), the neutral swimmer simply moves fluid from front to back. Considering the hydrodynamical signature of some biological swimmers, some examples of these micro-swimmers types are [40] Escherichia coli for pushers [107] with the propelling apparatus at the back of their cell bodies, Paramecium caudatum [108] for neutral swimmers with mobile cilias around all its body, and Chlamydomonas reinhardtii [109] for pullers having their flagella in front of the cell body. The squirmer model was widely used, in the modeling of the hydrodynamic interactions of pair of squirmers and Paramecias [108, 110], in the collective motion of squirmers in a quiescent fluid [111, 112] and in the flow [113, 114].

### 2.1.4 Transport equations

In the framework of transport mechanism, we can consider a solute that diffuses in a fluid and describe its evolution trough the concentration $c'$, considering the conservation of mass of the solute locally

$$\frac{\partial c'}{\partial t'} + \nabla' \cdot \boldsymbol{j'} = g', \tag{2.33}$$

where $g'$ is the solute volumetric generation. The term $\boldsymbol{j'}$ is the solute flux, including both the advective and diffusive terms (that in the case of the Fick's law) becomes:

$$\boldsymbol{j'} = \boldsymbol{u'}c' - D\nabla' c', \tag{2.34}$$

where $D$ is the solute diffusivity. Considering this flux definition, the solute conservation of mass becomes the advection-diffusion-reaction equation:

$$\frac{\partial c'}{\partial t'} + \boldsymbol{u'} \cdot \nabla' c' = D\nabla'^2 c' + g'. \tag{2.35}$$

As previously, this equation could be made dimensionless by introducing the characteristic length scale $L$, time scale $T$, velocity scale $U$ of the flow and the solute concentration scale $C$. These quantities can be used to define the dimensionless variables $c = c'/C$, $t = t'/T$, $\boldsymbol{u} = \boldsymbol{u'}/U$, $g = g'/(DC/L^2)$ and $\nabla = L\nabla'$ as follow

$$\mathrm{Pe}\left(\mathrm{St}\frac{\partial c}{\partial t} + \boldsymbol{u} \cdot \nabla c\right) = \nabla^2 c + g. \tag{2.36}$$

where the dimensionless Péclet number have been introduced as an ratio between the advective and diffusive transport

$$\mathrm{Pe} = \frac{|\boldsymbol{u'} \cdot \nabla' c'|}{|D\nabla'^2 c'|} = \frac{UL}{D} \tag{2.37}$$

and the Strouhal number has been introduced before in 2.10. Again, in the absence of any intrinsic time scale other than $L/U$, we could take $\mathrm{St} = 1$ and for the case of reactive suspensions,

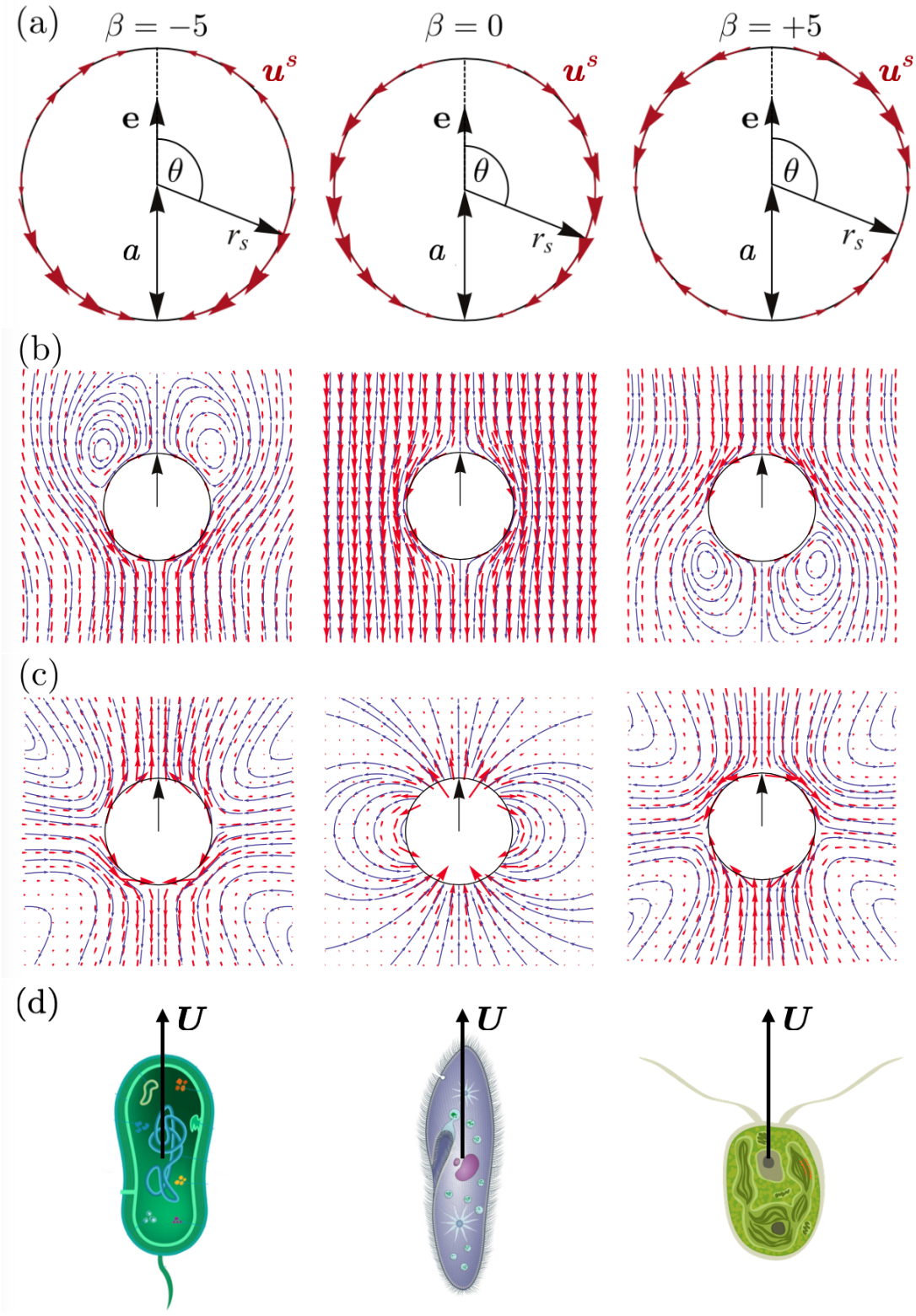


Figure 2.2: Different types of micro-swimmers according to the squirmer parameter $\beta$: a) Surface velocity $u^s_\theta$ for a pusher ($\beta < 0$), a neutral squirmer ($\beta = 0$) and a puller ($\beta > 0$). b) Corresponding velocity fields (red) and stream lines (blue) in the frame moving with the swimmer. c) Velocity fields (red) and stream lines (blue) in the lab frame. d) Corresponding biological swimmers: Escherichia coli, Paramecium and Chlamydomonas. Figures a), b) and c) adapted from [16].

normally Pe $\ll 1$, and so only the right hand side terms in 2.36 wil be relevant for our analysis reducing it to Poisson equation (or Laplace equation if there's no sources $g$):

$$\nabla^2 c = -g. \tag{2.38}$$

which also shares the Stokes equations properties of linearity, reversibility and instantaneity. In fact, given its linearity, the Green function approach could be use as well given the general solution

$$c(\boldsymbol{r}) = \int \Theta(\boldsymbol{r} - \boldsymbol{r}^*) g(\boldsymbol{r}^*)\, \mathrm{d}V^*, \tag{2.39}$$

where $\Theta(\boldsymbol{r})$ is the Green's function given by

$$\Theta(\boldsymbol{r}) = \frac{1}{4\pi r}, \tag{2.40}$$

The most basic solution is the case of the *source monopole* $g = q_0 \delta(\boldsymbol{r} - \boldsymbol{Y}_0)$, located at $\boldsymbol{Y}_0$ in an unbounded medium. The solution for this case, is the fundamental solution to the Laplace equation:

$$c_M(\boldsymbol{r}_0) = \frac{q^M}{4\pi r_0}, \tag{2.41}$$

where $\boldsymbol{r}_0 = \boldsymbol{r} - \boldsymbol{Y}_0$ and $r_0 = |\boldsymbol{r}_0|$. This solution decays slowly as $r_0^{-1}$ and it describes the concentration far from reactive objects. One can also construct higher order solutions using a singular multipole expansion of the concentration field [97], being the next contributions called *source dipole* $r_0^{-2}$,

$$c_D(\boldsymbol{r}_0) = \frac{\mathbf{q}^D \cdot \mathbf{r}_0}{4\pi r_0^3}, \tag{2.42}$$

source quadrupole $r_0^{-3}$, and so on.

A boundary condition of interest for the case of autophoretic particles is the constant flux condition. It defines the surface chemical forces that generate the chemical gradients in which the particle will drift autonomously. In the reference frame of the particle and neglecting advection effects (valid for small Pe) the solute obeys

$$\boldsymbol{n} \cdot \boldsymbol{j} = -\boldsymbol{n} \cdot \nabla c = \alpha(\boldsymbol{n}), \tag{2.43}$$

where $\alpha(\boldsymbol{n})$ is called the *chemical activity* and it is function of the position on the particle's surface. It measures the generation ($\alpha > 0$) or consumption ($\alpha < 0$) of the solute by chemical reactions. In general, the description of this process involves additional coupled transport problems for several species involved in the surface reactions, however, for simplicity we use here fixed local values of $\alpha$.

### 2.1.5 Phoretic transport and diffusiophoresis

As stated previously, in the low Reynolds number limit, the micro-swimmers need to introduce some symmetry-breaking to produce propulsion in this context. For instance, metachronal waves along Paramecia lead to self-propulsion generating a net directional slip velocity on its surface [102]. The interface between the swimmer and the surrounding medium is a small region with finite thickness where dynamic processes happen in both biological and catalytic swimmers. From a macroscopic point of view (at the scale of the swimmers or suspensions of

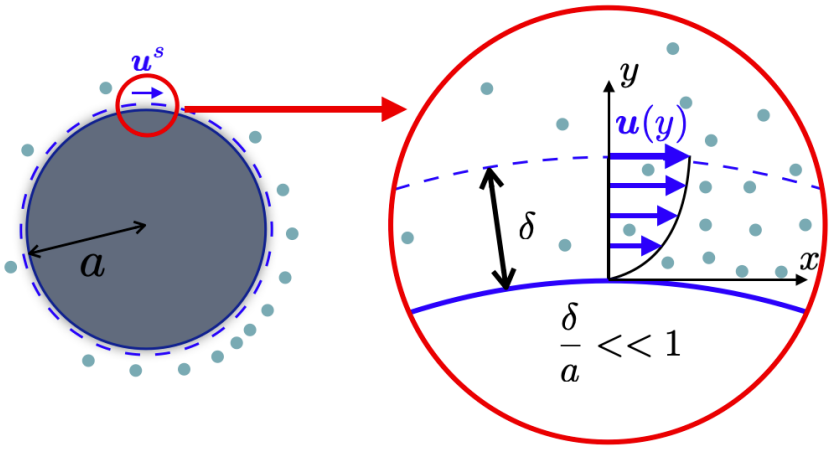


Figure 2.3: Schematic of the phoretic transport with its two scales: the macroscopic scale ($L \approx a$) and the interaction layer ($L \approx \delta$) showing the fluid velocity at each scale. The green points represents the solute molecules in the fluid.

swimmers), this results in a surface slip velocity which is, at least partially, counter-intuitive considering the classical no-slip condition on solid bodies.

In this section, we will focus on (passive) colloidal particles that experience phoresis, which is the motion of particles in a fluid, induced by the interaction of some external imposed gradient $\nabla\xi$ with the particles' surface [64, 115, 116, 117]. In a thin layer $\delta \ll a$ above the particle surface (considering a sphere of radius $a$), the field gradient $\nabla\xi$ induces a tangential near-surface flow, which increases from zero (no-slip boundary condition) in the radial direction and saturates at an effective radius $a_e = a + \delta$ to a constant value (Figure 2.3).

The field $\xi$ could be a chemical concentration field $c$, a temperature field $T$, or an electric potential $\phi$, and the corresponding colloidal transport mechanism are called diffusiophoresis, thermophoresis, and electrophoresis. From now, we will focus mainly on diffusiophoresis. Since the interfacial layer is usually very thin, the velocity appears discontinuous at the length scale of the particle $a$, but in fact, is continuous with a smooth variation over the interfacial layer $\delta$.

In order to account approximately the effect of the excluded volume, the dipole interactions (in the case of ionic solute molecules) and the van der Waals forces, a potential energy $\phi(y)$ such that $-\nabla\phi$ is the force experienced by a molecule at distance $y$ from the (almost flat) surface is proposed in the interaction layer as follow. If $c'$ is concentration of solute molecules at steady state, it should satisfy the conservation of mass of the solute equation (2.33) for the flux $\boldsymbol{j'} = -D\left(\nabla' c' + \frac{c'\nabla'\phi}{kT}\right)$ with the boundary conditions $\boldsymbol{n} \cdot \boldsymbol{j'}|_{y=0} = 0$ and $c'|_{y\to\infty} = c^s$, giving explicitly [64],

$$c'(x, y) = c^s(x) e^{(-\phi(y)/kT)}, \tag{2.44}$$

where $c^s$ is the concentration at the macroscopic scale which varies only at this scale. Considering a viscous and incompressible fluid, with the boundary conditions $\boldsymbol{u'}|_{y=0} = \boldsymbol{0}$ and $\boldsymbol{u'}|_{y\to\infty} = \boldsymbol{u}^s$, forced by the volume force $\boldsymbol{f'} = -c'\nabla\phi$ provided by the interactions between solute molecules and the surface, they should obey the Stokes equation (2.12). Given the relation $\delta \ll a$ in the interaction layer, one can use the boundary layer theory obtaining a parallel flow variable along $y$ [115], as in figure 2.3

$$u'_x(x, y) = \left[\frac{-kT}{\mu}\int_0^y y' \, (e^{(-\phi(y')/kT)} - 1)\, dy'\right] \frac{\partial c'(x)}{\partial x}. \tag{2.45}$$

Considering the matching boundary condition between the two regions $\boldsymbol{u'}|_{y\to\infty} = \boldsymbol{u}^s$, we could write at the macroscopic scale $u'_x(x) = M\,\frac{\partial c'(x)}{\partial x}$, with $M$ a new property of the interaction layer known as *phoretic mobility*

$$M = \frac{-kT}{\mu}\int_0^\infty y'\,(e^{(-\phi(y')/kT)} - 1)\,dy', \tag{2.46}$$

which can be either positive or negative depending on how the solute interacts with the particles surface. As it will be explained later, the sign of the mobility $M$ is vital to determine the repulsive or attractive nature of inter-particle phoretic interactions. Its experimental determination is not easy since it requires detailed knowledge of the surface property $\phi$.

In the macroscopic scale, the relation for the slip velocity could be generalized, considering that in the interaction layer the direction $x$ is simply the tangential direction and $y$ is the normal direction

$$\boldsymbol{u}^s = M(\mathbf{n})\,\nabla_{||}c = M(\mathbf{n})\,(\boldsymbol{I} - \boldsymbol{nn})\cdot\nabla c. \tag{2.47}$$

where $\mathbf{n}$ is the normal vector to the particle surface and the mobility $M$ is in general a value dependent of the point in consideration over the particle surface.

## 2.2 Reactive suspensions modeling

### 2.2.1 Governing equations summary

Here, a concise summary of the relevant equations and assumptions for the type of systems we will consider in the rest of the manuscript is provided to simplify future references.

The coupled motion of $N$ identical and spherical phoretic particles of equal radius $a$ is considered within a viscous fluid of density $\rho$ and viscosity $\mu$. Particle $n$ occupies a volume $V_n$ bounded by its surface $S_n$ and centred at $\boldsymbol{Y}_n(t)$, and has orientation $\boldsymbol{p}_n$; $\boldsymbol{U}_n$ and $\boldsymbol{\Omega}_n$ are its translation and rotation velocities. The fluid domain is noted $V_f$ and may be bounded or unbounded (figure 2.4a).

Each particle emits a chemical solute of diffusivity $D$ on the catalytic parts of its surface with a fixed spatially-dependent rate of characteristic magnitude $\alpha_0$ and can generate a slip flow in response to a surface concentration gradient, with characteristic phoretic mobility $M_0$. In the following, all variables and equations are made dimensionless using $a$, $U_0 = \alpha_0 M_0/D$, and $C = a\alpha_0/D$ as characteristic length, velocity, and concentration scales.

As a result of its surface activity, the dimensionless relative concentration $c$ (with respect to its background value far from the particles) satisfies the following Neumann condition on the surface of particle $n$:

$$-\boldsymbol{n}\cdot\nabla c = \alpha_n(\boldsymbol{n}) \qquad \text{on } S_n, \tag{2.48}$$

where $\alpha_n(\boldsymbol{n})$ is the dimensionless activity distribution (i.e. emission rate) and $\boldsymbol{n}$ is the outward normal unit vector on $S_n$. For sufficiently small particles, the solute's dynamic is purely diffusive, i.e. the relevant Péclet number $\mathrm{Pe} = aU_0/D \ll 1$, so that $c$ obeys Laplace's equation outside the particles,

$$\nabla^2 c = 0 \qquad \text{in } V_f. \tag{2.49}$$

Together with an appropriate boundary conditions at the external boundary of $V_f$ (e.g. $c \to 0$ for $|\boldsymbol{r}| \to \infty$ in unbounded domains), these equations form a well-posed problem for the distribution of solute in the fluid domain $V_f$.

In response to non-uniform solute distribution at the particles' surface, a phoretic slip flow $\boldsymbol{u}_n^s$ develops outside a thin interaction layer [63, 64] so that effectively, the hydrodynamic boundary condition on $S_n$ becomes

$$\boldsymbol{u} = \boldsymbol{U}_n + \boldsymbol{\Omega}_n \times \boldsymbol{r}_n + \boldsymbol{u}_n^s, \qquad \text{with } \boldsymbol{u}_n^s = M_n(\mathbf{n})\nabla_{||} c \qquad \text{on } S_n. \tag{2.50}$$

In the previous equation, $\nabla_{||} = (\boldsymbol{I} - \boldsymbol{nn}) \cdot \nabla$ is the tangential gradient on the particle's surface, $\boldsymbol{r}_n = \boldsymbol{r} - \boldsymbol{Y}_n$ is the generic position relative to the $n$ particle's centre, and $M_n(\boldsymbol{n})$ denotes the dimensionless and spatially-dependent phoretic mobility of the surface of particle $n$. For small particles, inertial effects are negligible (i.e Re $= \rho U_0 a/\mu \ll 1$), and the dimensionless fluid's velocity and pressure $(\boldsymbol{u}, p)$ satisfy Stokes' equations:

$$\nabla p = \nabla^2 \boldsymbol{u}, \qquad \nabla \cdot \boldsymbol{u} = 0 \qquad \text{in } V_f, \tag{2.51}$$

with appropriate condition at the outer boundary of $V_f$ (e.g. $\boldsymbol{u} \to 0$ for $|\boldsymbol{r}| \to \infty$). Neglecting any outer forcing such as gravity, each particle is hydrodynamically force- and torque-free [64, 70] at all times,

$$\boldsymbol{F}_n = \int_{S_n} \boldsymbol{\sigma} \cdot \boldsymbol{n} \, \mathrm{d}S = \mathbf{0}, \qquad \boldsymbol{T}_n = \int_{S_n} \boldsymbol{r}_n \times (\boldsymbol{\sigma} \cdot \boldsymbol{n}) \, \mathrm{d}S = \mathbf{0}, \tag{2.52}$$

with $\boldsymbol{\sigma} = -p\mathbf{I} + (\nabla\mathbf{u} + \nabla\mathbf{u}^T)$ the dimensionless Newtonian stress tensor, and their dominant hydrodynamic signature is therefore that of a force dipole or stresslet $\boldsymbol{S}_n$ [118].

For a given concentration distribution $c$, Equations (2.50)–(2.52) form a well-posed problem for the fluid velocity and pressure, and particle velocities, so that at a given time $t$, and for given particle positions and orientations, $\boldsymbol{Y}_n(t)$ and $\boldsymbol{p}_n(t)$, the successive Laplace and Stokes problems presented above uniquely determine the instantaneous particle velocities $\boldsymbol{U}_n(t)$ and $\boldsymbol{\Omega}_n(t)$, from which the motion of the particles is obtained:

$$\frac{\mathrm{d}\boldsymbol{Y}_n}{\mathrm{d}t} = \boldsymbol{U}_n, \qquad \frac{\mathrm{d}\boldsymbol{p}_n}{\mathrm{d}t} = \boldsymbol{\Omega}_n \times \boldsymbol{p}_n. \tag{2.53}$$

For a single isolated particle, the Lorentz Reciprocal Theorem to Stokes flows provides the particle's translation and rotation velocities directly in terms of the phoretic slip [103]:

$$\boldsymbol{U} = -\langle \boldsymbol{u}^s \rangle, \qquad \boldsymbol{\Omega} = -\frac{3}{2a}\langle \boldsymbol{n} \times \boldsymbol{u}^s \rangle, \tag{2.54}$$

where $\langle \cdot \rangle$ is the spatial average over the particle's surface. Similarly, the stresslet $\boldsymbol{S}$ of the particle is obtained as [119],

$$\boldsymbol{S} = -10\pi a^2 \langle \boldsymbol{n}\boldsymbol{u}^s + \boldsymbol{u}^s\boldsymbol{n} \rangle. \tag{2.55}$$

### 2.2.2 Isotropic and hemispheric Janus phoretic particles

Most phoretic particles have a Janus-type surface consisting of two different materials or surface coatings with distinct physicochemical properties (e.g., a catalytic side and a passive one) [13, 57, 60, 61]. These provide the particles with a built-in chemical asymmetry that triggers the inhomogeneity of the concentration distribution at their surface at the heart of their self-propulsion. Isotropic particles are not capable of performing self-propulsion isolated, but once they interact with other particles, they can swim to form clusters, and they swim with a rigid body motion [120, 17], and so both kinds of particles are of interest for us, and we will consider them. Other examples of phoretic particle design are reported in [63].

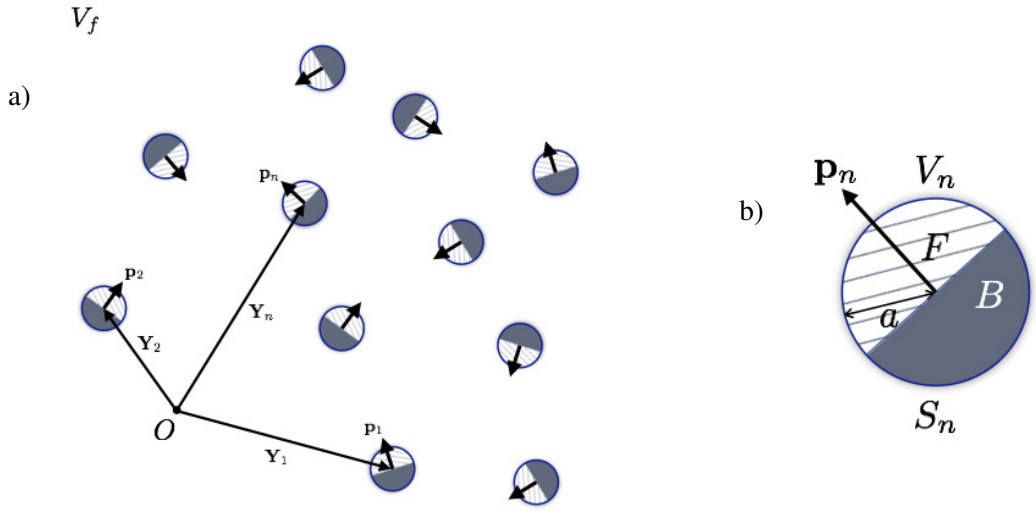


Figure 2.4: (a) Geometric description and parameter definition for (a) a reactive suspension system and (b) an individual active particle; including the fluid domain $V_f$, the particles' domain $V_n$ and the fluid-particle boundaries $S_n$, as well the phoretic particles' positions $\boldsymbol{Y}_n$, orientations $\boldsymbol{p}_n$ and their radius $a$. The particle's orientation $\boldsymbol{p}_n$, allows for the definition of its front caps (noted $F$ and $B$ respectively). The different colours of the caps (white or grey) illustrate their different chemical activity, while their pattern (striped and solid) illustrate their different mobilities.

In the following, we thus consider such hemispheric Janus particles with uniform but distinct mobilities $(M_n^F, M_n^B)$ and activities $(\alpha_n^F, \alpha_n^B)$ on their front (F) and back (B) hemispheres, as defined with respect to their orientation $\boldsymbol{p}_n$ (figure 2.4b), e.g. the surface mobility of particle $n$ writes

$$M_n(\boldsymbol{n}) = \overline{M}_n + M_n^* \operatorname{sign}(\boldsymbol{p}_n \cdot \boldsymbol{n}), \tag{2.56}$$

with $\overline{M}_n = (M_n^F + M_n^B)/2$ and $M_n^* = (M_n^F - M_n^B)/2$ the mean mobility and mobility contrast, and similar definitions for the spatially-dependent activity $\alpha_n(\boldsymbol{n})$ at the particle's surface

$$\alpha_n(\boldsymbol{n}) = \overline{\alpha}_n + \alpha_n^* \operatorname{sign}(\boldsymbol{p}_n \cdot \boldsymbol{n}), \tag{2.57}$$

with $\overline{\alpha}_n = (\alpha_n^F + \alpha_n^B)/2$ and $\alpha_n^* = (\alpha_n^F - \alpha_n^B)/2$ the mean activity and activity contrast.

Note, that the special case of a particle with uniform properties thus corresponds to $\overline{M}_n = M_n^0$ and $M_n^* = 0$ in mobility and $\overline{\alpha}_n = \alpha_n^0$ and $\alpha_n^* = 0$ in the activity.

## 2.3 Analytic & numerical methods to study phoretic particles

In this context, obtaining the swimming velocities of phoretic Janus particles, therefore, requires solving two different problems sequentially, namely (i) a diffusion (Laplace) problem for the solute concentration around the colloids and (ii) a hydrodynamic (Stokes) problem for the fluid flow around them. The analytical solution is, in general, amenable only for single particles [63], although determining the coupled motion of two Janus colloids is also possible semi-analytically [121, 122, 123]. For more than two particles, a complete description of the phoretic motion requires numerical treatment , but with a computational cost that increases rapidly with the number of particles, motivating the use of reduced models for the particles' interactions.

### 2.3.1 Isolated particle analytical solution

In the simplest case of an isolated spherical particle, an exact solution for the concentration field could be obtained for an axisymmetric particle [63] in terms of Legendre polynomials $L_n$, considering the Laplace equation (2.38 without volume sources $g = 0$) with a constant flux condition 2.43

$$c(r,\theta) - c_\infty = a \sum_{l=0}^{\infty} \frac{\alpha_l}{l+1} \left(\frac{a}{r}\right)^{l+1} P_l(\cos(\theta)), \tag{2.58}$$

where $c_\infty$ is the concentration at infinity, $\theta$ is measured from the particle orientation $\boldsymbol{p}$ and $\alpha_l$ are the Legendre coefficients for the activity $\alpha(\boldsymbol{n}) = \alpha(\theta) = \sum_{l=0}^{\infty} \alpha_l P_l(\cos(\theta))$. If a Janus design sphere is considered (section 2.2.2), using 2.54 the velocities of the isolated particle becomes [63]

$$\boldsymbol{U}_{isol} = -\frac{1}{2}\alpha^* \bar{M} \boldsymbol{p} \qquad\qquad \boldsymbol{\Omega}_{isol} = \boldsymbol{0}, \tag{2.59}$$

indicating a persistent motion in straight line without rotation at all. Note that to induce the particle propulsion, the asymmetry in concentration is needed ($\alpha^* \neq 0$), but also a non zero mean mobility ($\bar{M} \neq 0$ otherwise only a pumping mode in the fluid around the particle will be present).

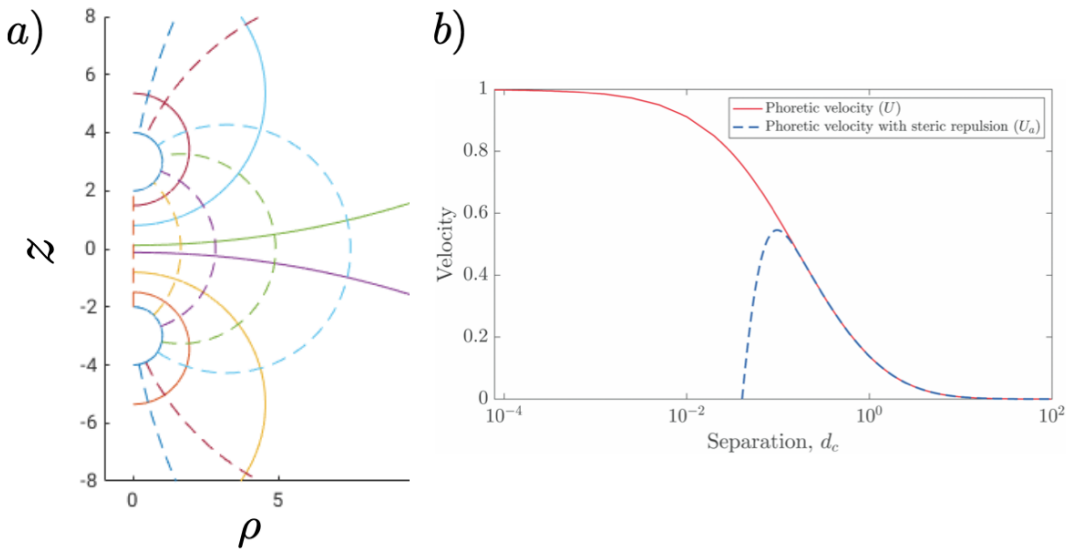


Figure 2.5: Bi-Spherical Coordinate system: a) geometry with constant $\tau$ and $\mu$ lines (solid and dashed lines respectively), b) velocity solution for two isotropic particles varying its surface-to-surface distance, without and with repulsive velocity to include steric repulsion (red solid and blue dashed lines respectively). Image b) adapted from [17].

### 2.3.2 Pair of particles semi-analytical solution

Determining the coupled motion of two colloids is also possible semi-analytically: particularly for Janus particles [121, 122, 123] but as well for isotropic particles [17, 120] solving the coupled problem in the Bi-Spherical Coordinates. In figure 2.5.a) there is a 2D representation of such coordinates, where several lines of constants $\tau$ and $\mu$ values where presented, in a semi-plane of constant $\phi$. Lines with constant $\tau$ values correspond to spheres centered in the $z$-axis, from where the minimum value $\tau_-$ defines the lower sphere and the maximum value $\tau_+$ defines the upper sphere. In this coordinate system, the solution for the concentration field is:

$$c(\tau,\mu) = \sqrt{\cosh(\tau) - \mu} \sum_{l=0}^{\infty} c_l(\tau) L_l(\mu), \tag{2.60}$$

where $L_l$ is the Legendre polynomial of degree $l$ and $c_l$ can be determined based on the boundary conditions. Although the solution is formally analytic, in practice, the precision of the solution depends in the number of modes included in 2.60. Then the surface slip velocity $\boldsymbol{u}^s$ could be calculated through 2.47 and the reciprocal theorem for Stokes flow 2.24 can be used to determine the particles velocities from the slip velocity, the results is shown in figure 2.5.b).

### 2.3.3 Simulation methods

We must rely on numerical methods to solve the problem for systems with more than two particles. A straightforward approach is to consider ensembles of active particles and include some simple approximation of the phoretic far-field interactions but without considering hydrodynamic interactions, for example, by coupling Brownian dynamics simulations to finite difference solvers for the phoretic field [124]. Or by using the Active Brownian Particles that only considers the self-propulsion in active particles and the drift in passive particles [125]. However, more

sophisticated numeric schemes are required to consider the hydrodynamic interactions or the phoretic interactions in a more detailed way.

In dilute suspensions, i.e., when particles are far apart, their hydro-chemical interactions can be accounted for through the slowest-decaying chemical and hydrodynamic signatures of individual particles and their effect on their neighbours [121, 126]. Due to their simplicity, the small computational cost for a large number of particles, and their ability to handle the effect of confinements through image systems, far-field models have been extensively used to analyze the motion of active suspensions [see, e.g. 127, 128, 129]. An alternative mean-field approach describes the particles' motion in the ambient chemical and hydrodynamic fields generated by the superposition of their individual far-field signatures [130, 131].

For more concentrated suspensions, i.e., when the inter-particle distances are reduced, far-field models are not accurate as finite-size effects of the particles are no longer negligible. Although it is possible to include higher-order corrections using the Method of Reflections [121], more complex numerical models are, in general, required to solve the dual hydro-chemical problem accurately within not-so-dilute suspensions. Due to the mathematical similarities between Laplace and Stokes's problems, it is possible to draw inspiration from and build upon a large variety of methods already used in recent years for the numerical modeling of passive and active suspensions. A famous example is the Stokesian dynamics and its more recent extensions [132, 133, 134, 135], from which an analogous approach was proposed to solve for the chemical concentration field in diffusiophoretic active colloids [136]. Other possible routes include Boundary Element Methods (BEM) [110, 137, 138] or the Immersed Boundary Methods (IBM) [139, 140, 141]. The Lattice-Boltzmann approaches (LB) [142, 143], where a simplified and discretized version of the Boltzmann equation is solved from which the Navier-Stokes can be derived, was recently extended to include coupled hydrochemical interactions [144]. Multi-Particle Collision Dynamics (MPCD) [16, 145, 146, 147] that construct collisions representing many microscopic collisions, based on the idea that only their net effect are important has been used in the study of self-diffusiophoretic colloids [148]. Another approach to model self-propelled active colloids was formulated based on spectral expansions of the Laplace and Stokes equations [149, 150] which is available in a Python library called PyStokes.

Table 1 summarizes some of the most relevant publications of the previous methods, in which a large set of phoretic particles was considered to study collective motions in reactive suspensions, but considering the chemical interactions and, in the majority of them, the hydrodynamic interactions formally. Most of these models consider periodic domains (simulation boxes of size $L$ and apply periodic boundary conditions on the walls) in which the domain ratio is specified ($L/a$). In contrast, one of them considers an infinite space. Two of them consider fully 3D models, while the other two consider quasi-2D models, in which the fields are solved in 3D, but the motion of the particles is restricted to a plane with zero flux and zero velocity (very representative of some experimental realizations like in [13, 14]).

The first method reported in Table 1 is the Accelerated Laplacian Dynamics (ALD), in which a multipole expansion for the concentration field up to the quadrupole term is considered; one of its advantages is the use of a matrix-free method with which it reaches computational scalability of $O(N\log(N))$ (instead the intrinsic one of $O(N^2)$). The disadvantage of this method is that it neglects the hydrodynamic interactions between particles in the current version. However, the authors mention the possibility of integrating this method with the Accelerated Stokesian Dynamics [134] to consider the hydrodynamics formally with the advantage of its scaling $O(N\log(N))$. The second method is the PyStokes library [150], which formally solves the coupled physics (Laplace and Stokes equations) by using Green's functions, and that's why the domain, in this case, is unbounded. This method's disadvantage is the scaling for a large number

of particles ($O(N^2)$) that could become prohibitive.

The last two methods in Table 1 are mesoscopic simulation methods, which involve a coarse-grained description of the problem. In the case of the Lattice Boltzmann method (LB), it solves the problem for non-zero Reynolds numbers (i.e., Navier-Stokes instead of Stokes equations), but also the complete advection-diffusion-reaction equation for the chemistry, which in general is more versatile and general, but for the case of very small Reynolds and Peclet numbers (usually the case for suspensions of reactive Janus particles) might require more computational resources than necessary. Finally, the Multiparticle Collision Dynamics (MPCD) cited implementation uses a combination of MPCD for hydrodynamics and Molecular Dynamics (MD) for the chemical problem, taking into account a very detailed description of the chemistry and including the Brownian motion. By considering the advantages and disadvantages of the previous methods, one interesting option is to consider the Force Coupling Method (FCM) [151, 152], given its linear scalability with the number of particles [106].

| **Name of the method** | **Accelerated Laplacian Dynamics** | **PyStokes library** | **Lattice Boltzmann** | **Multiparticle Collision Dynamics** |
|---|---|---|---|---|
| **Number of particles** $N$ | 2503 | 2048 | 6400 | 100, 200, 500 |
| **Dimensions** | 3D | q2D | q2D | 3D |
| **Domain & size** | Periodic with $L/a = 64$ | Infinite | Periodic with $L/a = 410$ | Periodic with $L/a = 24$ |
| **Volume fraction** $\phi$ | 0.04 | — | 0.12 | 0.05, 0.10, 0.20 |
| **Computational scalability** | $O(N\log(N))$ | $O(N^2)$ | — | — |
| **Type of particles** | Isotropic and Janus | Isotropic and Janus | Janus | Janus |
| **Reference** | [136] | [149] | [144] | [148] |

Table 1. Some of the most relevant methods and recent publications in reactive suspensions that study collective motion by formally considering the hydro-chemical interactions. When the domain is finite and periodic, the quantity $L/a$ is the ratio between the simulation box size $L$ and the particles' radius $a$. The simulation dimension specified as q2D, represents quasi 2D models, in which the fields are solved in 3D, but the particles are free to move in a plane where zero flux and zero velocity boundary conditions applies.

The Force Coupling Method (FCM) used to solve the hydrodynamic interactions of particles in a fluid relies on the classical multipolar expansion of the solution for Stokes' equation [97] but proposes a regularised alternative to singular Green's function in the form of smoothed Gaussian kernels. Beyond the obvious numerical advantage of such a regularization, it also provides an indirect route to account for the finite size of the particles through the finite support of these kernels.

The FCM framework was initially proposed twenty years ago by Maxey and coworkers [151, 152] to analyze the joint dynamics of passive spherical particles sedimenting in a viscous fluid. It has since then been extended to account for finite inertia [153], lubrication effects [154] and non-sphericity of the particles [155] leading to a powerful method to study the hydrodynamic interactions of large suspensions. More recently, FCM was also adapted to account for the activity of the colloids and enabled the analysis of microswimmer suspensions

incorporating the squirmer model [106].

In this thesis, an FCM-based method is presented to solve the Laplace problem for the concentration field in phoretic suspensions of spherical Janus particles, using a regularized multipole representation of the concentration based on smoothed kernels instead of the classical singular monopole and dipole singularities. This provides the phoretic forcing introduced by the local inhomogeneity of the concentration field on each particle, from which the hydrodynamic problem can be solved using the existing FCM approach for active suspensions [106]. Taken together, this provides an integrated framework to solve the complete diffusiophoretic problem, or Diffusiophoretic Force Coupling Method, whose fundamental justification and validation is the main objective of the next chapter.

# Chapter 3

# A Force Coupling inspired method to model phoretic particles

*This chapter contains a modified version of the article Hydrochemical interactions of phoretic particles: a regularized multipole framework, by F. Rojas-Pérez, B. Delmotte, and S. Michelin, published to Journal of Fluid Mechanics, 2021.*

Once the complexity of the physics of the reactive suspension was introduced previously, it is clear why some approximations are usually introduced to reduce the difficulty and allow their study. In this chapter, we will present our new numerical development to consider both the hydrodynamical and chemical interactions and their numerical validation for a small number of phoretic particles.

In the purely diffusive and viscous limit, solving for the particles' dynamics, therefore, amounts to solving two linear problems, namely a Laplace problem for $c$ and a Stokes swimming problem for the hydrodynamic fields and particles' velocities. Although the exact solution to this joint problem can be obtained analytically for the single- and two-particle cases [63, 121, 123], analytical treatment becomes intractable beyond $N \geq 3$ due to the geometric complexity of the fluid domain and despite the problem's linearity. Numerical simulations are therefore critically needed, and several numerical strategies have been proposed recently and reviewed at the end of Chapter 2. To analyse the collective dynamics accurately in a suspension of Janus phoretic particles, such a method must combine an efficient solution of the Laplace and Stokes problems outside a large number of finite-size objects while providing an accurate representation of the coupling at the surface of each particle between chemical and hydrodynamic fields.

With that double objective in mind, we propose and present here a novel numerical framework to solve the reactive suspension problem presented in Section 2.2, based on the classical Force Coupling Method (FCM) used for pure hydrodynamic simulations of passive particles or microswimmers, thereby generalizing its application to the solution of the chemical diffusion problem and its coupling with the already-established hydrodynamic FCM [106, 151, 152, 156]. Section 3.1 develops the regularized Laplace problem and associated Reactive FCM, while Sec. 3.2 presents a brief review of the existing hydrodynamic FCM, and Sec. 3.3 combines both to obtain a new Diffusio-phoretic Force Coupling Method (hereinafter referred to as DFCM).

The fundamental idea of the Force Coupling Method is to replace a solution of the Stokes equations only within the fluid domain $V_f$ *outside* the forcing particles with a solution of these equations over the entire domain $V_F = V_f \cup V_1 \cup \ldots \cup V_N$ (i.e., both outside and inside the particles), replacing the surface boundary conditions with a distributed regularised forcing over a compact envelope calibrated to reproduce certain physical features of the problem and account for a weak form of the surface boundary conditions (check figure 3.1 and compare with figure 2.4). In doing so, the costly discrete resolution and time-dependent meshing of the particles are no longer necessary, so efficient (e.g., spectral) Laplace and Stokes solvers on a fixed, regular grid may be used at all times, offering significant performance and scalability advantages concerning other approaches (e.g., Boundary Element Methods). More specifically, FCM associates with each particle a finite set of regularized hydrodynamic singularities (force monopoles, dipoles, and so on) chosen to satisfy a weak form of the surface boundary conditions.

## 3.1 Reactive FCM

We extend here this approach to the solution of the Laplace problem for $c$ in Eqs. (2.48)–(2.49). Replacing each particle by a distributed forcing modifies Laplace's equations into a Poisson equation over the entire domain $V_F$ (including both fluid and particles),

$$\nabla^2 c = -g(\boldsymbol{r}, t) \qquad \text{in } V_F, \tag{3.1}$$

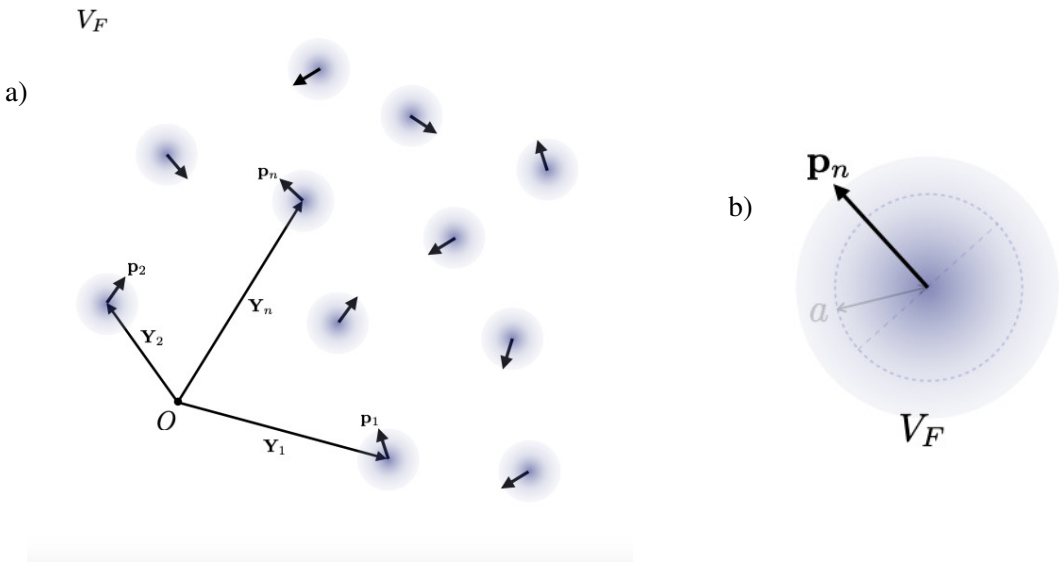


Figure 3.1: Regularized representation of (a) the reactive suspension system and (b) individual particles in the DFCM framework. The chemical and hydrodynamic fields are now defined over the entire domain $V_F$ with distributed forcings defined relative to each particle's position $\boldsymbol{Y}_n$ and orientation $\boldsymbol{p}_n$. The boundary $S_n$ of the real particle (dashed) and its radius $a$ are plotted only as reference.

### 3.1.1 Standard multipole expansion for Laplace problem

The exact solution of the Laplace problems can in fact be recovered from Eq. (3.1), when the function $g(\boldsymbol{r}, t)$ is taken as a (possibly infinite) set of singularities centred on each particle [97],

$$g(\boldsymbol{r}, t) = \sum_{n=1}^{N} \Big[ q_n^M \delta(\boldsymbol{r}_n) + \boldsymbol{q}_n^D \cdot \nabla\delta(\boldsymbol{r}_n) + ... \Big], \tag{3.2}$$

where $\delta(\boldsymbol{r}_n)$ is the Dirac delta distribution, and $(q_n^M, \boldsymbol{q}_n^D, ...)$ are the intensity of the singularities associated with particle $n$, and are constant tensors of increasing order. This equation can be solved explicitly for the concentration field $c$ as a multipole expansion for each particle in terms of source monopoles, dipoles, etc...

$$c(\boldsymbol{r}, t) = \sum_{n=1}^{N} \Big[ q_n^M G^M(\boldsymbol{r}_n) + \boldsymbol{q}_n^D \cdot \boldsymbol{G}^D(\boldsymbol{r}_n) + ... \Big], \tag{3.3}$$

where $G^M$ and $\boldsymbol{G}^D$ are the monopole and dipole Green's functions and satisfy

$$\nabla^2 G^M = -\delta(\boldsymbol{r}_n), \qquad \nabla^2 \boldsymbol{G}^D = -\nabla\delta(\boldsymbol{r}_n), \tag{3.4}$$

together with appropriate decay or boundary conditions on the domain's outer boundary. For unbounded domains with decaying conditions in the far-field, the singular monopole and dipole Green's functions are simply (as in section 2.1.4)

$$G^M(\boldsymbol{r}_n) = \frac{1}{4\pi r_n} \quad \text{and} \quad \boldsymbol{G}^D(\boldsymbol{r}_n) = -\nabla G^M = \frac{\boldsymbol{r}_n}{4\pi r_n^3}. \tag{3.5}$$

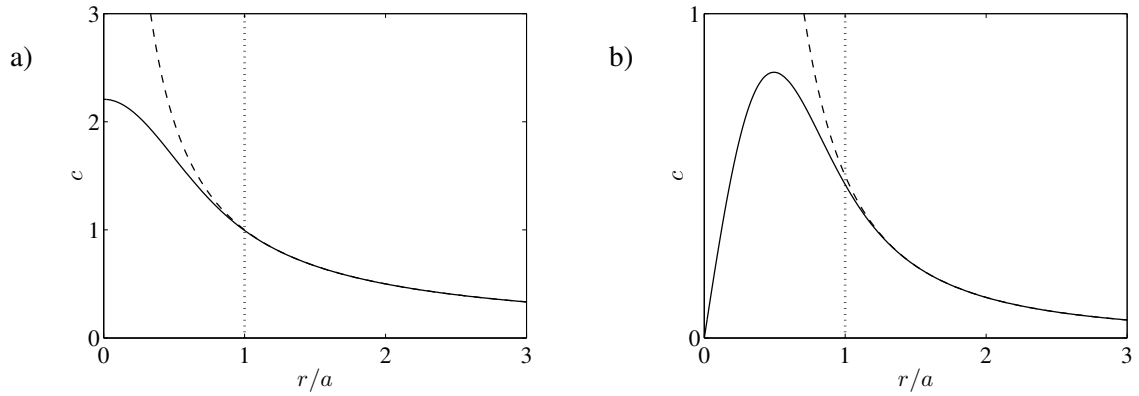


Figure 3.2: Singular (dashed lines) and regularized (solid lines) concentration distributions along the axial polar direction associated to the Greens' Functions for the Laplace equation for: a) monopole terms and b) dipole terms. The line $r/a = 1$ represents the particle surface.

The concentration distributions associated to these singular Green's functions are displayed in figure 3.2. Higher-order derivatives of $G^M(\boldsymbol{r})$, Eq. (3.5), are also solutions of Laplace's equation leading to singularities of increasing order (quadrupole, octopole,...).

### 3.1.2 Truncated regularized multipole expansion

The previous approach, based on an infinite set of singular sources, is known as the standard multipole expansion of the Laplace problem. Although satisfying from a theoretical point of view, since it can recover an accurate representation of the analytical solution outside the particles for a large enough number of singular monopoles, it is not well-suited for a versatile numerical implementation because of (i) the singular behavior of the forcing terms in the modified Laplace equation, Eq. (3.1), and (ii) the *a priori* infinite set of singularities required for each particle.

To avoid the latter issue, the infinite expansion is truncated here after the first two terms, thus retaining the monopole and dipole contributions only. Physically, this amounts to retaining the two leading physical effects of the particle on the concentration field, i.e., a net emission with a front-back asymmetric distribution. In order to overcome the former problem, the standard FCM replaces the singular Dirac distributions $\delta(\boldsymbol{r})$ by regular Gaussian spreading functions $\Delta(\boldsymbol{r})$:

$$\triangle(\boldsymbol{r}) = (2\pi\sigma^2)^{-3/2}\exp\Big(-\frac{r^2}{2\sigma^2}\Big), \tag{3.6}$$

where $\sigma$ denotes the finite-size support of this envelop and acts as a smoothing parameter of the method, thus eliminating the singular behaviour of the delta distribution $\delta(\boldsymbol{r})$ near the origin, thereby allowing for a more accurate numerical treatment. The original singular distribution is recovered when $\sigma \ll r$, i.e. the solution of the regularised problem is an accurate representation of the true solution away from the particle. This approach using regular distributions allows for a more versatile and robust numerical solution of the physical equations than their singular counterparts [151, 152].

Combining these two approximations, we therefore consider a truncated regularized expansion including only the monopole and the dipole terms as:

$$g(\boldsymbol{r}, t) = \sum_{n=1}^{N}\Big[q_n^M\Delta^M(r_n) + \boldsymbol{q}_n^D\cdot\nabla\Delta^D(r_n)\Big], \tag{3.7}$$

with the Gaussian spreading operators $\Delta^M$ and $\Delta^D$ defined as:

$$\Delta^M(r) = (2\pi\sigma_M^2)^{-3/2}\exp\Big(-\frac{r^2}{2\sigma_M^2}\Big), \qquad \Delta^D(r) = (2\pi\sigma_D^2)^{-3/2}\exp\Big(-\frac{r^2}{2\sigma_D^2}\Big), \tag{3.8}$$

where $M$ and $D$ once again denote monopole and dipole, and $\sigma_M$ and $\sigma_D$ are the finite support of each regularized distribution and are free numerical parameters of the method that need to be calibrated. Note that in all generality, these do not need to be identical [152].

The corresponding truncated regularized solution for $c$ is then finally obtained as:

$$c(\boldsymbol{r},t) = \sum_{n=1}^{N}\Big[q_n^M G^M(\boldsymbol{r}_n) + \boldsymbol{q}_n^D \cdot \boldsymbol{G}^D(\boldsymbol{r}_n)\Big], \tag{3.9}$$

with the regularized monopole and dipole Green's functions

$$G^M(\boldsymbol{r}) = \frac{1}{4\pi r}\mathrm{erf}\Big(\frac{r}{\sigma_M\sqrt{2}}\Big), \tag{3.10}$$

$$\boldsymbol{G}^D(\boldsymbol{r}) = \frac{\boldsymbol{r}}{4\pi r^3}\Big[\mathrm{erf}\Big(\frac{r}{\sigma_D\sqrt{2}}\Big) - \sqrt{\frac{2}{\pi}}\Big(\frac{r}{\sigma_D}\Big)\exp\Big(-\frac{r^2}{2\sigma_D^2}\Big)\Big]. \tag{3.11}$$

These clearly match the behaviour of their singular counterpart, Eq. (3.5), when $r$ is greater than a few $\sigma_M$ or $\sigma_D$, respectively, while still maintaining finite values within the particle (figure 3.2), e.g. $\boldsymbol{G}^D(\boldsymbol{r}=\boldsymbol{0}) = \boldsymbol{0}$.

### 3.1.3 Finding the intensities of the singularities

Up to this point, no information was implemented regarding the surface boundary conditions on $c$ in Eq. (2.48). We now present how to determine the intensities of the monopole and dipole distributions associated with each particle, $q_n^M$ and $\boldsymbol{q}_n^D$, to satisfy a weak form of the Neuman boundary condition, Eq. (2.48), i.e. its first two moments over the particle's surface. Using the multipole expansion of the fundamental integral representation of the concentration (see Appendix A), the monopole and dipole intensities of particle $n$, $q_n^M$ and $\boldsymbol{q}_n^D$, are obtained as [136]:

$$q_n^M = \int_{S_n}\alpha_n \mathrm{d}S, \qquad \boldsymbol{q}_n^D = a\int_{S_n}\alpha_n \boldsymbol{n}\mathrm{d}S + 4\pi a^2\langle c\boldsymbol{n}\rangle_n \tag{3.12}$$

where the second term in $\boldsymbol{q}_n^D$ is proportional to the concentration polarity at the surface of particle $n$, i.e. its first moment $\langle c\boldsymbol{n}\rangle_n$, and is defined using the surface average operator $\langle\cdot\rangle_n$ over particle $n$'s surface. Note that the activity distribution at the particle's surface is known, and thus Eq. (2.56) explicitly provides the monopole intensity and the first term in the dipole intensity. The second contribution to the latter requires, however, knowledge of the solution on the particle's surface – which is not explicitly represented in the current FCM approach. Therefore, this term must be solved as part of the general problem. In the previous equation, it should be noted that the dimensionless particle radius is $a = 1$, but will be kept in the equations to emphasize the relative scaling of the numerical spreading envelopes (e.g., $\sigma_M$ and $\sigma_D$) with respect to the particle size.

Here, we use an iterative approach to solve this linear joint problem for the dipole intensity and concentration field, solving alternatively Eqs. (3.7) and (3.12) until convergence is reached, as defined by the following criterion between two successive iterations:

$$\left\|\frac{\langle c\boldsymbol{n}\rangle^{k+1} - \langle c\boldsymbol{n}\rangle^{k}}{\langle c\boldsymbol{n}\rangle^{k+1}}\right\|_\infty < \epsilon, \tag{3.13}$$

where $\langle c\boldsymbol{n}\rangle^k$ is the vector collecting the polarities of the $N$ particles at iteration $k$. For the results presented in this chapter, we set the tolerance to $\epsilon = 10^{-10}$ in our calculations.

### 3.1.4 Regularized moments of the concentration distribution

Finding the dipole intensity, $\boldsymbol{q}_n^D$, requires computing the polarity $\langle c\boldsymbol{n}\rangle_n$ which is in principle defined *at the particle's surface*. To follow the spirit of FCM and allow for efficient numerical treatment, this surface projection is replaced by a weighted projection over the entire volume $V_F$:

$$\langle c\boldsymbol{n}\rangle_n = \frac{1}{4\pi a^2}\int_{S_n} c\boldsymbol{n}\mathrm{d}S \quad \longrightarrow \quad \{c\boldsymbol{n}\}_n = \int_{V_F} c\boldsymbol{n}_n\Delta^P(\boldsymbol{r}_n)\mathrm{d}V, \tag{3.14}$$

with $\boldsymbol{n}_n$ now defined as $\boldsymbol{n}_n = \boldsymbol{r}_n/r_n$, and the regular averaging kernel $\Delta^P$ for the polarity as:

$$\Delta^P(\boldsymbol{r}) = \frac{r}{8\pi\sigma_P^4}\exp\left(-\frac{r^2}{2\sigma_P^2}\right). \tag{3.15}$$

Beyond its importance for determining the dipole intensity associated with a given particle, we will later show that the polarity of the concentration at particle $n$'s surface is directly related to its self-induced phoretic velocity, Eq. (2.54), and that, similarly, the self-induced hydrodynamic stresslet signature of the particle is in general associated to the first two moments of the surface concentration. Similarly to the polarity, the second surface moment, $\langle c(\boldsymbol{nn} - \boldsymbol{I}/3)\rangle_n$ will be replaced in our implementation by a weighted volume projection $\{c(\boldsymbol{nn} - \boldsymbol{I}/3)\}_n$:

$$\langle c(\boldsymbol{nn}-\boldsymbol{I}/3)\rangle_n = \frac{1}{4\pi a^2}\int_{S_n} c\left(\boldsymbol{nn} - \frac{\boldsymbol{I}}{3}\right)\mathrm{d}S \longrightarrow \{c(\boldsymbol{nn}-\boldsymbol{I}/3)\}_n = \int_{V_F} c\left(\boldsymbol{n}_n\boldsymbol{n}_n - \frac{\boldsymbol{I}}{3}\right)\Delta^S(\boldsymbol{r}_n)\mathrm{d}V, \tag{3.16}$$

where the projection kernel for the second moment of concentration, $\Delta^S$, is defined as:

$$\Delta^S(\boldsymbol{r}) = \frac{r^2}{3(2\pi)^{\frac{3}{2}}\sigma_S^5}\exp\left(-\frac{r^2}{2\sigma_S^2}\right). \tag{3.17}$$

The envelopes $\sigma_P$ and $\sigma_S$ are free parameters in the method that need to be calibrated. In our reactive FCM formulation, we use modified forms of the Gaussian operator $\Delta$ as projection operators, Eqs. (3.15) and (3.17), in order to ensure a fast numerical convergence of the integration for the first and second moments calculation, Eqs. (3.14) and (3.16) respectively. The integrals over the entire volume $V_F$ of these averaging functions are still equal to one. Their weight is shifted from the particle center and toward the particle surface (figure 3.3), which is both numerically more accurate and more intuitive physically as these operators are used to obtain the properties of the particle on their surface.

### 3.1.5 Calibrating the spreading/averaging envelopes

Our method relies on four numerical parameters ($\sigma_M$, $\sigma_D$, $\sigma_P$, $\sigma_S$) that we choose to calibrate to ensure that several key results in reference configurations are obtained exactly. In particular, to properly account for the phoretic drift induced by the other particles, we ensure that the polarity $\langle c\boldsymbol{n}\rangle$ of an isolated particle placed in an externally-imposed uniform gradient of concentration can be exactly recovered using the regular representation and averaging operators. A similar approach is then followed for the particle's second moment of concentration $\langle c(\boldsymbol{nn} - \boldsymbol{I}/3)\rangle$ in a

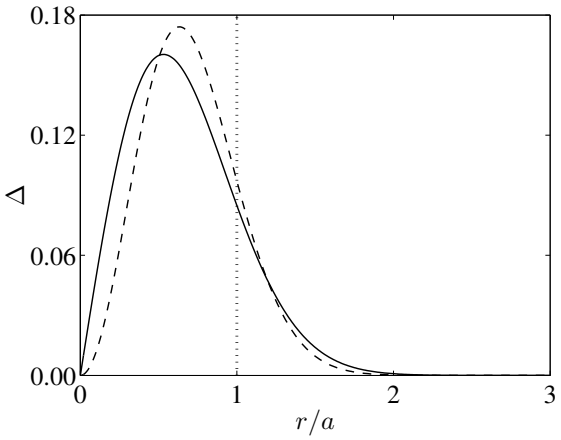


Figure 3.3: Averaging envelopes for the first and second moments of concentration, $\Delta^P$ (solid, Eq. (3.15)) and $\Delta^S$ (dashed, Eq. (3.17)) respectively. The numerical values for $\sigma_P$ and $\sigma_S$ are set from Eqs. (3.21) and (3.24).

quadratic externally-imposed field.

**Isolated passive particle in an external linear field** – We first consider a single particle placed at the origin in an externally-imposed linear concentration field so that for $r \gg a$, $c \approx c_E$ with

$$c_E = \boldsymbol{L}_E \cdot \boldsymbol{r}, \tag{3.18}$$

where $\boldsymbol{L}_E$ is the externally-imposed uniform gradient. For a passive particle (i.e. $\alpha = 0$), satisfying the boundary condition, Eq. (2.48), at the surface of the particle imposes that the exact concentration distribution around the particle is $c = c_E + c_I^o$, with $c_I^o(\boldsymbol{r}) = a^3 \boldsymbol{L}_E \cdot \boldsymbol{r}/(2r^3)$ a singular dipole induced field. The polarity of the external and induced parts, $c_E$ and $c_I$, can be obtained analytically as:

$$\langle c_E \boldsymbol{n} \rangle = \frac{a}{3} \boldsymbol{L}_E, \qquad \langle c_I^o \boldsymbol{n} \rangle = \frac{a}{6} \boldsymbol{L}_E. \tag{3.19}$$

Following the framework presented above, the regularized solution can be written $c = c_E + c_I^r$ with $c_i^r$ a regularized dipole, and the corresponding regularized-volume moments based on Eq. (3.14) are obtained using Eq. (3.11), as

$$\{c_E \boldsymbol{n}\} = \sqrt{\frac{\pi}{8}} \sigma_P \boldsymbol{L}_E, \qquad \{c_I^r \boldsymbol{n}\} = \frac{a^3 \sigma_P}{12(\sigma_D^2 + \sigma_P^2)^{\frac{3}{2}}} \boldsymbol{L}_E. \tag{3.20}$$

Identification of the regularized result (3.20) to the true solution (3.19), determines $\sigma_P$ and $\sigma_D$ uniquely as:

$$\frac{\sigma_P}{a} = \frac{1}{3}\sqrt{\frac{8}{\pi}} \approx 0.5319, \qquad \frac{\sigma_D}{a} = \sqrt{\left(\frac{\sigma_P}{2a}\right)^{2/3} - \left(\frac{\sigma_P}{a}\right)^2} \approx 0.3614. \tag{3.21}$$

**Isolated passive particle in an external quadratic field** – Similarly, in an external quadratic field $c_E$ of the form:

$$c_E(\boldsymbol{r}) = \boldsymbol{r} \cdot \boldsymbol{Q}_E \cdot \boldsymbol{r}, \tag{3.22}$$

with $\boldsymbol{Q}_E$ a second-order symmetric and traceless tensor, the concentration distribution around a passive particle ($\alpha = 0$) takes the form $c = c_E + c_I^o$ with $c_I^o(\boldsymbol{r})$ an induced singular quadrupole. The exact and regularized second moments of the external field $c_E$ at the particle surface is equal to

$$\langle c_E(\boldsymbol{nn} - \boldsymbol{I}/3)\rangle = \frac{2a^2}{15}\boldsymbol{Q}_E, \qquad \{c_E(\boldsymbol{nn} - \boldsymbol{I}/3)\} = \frac{2\sigma_S^2}{3}\boldsymbol{Q}_E. \tag{3.23}$$

Identifying both results determines the size of the averaging envelope for the second moment uniquely, as

$$\frac{\sigma_S}{a} = \sqrt{\frac{1}{5}} \approx 0.4472. \tag{3.24}$$

Note that we do not enforce here a constraint on the representation of the second moment of the induced field $c_I$ since the particles' representations omit a regularized quadrupole in our method.

The value $\sigma_M$ remains a free parameter at this point and cannot be calibrated with a similar approach. In the following, to minimize the number of distinct numerical parameters and to minimize the departure of the regularized solution from its singular counterpart, we set its value equal to the smallest envelope size, namely $\sigma_M = \sigma_D$. These specific values of the parameters were used in figures 3.2 and 3.3.

## 3.2 Hydrodynamic FCM

To compute the hydrodynamic interactions between phoretic particles, we rely on the Force Coupling Method (FCM). This section briefly describes the existing FCM framework developed for the simulation of passive and active suspensions in Stokes flow.

### 3.2.1 FCM for passive suspensions

With hydrodynamic FCM, the effect of the particles on the fluid is accounted for through a forcing term $\boldsymbol{f}$ applied to the dimensionless Stokes equations (Eq. (2.12))

$$\nabla p - \nabla^2 \boldsymbol{u} = \boldsymbol{f}(\boldsymbol{r}, t) \qquad \text{in } V_F. \tag{3.25}$$

As for reactive FCM, this forcing arises from a truncated regularized multipolar expansion including the monopole terms [151] and the dipole terms [152]

$$\boldsymbol{f}(\boldsymbol{r}, t) = \sum_{n=1}^{N} \Big[\boldsymbol{F}_n \Delta(r_n) + \boldsymbol{D}_n \cdot \nabla\Delta^*(r_n)\Big], \tag{3.26}$$

where the spreading envelopes are defined by

$$\Delta(r) = (2\pi\sigma^2)^{-3/2}\exp\left(-\frac{r^2}{2\sigma^2}\right), \qquad \Delta^*(r) = (2\pi\sigma_*^2)^{-3/2}\exp\left(-\frac{r^2}{2\sigma_*^2}\right). \tag{3.27}$$

$\boldsymbol{F}_n$ and $\boldsymbol{D}_n$ are the force monopole and dipole applied to particle $n$. The force dipole can be split into a symmetric part, usually called the stresslet $\boldsymbol{S}$, and an antisymmetric one related to the external torque $\boldsymbol{T}$:

$$\boldsymbol{D}_n = \boldsymbol{S}_n + \frac{1}{2}\boldsymbol{\epsilon} \cdot \boldsymbol{T}_n, \tag{3.28}$$

with $\boldsymbol{\epsilon}$ the third-order permutation tensor. The corresponding regularized solution for the fluid velocity $\boldsymbol{u}$ is then obtained as:

$$\boldsymbol{u} = \boldsymbol{u}(\boldsymbol{r}) = \sum_{n=1}^{N} \left[ \boldsymbol{F}_n \cdot \boldsymbol{J}(\boldsymbol{r}_n) + \boldsymbol{D}_n : \boldsymbol{R}^*(\boldsymbol{r}_n) \right]. \tag{3.29}$$

For unbounded domains with vanishing perturbations in the far-field (i.e. $\|\boldsymbol{u}\| \to 0$ when $r \to \infty$), the regularized Green's function $\boldsymbol{J}(\boldsymbol{r})$ reads

$$\boldsymbol{J}(\boldsymbol{r}) = \frac{1}{8\pi r} \left( A(r)\boldsymbol{I} + B(r)\frac{\boldsymbol{r}\boldsymbol{r}}{r^2} \right), \tag{3.30}$$

with

$$A(r) = \left(1 + \frac{\sigma^2}{r^2}\right) \mathrm{erf}\left(\frac{r}{\sigma\sqrt{2}}\right) - \frac{\sigma}{r}\sqrt{\frac{2}{\pi}} \exp\left(-\frac{r^2}{2\sigma^2}\right), \tag{3.31}$$

$$B(r) = \left(1 - \frac{3\sigma^2}{r^2}\right) \mathrm{erf}\left(\frac{r}{\sigma\sqrt{2}}\right) + \frac{3\sigma}{r}\sqrt{\frac{2}{\pi}} \exp\left(-\frac{r^2}{2\sigma^2}\right), \tag{3.32}$$

and $\boldsymbol{R}^* = \nabla \boldsymbol{J}^*$ is the FCM dipole Green's function evaluated with the parameter $\sigma_*$.

The particle's translational and angular velocities, $\boldsymbol{U}_n$ and $\boldsymbol{\Omega}_n$, are obtained from a volume-weighted average of the local fluid velocity and vorticity

$$\boldsymbol{U}_n = \int_{V_F} \boldsymbol{u}\, \Delta(\boldsymbol{r}_n) \mathrm{d}V, \qquad \boldsymbol{\Omega}_n = \frac{1}{2} \int_{V_F} [\nabla \times \boldsymbol{u}] \Delta^*(\boldsymbol{r}_n) \mathrm{d}V. \tag{3.33}$$

The Gaussian parameters, $\sigma$ and $\sigma^*$ are calibrated to recover the correct Stokes drag, $\boldsymbol{F} = 6\pi a \mu \boldsymbol{U}$, and viscous torque, $\boldsymbol{T} = 8\pi a^3 \mu \boldsymbol{\Omega}$, of an isolated particle [151, 152], leading to

$$\frac{\sigma}{a} = \frac{1}{\sqrt{\pi}} \approx 0.5641, \qquad \frac{\sigma_*}{a} = \frac{1}{(6\sqrt{\pi})^{1/3}} \approx 0.4547. \tag{3.34}$$

The rigidity of the particle is similarly weakly enforced by imposing that the volume-averaged strain rate $\boldsymbol{E}_n$ over the envelope of particle $n$ vanishes:

$$\boldsymbol{E}_n = \frac{1}{2} \int_{V_F} [\nabla \boldsymbol{u} + (\nabla \boldsymbol{u})^{\mathrm{T}}] \Delta^*(\boldsymbol{r}_n) \mathrm{d}V = \boldsymbol{0}, \tag{3.35}$$

which determines the stresslet $\boldsymbol{S}_n$ induced by particle $n$. Note that, unlike forces and torques, which are typically set by external or inter-particle potentials, the stresslets result from the constraint on the flow given by Eq. (3.35) and, consequently, need to be solved for as part of the general flow problem. The resulting linear system for the unknown stresslet coefficients is solved directly or iteratively, with the conjugate gradients method, depending on the number of particles considered [152, 156]. In the following, we consider pairs of particles (see Section 3.4) and therefore use direct inversion.

Note that the averaging envelopes used to recover the translational and rotational velocities, $\triangle_n$ and $\triangle_n^*$, are exactly the same as the spreading operators in (3.26), all of them Gaussian functions. As a result, the spreading and averaging operators are adjoints to one another. Also, note that only two envelope lengths are required for the hydrodynamic problem: $\sigma$ and $\sigma_*$. In contrast, the new reactive FCM extension presented in Section 3.1 uses spreading and averaging operators that are not adjoint. To recover the first (3.14) and second (3.16) moments of concentration we have two non-Gaussian averaging envelopes ($\Delta^P$ and $\Delta^S$), that differ from the Gaussian spreading envelopes ($\Delta^M$ and $\Delta^D$) in (3.7). While having adjoint operators is crucial in hydrodynamic FCM to satisfy the fluctuation-dissipation balance, the lack of adjoint properties for the Laplace problem does not raise any issue in the deterministic setting.

### 3.2.2 Active hydrodynamic FCM

In recent years, FCM has been extended to handle suspensions of active particles, such as microswimmers. In addition to undergoing rigid body motion in the absence of applied forces or torques ($\boldsymbol{F} = \boldsymbol{T} = \boldsymbol{0}$), active and self-propelled particles are also characterized by the flows they generate. These flows can be incorporated into FCM by adding an appropriate set of regularized multipoles to the Stokes equations. This problem was solved previously for the classical squirmer model [106], a spherical self-propelled particle that swims using prescribed distortions of its surface [104], as seen in section 2.1.3. In the most common case where radial distortions are ignored, the squirmer generates a tangential slip velocity on its surface, just like phoretic particles, which can be expanded into spherical harmonics modes [104, 105, 157]. Consistently with the phoretic problem presented above, only the first two modes are included in the following.

The FCM force distribution produced by $N$ microswimmers self-propelling with a surface slip velocity is given by

$$\boldsymbol{f}(\boldsymbol{r}, t) = \sum_{n=1}^{N} \left[ \boldsymbol{S}_n \cdot \nabla \Delta^*(r_n) + \boldsymbol{S}_n^a \cdot \nabla \Delta(r_n) + \boldsymbol{H}_n^a \nabla^2 \Delta^*(r_n) \right], \tag{3.36}$$

where $\boldsymbol{S}_n^a$ is the active stresslet and $\boldsymbol{H}_n^a$ is the active potential dipole associated to the swimming disturbances of swimmer $n$. The latter is defined as

$$\boldsymbol{H}_n^a = -2\pi a^3 \boldsymbol{U}_n^a, \tag{3.37}$$

where $\boldsymbol{U}_n^a$ is the swimming velocity arising from the slip velocity on the swimmer surface $\boldsymbol{u}^s$ (2.54). Note that the rigidity stresslet $\boldsymbol{S}_n$ is included in (3.36) to enforce the absence of deformation of the swimmers, Eq. (3.35). The resulting velocity field reads

$$\boldsymbol{u}(\boldsymbol{r}, t) = \sum_{n=1}^{N} \left[ \boldsymbol{S}_n : \boldsymbol{R}^*(\boldsymbol{r}_n) + \boldsymbol{S}_n^a : \boldsymbol{R}(\boldsymbol{r}_n) + \boldsymbol{H}_n^a \cdot \boldsymbol{A}^*(\boldsymbol{r}_n) \right], \tag{3.38}$$

where $\boldsymbol{R}$ is the FCM dipole Green's function evaluated with the parameter $\sigma$ instead of $\sigma_*$. The second order tensor $\boldsymbol{A}^*$ is the FCM Green's function for the potential dipole

$$\boldsymbol{A}^*(\boldsymbol{r}) = \frac{1}{4\pi r^3} \left[ \boldsymbol{I} - \frac{3\boldsymbol{r}\boldsymbol{r}}{r^2} \right] \operatorname{erf}\left( \frac{r}{\sigma_* \sqrt{2}} \right) - \frac{1}{\mu} \left[ \left( \boldsymbol{I} - \frac{\boldsymbol{r}\boldsymbol{r}}{r^2} \right) + \left( \boldsymbol{I} - \frac{3\boldsymbol{r}\boldsymbol{r}}{r^2} \right) \left( \frac{\sigma_*}{r} \right)^2 \right] \Delta^*(r). \tag{3.39}$$

The particles' velocity, angular velocity and mean strain rate are then computed as

$$\boldsymbol{U}_n = \boldsymbol{U}_n^a - \boldsymbol{W}_n + \int_{V_F} \boldsymbol{u}\, \Delta(\boldsymbol{r}_n) \mathrm{d}V, \tag{3.40}$$

$$\boldsymbol{\Omega}_n = \boldsymbol{\Omega}_n^a + \frac{1}{2} \int_{V_F} [\nabla \times \boldsymbol{u}] \Delta^*(\boldsymbol{r}_n) \mathrm{d}V, \tag{3.41}$$

$$\boldsymbol{E}_n = -\boldsymbol{K}_n + \frac{1}{2} \int_{V_F} [\nabla \boldsymbol{u} + (\nabla \boldsymbol{u})^{\mathrm{T}}] \Delta^*(\boldsymbol{r}_n) \mathrm{d}V = \boldsymbol{0}, \tag{3.42}$$

where the active swimming velocities $\boldsymbol{U}_n^a$ and rotation rates $\boldsymbol{\Omega}_n^a$ correspond to the intrinsic velocities of particle $n$, if it was alone (i.e. in the absence of external flows or other particles), and $\boldsymbol{W}_n$ and $\boldsymbol{K}_n$ are defined as

$$\boldsymbol{W}_n = \int_{V_F} (\boldsymbol{H}_n^a \cdot \boldsymbol{A}^*(\boldsymbol{r}_n)) \Delta(\boldsymbol{r}_n) \mathrm{d}V, \tag{3.43}$$

$$\boldsymbol{K}_n = \frac{1}{2} \int_{V_F} [\boldsymbol{S}_n^a : \nabla \boldsymbol{R}(\boldsymbol{r}_n) + (\boldsymbol{S}_n^a : \nabla \boldsymbol{R}(\boldsymbol{r}_n))^{\mathrm{T}}] \Delta^*(\boldsymbol{r}_n) \mathrm{d}V, \tag{3.44}$$

and are included to subtract away the spurious self-induced velocities and local rates of strain arising from the integration of the full velocity field $\boldsymbol{u}$, which already includes the contribution of $\boldsymbol{H}_n^a$ and $\boldsymbol{S}_n^a$ [106].

## 3.3 Diffusio-phoretic FCM (simply DFCM)

At this point, we have described our new reactive FCM framework and have reviewed the key aspects of the existing active hydrodynamic FCM. These two steps provide respectively the solution (i) for the concentration field and its moments at the surface of each particle in terms of their position and orientation, and (ii) the particles' velocity in terms of their active hydrodynamic characteristics, i.e., their intrinsic velocities and stresslet, $\boldsymbol{U}_n^a$, $\boldsymbol{\Omega}_n^a$ and $\boldsymbol{S}_n^a$. To solve for the full diffusio-phoretic problem (i.e., obtain the velocity of the particle in terms of its position and orientation), these quantities must be determined from the chemical environment of the particles. The following section details how to obtain these active characteristics from the output of the reactive problem and provides algorithmic details on the numerical implementation. This new diffusio-phoretic framework based on the Force Coupling Method is referred to as DFCM hereafter.

### 3.3.1 DFCM: coupling Reactive and Hydrodynamic FCM

The active swimming speed $\boldsymbol{U}_n^a$ involved in the potential dipole $\boldsymbol{H}_n^a$, (3.37), is the phoretic response of particle $n$ to the chemical field, if it was hydrodynamically isolated (i.e. neglecting the presence of other particles in solving the swimming problem). It thus includes its self-induced velocity (i.e. the response to the concentration contrasts induced by its own activity) and the drift velocity induced by the activity of the other particles. The swimming problem for a hydrodynamically-isolated particle in unbounded flows can be solved directly using the reciprocal theorem [103], and using the definition of the phoretic slip flow

$$\boldsymbol{U}_n^a \;=\; -\langle \boldsymbol{u}^s \rangle_n \;=\; -\langle M \nabla_{\|} c \rangle_n. \tag{3.45}$$

After substitution of the mobility distribution at the surface of particle $n$, Eq. (2.56), using a truncated multipolar expansion of the surface concentration on particle $n$ (up to its second-order moment) and integrating by parts, the intrinsic swimming velocity is obtained in terms of the first two surface concentration moments (see Appendix B for more details)

$$\boldsymbol{U}_n^a = -\frac{2\overline{M}_n}{a}\langle c\boldsymbol{n}\rangle_n - \frac{15M_n^*}{8a}\Big[2\langle c(\boldsymbol{nn}-\boldsymbol{I}/3)\rangle_n \cdot \boldsymbol{p}_n + \big(\langle c(\boldsymbol{nn}-\boldsymbol{I}/3)\rangle_n : \boldsymbol{p}_n\boldsymbol{p}_n\big)\,\boldsymbol{p}_n\Big]. \tag{3.46}$$

Similarly, the active stresslet $\boldsymbol{S}_n^a$, is defined as in Eq. (2.55),

$$\boldsymbol{S}_n^a = -10\pi a^2 \langle \boldsymbol{n}\boldsymbol{u}^s + \boldsymbol{u}^s\boldsymbol{n}\rangle_n = -10\pi a^2 \langle M(\boldsymbol{n}\nabla_{||}c + (\nabla_{||}c)\boldsymbol{n})\rangle_n, \tag{3.47}$$

and rewrites in terms of the moments of concentration (see Appendix B for more details)

$$\boldsymbol{S}_n^a = -60\pi a\overline{M}_n\langle c(\boldsymbol{nn}-\boldsymbol{I}/3)\rangle_n + \frac{15\pi a M_n^*}{2}\Big[(\langle c\boldsymbol{n}\rangle_n\cdot\boldsymbol{p}_n)(\boldsymbol{I}-\boldsymbol{p}_n\boldsymbol{p}_n) - \langle c\boldsymbol{n}\rangle_n\boldsymbol{p}_n - \boldsymbol{p}_n\langle c\boldsymbol{n}\rangle_n\Big]. \tag{3.48}$$

Finally, the active rotation $\boldsymbol{\Omega}_n^a$, Eq. (2.54), is obtained in terms of the moments of concentration and the mobility contrast (see Appendix B)

$$\boldsymbol{\Omega}_n^a = -\frac{9M_n^*}{4a^2}\,\boldsymbol{p}_n \times \langle c\boldsymbol{n}\rangle_n. \tag{3.49}$$

For uniform mobility, the swimming velocity and stresslet are directly related to the first and second of surface concentrations, but non-uniform mobility introduces a coupling of the different concentration moments. Here, the surface concentration is expanded up to its second-order moment only.

In our regularized approach, the surface concentration moments appearing in the previous equations will conveniently be computed as weighted volume averages over the entire domain $V_F$ as detailed in Eqs. (3.14) and (3.16).

Computing the second moment of concentration, however, requires an additional step: as detailed in Section 3.1.5, the second moment of concentration in an external field arises from the second gradient of that external field, and includes both an externally-induced component $\langle c_E(\boldsymbol{nn} - \boldsymbol{I}/3)\rangle_n$ (i.e. the moment of that externally-imposed field) and a self-induced component which corresponds to the second moment of the induced field generated by the particle to ensure that the correct flux boundary condition is satisfied at the particles' surface. For a chemically-inert particle ($\alpha = 0$), the self-induced contribution is obtained exactly as $\langle c_I^o(\boldsymbol{nn} - \boldsymbol{I}/3)\rangle_n = \frac{2}{3}\langle c_E(\boldsymbol{nn} - \boldsymbol{I}/3)\rangle$.

However, our representation of the particles in the chemical problem is truncated at the dipole level, Eq. (3.9), and as a result, the quadrupolar response of the particle to the external field can not be accounted for directly. To correct for this shortcoming, we first compute the external second moment produced by the other particles on particle $n$ using (3.16) and (3.9) and then multiply the resulting value by $5/3$ to account for the full second moment induced by the concentration field indirectly.

Finally, the particles are themselves active and may generate an intrinsic quadrupole. Its effect on the second surface concentration moment can be added explicitly in terms of the second activity moment, so that the total second moment on particle $n$ is finally evaluated as

$$\langle c(\boldsymbol{nn} - \boldsymbol{I}/3)\rangle_n = \frac{5}{3}\{c_E(\boldsymbol{nn} - \boldsymbol{I}/3)\}_n + \frac{a}{D}\langle \alpha(\boldsymbol{nn} - \boldsymbol{I}/3)\rangle_n. \tag{3.50}$$

In summary, at a given time step, the particles' velocities are obtained from their instantaneous position and orientation as follows. The first two surface concentration moments are first obtained using our new reactive FCM framework by solving the Poisson problem, Eq. (3.7). These moments are then used to compute the phoretic intrinsic translation and rotation velocities, Eqs. (3.46) and (3.49), as well as the active stresslets and potential dipoles, Eqs. (3.48) and (3.37). The Stokes equations forced by the swimming singularities Eq. (3.36), and subject to the particle rigidity constraint, Eq. (3.42), are finally solved to obtain the total particle velocities, Eqs. (3.40)–(3.41).

## 3.4 Validation of the method and results

In this section, we evaluate the accuracy of the present novel DFCM framework in three different canonical or more generic configurations involving pairs of isotropic and Janus phoretic particles, as shown in figure 3.4. The particles' motions are restricted to a plane within a three-dimensional unbounded domain for the sake of clarity in visualizing the results.

In this validation process, DFCM is compared with three existing methods providing either a complete or approximate solution to the problem. The simplest one, the Far-Field Approximation model [71, 121], relies on a multipolar expansion of the reactive and hydrodynamic singularities up to the dipole level generated by each particle but neglects the finite size of the

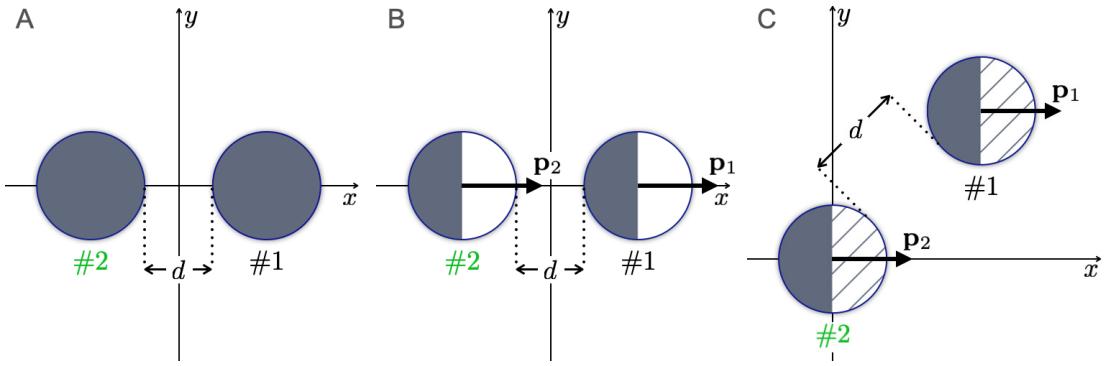


Figure 3.4: Validation cases considered: a) Case A: Isotropic particles with uniform mobility, b) Case B: Hemispheric Janus particles with uniform mobility, c) Case C: Hemispheric Janus particles with non-uniform mobility. In each case, both particles have exactly the same orientation and phoretic properties. Their (surface) inter-particle dimensionless distance is noted $d$.

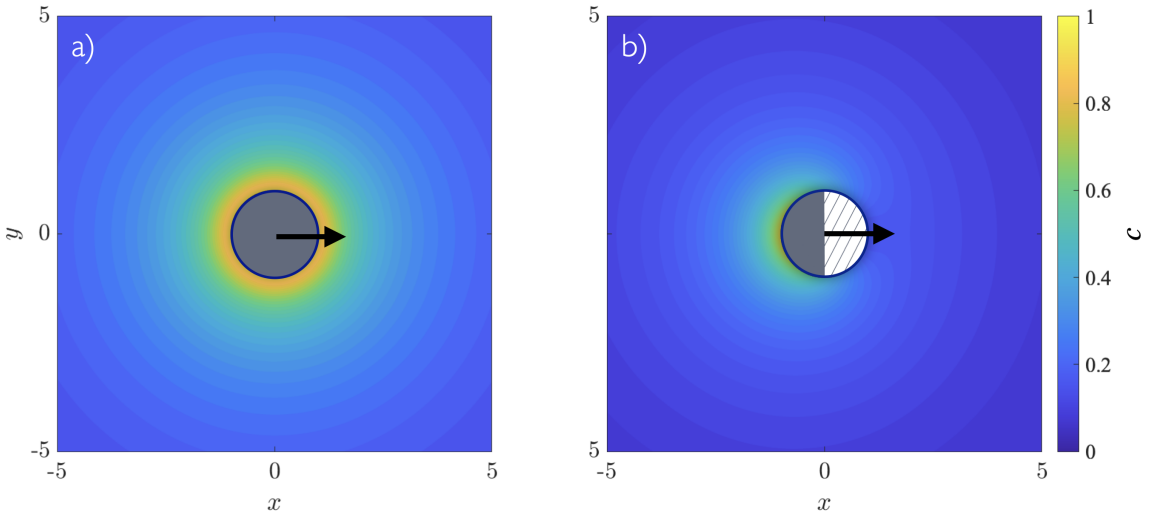


Figure 3.5: Concentration field around isolated particles, in particular: a) isotropic, b) 1/2 Janus.

particles (i.e., without reflections on the polarity and rigidity stresslet). Our results are also compared to the complete (exact) solution of the problem (i.e., solving the complete hydrodynamic and chemical fields regardless of the particles' distance, accounting for their finite size). For axisymmetric problems, this solution is obtained semi-analytically using the Bi-Spherical Coordinates approach [75, 121], whose accuracy is only limited by the number of Legendre modes used to represent the solution. For non-axisymmetric configurations, the complete solution is obtained numerically using the regularized Boundary Element Method [138]. These reference solutions are referred to in the following as FFA, BSC, and BEM, respectively.

### 3.4.1 Proof of concept DFCM code

All the following results were performed with the first version of the DFCM code, based on Green's functions described in the theoretical section. The main objective of this implementation was to provide the required environment for the validation of the framework, and it was developed

in Matlab. It implements the analytical solution for the fluid fields (concentration $c$ Eq. 3.9 and velocity $\boldsymbol{u}$ Eq. 3.38), reproduced here:

$$c(\mathbf{r},t) = \sum_{n=1}^{N} \left[ q_n^M G^M(\mathbf{r}_n) + \mathbf{q}_n^D \cdot \mathbf{G}^D(\mathbf{r}_n) \right], \tag{3.51}$$

$$\boldsymbol{u}(\boldsymbol{r},t) = \sum_{n=1}^{N} \left[ \boldsymbol{S}_n : \boldsymbol{R}^*(\boldsymbol{r}_n) + \boldsymbol{S}_n^a : \boldsymbol{R}(\boldsymbol{r}_n) + \boldsymbol{H}_n^a \cdot \boldsymbol{A}^*(\boldsymbol{r}_n) \right], \tag{3.52}$$

The volume integrals required to compute the concentration moments and the hydrodynamic quantities are performed with a Riemann sum on Cartesian grids centered at each particle position. However, other schemes were considered, like Gauss-Hermite integration. To ensure a sufficient resolution, the grid size, $\Delta x$, is chosen so that the smallest envelope size $\sigma_D$ satisfies $\sigma_D = 1.5\Delta x = 0.3614a$, which corresponds to roughly 4 grid points per radius. Owing to the fast decay of the envelopes, the integration domain is truncated so that the widest envelope (that with the largest $\sigma$) essentially vanishes on the boundary of the domain, $\Delta(r) < \gamma = 10^{-16}$, which, given the grid resolution, requires 39 integration points in each direction. By doing so, the numerical integrals yield spectral accuracy. Setting instead $\gamma = \epsilon = 10^{-10}$, where $\epsilon$ is the relative tolerance for the polarity in the iterative procedure, Eq. 3.13, reduces that number to 31 integration points along each axis while keeping a spectral convergence.

### 3.4.2 Isotropic pair of particles

The first configuration, Case A (figure 3.4.a)), consists of two identical isotropic particles with uniform activity and mobility ($\alpha_n^F = \alpha_n^B = 1$, $M_n^F = M_n^B = 1$) separated by a distance $d$ along the $x$-axis [17, 120]. Phoretic particles require an asymmetry in their surface concentration field to self-propel [63, 158], something not present in this case (check figure 3.5.a)), so that an isolated isotropic particle can not swim (Eq. 2.59). In the configuration considered here, however, the concentration gradient produced by a second isotropic particle introduces the required asymmetry to generate motion along the $x$-axis.

Figure 3.6.a) shows the concentration field induced by two isotropic particles for $d = 1$. The DFCM solution (upper panel) is in good agreement with BSC (lower panel), except near the particles' boundaries in the gap, where the low-order multipolar expansion of DFCM and inaccurate resolution of the particle's surface underestimates the concentration field. The increase in concentration between the particles is a direct result of the confinement between their active surfaces. It produces a surface concentration gradient and phoretic slip flow on each particle's boundary that pumps the fluid toward this high concentration zone and thus drives the particles away from each other (figure 3.6.d)). This effect is magnified as $d$ is reduced, leading to higher particle velocities and higher moments of concentration for shorter distances.

The evolution with the interparticle distance of the particles' polarity, a measure of the net concentration gradient over their surface, is shown in figure 3.6.b) as obtained with the DFCM, BSC, and FFA approaches. While both FFA and DFCM are in good agreement with the exact solution (BSC), even for relatively small distances, the DFCM approach provides a noticeable improvement over the cruder representation of FFA in the near field ($d < 1$), where the iterative corrections for the mutually-induced polarity (3.13) contribute significantly. The expected decay of the polarity as $1/d^2$ is recovered (figure 3.6.b), inset) in all three methods as the dominant contribution to the polarity is proportional to the gradient of the leading order monopolar concentration field. Similar results are obtained for the second moment of

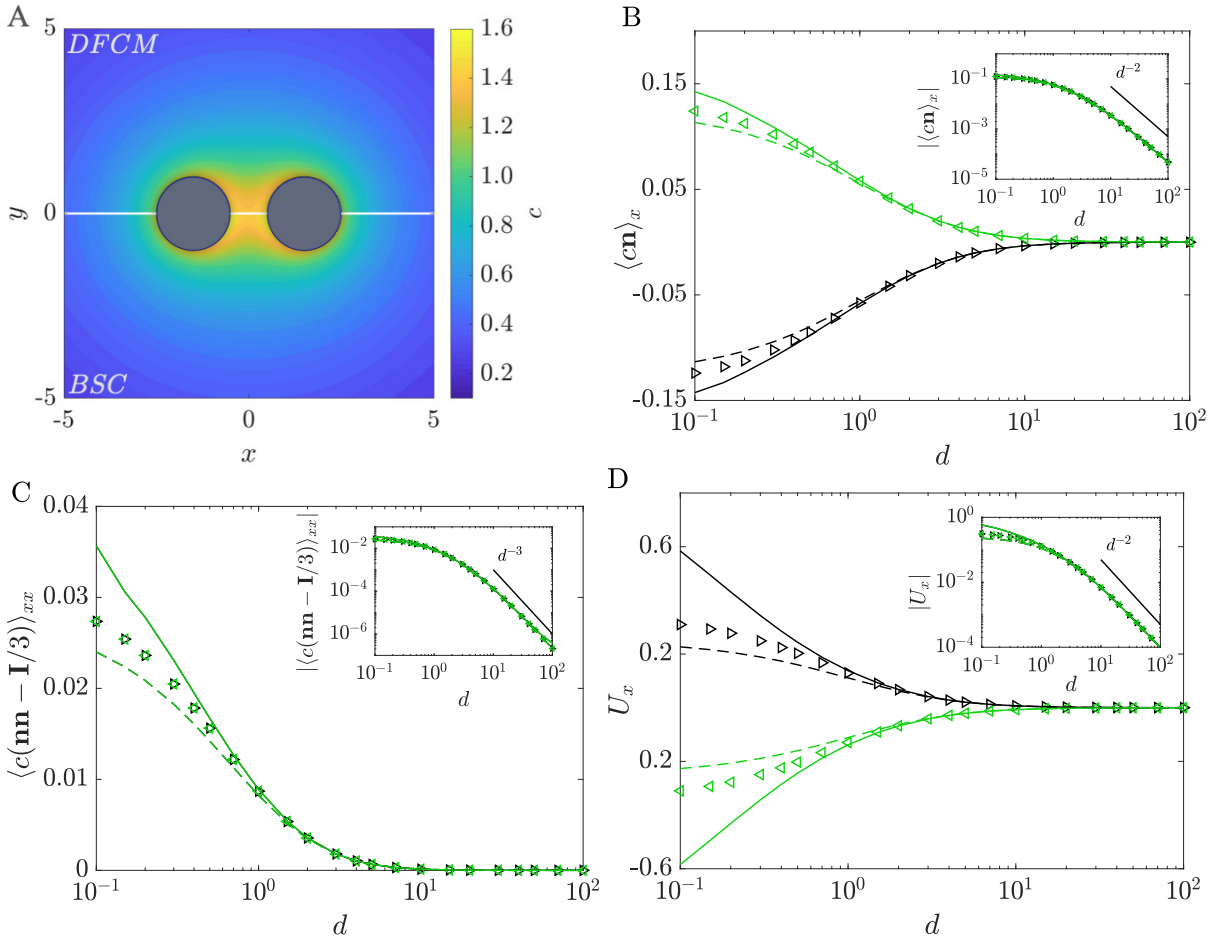


Figure 3.6: Case A: a) concentration field for $d = 1$ (upper half: DFCM, lower half: BSC), b) first moment of concentration $\langle c\boldsymbol{n}\rangle_x$, c) second moment of concentration $\langle c(\boldsymbol{nn} - \boldsymbol{I}/3)\rangle_{xx}$, d) velocity $U_x$. The black lines (and markers) correspond to particle 1 and the light green ones to particle 2. The triangle markers correspond to DFCM, the solid lines correspond to BSC, while the dashed lines to FFA. The inset shows the absolute values in logarithmic scale and the corresponding decay. The surface averages $\langle\ldots\rangle$ were used for BSC and FFA, while the volume average $\{\ldots\}$ for DFCM. All the omitted components of $\langle c\boldsymbol{n}\rangle$, $\langle c(\boldsymbol{nn} - \boldsymbol{I}/3)\rangle$, $\boldsymbol{\Omega}$ and $\boldsymbol{U}$ are zero, except for $\langle c(\boldsymbol{nn} - \boldsymbol{I}/3)\rangle_{yy} = \langle c(\boldsymbol{nn} - \boldsymbol{I}/3)\rangle_{zz} = -\frac{1}{2}\langle c(\boldsymbol{nn} - \boldsymbol{I}/3)\rangle_{xx}$.

concentration (figure 3.6.c)), with an expected $1/d^3$-decay proportional to the second gradient of the leading order of the concentration field. We note that isotropic particles do not drive any flow when isolated (and therefore do not have any hydrodynamic signature) but acquire a net stresslet due to their chemical interactions, behaving as pusher swimmers.

The resulting translational velocities are shown in figure 3.6.d): again, DFCM performs better than FFA in the range $d < 2$ since it additionally considers the hydrodynamic interactions of the particles (e.g., the effect of the rigidity constraint through the rigidity stresslet, see Eq. (3.42)) in addition to the active flows, while FFA does not. Such discrepancy arises from the accumulated errors in the successive truncated multipolar expansions: using the BSC solution as a reference, we can determine that near-field interactions of the two particles around the $25\% - 30\%$ of the DFCM error comes from the Reactive FCM approximation (3.7), while the other $70\% - 75\%$ comes from the Hydrodynamical FCM approximation (3.36). As expected, in the far-field limit, the velocity decays as $1/d^2$ since it is proportional to the polarity to the leading order. This dominant contribution does not involve any hydrodynamic interactions: these would correspond in leading order to the contribution of the stresslet generated by the presence of the other particles and decay as $1/d^5$ [121].

### 3.4.3 Janus particles - axisymmetric configuration

Our second configuration of interest, Case B (figure 3.4.b)), focuses on Janus particles, which are currently the most commonly used configuration for self-propelled phoretic particles in both experiments and theoretical models. Their motion stems from the self-induced concentration gradients produced by the difference in activity between their two hemispheres, check figure 3.5.b) as reference. Here we consider two identical Janus particles with uniform mobility ($M_n^F = M_n^B = 1$), a passive front cap ($\alpha_n^F = 0$) and an active back cap ($\alpha_n^B = 1$), leading to a self-propulsion velocity of $\boldsymbol{U}^\infty = \frac{1}{4}\boldsymbol{e}_x$ (Eq. 2.59). We further focus here on an axisymmetric setting where the particles' orientation coincides with the line connecting their centers, for which an exact semi-analytic solution of the complete hydrochemical problem is available using bispherical coordinates (BSC) as exploited in several recent studies [121, 122]. Furthermore, both particles point in the same direction so that, when far enough apart, they swim at the same velocity in the same direction.

Figure 3.7.a) shows the concentration field for $d = 1$: again, DFCM closely matches the BSC predictions. Here, both particles pump fluid from their front to their active back cap, where an excess solute concentration is produced and therefore move along the $+\boldsymbol{e}_x$ direction. As the interparticle distance shortens, the concentration increases in the gap, leading to enhanced (resp. decreased) surface gradients on the leading (resp. trailing) particle.

This physical intuition is confirmed by the evolution of the concentration polarity with the interparticle distance (figure 3.7.b)). The polarity matches that of an isolated particle $\langle c\boldsymbol{n}\rangle^\infty = -\frac{1}{8}\boldsymbol{e}_x$ for large distances $d \gg 1$, and is increased in magnitude for particle 1 (leader) while its magnitude decreases for particle 2 (follower) as $d$ is reduced. The DFCM solution remains in close agreement with BSC for all distances (even down to a tenth of a radius), in particular capturing the asymmetric effect of the interaction on the two particles. In contrast, FFA predicts a symmetric progression of the polarity, leading to large discrepancies for $d < 3$. Similar behavior is observed for the second moment (figure 3.7.c)), except for particle 1 which is underestimated by DFCM in the near field ($d < 1$). We note that although isolated Janus particles with uniform mobility behave as a neutral swimmers (exerting no force dipole or active stresslet on the fluid), their interaction leads to both of them acting as effective pushers on the fluid (negative stresslet, see Eq. (2.55)).

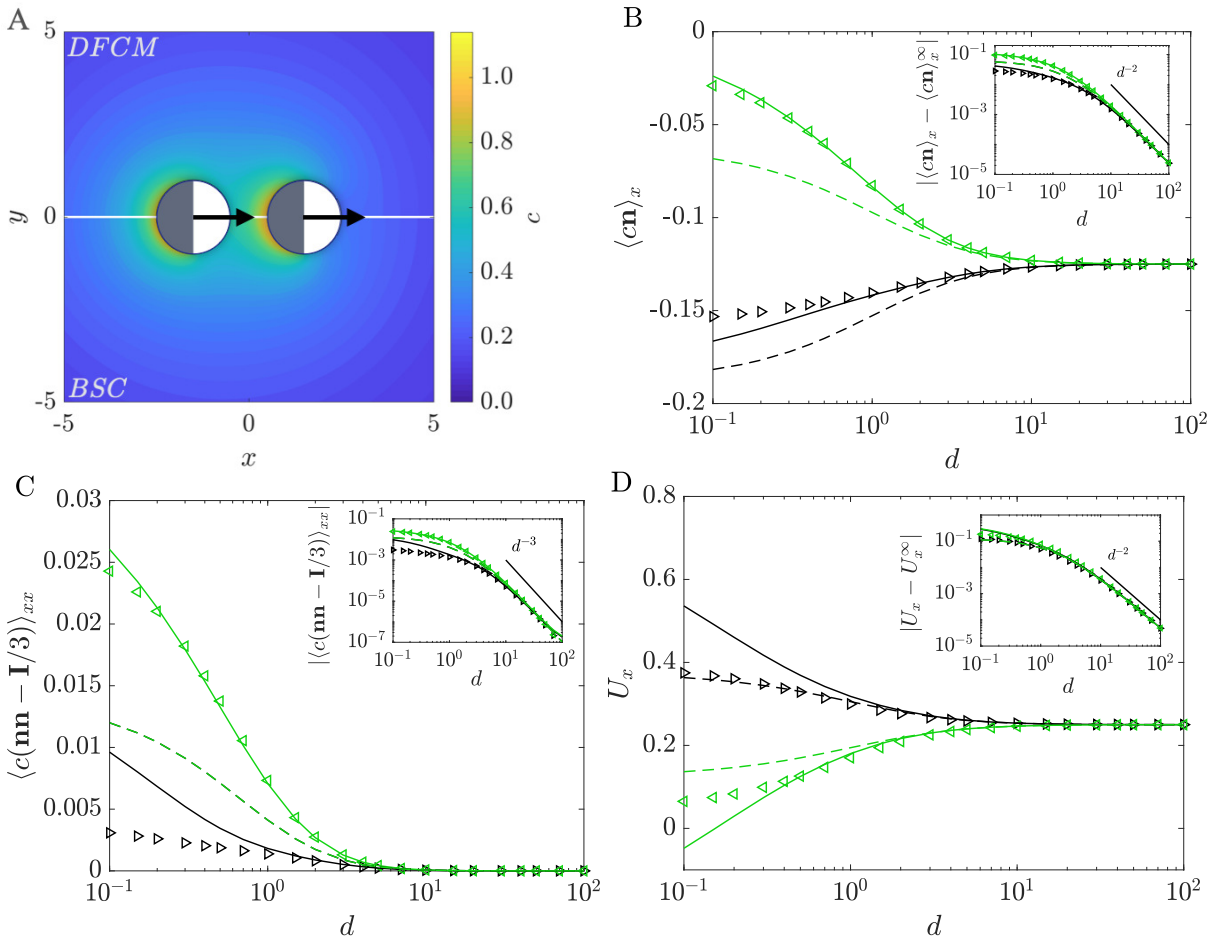


Figure 3.7: Case B: a) concentration field for $d = 1$ (upper half: DFCM, lower half: BSC), b) first moment of concentration $\langle c\boldsymbol{n}\rangle_x$, c) second moment of concentration $\langle c(\boldsymbol{nn} - \boldsymbol{I}/3)\rangle_{xx}$, d) velocity $U_x$. The black lines (and markers) correspond to particle 1 and the light green ones to particle 2. The triangle markers correspond to DFCM, the solid lines correspond to BSC, while the dashed lines to FFA. The inset shows the absolute values in logarithmic scale and the corresponding decay. The surface averages $\langle ...\rangle$ were used for BSC and FFA, while the volume average $\{...\}$ for DFCM. All the omitted components of $\langle c\boldsymbol{n}\rangle$, $\langle c(\boldsymbol{nn} - \boldsymbol{I}/3)\rangle$, $\boldsymbol{\Omega}$ and $\boldsymbol{U}$ are zero, except for $\langle c(\boldsymbol{nn} - \boldsymbol{I}/3)\rangle_{yy} = \langle c(\boldsymbol{nn} - \boldsymbol{I}/3)\rangle_{zz} = -\frac{1}{2}\langle c(\boldsymbol{nn} - \boldsymbol{I}/3)\rangle_{xx}$.

The velocity matches that of an isolated particle when $d \gg 1$, and the corrections introduced by the particles' interaction scale as $1/d^2$, as a result of the dominant phoretic repulsion (as for case A): all three methods can capture that property (see figure 3.7.b),d), inset). Similarly, the second moment of surface concentration decreases as $1/d^3$ (figure 3.7.c)). As $d$ is reduced, the combined effects of strong phoretic repulsion and hydrodynamic coupling (including the repulsion by the active stresslet) slow down and may even eventually reverse the swimming direction of particle 2 (figure 3.7.d)). Both our FCM solution and the FFA prediction show a qualitative agreement with the complete solution (BSC) and predict the increase in velocity for the leading particle while the trailing particle is slowed down. However, they fail to predict the reversal of particle 2's velocity observed in the complete solution, although DFCM exhibits an appreciable improvement over FFA in the near field. A possible reason for this may be found in a dominant role of the lubrication layer separating the particles, which is not well resolved in either approximation.

### 3.4.4 Janus particles - asymmetric configuration

Case B was still highly symmetric and further considered only uniform mobility which is known to affect the hydrodynamic signature of the particle significantly [119]. In our third and final configuration, Case C (figure 3.4.c)), we consider a more generic interaction of two identical Janus particles with non-uniform mobility ($\alpha_n^F = 0$, $\alpha_n^B = 1$, $M_n^F = 0$, $M_n^B = 1$) positioned at an angle $\pi/4$ relative to $x$ axis. Surface mobility results from the differential short-range interaction of solute and solvent molecules with the particle surface and, as such, is an intrinsic property of the particle's surface coating and may thus differ between the two caps of a Janus particle. For these particles, when isolated, the non-dimensional self-propulsion velocity is given by $\boldsymbol{U}^\infty = \frac{1}{8}\boldsymbol{e}_x$ (Eq. 2.59). The convenient bispherical coordinate approach is not usable in this non-axisymmetric setting, and although an extension to generic interactions of Janus particles is possible using full bispherical harmonics [123], it is sufficiently complex that direct numerical simulations using BEM proves, in general, more convenient, although the discontinuity of the mobility at the equator may introduce numerical errors, due to the singularity of the surface concentration gradient for a Janus particle [158]. In the following, we, therefore, compare our DFCM predictions with the solution obtained using BEM and the prediction of the far-field analysis (FFA).

The asymmetric concentration field obtained with DFCM for that configuration when $d = 1$ is shown on figure 3.8.a). Besides their intrinsic self-propulsion along $+\boldsymbol{e}_x$ due to their self-generated surface chemical polarity, the accumulation of solute in the confined space between the particles introduces a phoretic repulsion along their line of centers (as for case B), leading to an enhancement (resp. reduction) of both components of the velocity ($U_x$ and $U_y$) for particle 1 (resp. particle 2). This behaviour is well-captured by all three methods (figure 3.8.b-c)). Additionally, in the present configuration (case C), the mobility is non-uniform: specifically, here, we consider the case where the surface mobility of the front hemisphere is zero so that only the back hemisphere generates a phoretic slip. As a result of the arrangement of the particles, the dominant slip along the surface of particle 1 (resp. particle 2) is therefore counter-clockwise (resp. clockwise), leading to a negative (resp. positive) rotation velocity $\Omega_z$ for that particle. This rotation rate is proportional to the polarity and therefore decays as $1/d^2$ in the far-field. These intuitive trends are confirmed by the results of all three methods in figure 3.8.b-d).

As for case B, when the interparticle distance $d$ is reduced, these effects become more pronounced, and the results obtained with DFCM for the translation velocity are, in that regard, slightly better than the predictions of FFA. However, FFA predicts a symmetric evolution of

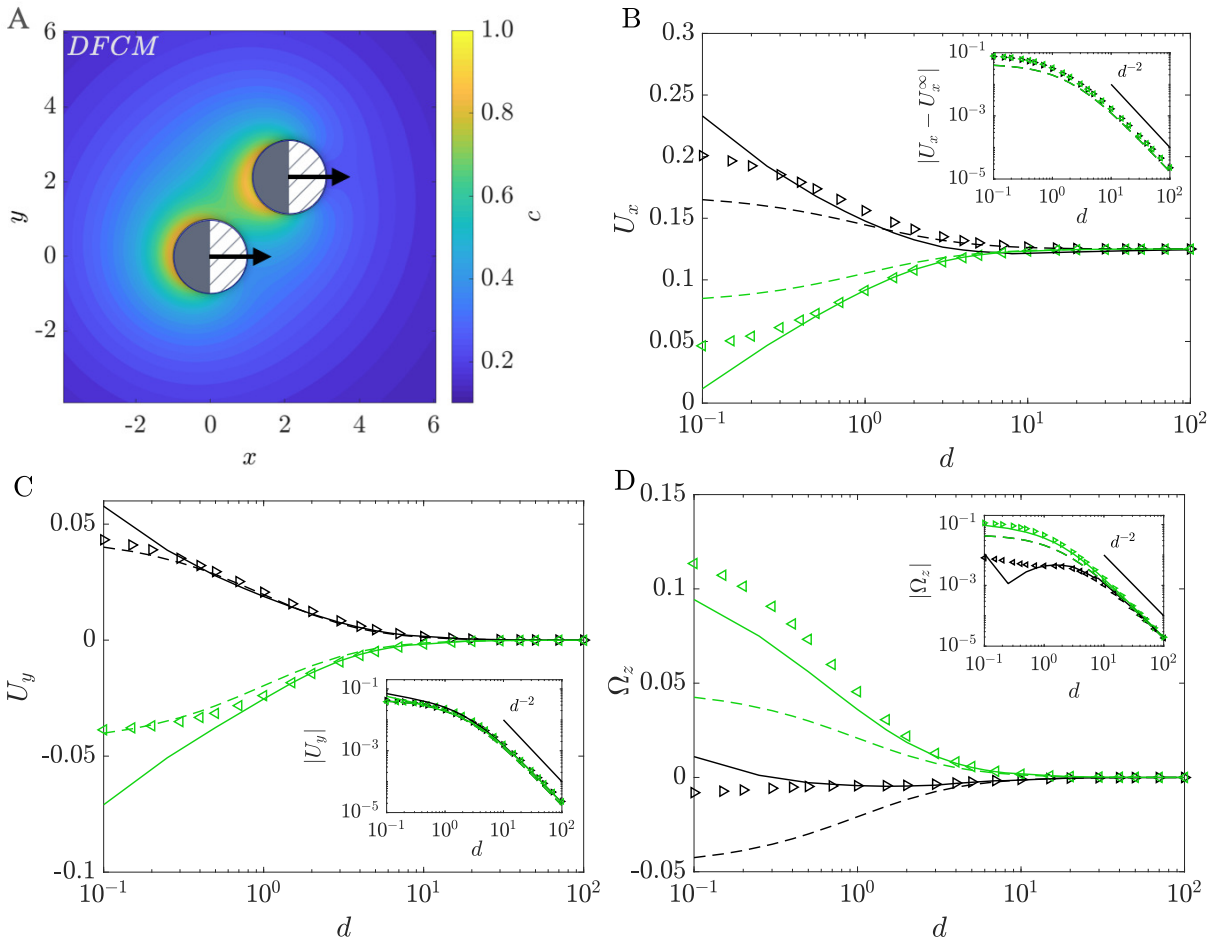


Figure 3.8: Case C: a) DFCM concentration field for $d = 1$, b) velocity $U_x$, c) velocity $U_y$, d) angular velocity $\Omega_z$. The black lines (and markers) correspond to particle 1 and the light green ones to particle 2. The triangle markers correspond to DFCM, the solid lines correspond to BEM, while the dashed lines to FFA. The inset shows the absolute values in logarithmic scale and the corresponding decay. All the omitted components of $\boldsymbol{\Omega}$ and $\boldsymbol{U}$ are zero.

$\Omega_z$ with distance. At the same time, BEM, the most accurate solution, shows that particle 1 rotates slower than particle 2 for $d < 10$ and changes direction in the near field $d < 0.2$. DFCM is able to capture this non-trivial and asymmetric evolution of the rotation velocity but fails to capture the direction reversal of particle 1; as for case B, this may stem from the inability of DFCM to resolve correctly the lubrication flows within the thin fluid gap between the particles.

Nevertheless, over all three cases considered and in particular in the most generic setting of Janus particles with non-uniform mobility in non-axisymmetric settings, our results show the importance of the proper resolution of higher-order hydro-chemical multipolar signatures (e.g., induced polarities and rigidity stresslets) to capture accurately non-trivial feature of the hydro-chemical interactions between particles. DFCM may not be able to resolve the details of the chemical and hydrodynamic fields in the gap between the surface of the particles when they are close to each other (e.g., $d \lesssim 0.5$) as it does not actually represent the exact position of the surface. Yet, this new numerical approach offers significant improvements in capturing such complex effects both qualitatively and quantitatively in comparison with simpler analytical or numerical models while providing a significant reduction in complexity in comparison with detailed numerical simulations such as BEM, opening significant opportunities for the numerical analysis of larger number of particles and suspension dynamics.

## 3.5 Discussion

In this chapter, we presented a generalization called Diffusiophoretic Force Coupling Method (DFCM) of the approach of the hydrodynamic FCM to compute hydro-chemical interactions within reactive suspensions of Janus particles with non-uniform surface activity and mobility. Following the standard hydrodynamic FCM, we rely on a truncated regularized multipolar expansion at the dipole level to solve the Laplace problem for the reactant concentration field and its moments at the particle surface. While the monopole is directly obtained from the prescribed fluxes on the swimmer surface, the dipole is found iteratively by accounting for the effect of other particles on their polarity. Instead of using surface operators, which are difficult to handle on Eulerian grids, our method relies on spectrally convergent weighted volume averages to compute successive concentration moments. Unlike standard FCM, the averaging envelopes are non-Gaussian as their weight is shifted toward the particle's surface and thus differs from the Gaussian spreading envelopes associated with each singularity. The first two moments of concentration around the particle are directly related to the intrinsic phoretic velocity and rotation of the particles (i.e., those obtained for an isolated particle experiencing the same hydrodynamic surface slip in an unbounded domain) but also to the singularities characterizing their hydrodynamic signatures, i.e., an intrinsic active stresslet and a potential dipole. These multipoles are then used as inputs for the solution of the hydrodynamic (swimming) problem, solved using the existing hydrodynamic FCM framework to obtain the total particle velocities.

Even though our approximate method does not resolve the particle surface exactly (and is as such unable to capture lubrication or strong confinement effects), its predictions for the dynamics of two particles compare well with analytical or accurate numerical solutions for distances larger than half a radius ($d \gtrsim 0.5$), which is relevant for dilute and semi-dilute suspensions. Most importantly, in all the results presented above, DFCM provides significant improvements over far-field models that neglect mutually-induced polarities and rigidity stresslets. Our case study has shown the importance of properly resolving these dipolar singularities to capture non-trivial hydro-chemical interactions between particles.

Although the present work purposely focuses on the presentation of the framework and

detailed validation of pairwise interactions of phoretic particles, our diffusio-phoretic framework readily generalizes to $N$ particles. A remarkable feature of FCM is that the spreading and averaging operations are volume-based and independent of the Stokes and Laplace solvers. Instead of using Green's functions for specific geometries, the reactant concentration $c$ and fluid velocity $\boldsymbol{u}$ can be solved for with any numerical method (e.g., finite volume, spectral methods) on an arbitrary domain where the FCM spreading and averaging operations are performed on the fixed computational grid [151, 155, 156]. As shown in previous work [106], the corresponding cost scales linearly with the particle number $O(N)$, while Green's function-based methods, such as Stokesian Dynamics [132] and the method of reflections [121], are restricted to simple geometries and require sophisticated techniques to achieve similar performances instead of their intrinsic quadratic scaling $O(N^2)$ [135, 159, 160]. In addition to improving far-field models, our method, therefore, offers a scalable framework for large-scale simulations of reactive particles. We will use these capacities to study their collective motion and micro-structure in Chapter 4.

# Chapter 4

# Organization and collective motion of reactive suspensions

Using the newly developed numerical framework (DFCM), a scalable code in parallel is developed, presented, and validated. In this case, the physical system has new features since now it is considered a cubic domain with periodic boundary conditions. The addition of a time integration scheme and steric repulsive forces between particles close to contact is required, and the details are presented. A new cluster definition is considered and described in detail. A parametric study is proposed, including several values of the mobility ratio, and the activity ratio, while for some specific cases, the volume fraction was considered as well. Later, a classification procedure based on the results statistic is proposed, and the emerging regimes are presented and rationalized.

## 4.1 Scalable simulation code, and numerical aspects

### 4.1.1 Scalable DFCM code

Once the validation of the method for small number of particles was performed (section 3.4), I implemented a highly scalable DFCM code capable to model large set of particles, analogously to the previous developed by [106, 156]. For this version, I do not rely on the approach based on Green's functions (as in the proof of concept code, section 3.4.1) but instead on the direct numerical solution of the modified Laplace and Stokes equations (Eq. 3.7 for $c$ and Eq. 3.36 for $\boldsymbol{u}$ respectively) presented here:

$$\nabla^2 c = -\sum_{n=1}^{N} \left[ q_n^M \Delta^M(r_n) + \mathbf{q}_n^D \cdot \nabla \Delta^D(r_n) \right], \tag{4.1}$$

$$\nabla p - \nabla^2 \boldsymbol{u} = \sum_{n=1}^{N} \left[ \boldsymbol{S}_n \cdot \nabla \Delta^*(r_n) + \boldsymbol{S}_n^a \cdot \nabla \Delta(r_n) + \boldsymbol{H}_n^a \nabla^2 \Delta^*(r_n) \right]. \tag{4.2}$$

This scalable implementation was performed based on the previous Fortran code provided by Blaise Delmotte, which extends the FCM for active particles by including the squirmer model in it [106]. It includes parallel processing in the Fourier space for tri-periodic domains to study suspensions in bulk, allowing fast simulations of large suspensions of microswimmers ($10^4 - 10^5$ particles). It uses high performance computing (HPC) tools to perform efficiently the simulations, including the MPI, P3DFFT, and FFTW libraries, the simulations were launched in the national french supercomputer called Jean-Zay, at the Institute for Development and Resources in Intensive Scientific Computing (IDRIS), of the Centre National de la Recherche Scientifique (CNRS), for more information check http://www.idris.fr/eng/jean-zay/cpu/jean-zay-cpu-hw-eng.html.

To do that, one global Cartesian grid is implemented in a cubic box with an equal number of grid points $N_x$ in each direction (between 80 and 120 for the following results). The volume integrals required to compute the concentration moments, Eqs. 3.14 and 3.16 (as well as the hydrodynamic velocities, Eqs. 3.40 and 3.41) are performed with a Riemann sum, given its facility for parallel calculations (using up to 30 points in each direction).

### 4.1.2 Validation results

The validation of the scalable Fortran DFCM code was performed by reproducing the results of the previous cases A, B, and C (figures 3.4, 3.6, 3.7 and 3.8), but in the new three-dimensional box of size $L$ with periodic boundary conditions (see figure 4.2 as reference). The results should

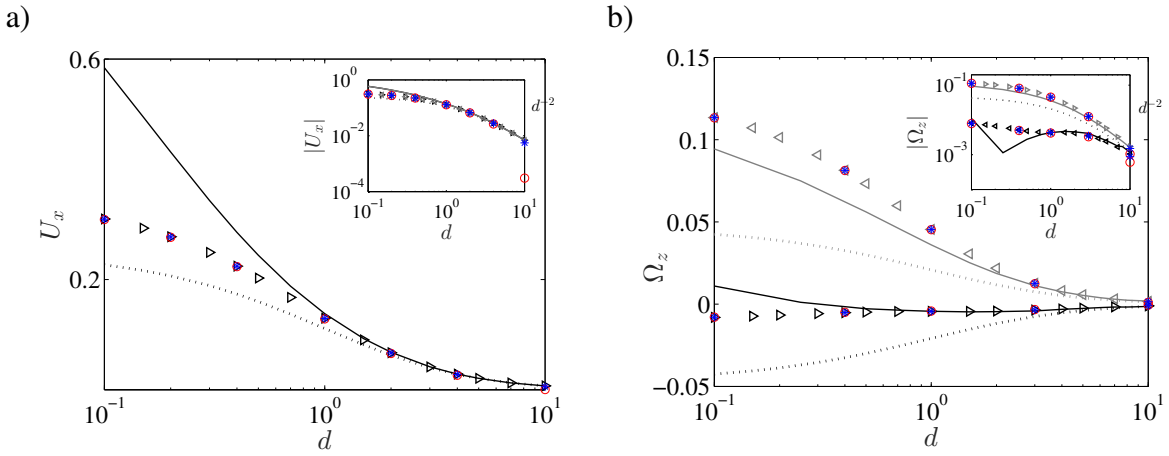


Figure 4.1: Superimposed results of scalable code over proof of concept code validation results for a) $U_x$ for case A, and b) $\Omega_z$ for case C (using $N_x = 80$ (red circles) and $N_x = 120$ (blue asterisks)). Dotted lines represents the FFA solution, solid lines the exact solution (BSC in a) and BEM in b)) and the triangular markers the proof of concept code results.

tend to the desired results by increasing the ratio domain-length vs. particle-radius $L/a$, since it reduces the effect of the boundary conditions in the particle pair centered in box. In practice, I do it increasing the number of points $N_x$ in the grid, since I prescribed the number of grid points per particle radii. Figure 4.1 shows some of the obtained results.

The techniques that brought the exact solutions for the validation examples considered previously (BSC and BEM) solve in 3D the Laplace and Stokes equations. However, BSC is restricted only to two particles and axisymmetric configurations because it uses a Legendre decomposition instead of spherical harmonics, BEM has no limitation regarding the symmetry of the problem and the number of particles. However, the available code for BEM only solves the particle's position and orientation in 2D [138].

Since the new high performance computing DFCM code is fully 3D (solution of fluid fields as well the dynamics of the particles), and given the limitations of the BSC and BEM codes, I also considered several 3D rotations of these validation cases to check the new code in depth. To do so, I compared the results generated with the scalable DFCM code rotating the inputs (position and orientations) of the cases A, B, C, with the known exact results generated with the proof of concept code results but transformed considering these rotations. Convergent numerical results are observed upon increasing the number of points in the grid as expected.

### 4.1.3 Time integration

Unlike the validation cases presented before, now we want to consider free particles in suspensions and let them evolve in time to study the emerging patterns. So we need a time integrator for the positions and orientations of the particles. Following [106], we have considered a fixed four-step Adam-Bashforth method and use the time step as

$$\triangle t = \epsilon \frac{a}{U^i} \tag{4.3}$$

where $a$ is the particle radius, $U^i$ is the intrinsic speed (the self-induced velocity for an isolated particle), $\frac{a}{U^i}$ is the time required for an isolated particle to swim a half-body length and $\epsilon$ is a

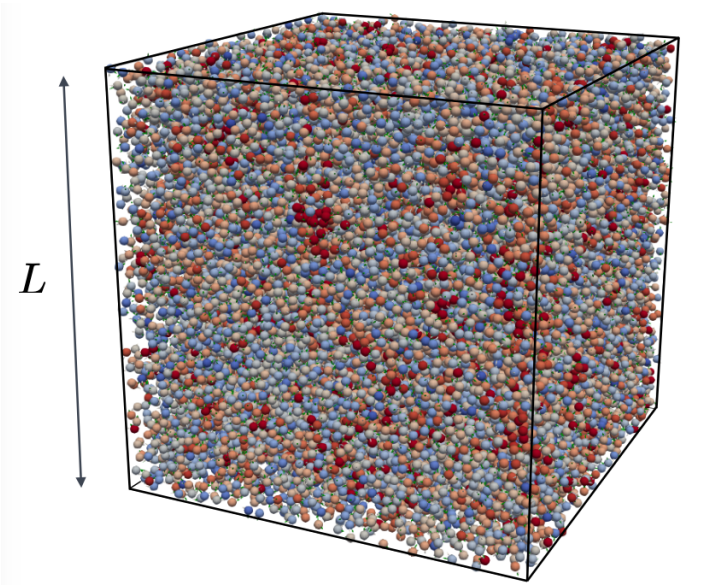


Figure 4.2: Model in 3D - cubic box of size $L$ with periodic boundary conditions with $N = 34133$ particles of radius $a$. The color correspond to the particle velocity.

numerical factor lower than one so that we could integrate the particles' position properly and in practice, it is in the range $\epsilon \in [1/20, 1/200]$.

However, as soon as we consider a larger number of particles (above some hundreds), we start to have problems with particles' partial superposition in cases where larger clusters are obtained. Eventually, this implies two issues: first, the obtained solution is non-physical, and second numerically, it will induce high repulsive forces (equivalently high repulsive velocities), destabilizing the clusters' formation. The root of the problems starts when clusters start to be formed: on the one hand, the attraction reduces the inter-particle distances increasing its attractive velocity, but on the other hand, the particles are rigid, and some repulsive force is needed to be included to prevent particle superposition (see section 4.1.4) inducing a repulsive velocity in the particles. Suppose the time step is wrongly selected (too big). In that case, the balance between these two velocities could lead to undesired oscillations of increasing magnitude that result in non-physical high velocities and eventually in the superposition of the particles.

Although the velocity $U^i$ is a good reference for free particles, other velocity reference needs to be defined once they form clusters to avoid these non-physical oscillations. I called this reference velocity $U_R$; it is provided by a numeric calculation considering the phoretic properties of the particles (activity and mobility) and the number of particles in the system of interest; it is detailed in Appendix C. In short, it considers a critical case in which a compact cubic geometry of particles in contact interacts, the particles have the phoretic properties of interest, and the repulsive force is suppressed. The instantaneous maximum velocity obtained in this configuration brings us $U_R$.

Finally, we used a fixed two-step Adam-Bashforth method for our simulations, which proved to delay the non-physical oscillations (compared to the four-step method) when the time step was chosen badly during our tests. The time step that I considered for the simulations is provided by the following equation fixing $\epsilon = 1/200$:

$$\triangle t = \epsilon \frac{a}{U_R}. \tag{4.4}$$

### 4.1.4 Steric repulsive force

In the validation cases presented in Chapter 3, the inter-particle distance $d$ is an input parameter, physically $d \geq 0$ since the particles are rigid and they can not superpose ($d = 0$ means particles in contact). For the cases of interest in this chapter, we will consider free particles in a suspension and let them evolve in time. Previously the particles' superposition has been avoided simply by respecting the range of $d$, but now a repulsive force needs to be included to simulate the contact between particles' surfaces. This has been done by including some short-ranged repulsive force that acts between pair of particles that are in close contact ($d \leq 0.2$); this force is included according to the FCM formalism in the right-hand side of the equation 4.2 when the close contact criterion is fulfilled (first term in equation 3.26).

Following [106], we have considered the steric barrier described in [161], in which the repulsive force between two particles separated by a distance $r_{nm} = |\boldsymbol{r}_{nm}|$, where $\boldsymbol{r}_{nm} = \boldsymbol{Y}_m - \boldsymbol{Y}_n$ is given by

$$\mathbf{F}_n = -\frac{F_{ref}}{2a}\left[\frac{r_{ref}^2 - r_{nm}^2}{r_{ref}^2 - 4a^2}\right]^{2\gamma} \boldsymbol{r}_{nm}, \qquad \text{if } r_{nm} < r_{ref} \tag{4.5}$$

where $F_{ref}$ is the magnitude of the force, $r_{ref}$ is the cut-off distance where the force starts to act and the exponent $\gamma$ is used to control the stiffness of the force. Suggested values by the authors [106, 161] were used working well for some examples ($F_{ref}/6\pi a U^i \in [4, 32]$, $r_{ref}/a = 2.2$ and $\gamma \in [1, 3]$), but as soon we consider larger number of particles (above some hundreds) we started to have problems of particles superposition in cases where larger clusters are obtained.

After considering several variations on these parameters and other ways to model this repulsive force so that simulations are safe from particle superposition, we finally move to another description considering the Lennard-Jones potential $V_{LJ} = 4\xi\left[\left(\frac{\lambda}{r}\right)^{12} - \left(\frac{\lambda}{r}\right)^{6}\right]$, where $\lambda$ is the particle size, $\xi$ is the potential depth, and $r$ is the inter-particle distance. Taking its negative gradient and considering only the repulsive part of this potential ($r^{-12}$ term) we got the repulsive Lennard-Jones force $\mathbf{F}_{LJ} = \frac{48\xi\mathbf{r}}{r}\left(\frac{\lambda}{r}\right)^{12}$. Particularly for our simulations, we have considering the truncated and shifted repulsive Lennard-Jones force defined by

$$\mathbf{F}_{LJTS} = 48\xi\boldsymbol{r}_{nm}\left[\frac{1}{r_{nm}}\left(\frac{\lambda}{r_{nm}}\right)^{12} - \frac{1}{r_{ref}}\left(\frac{\lambda}{r_{ref}}\right)^{12}\right] \qquad \text{if } r_{nm} < r_{ref} \tag{4.6}$$

where the following values are used: $\lambda = 2a$, $r_{ref} = 1.1\lambda = 2.2a$. The value of $\xi$ was selected to prevent particles overlap and scaled using the reference velocity $U_R$ (instead the intrinsic velocity $U^i$), in detail $\xi/6\pi a U_R \in [32, 64]$.

### 4.1.5 Clusters definition

Considering figure 1.10, we will expect to have clusters of particles during our simulations as observed in experiments [13, 14, 18]. An important question at this point is, what do we mean by a cluster? Of course, we are talking about groups of particles in contact (or close contact) between them, but is it just because two particles are in contact that it becomes a cluster? Is there a minimum number of particles to consider a group of particles a cluster? Is there something more than the contact to be considered at this point? Typically the cluster definition used in experiments and simulations is purely geometric [12, 162, 163, 164] in which all the particles with a surface-to-surface distance smaller than a certain threshold distance share a connection (typically $d \in [0, 1]$). Then, a cluster is the set of all mutually connected particles.

An interesting alternative was provided recently [18], in which a more restrictive definition of a cluster is used considering triplets of particles forming triangles and not only pairs (see

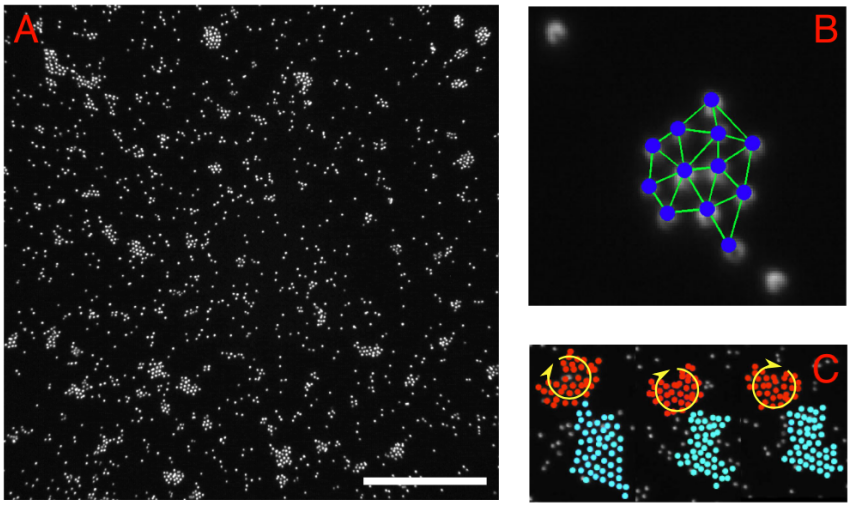


Figure 4.3: Experimental realization of active clusters showing: a) a snapshot of the cluster phase (scale bar $40\mu m$), b) geometric constraint on their kinetic definition of clusters, note the adjacent triangles and the isolated particles, c) series of snapshots showing how two different clusters touch each other without merging into a single cluster. Adapted from [18].

figure 4.3.b) as well as a time persistence constraint of the cluster. By doing this, they better resolve the cluster by discarding, for example, single particles that just explore their neighborhood by touching clusters without joining them or the case of neighbor clusters that interact by touching each other but without merging and with clearly definite different motions (see figure 4.3.c).

In this thesis, I consider an intermediate definition of a cluster focusing only on the geometric aspect. However, since our models are in three dimensions, we define a cluster based on tetrahedral geometry as a building block (instead of triangles in two dimensions like in [18]). In practice, we use the concept of k-clique to identify the clusters. In the context of graphs theory and networks, a k-clique is a subset of $k$ nodes in a network, such that every node is connected to each other on it [165]. The simplest examples of k-cliques structures are shown in figure 4.4 which illustrates the concept intuitively. We defined that two particles are connected when they are less distant than a given threshold. Then in a k-clique, all particles are connected to each other.

Consequently, at least we need four mutually connected particles to have a cluster (a tetrahedron). The connection of adjacent tetrahedrons could form bigger clusters (sharing a triangular face), analogous to the adjacent triangles in two dimensions sharing one edge (see figure 4.3.c). We implement the identification of the 3D clusters, first collecting a list of connected particle pairs (using the threshold $d \leq 1.2$) and second processing this list using the k-clique percolation algorithm [165] setting $k = 4$. A couple of clarifications are pertinent here:

- Although in principle, the algorithm could only give us lists with 4-clicks, in reality, it provides us lists with large networks formed from the union of several 4-clicks (when it applies). In other words, it bring us directly the list with the physical (big) clusters in the simulation and not the (small) clusters that work as building blocks.

- Our threshold distance ($d \leq 1.2$) was selected based on the calibration with some examples in our simulations, in which there are very well-defined clusters (being consistent with the values in [18]).

Although the proposed procedure to define the clusters does not include the kinetic approach

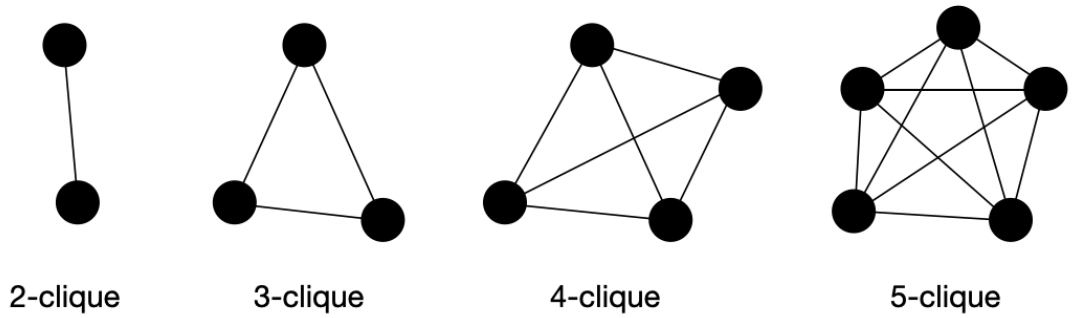


Figure 4.4: Representation of first k-cliques ($k = 2, 3, 4, 5$), where $k$ is the number of connected nodes (distance criterion) to each other (particles in our case of interest).

considered by [18]; it could also avoid counting as a single cluster, two clusters that contact each other like in the case considered in image 4.3.c), because it will represent only a 2-clique or 3-clique event, so it represents an improvement over the typical approach previously mentioned.

### 4.1.6 Motion quantification in persistent clustering regimes

As we will see during this chapter, in our simulations some combinations of the system properties leads to persistent clusters with a very well defined structure behaving with a solid rigid body motion. In these cases, the translational and angular velocities of the cluster have been quantified during all the simulation using the particles positions $\mathbf{Y}_i$ and velocities $\mathbf{U}_i$ as well as the lists of particles in each cluster. The starting point to do this is the calculation of the cluster's velocity $\mathbf{U}_c$ (or center of mass velocity), defined by

$$\mathbf{U}_c = \frac{1}{N_{pc}} \sum_{i}^{N_{pc}} \mathbf{U}_i \tag{4.7}$$

where $N_{pc}$ is the number of particles in the cluster in consideration and $\mathbf{U}_i$ is the velocity of the $i$ particles in the cluster. On the other hand the angular velocity of the cluster $\mathbf{\Omega}_c$ could be calculated in the following way. Knowing the relation between angular momentum $\mathbf{L}$ and angular velocity $\mathbf{\Omega}$ by the relation $\mathbf{L} = \mathbf{I} \cdot \mathbf{\Omega}$, we could write

$$\mathbf{\Omega}_c = \mathbf{I}_c^{-1} \cdot \mathbf{L}_c \tag{4.8}$$

where $\mathbf{I}_c$ is the cluster's inertia tensor and $\mathbf{L}_c$ is the cluster's angular momentum. This 2 quantities could be calculated as follow

$$\mathbf{I}_c = \sum_{i}^{N_{pc}} ( \mathbf{I} \, |\mathbf{r}_i^{cm}|^2 - \mathbf{r}_i^{cm} \mathbf{r}_i^{cm}) \tag{4.9}$$

$$\mathbf{L}_c = \sum_{i}^{N_{pc}} \mathbf{r}_i^{cm} \times \mathbf{U}_i \tag{4.10}$$

where $\mathbf{I}$ is the identity tensor, $\mathbf{r}_i^{cm}$ is the particle position in the cluster respect to its center of mass $\mathbf{R}$ calculated through

$$\mathbf{r}_i^{cm} = \mathbf{Y}_i - \mathbf{R} \tag{4.11}$$

$$\mathbf{R} = \frac{1}{N_{pc}} \sum_{i}^{N_{pc}} \mathbf{r}_i \tag{4.12}$$

Once all the cluster velocities are calculated, the average of its magnitudes will be presented as time series during the simulation.

## 4.2 Reactive suspensions parameters and numerical study

In the suspensions in our models, we will have $N$ identical Janus particles of radius $a$ in a cubic domain of length L; each particle is characterized by its phoretic activity $\overline{\alpha}$, $\alpha^*$ and phoretic mobility $\overline{M}$, $M^*$ (mean and contrast respectively according to section 2.2.2). The system is fully characterized by these seven parameters, which only have three dimensions (length, time, and concentration), so the system will have four dimensionless parameters. In particular, I defined:

$$\frac{\overline{\alpha}}{\alpha^*}, \frac{M^*}{\overline{M}}, \phi, \frac{L}{a} \tag{4.13}$$

where:

- the activity ratio $\frac{\overline{\alpha}}{\alpha^*}$ measures the relative intensity of the monopolar and dipolar strength in the particles population.
- the mobility ratio $\frac{M^*}{\overline{M}}$ measures the contrast in mobility, with respect to its mean value.
- the volume fraction $\phi = \frac{V_{particles}}{V_{fluid}} = \frac{4\pi a^3 N}{3L^3}$, measures the volume occupied by all the particles relative to the domain volume.
- the length ratio $\frac{L}{a}$ measures the ratio between domain size $L$ and particle radius $a$.

I mainly focused my research on the first two parameters since they are the ones that characterize the Janus particles entirely, and I was more interested in the study of the different patterns (micro-structures and collective motions) that emerge from the different kinds of reactive suspension. Later, I considered the third parameter $\phi$ in some specific cases to study how it affects the suspension properties.

### 4.2.1 Activity ratio: monopolar and dipolar strength of the particles

Considering equation 4.1 which quantifies the volume effects that will have each particle in the concentration field, while the first set of terms on the right-hand side of this equation quantifies the monopolar contributions of each particle (isotropic at the level of each particle and related to the net generation of solute), the second set of terms quantifies the dipolar contributions (anisotropic at each particle representing the front-back asymmetry of the Janus particle). It could be shown that at each particle, the monopolar term is proportional to $\overline{\alpha}$, while the dipolar term is proportional to $\alpha^*$.

Based on this, we could understand this dimensionless number as an indicator of the intrinsic polarity of the particle, being very polar when $\overline{\alpha}/\alpha^* \ll 1$ and mostly monopolar (or isotropic) when $\overline{\alpha}/\alpha^* \gg 1$. This is summarized in the figure 4.5 where the two dominant ranges are shown (monopolar or dipolar dominantly) and where the concentration field around the particles is

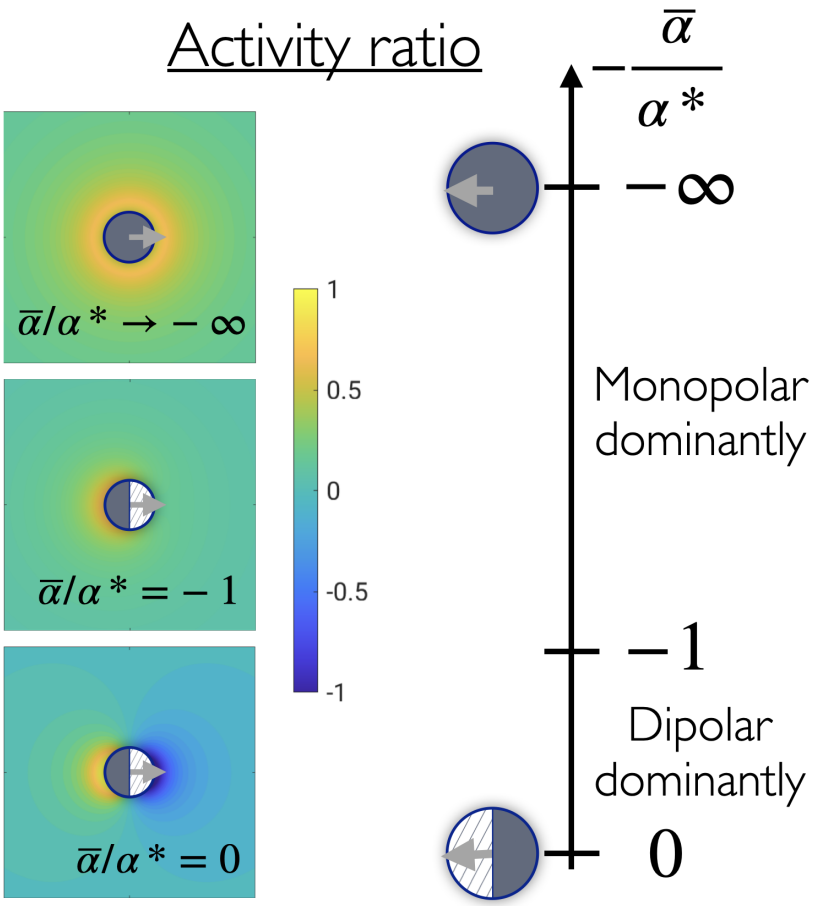


Figure 4.5: Activity ratio, the corresponding two extreme cases and the particle that it represents are presented. For each extreme case (and an intermediate one) its concentration field is shown, having a very symmetric field for high values, a very non-symmetric (and highly oriented through the particle axis) for null values and something intermediate for the classical (active-passive) Janus particle. The particles' orientation $\mathbf{p}_n$ is represented with the gray arrow.

provided for these two extreme cases and an intermediate case, which represents a very common Janus particle (with an active (emitting) hemisphere and a passive one). By analysing both terms individually, we must note that the activity contrast defines the intrinsic self-propulsion of the particle while the activity mean affects the coupling with other particles.

### 4.2.2 Mobility ratio: Phoretic drift and chemotaxis

Considering the *active* translation movement in the coupled problem $\boldsymbol{U}^a$ given by Eq. 3.46, and using only its leading order term (proportional to its first moment of concentration ), we have

$$\boldsymbol{U}_n^a = -\frac{2\overline{M}_n}{a}\langle c\boldsymbol{n}\rangle_n. \tag{4.14}$$

We see that considering an external gradient $\nabla c^E$, it will generate a polarity $\langle c^E \boldsymbol{n}\rangle_n$ (parallel to it), and that if $\overline{M} > 0$ the particle will drift away from this gradient. At the same time, if it is negative, the particle will drift towards this gradient. Since in our suspensions, we will consider only particles that effectively act as net sources ($\overline{\alpha} \geq 0$), and since the external gradient induced

in each particle is going to be generated by the other particles, this translates to a repulsive effect between particles if $\overline{M} > 0$ usually called phoretic repulsion and into an attractive effect between particles when $\overline{M} < 0$ known as phoretic attraction.

The polarity $\langle c\boldsymbol{n}\rangle_n$ for the particle $n$ takes into account both the *intrinsic* part of the polarity, caused by its own built-in asymmetry by design, and the *external* part of the polarity, caused by the interaction with other particles, which causes the translational *drift* in the suspension chemical field. The corresponding velocity contributions are identified in figure 4.6 (for the particle $n$) as the intrinsic velocity $\mathbf{U}_n^i$ and the *first component* of the drift velocity $\mathbf{U}_n^{d_1}$.

Considering the *active* rotation movement, the angular velocity $\boldsymbol{\Omega}_n^a$ is given by Eq. 3.49:

$$\boldsymbol{\Omega}_n^a = -\frac{9M_n^*}{4a^2}\ \boldsymbol{p}_n \times \langle c\boldsymbol{n}\rangle_n. \tag{4.15}$$

where we see that considering an external gradient $\nabla c^E$, it will generate a polarity $\langle c^E\boldsymbol{n}\rangle_n$ (parallel to it), and that if $M^* > 0$, the particle will reorient rotating against this gradient making the particle swims against (if isolated) this gradient (anti-chemotactic effect). In contrast, if $M^* < 0$, the particle will reorient, rotating towards this gradient and making the particle swims towards (if isolated) this gradient (chemotactic effect). This is true if in the particle in consideration its orientation $\mathbf{p}_n$ is parallel to its intrinsic (or self-induced) velocity $\mathbf{U}_n^i$: check signs in Eq. 2.59 and in Eq. 4.15 but also check figure 4.6.b). Still, the tendency is inverted if these two quantities ($\mathbf{p}_n$ and $\mathbf{U}_n^i$) are anti-parallel since the active rotation $\boldsymbol{\Omega}_n^a$ considers the orientation but not the intrinsic velocity, as shown in figure 4.6.a).

### 4.2.3 Parametric study values

By using this scaling and sweeping the mobility ratio with $\overline{M} = +1$, we got the solid blue line in figure 4.7, which is consistently valid for suspensions with phoretic repulsion (both chemotactic and anti-chemotactic, depending on the sign of the mobility ratio). Equivalently by using $\overline{M} = -1$, we consider suspensions with phoretic attraction (both chemotactic and anti-chemotactic, depending on the sign of mobility ratio), as can be seen in the blue dashed line in figure 4.7. I have considered several values of the activity and mobility ratio to perform a parametric study, the corresponding values are indicated in Table 2.

| **Parameter** | **Values** |
|---|---|
| $L/a$ | 24.25 |
| $\phi$ | 0.15 |
| $\alpha^*$ | -1 |
| $\overline{M}$ | -1, +1 |
| $\overline{\alpha}/\alpha^*$ | 0, -0.1, -1, -5 |
| $M^*/\overline{M}$ | -10, -1, -0.1, 0, +0.1, +1, +10 |

Table 2. Values considered for the parametric study, in particular $N = 515$ and $U^i = 1/2$.

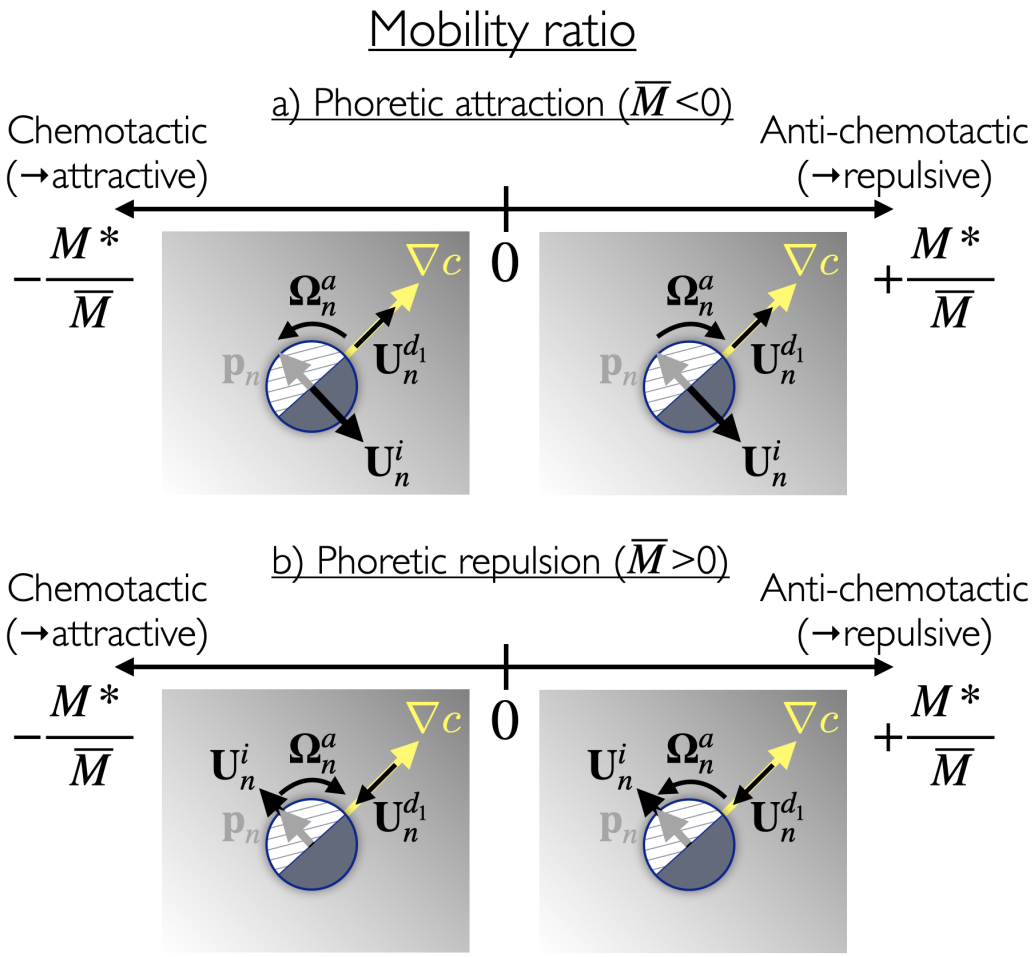


Figure 4.6: Mobility ratio and their physical effects for particles with negative activity contrast ($\alpha^* < 0$) under: a) phoretic attraction, b) phoretic repulsion. In both cases the positive or negative chemotaxis (chemotaxis or anti-chemotaxis) depends on the mobility ratio as shown. The local external chemical gradient on the particle $n$ (produced by the other particles) is represented both by the background with gray-scale and the yellow arrow. The black arrows represent the *active* particles velocities (intrinsic $\mathbf{U}_n^i$, drift $\mathbf{U}_n^{d_1}$ and rotation $\mathbf{\Omega}_n^a$), while the gray arrow represent the particle orientation $\mathbf{p}_n$.

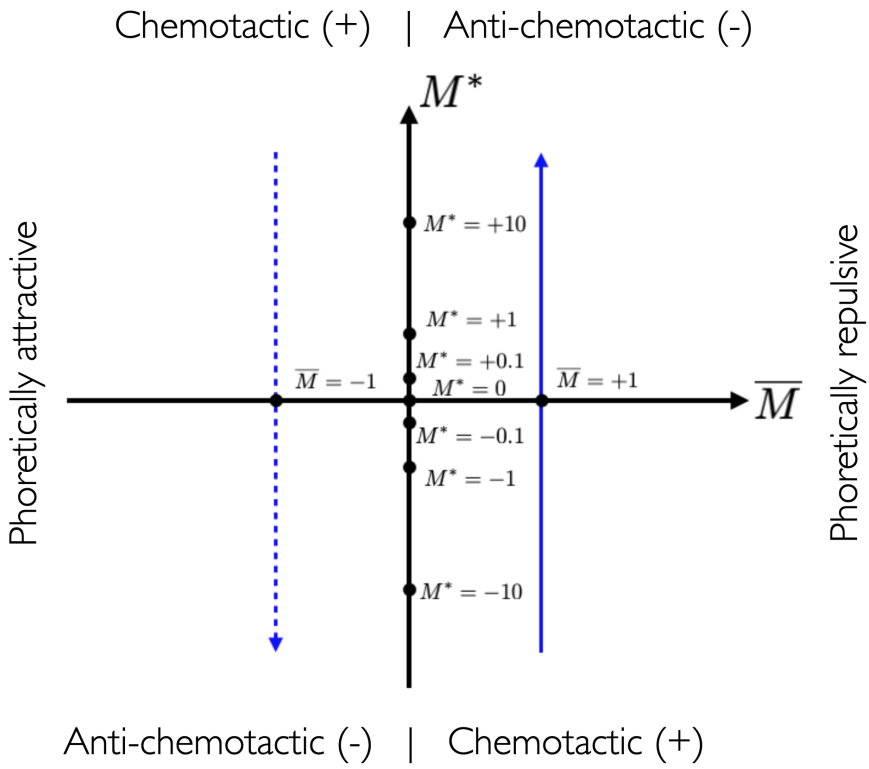


Figure 4.7: Mean-contrast mobility space and sweep proposed.

## 4.3 Observed regimes

In the following, we will use the intrinsic velocity $U^i$ (self-induced velocity of an isolated particle, Eq. 2.59) as the velocity reference $U$ to scale the particles velocities ($U = U^i$). We will use as well this velocity to express the time-dependent variables as function of the dimensionless time $tU/a$, where $a/U$ is the time required for an isolated particle to swim one particle radius.

### 4.3.1 Tools

To classify the emerging regimes in the suspensions, the previously described k-clique algorithm was used, specifying the basic structure to be considered: tetrahedrons ($k = 4$) and the threshold distance to consider two particles connected ($d \leq 1.2$). Once the k-clique lists are created for each time step, we use them to create the following statistics:

- Number of clusters $N_c$ allows measuring the number of clusters over time.
- Ratio of particles in clusters $R_p$, as the ratio between the particles in clusters $N_p$ and the total number of particles $N$, over time.
- Cluster size distribution $S$, measured in the number of particles, where at a given time, all the sizes of the clusters are presented (in a histogram).
- Cluster size statistics $S_{mean}, S_{stde}, S_{mini}, S_{maxi}$ taken instantaneously over the different clusters, measured in number of particles, and represented in time series (mean, standard deviation, minimum, maximum respectively).

- Average $\mu_X$ and standard deviation $\sigma_X$ of time series $X$ over time. They were introduced to define a permanent state (analogous to the stationary state) since many time series show continuous fluctuations. They were calculated using the data in a stretching window between the fixed initial time $t_0$ and the floating final time $t^*$, so $\mu_X = \mu_X(t^*)$ and $\sigma = \sigma_X(t^*)$.

- Clustering permanent time $t^{clus}_{perm}$, it represents the starting point of the permanent state of the clustering in the simulation, and it is defined by the first time by which the statistics $\sigma_X$ reach its global maximum. The statistics used were $X = S_{mean}$ and $X = S_{maxi}$, defining $t^{clus}_{perm}$ as $t^{clus}_{perm} = max(t|_{S_{mean}}, t|_{S_{maxi}})$.

- Persistence time of particles in clusters $P_p$ represents the total time in which each particle is attached to any cluster. It is represented as a histogram considering all the particles' persistence, only during the permanent state of the simulation $t \in [t^{clus}_{perm}, T]$. It is presented in two different ways: in dimensionless physical time ($tU/a$, like in the time series) and as a fraction of the stationary regime time ($(t - t^{clus}_{perm})/(T - t^{clus}_{perm})$), where $T$ is the final simulation time.

- Pair distribution function $g = g(r)$, representing the probability of find a second particle $j$ respect to some labelled particle $n$, at a distance $r = |\mathbf{Y}_j - \mathbf{Y}_n|$. It is averaged for all the particles during all the permanent state of the simulation $t \in [t^{clus}_{perm}, T]$ and defined by:

$$g(r) = \left[\frac{N(r)}{V(r)}\right] / \frac{N}{V_T}, \tag{4.16}$$

  in which centering in a single particle, a series of concentric shells of radius $r$ (and $r + dr$) were constructed, the number of particles in the shell is given by $N(r)$ and the shell's volume by $V(r)$. This distribution is normalized by the factor $\frac{N}{V_T}$ which is the total number of particles $N$ in the total volume $V_T$ considered in the calculation.

- Orientation $I_p = I_p(r)$ and velocity $I_U = I_U(r)$ correlation functions: measuring the spacial orientation (and velocity) alignment between particles separated by a distance $r$. They are given by:

$$I_p(r) = \left[\mathbf{p}(\mathbf{Y}) \cdot \mathbf{p}(\mathbf{Y} + \mathbf{r})\right]_{p,t} \tag{4.17}$$

$$I_U(r) = \left[\frac{\mathbf{U}(\mathbf{Y}) \cdot \mathbf{U}(\mathbf{Y} + \mathbf{r})}{|\mathbf{U}(\mathbf{Y})||\mathbf{U}(\mathbf{Y} + \mathbf{r})|}\right]_{p,t} \tag{4.18}$$

  In both correlation functions the averaging operator $\left[...\right]_{p,t}$ is performed over all the particles and times in the clustering permanent state $t \in [t^{clus}_{perm}, T]$. The number of particles in each shell previously introduced $N(r)$ is used to perform the averages at each discrete interval of distance $r$.

- Cluster velocities mean (translational and angular): $|\mathbf{U}_c|_{mean}, |\mathbf{\Omega}_c|_{mean}$ taken at a given instant and averaged over the different clusters that exist at that time. They are represented in time series and measured in dimensionless units. The translation velocity is made dimensionless with the intrinsic velocity ($U^i = U$), while the rotational velocity with the inverse of the time required by an isolated particle to swim one particle radius $a/U$.

- Velocity direction autocorrelation function: $I_U^* = I_U^*(t)$, measuring the persistence of the direction of the velocity of the particles during all the simulation. It is given by:

$$I_U^*(t) = \left[ \frac{\mathbf{U}(t=0) \cdot \mathbf{U}(t)}{|\mathbf{U}(t=0)||\mathbf{U}(t)|} \right]_p \tag{4.19}$$

  where the averaging operator $\left[...\right]_p$ is performed over all the particles during all the simulation.

- Motion permanent time $t_{perm}^{moti}$, it represents the starting point of the permanent state of the motion in the simulation, and it is defined by the last time by which the statistics $\sigma_{I_U^*}$ reach its local maximum.

### 4.3.2 Classification and classification procedure

Several organization patterns have emerged in the simulations, ranging from gas-like to fully clustered configurations. In particular, I identified and defined five regimes in which all of them could be classified:

- Regime 1: Gas-like, characterized by a majority of particles that swims freely, except by the formation of temporal clusters caused by local blocking of particles given the excluded volume effect and the steric interactions (figure 4.8.a).

- Regime 2: Big cluster with persistent motion, identified by the total collapse of all the particles into a single persistent cluster and the subsequent persistent translation (low) motion (figure 4.8.b). Two clusters with persistent translation have been identified in this regime in a particular configuration.

- Regime 3: Many small clusters with chaotic motion, identified by the total collapse of all the particles into a large set of small persistent clusters that interacts chaotically with relatively high motion, including translation and rotation (figure 4.8.c).

- Regime 4: Coexistence of many clusters with gas-like, characterized by the presence of a small set of persistent clusters at the same time that free particles (figure 4.8.d). There is an exchange of particles between both populations.

- Regime 5: Coexistence of big cluster with gas-like, described by the formation of a big cluster that attracts the majority of the particles in the system, co-existing with a set of free particles and intermittent small clusters (figure 4.8.e). There is an exchange of particles between both populations.

In order to classify the emerging regimes, some of the previous clustering tools were used, in particular based on the time series of $R_p$, $S_{mean}$, $S_{stde}$, $S_{maxi}$ as well the statistic of the time series of $\sigma_{S_{maxi}}$ and $\mu_{S_{maxi}}$; their averaged values in the (clustering) permanent state $t \in [t_{perm}^{clus}, T]$ were calculated and the numeric values: $[R_p]_t$, $[S_{mean}]_t$, $[S_{stde}]_t$, $[\sigma_{S_{maxi}}]_t$ and $[\mu_{S_{maxi}}]_t$ were obtained.

As well, motion tools were used, in particular the time series of $I_U^*$, its standard deviation $\sigma_{I_U^*}$ and its averaged value in the (motion) permanent state $t \in [t_{perm}^{moti}, T]$ obtaining the numeric value $[\sigma_{I_U^*}]_t$.

The other tools were used as a complement or just for the description of each regime. The next list enumerate the used steps to classify all the results, while Figures 4.9, 4.10, 4.11, 4.12

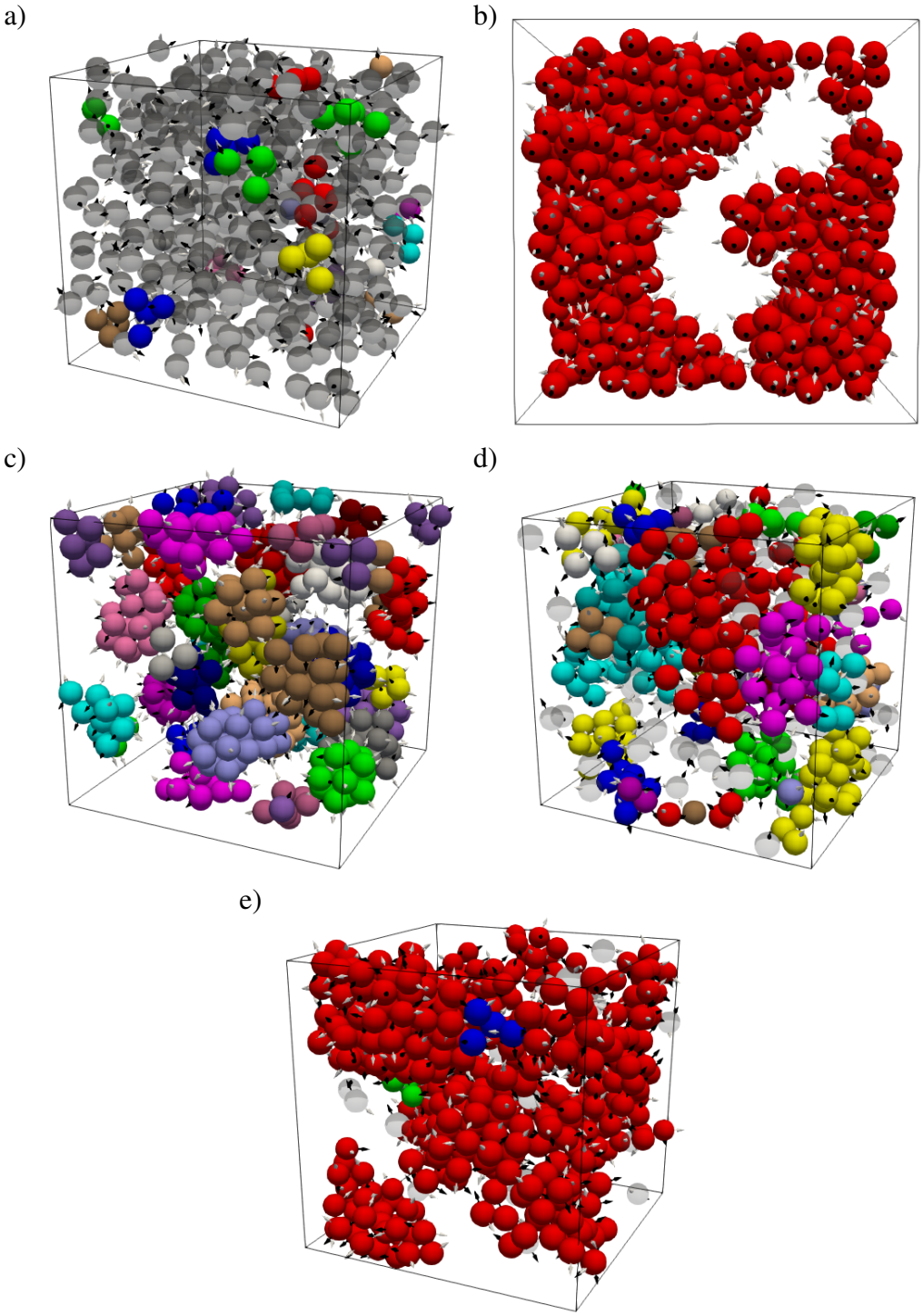


Figure 4.8: Representative snapshots of different regimes: a) Regime 1 (Gas-like), b) Regime 2 (Big cluster with persistent motion), c) Regime 3 (Many small clusters with chaotic motion), d) Regime 4 (Coexistence of many clusters with gas-like), and e) Regime 5 (Coexistence of big cluster with gas-like). The particles' surface color is used to identify the clusters (cluster number), while the transparency in the surfaces of the particles is used to identify free particles. Gray arrows represent the orientation of the particles and the black ones (translation) velocity.

and 4.13 present the most relevant results for each regime.

Regarding the following filters in the classification procedure, we could add some comments on what is behind this set of rules and numeric values. First of all, we need to verify if clustering is happening in the suspension, to do so, we check if the parameter $[\mu_{S_{maxi}}]_t$ is zero or not; if affirmative, the suspensions will be in Regime 1, filter **1.** ($[\mu_{S_{maxi}}]_t = 0$), if negative we move to the following filters. The first used parameter is $[\sigma_{S_{maxi}}/\mu_{S_{maxi}}]_t$, which provides information about the size variability of the (single) largest cluster. In the case of very persistent clusters (like in Regimes 2 and 3), once they are formed, they rarely change, and so their variability is minimal (or directly zero in many cases), allowing us to define the first part of the filter **2.** ($[\sigma_{S_{maxi}}/\mu_{S_{maxi}}]_t \leq 0.05$). Then, because of the persistent properties of these two regimes, all the particles (or most of them) stay all the time in some cluster leading to the second part of the filter **2.** ($[R_p]_t \geq 0.98$). To separate between these two regimes, we consider their motion in the permanent state: since for regime 2, the clusters move ballistically, their swimming direction is almost fixed (in the permanent state), and their variation should be small, leading to the filter **2.(a)** ($[\sigma_{I_U^*}]_t \leq 0.05$). On the other hand, for regime 3, the motion is chaotic so the variability should be bigger, (and so **2.(b)** ($[\sigma_{I_U^*}]_t > 0.05$). Since in Regime 5 there is a dominant big cluster (but still with some free particles and small intermittent clusters), the variability of the biggest cluster size will be more significant than in regimes 2 and 3; however, when normalized by their mean (which is big), this value becomes smaller leading to the filter **3.** ($[\sigma_{S_{maxi}}/\mu_{S_{maxi}}]_t \leq 0.10$). Finally, in regimes 1 and 4, there are small and not very persistent clusters. Consistently this results in the biggest values of the first parameter, and so the next filter becomes **4.** ($[\sigma_{S_{maxi}}/\mu_{S_{maxi}}]_t > 0.10$). To distinguish between these two regimes, the key point is that the clusters in regime 1 are very similar in size between them, obtaining small values of the clusters size variation $S_{stde}$, leading to the next filter **4.(a)** ($[S_{mean}]_t \geq 1.1[S_{stde}]_t$) and finally the last filter becomes **4.(b)** ($[S_{mean}]_t < 1.1[S_{stde}]_t$). The specific numeric values used in the filters were calibrated to the available data in our simulations.

Then, the ***classification procedure*** is defined as follows:

1. $[\mu_{S_{maxi}}]_t = 0 \rightarrow$ Regime 1
2. $[\sigma_{S_{maxi}}/\mu_{S_{maxi}}]_t \leq 0.05$ and $[R_p]_t \geq 0.98$
   (a) $[\sigma_{I_U^*}]_t \leq 0.05 \rightarrow$ Regime 2
   (b) $[\sigma_{I_U^*}]_t > 0.05 \rightarrow$ Regime 3
3. $[\sigma_{S_{maxi}}/\mu_{S_{maxi}}]_t \leq 0.10 \rightarrow$ Regime 5
4. $[\sigma_{S_{maxi}}/\mu_{S_{maxi}}]_t > 0.10$
   (a) $[S_{mean}]_t \geq 1.1[S_{stde}]_t \rightarrow$ Regime 1
   (b) $[S_{mean}]_t < 1.1[S_{stde}]_t \rightarrow$ Regime 4

### 4.3.3 Regime 1: Gas-like

Figure 4.9 shows the most representative results of this regime. In general, it's characterized by permanent and high fluctuations in all the time series during all the simulation. Figure 4.9.a) shows how the number of clusters $N_c$ presents sharp peaks between 10 and 30, indicating clusters' fast creation and destruction. This is consistent with the ratio of particles in clusters $R_p$,

which fluctuates very fast in an erratic way between 0.1 and 0.2, indicating that although many clusters have been formed, there is a persistent gas-like phase of free particles around them. Both quantities indicate a very fast transition from the initial condition to this regime. Figure 4.9.b) shows the statistics of the cluster size distribution, where the mean cluster size $S_{mean}$ oscillates in small groups between 4 and 5 particles with a relatively small standard deviation ($S_{stde} \approx 1$), indicating that the majority of the clusters are small and similar to the mean size. The minimal cluster size is the only constant value in time (which in principle could be variable as the others) with a fixed value ($S_{mini} = 4$), while the maximum size $S_{maxi}$ presents sharp peaks consistent with the very fluctuating tendency of the regime.

The next two sub-figures describe some properties in the suspension in their clustering permanent state ($t \in [t^{clus}_{perm}, T]$): for instance figure 4.9.c) shows the persistence time of the particles $P_p$, it clearly indicates that none particle always stays in some cluster, but neither does it always stay in the gas phase ($0.40 > (t - t^{clus}_{perm})/(T - t^{clus}_{perm}) > 0.03$), while most of the particles tends to stay only a small fraction of the permanent time in some cluster ($(t - t^{clus}_{perm})/(T - t^{clus}_{perm}) \approx 0.16$). Figure 4.9.d) presents the pair distribution function $g$, which says that the greatest probability of finding a second particle is at one diameter of distance (actually $r/a \approx 2.1$), indicating the presence of contact between particles, something expected given the presence of small clusters in the suspension, but at the same time the homogeneity for longer distances ($g = 1$).

### 4.3.4 Regime 2: Big cluster with persistent motion

In general, it is characterized by a fast transition from its initial conditions to well-defined and stable values for the rest of the simulation, representing very different behavior with respect to regime 1. Figure 4.10.a) shows the quick decay of the number of clusters $N_c$ just to one, while at the same time, the ratio of particles in clusters $R_p$ increases quickly up to 1. This means the total collapse of all the particles into a single cluster that persists for all the simulated time.

The cluster mean velocities $|\mathbf{U}_c|_{mean}$ and $|\mathbf{\Omega}_c|_{mean}$ are presented in figure 4.10.b) in which there are three time-intervals: the first one with high oscillations in both velocities that correspond to the transient state in which the formation of the clusters occurs. The second one corresponds to the time between the beginning of the permanent clustering state and the beginning of the motion permanent state in which there are still oscillations in the velocities but on a smaller scale. Finally, the third time interval corresponds to the full permanent state in which the single cluster has a well-defined structure and a fixed speed. In this final permanent state, the translational velocity is small ($|\mathbf{U}_c|_{mean}/U \leq .25$), and the angular velocity is very small ($|\mathbf{\Omega}_c|_{mean}\ a/U \leq 0.01$) respect to corresponding scales defined in section 4.3.1. The most interesting point here is the existence of constant values (in time) of both speeds. Figure 4.10.c), which presents the velocity direction autocorrelation functions, shows how after the full permanent state, the direction of motion reaches a fixed value, meaning that the single cluster swims with a fixed velocity in this permanent state in a persistent motion.

Figure 4.10.d) shows how almost all the particles stay in the cluster reaching the maximal persistence time $tU/a = 1$ during all the permanent state. Finally, figure 4.10.e) presents the pair distribution function $g$, which again establish the presence of contact between particles (first peak at $r/a \approx 2.1$), while the next 2 peaks in the distribution are very similar to the ones in a compact tetrahedral-based structure in 3D (section 4.3.8). Between these peaks are values close to 1, given that the cluster has some defects concerning this ideal structure (in which there are null values).

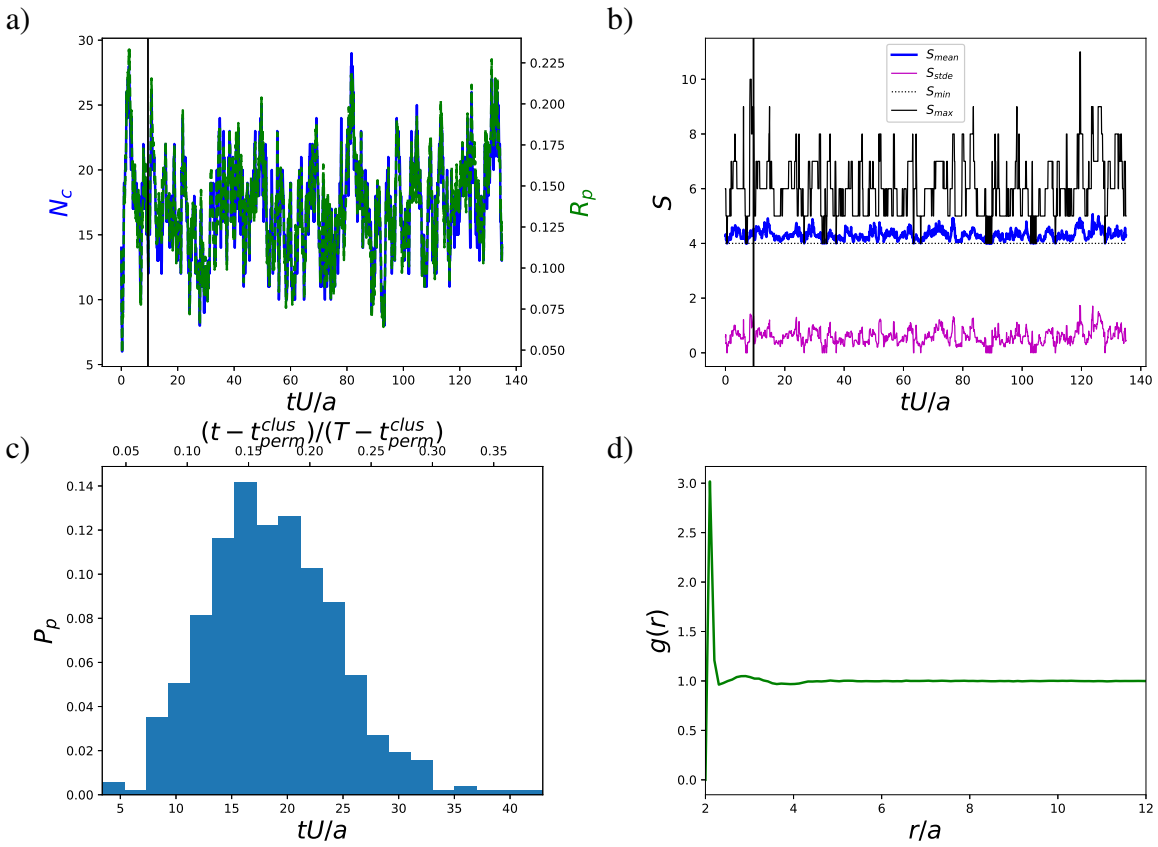


Figure 4.9: *Regime 1* - Gas-like regime showing the a) number of clusters $N_c$ and ratio of particles in clusters $R_p$, b) cluster size $S$ statistics, c) particle persistence $P_p$ distribution, d) pair distribution function $g$. The clustering permanent time $t^{clus}_{perm}$ is shown as the solid vertical line in images a) and b). In both figures the clustering permanent time $t^{clus}_{perm}$ is presented as the vertical line around $tU/a = 10$.

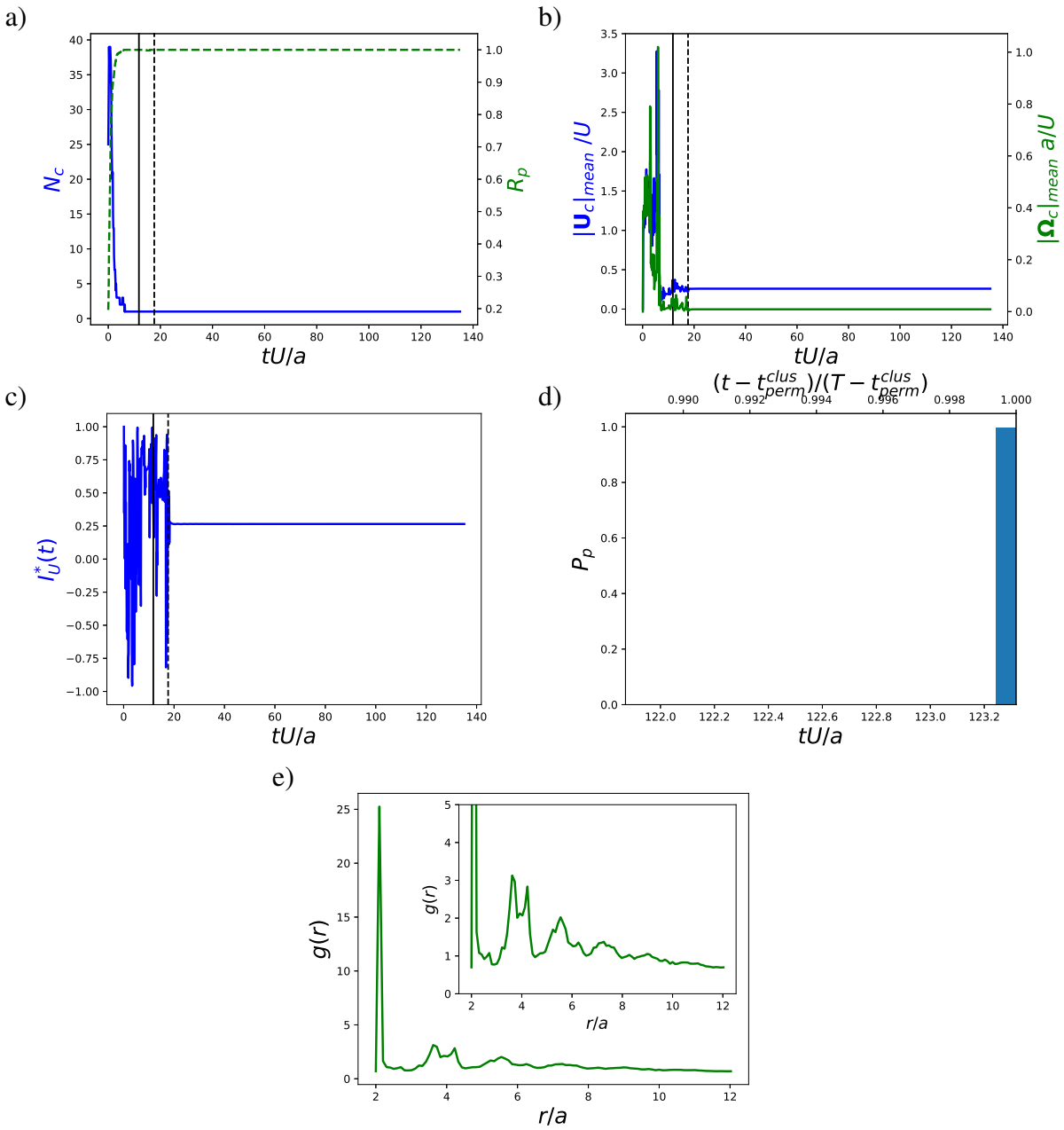


Figure 4.10: *Regime 2* - Big cluster with persistent motion regime showing the a) number of clusters $N_c$ and ratio of particles in clusters $R_p$, b) mean cluster velocities magnitude (translation and angular), c) the velocity direction autocorrelation function $I_U^*$, d) particle persistence $P_p$ distribution, and e ) pair distribution function $g$. The clustering permanent time $t_{perm}^{clus}$ and the motion permanent time $t_{perm}^{moti}$ are shown as the solid and dashed vertical lines in images a), b), and c).

### 4.3.5 Regime 3: Many small clusters with chaotic motion

As in regime 2, here, in general, the results show (mostly) stable clusters structures in the stationary state; however, in this case, we have many clusters, it took much more time to arrive up to this point, and the motion of the resultant clusters is quite different. Figure 4.11.a) shows how the number of clusters $N_c$ reaches the stationary values in two stages: a first quick stage in which its value is reduced to 33 approximately ($tU/a < 25$) and a second slow stage in which the final value of 25 is reached with small variations after this point ($t^{clus}_{perm} \approx 255$). On the other hand, $R_p$, reaches its final value in only one stage ($tU/a < 15$). Physically, this means the existence of two stages, the first one in which many small clusters are formed and a second stage in which they interact (exchanging particles) and modify their number and sizes. Figure 4.11.b) shows the statistics of the cluster size distribution, where the mean cluster size $S_{mean}$ grows in the two stages previously identified up to 15 particles (in the first) and 21 (in the second). It also presents small fluctuations during all the simulation; $S_{stde}$ is smaller than the mean in this case. On the other hand, $S_{maxi}$ reaches up to 33 particles (their final value) very quickly in only one stage.

Figure 4.11.c) shows the mean cluster's speeds, and we can see how they continuously fluctuate over all the considered time. In this case, only the clustering permanent state beginning is presented in the plots since only this one is well defined; before this time, the values oscillate with respect to a mean value that decays slowly in time, and after this time, the speeds seem to oscillate over a more constant mean value in time. However, the oscillations' amplitude is mainly stable during all the simulation. In addition, figure 4.11.d) shows how the mean velocity direction of the clusters (with respect to the initial time) is lost very quickly and oscillates randomly during all the simulation. All this together lets us conclude that, in this regime, the motion of the small clusters is entirely random and that both the translation and rotation are relevant in the motion, with average values of $|\mathbf{U}_c|_{mean}/U = 1.2$ for translation and $|\mathbf{\Omega}_c|_{mean}\, a/U = 0.45$ for the rotation considering the scales defined in section 4.3.1.

Almost all the particles stay in the clusters once formed, in a very persistent behavior (figure 4.11.e)). Figure 4.11.f) presents the pair distribution function $g$, which tells us some things about the cluster structure: the first peak shows the relatively high presence of contact between particles, while this and the following two peaks reveal as well the presence of the compact tetrahedral-based (pentagonal) structure in 3D (section 4.3.8). And maybe more interestingly, is the low values (approaching zero) of $g$ between these first peaks, while after $r/a \approx 6$, $g \to 1$. This indicates the presence of small clusters with a well-defined structure ($r/a < 6$) and a distribution mostly homogeneous after this distance.

### 4.3.6 Regime 4: Coexistence of many clusters with gas-like

Figure 4.12 summarizes the results of this regime. This regime generally presents mixed characteristics between regime 3 (many small clusters) and regime 1 (gas-like). Figure 4.12.a) shows a relatively fast decay of the number of clusters to a fluctuating value around $N_c = 25$. At the same time, the ratio of particles in clusters increases quickly up to fluctuating values around $R_p = 0.75$. It means that during all the simulation, there are always free particles (gas-like phase) at the same time that many clusters. Figure 4.12.b) shows the statistics of the cluster size distribution, where $S_{maxi}$ reach high values ($\approx 2N/5$) with high fluctuations. On the other hand, the minimal size keeps its value constant during all the simulation in the minimal possible $S_{mini} = 4$. So physically, we have a wide range of cluster sizes in the suspension. This makes that $S_{stde}$ becomes bigger than $S_{mean}$ which oscillates around a central values of $S_{mean} \approx 20$. This, added to the constant presence of free particles, makes this regime a different one from

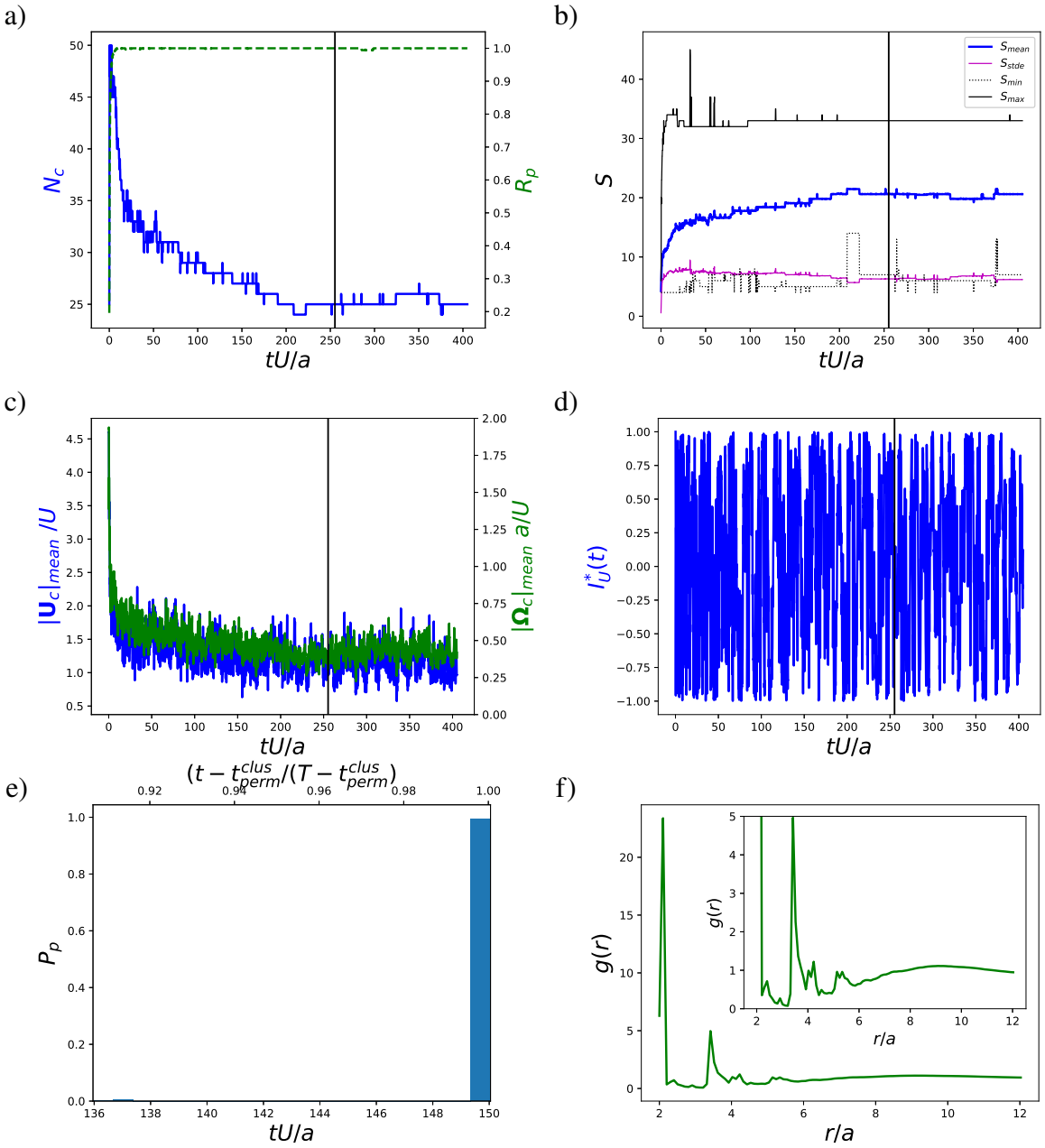


Figure 4.11: *Regime 3* - Many small clusters with chaotic motion regime showing the a) number of clusters $N_c$ and ratio of particles in clusters $R_p$, b) cluster size $S$ statistics, c) mean cluster velocities magnitude (translation and angular), f) the velocity direction autocorrelation function $I^*_U$, e) particle persistence $P_p$ distribution, and f) pair distribution function $g$. The clustering permanent time $t^{clus}_{perm}$ is shown as the solid vertical line in images a), b), c) and d).

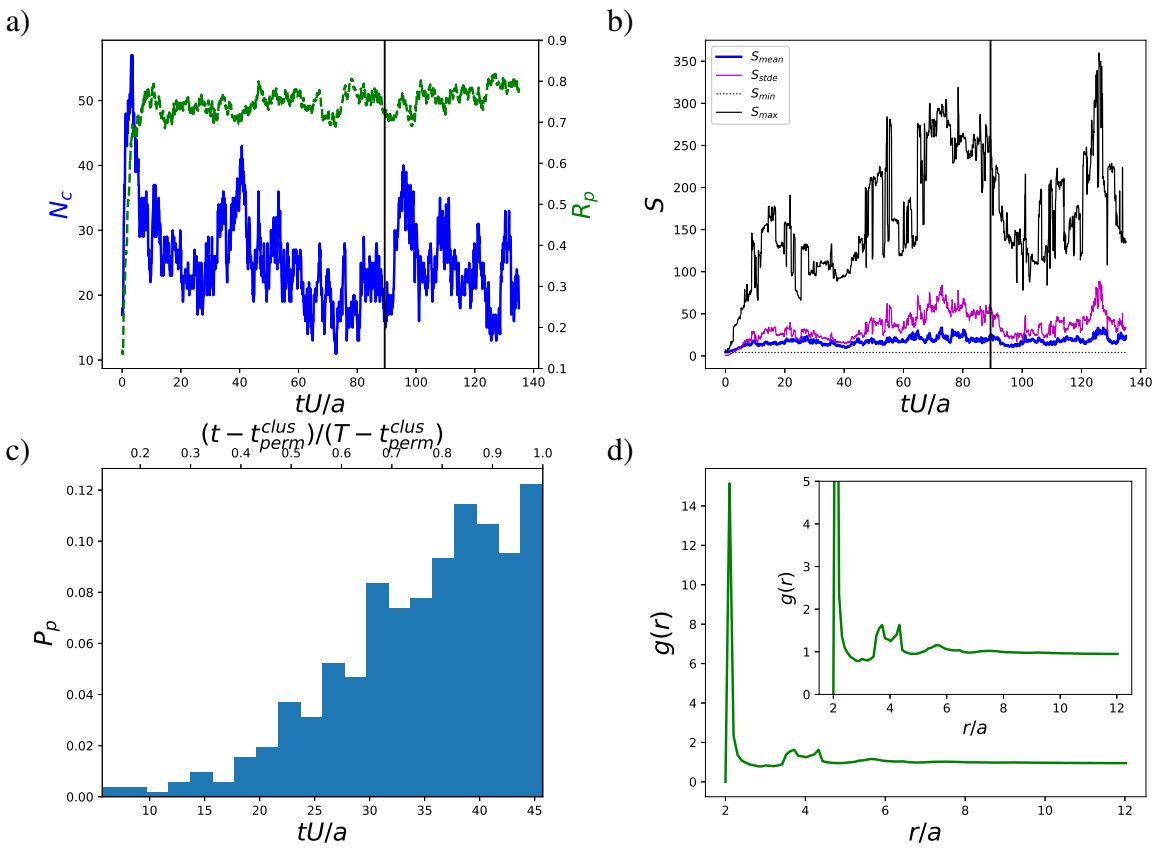


Figure 4.12: *Regime 4* - Coexistence of many clusters with gas-like regime showing the a) number of clusters $N_c$ and ratio of particles in clusters $R_p$, b) cluster size $S$ statistics, c) particle persistence $P_p$ distribution, d) pair distribution function $g$. The clustering permanent time $t^{clus}_{perm}$ is shown as the solid vertical line in images a) and b).

regime 1 but also from regime 3.

Given these high oscillations in $S_{mean}$ and $S_{maxi}$, it takes more time to reach the permanent clustering state ($t^{clus}_{perm} \approx 90$), time after the persistence time of the particles and the pair distribution function were calculated: figure 4.12.c) shows how the suspension presents a mixed behavior between the regimes 1 and 3: all the particles belong to some cluster at least for some short time like in regime 1 ($((t - t^{clus}_{perm})/(T - t^{clus}_{perm}) > 0.15$), but some particles stay on the clusters during all the time ($((t - t^{clus}_{perm})/(T - t^{clus}_{perm}) = 1$) something different from regime 1 (and more similar to regime 3). The majority of the particles (> 50%) stay in the cluster most of the time ($((t - t^{clus}_{perm})/(T - t^{clus}_{perm}) > 0.75$), indicating higher persistence of the particles on the large set of clusters, showing similarities with regime 3. Regarding the distribution of the particles, figure 4.12.d) presents $g$, which again establish the presence of contact between particles (first peak at $r/a \approx 2.1$). This distribution is similar to the one in regime 1. Still, it presents higher values in the first three peaks (of the compact tetrahedral-based structure in 3D), indicating a defined structure for these small clusters (but less defined) as in Regime 3.

### 4.3.7 Regime 5: Coexistence of big cluster with gas-like

Again a mixed regime including free particles is obtained as a result, from which some fluctuations can be observed in the time series. Figure 4.13.a) evidences how the number of clusters

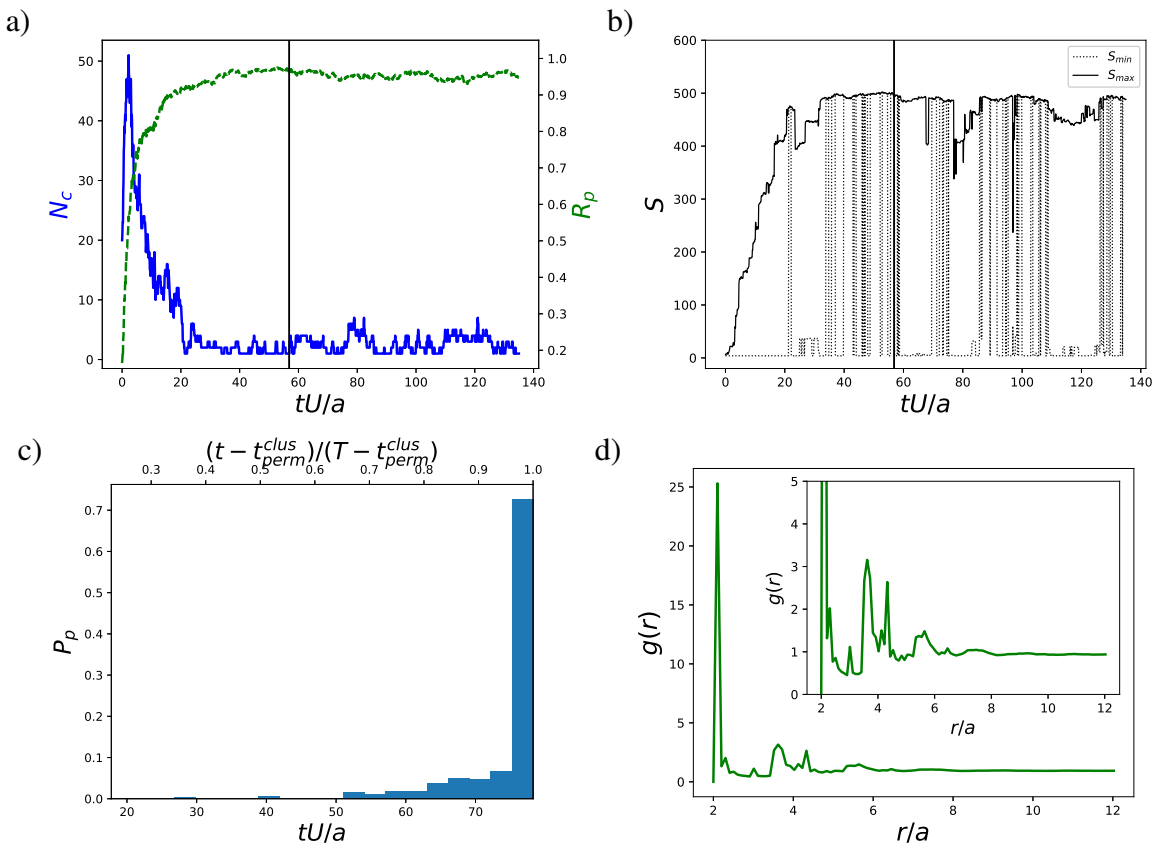


Figure 4.13: *Regime 5* - Coexistence of big cluster with gas-like regime showing the a) number of clusters $N_c$ and ratio of particles in clusters $R_p$, b) cluster size $S$ statistics, c) particle persistence $P_p$ distribution, d) pair distribution function $g$. The clustering permanent time $t^{clus}_{perm}$ is shown as the solid vertical line in images a) and b).

$N_c$ is reduced to a low value in the first stage ($tU/a \approx 20$) up to 1 cluster, but having some fluctuations up to 7 clusters. On the other hand, the ratio $R_p$ increases quickly in this same period up to 0.9 and then oscillates in the range $[0.90, 0.97]$. So, there is a continuous presence of free particles in the suspension coexisting with a very small set of clusters. Figure 4.13.b) shows the cluster size statistics, in which the first important thing to note is the presence of one "dominant" cluster with a fluctuating size around $S_{maxi} \approx 0.9N$. So physically, the system has one big cluster in coexistence with a gas-like phase that also interacts from time to time with some small clusters that detach from the big cluster (small periodic reductions on $S_{maxi}$). Equivalently $S_{mini}$ oscillates in the range $[4, S_{maxi}]$ which typically takes these two extreme values (also indicating the presence of small(s) cluster(s) or just the presence of the big one), and sometimes another low intermediate value.

Figure 4.13.c) presents a mixed $P_p$ distribution between regimes 2 and 4, on one hand the big majority ($\approx 0.7$) of the particles stays all the time in the cluster (high peak at $tU/a = 1$)) indicating a high persistence, while a minor population stay in it ($\approx 0.25$) most of the time (accumlated frequencies for $tU/a > 0.8$) and a tiny population ($\approx 0.05$) stays for a short time on it. Figure 4.13.d) shows similar peaks in the pair distribution function $g$ respect to regime 2 indicating a similar structure, but in this case it is more flat after $r/a > 6$.

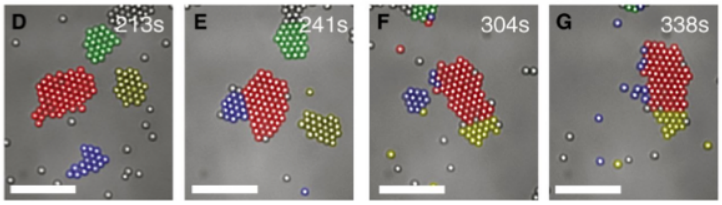


Figure 4.14: Typical clusters structure observed in 2D experiments. Adapted from [14].

### 4.3.8 Structure of clusters

In this section, we will try to understand the micro-structure in the regimes where clustering happens based on the pair distribution functions. Given the spherical shape of the considered Janus particles, the possible ways in which they could be arranged when they form clusters and the geometries of the clusters in many relevant publications [13, 14, 17, 18, 125], one may guess that the dominant structure present in our clusters will be the compact hexagonal. Similar to the ones shown in figure 4.14 constructed based on equilateral triangles of particles.

A natural 3D extension of this 2D structure is simply to successively assemble layers of hexagonally arranged particles, leading to greater structures. Following this concept, the smallest geometric model that constitutes the 3D extension of the base hexagon structure in 2D is presented in figure 4.15.a) and figure 4.15.b): the central hexagonal layer (particles in blue tones in the central $x-y$ plane) is the base from which other particles could join the cluster; in this structure, three above the plane and three below leading to a cluster of 13 particles that enclose the central particle (the darkest blue). Figure 4.15.c) is presented to show how the cluster could grow by adding new particles, showing the possible locations from which these new particles could reach a stable position. Two different kinds of locations were highlighted: red triangles and black squares in which there is space for only one particle.

The pair distribution function of this cluster configuration was calculated and presented in figure 4.15.d), where it is compared to its analogous function from the clusters in Regime 3 (small cluster with chaotic motion). As can be seen, the only coincidence between the two functions is the peak around $r/a \approx 2.15$, which makes sense, but it is trivial since we have particles in close contact in both cases. Neither the value at $r/a \approx 2.0$ nor the highest peaks of the considered structure match the Regime 3 function, so our initial guess about the cluster structure is essentially wrong. I chose Regime 3 since it has the cleanest peaks on $g$ and shares the same peaks with the other regimes.

In fact, in any of the pair distribution functions of the 5 regimes reported previously, there is a peak at $r/a \approx 3$, as in the case of this hexagonal structure. Analyzing the geometry, this peak originates in the four particles in the black squares highlighted in figure 4.15.c (related to the diagonal of this square $2.15 \times \sqrt{2} \approx 3.04$), so the structure of our clusters should not have this kind of configuration.

One alternative to the previous hexagonal three-dimensional structure is the pentagonal (or compact tetrahedral-based) structure proposed in figure 4.16.a). Considering the axial direction along the $z$ axis; there are two orthogonal planes of 5 particles each (blue and orange particles in figure 4.16.b)) with particles equidistant between them (except for axis particles). This 13-particle structure is constructed based only on adjacent tetrahedrons, eliminating the previous square structure issue as seen in figure 4.16.c), where it is explicit how the available locations

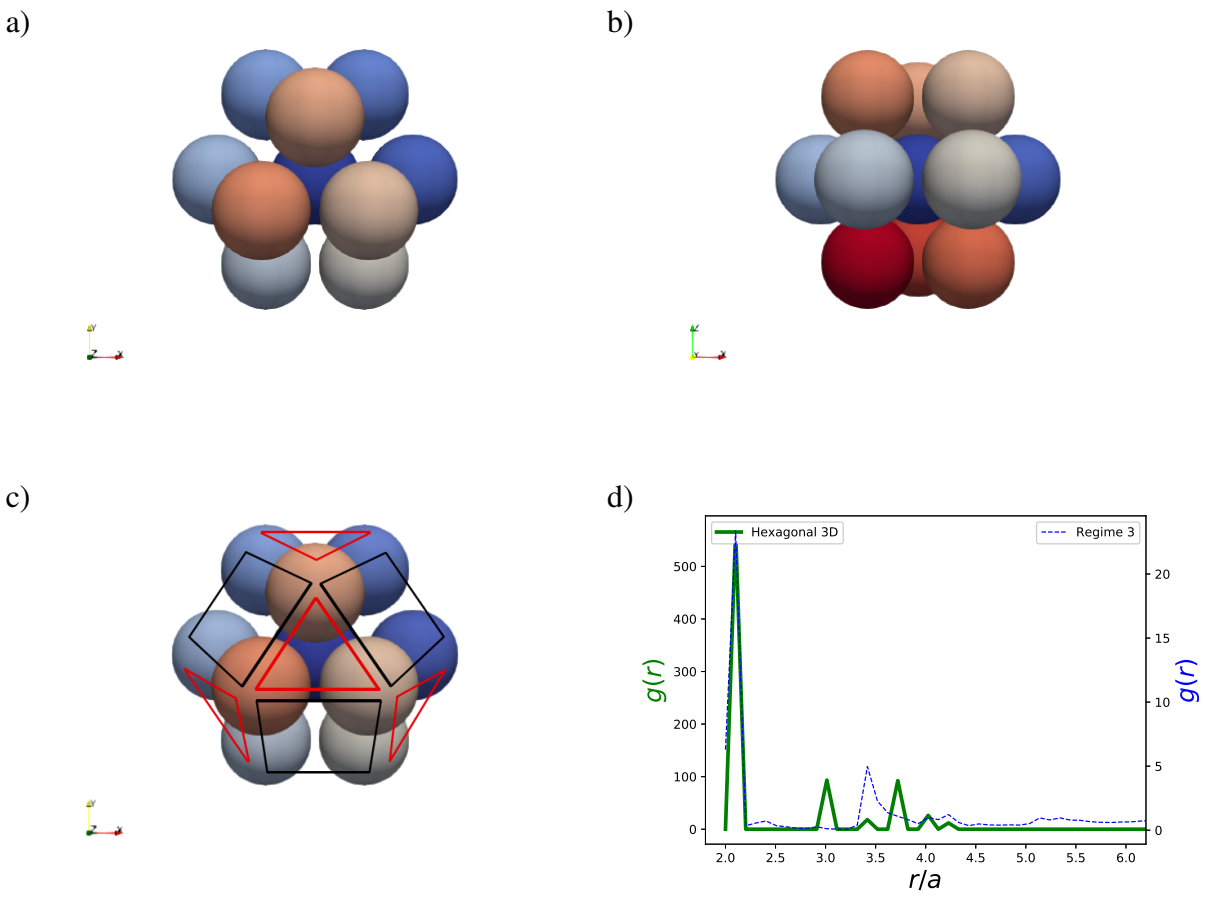


Figure 4.15: Hexagonal base structure including: a) 3D structure view 1, b) 3D structure view 2, c) available stable locations for new particles arriving to the cluster and d) pair distribution function $g$ compared to Regime 3. The color of the particles is used to identify better the geometry and orientation of the structure. The inter-particle distance is set $r/a = 2.16$, a representative value of what was observed in the cluster in our simulations.

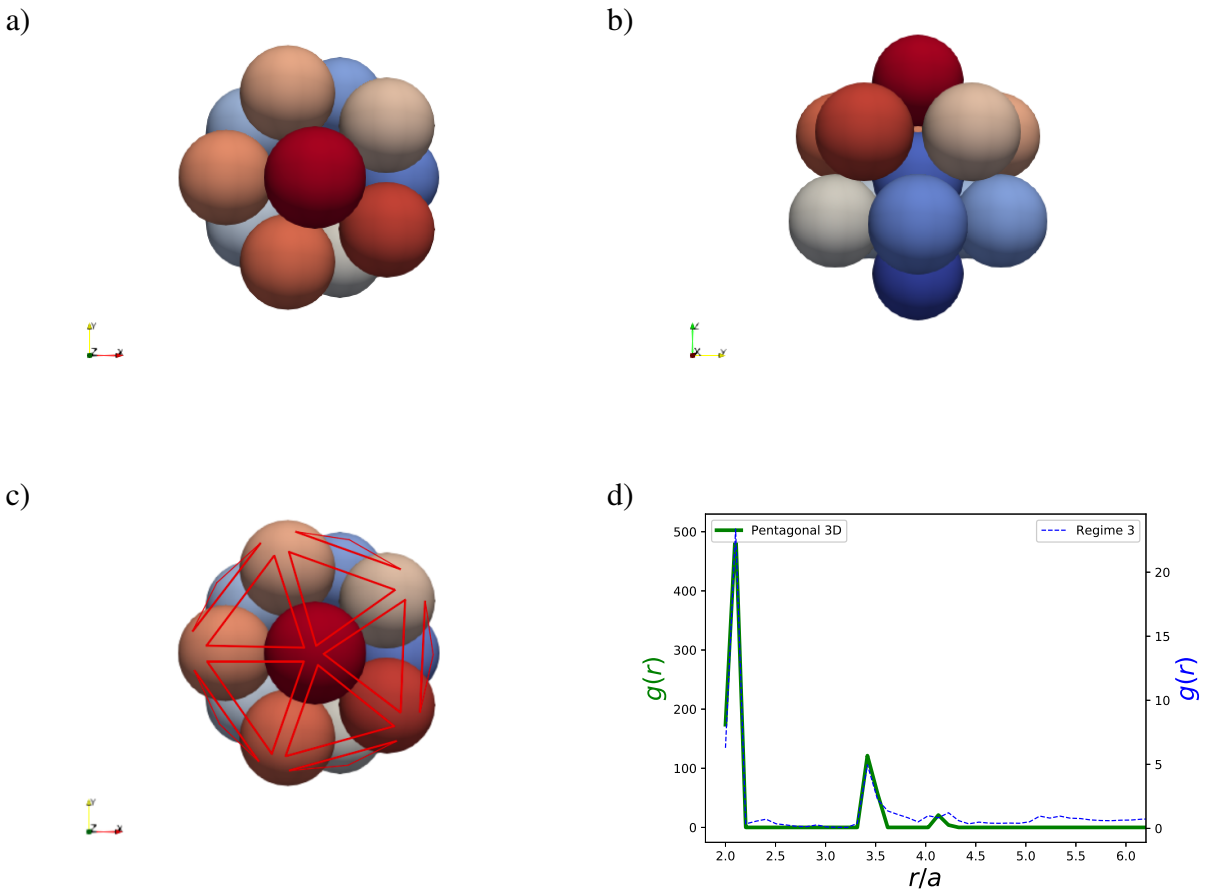


Figure 4.16: Pentagonal base structure (alternatively icosahedron or compact tetrahedral-based structure) including: a) 3D structure view 1, b) 3D structure view 2, c) available stable locations for new particles arriving to the cluster and d) pair distribution function $g$ compared to Regime 3. The color of the particles is used to identify better the geometry and orientation of the structure.

for new particles consist of triplets of particles indicated by the red triangles.

Finally, the pair distribution function for this pentagonal structure is presented in figure 4.16.d) and compared to the Regime 3 function, in which the match is extremely good at reproducing well the relevant peaks in the distribution, their relatives' sizes but also the voids in the range $r/a \in [2.2, 3.3]$. Of course, the match could not be exact because $g$ for Regime 3 is calculated over all the particles during the permanent time for many clusters, while $g$ for the pentagonal structure is for only 1 cluster.

Something interesting in this compact tetrahedral-based configuration is that since it is based only on tetrahedrons, once a new particles reach one of the stable locations (triangular base), it will form a new tetrahedron from which the basic pattern will be replicated continuously.

## 4.4 Phase diagram and regime transitions

Previously the five identified regimes were presented, describing their main characteristic quantitatively but without including any information on the type of particle in the suspension. After having simulated several reactive suspension models for the considered parameter space, the results indicating the regime for each type of particle are collected in figure 4.17.a) for the phoretic attractive cases and figure 4.17.b) for the phoretic repulsive cases.

### 4.4.1 Particles without chemotaxis

The simplest way to understand the results in these tables is to start with the cases with null mobility ratio $M^*/\overline{M} = 0$ (equivalently null mobility contrast $M^* = 0$, in the central column of each table) because the particles in this condition do not experience chemotaxis. In this case the chemical interactions reduce to the phoretic drift (pure attraction or repulsion) proportional to the first moment of concentration, the velocity equations (4.14 and 4.15) simplify to:

$$\boldsymbol{U}_n^a = -\frac{2\overline{M}}{a}\langle c\boldsymbol{n}\rangle_n, \qquad\qquad \boldsymbol{\Omega}_n^a = \mathbf{0}. \tag{4.20}$$

To facilitate the analysis, I will simplify the previous expression considering particles in pairs, where the polarity of the particle $n$, $\langle c\boldsymbol{n}\rangle_n$ which is immersed in an external chemical field produced by a second particle $j$, (and considering all the other particles) can be written like (only considering the leading order term):

$$\langle c\mathbf{n}\rangle_n = \langle c\mathbf{n}\rangle_n^i + \sum_j^{j\neq n}\langle c\mathbf{n}\rangle_{jn}^{ext} = \frac{a\alpha^*}{4}\mathbf{p}_n - \sum_j^{j\neq n}\frac{\overline{\alpha}a^3}{2r_{jn}^2}\mathbf{r}_{jn}, \tag{4.21}$$

where $\langle c\mathbf{n}\rangle_n^i$ holds for the *intrinsic* polarity (or self induced polarity) and $\langle c\mathbf{n}\rangle_{jn}^{ext}$ for the *external* polarity induced by the particle $j$ on the particle $n$. Additionally $\mathbf{p}_n$ is the orientation of the $n$ particle, $\mathbf{r}_{jn}$ is a unitary vector that points from $j$ particle to $n$ particle (figure 4.18). Considering this simplification on (4.20), we get:

$$\mathbf{U}_n^a = \mathbf{U}_n^i + \sum_j^{j\neq n}\mathbf{U}_{nj}^{d_1} = U_n^i\,\mathbf{p}_n + \sum_j^{j\neq n}\overline{M}\overline{\alpha}\Big(\frac{a^2}{r_{jn}^2}\Big)\mathbf{r}_{jn}, \tag{4.22}$$

where we verify that the intrinsic (self-induced) velocity of the particles $\mathbf{U}_n^i$ could be parallel or anti-parallel to their orientation $\mathbf{p}_n$ based on the sign of $U_n^i = -\overline{M}\alpha^*/2$ (consistent with Eq. 2.59), being $|U_n^i| = 1/2$ for all the considered cases. Given the fact that, we consider only net sources (or zero production $\overline{\alpha} \geq 0$), the direction of the *first contribution* of the drift velocity $\mathbf{U}_{nj}^{d_1}$ is function only of the mean mobility $\overline{M}$, inducing repulsive effects for positive values (parallel to $\mathbf{r}_{jn}$) and attractive for negative values (anti-parallel to $\mathbf{r}_{jn}$). The reorientation of the particles in this case will be generated only from hydrodynamical interactions, and in the case of particles in contact by the steric forces.

Starting in figure 4.17.b), we see that in the top cases ($\overline{\alpha}/\alpha^* = -5, -1, M^*/\overline{M} = 0$) the suspensions are in regime 1 (gas-like), something consistent with equation 4.22 for positive $\overline{M}$. Since the particles do not reorient significantly, their self velocity is fixed in direction, but the total active velocity (including the drift contribution) will prevent the collision of particles.

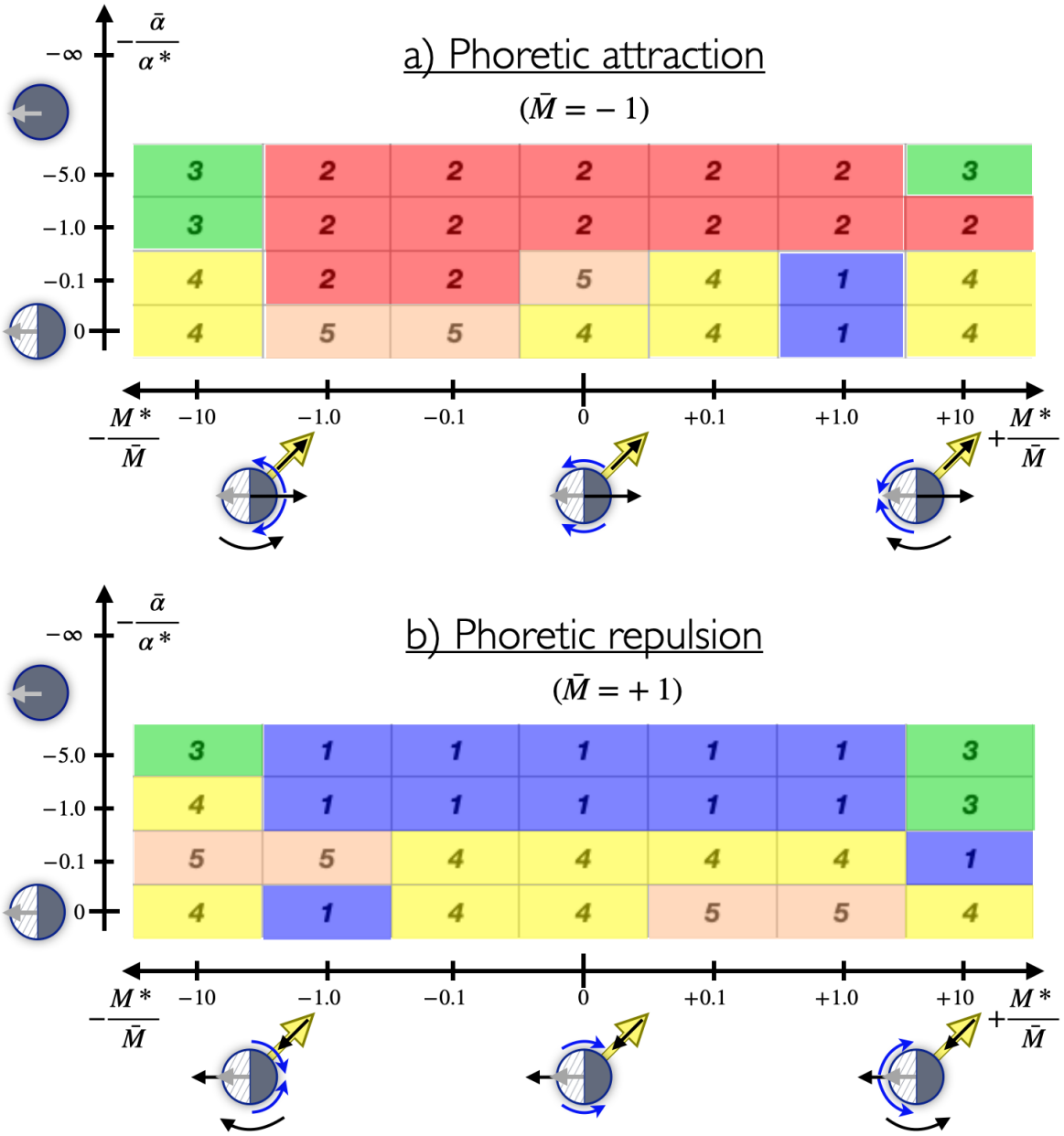


Figure 4.17: Phase diagrams for the considered parameter space (Table 2): a) particles with phoretic attraction ($\overline{M} = -1$) sweeping from chemotactic/puller to anti-chemotactic/pusher swimmers (from left to right), b) particles with phoretic repulsion ($\overline{M} = +1$) sweeping from chemotactic/pusher to anti-chemotactic/puller swimmers (from left to right). In both figures, in the central column there are neutral swimmers (hydrodynamically) without chemotaxis. The five regimes reported before in section 4.3 are reported in color code: *Regime 1* - Gas-like in blue, *Regime 2* - Big cluster with persistent motion in red, *Regime 3* - Many small clusters with chaotic motion in green, *Regime 4* - Coexistence of many clusters with gas-like in yellow and *Regime 5* - Coexistence of big cluster with gas-like in light-orange. The particle orientation is represented with the gray arrow, the external concentration gradient is represented by the big yellow arrow (and the superimposed black arrow is the phoretic translation drift, while the phoretic rotation drift is represented with the curly black arrow) and finally the intrinsic (or self-induced) velocity is the black arrow from the particle center.

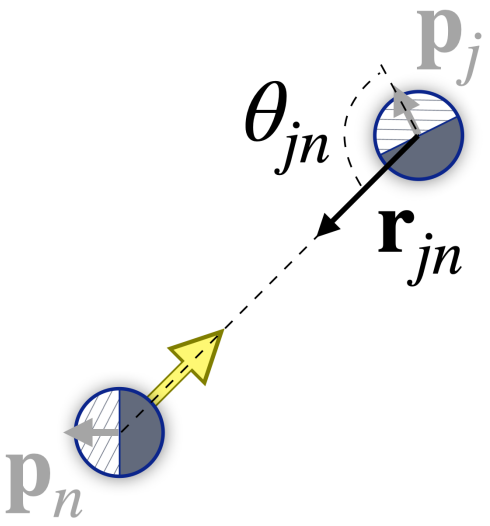


Figure 4.18: Interaction of pair of particles, indicating the orientations of particles $n$ and $j$ ($\mathbf{p}_n$ and $\mathbf{p}_j$ respectively), as well the relative position (unitary) of the particle $n$ respect to particle $j$: $\mathbf{r}_{jn}$, which determine the angle $\theta_{jn}$ with the orientaton of the particle $j$. The yellow arrow represents the external concentration gradient for the particle $n$ in this pairwise configuration.

However, if the volume fraction is high enough, some collisions will be inevitable, and the accumulated particles could be the initiation core of some short-lived clusters (section 4.5.1). In any case, the phoretic repulsive force is stronger when there are particles in contact, and this should destroy relatively fast these small clusters. Even more, when a small cluster is created, this increases the concentration locally, thus increasing the repulsive effect and preventing other particles from joining the cluster. All of this is consistent with the small mean cluster size and short persistence time observed in the results for this regime (figure 4.9.b) and 4.9.c)). These results are consistent with the *no clustering* state reported by [149] when the chemical repulsion is dominant, and the particle is monopolar dominantly ($\overline{\alpha}/\alpha^* \geq 1$).

On the other hand, the corresponding suspensions in figure 4.17.a) ($\overline{\alpha}/\alpha^* = -5, -1, M^*/\overline{M} = 0$) are in regime 2 (big cluster with persistent motion) and this in fact is consistent with equation 4.22 for negative $\overline{M}$. If in the previous case there were always small clusters $S_{mean} \approx 4.5$ (being the particles repulsive), in this attractive case, we could assume the existence of clusters of this size since the beginning. Assuming a small cluster of 4 particles in a regular tetrahedral configuration with an inter-particle distance of $d/a = 2.2$, the attractive drift velocity for any of the particles will be $|\sum_j \mathbf{U}_{nj}^{d_1}| \approx 0.5061$ towards the centroid of the other three particles. This velocity is in the same order of magnitude as $|\mathbf{U}_n^i| = 0.5$, which in principle could be in any direction, given that there is not a strong reorientation mechanism in this case. These velocity scales guarantee that these small clusters will persist for a long time. Since this clustering process increases the local concentration, external free particles will have enough time to join these initial clusters by the drift effect. All this produces positive feedback that will only allow the size of the clusters to increase until they finally collapse into one, consistent with the clustering results in figure 4.10. These results are consequent with the stable single clusters reported by [136] for attractive phoretic particles and with the *full aggregation* state reported by [149].

Still, in the central column of both tables, we could see that the suspensions in the bottom part of them show the same results, regime 4 (coexistence of many clusters with gas-like). In terms of our parameters, these cases have the values ($\overline{\alpha}/\alpha^* = 0, M^*/\overline{M} = 0$), indicating not only a null mobility contrast $M^*$, but now a null mean activity $\overline{\alpha} = 0$. Physically this implies that the particles now behave as pure dipoles with null net solute generation. Considering this in equation 4.22, all the interaction terms become null, which makes sense given the leading order considered on it (monopolar terms). For these cases, the leading order term in the polarity should be now the dipolar term:

$$\langle c\mathbf{n}\rangle_n = \langle c\mathbf{n}\rangle_n^i + \sum_j^{j\neq n}\langle c\mathbf{n}\rangle_{jn}^{ext} = \frac{a\alpha^*}{4}\mathbf{p}_n - \sum_j^{j\neq n}\frac{\alpha^* a^4(\mathbf{p}_j\cdot\mathbf{r}_{jn})}{2r_{jn}^3}\mathbf{r}_{jn}, \tag{4.23}$$

which in terms of the particles velocities becomes:

$$\mathbf{U}_n^a = \mathbf{U}_n^i + \sum_j^{j\neq n}\mathbf{U}_{nj}^{d_1} = U_n^i\,\mathbf{p}_n + \sum_j^{j\neq n}\overline{M}\alpha^*(\mathbf{p}_j\cdot\mathbf{r}_{jn})\Big(\frac{a^3}{r_{jn}^3}\Big)\mathbf{r}_{jn}, \tag{4.24}$$

where $\mathbf{p}_j$ is the orientation of particle $j$ and $\mathbf{p}_j\cdot\mathbf{r}_{jn} = \cos(\theta_{jn})$ measures the relative position of particle $n$ (respect to the orientation of particle $j$, check figure 4.18), that now becomes relevant since the dipoles have a well defined directionality.

Now the interaction direction depends not only on the mean mobility $\overline{M}$ but on the activity contrast $\alpha^*$ and the relative orientation of the particles since now they have one generation hemisphere and one consumption hemisphere of the same intensity ($\overline{\alpha} = 0$). In general, regardless of the sign of the product $\overline{M}\alpha^*$, we will have phoretic attraction or repulsion between particles depending on their relative orientations. One key point of these interactions is that in this case, the phoretic attraction is not isotropic (or dominantly isotropic) like in the case of regime 2 previously discussed. So the possible attractive configurations for a set of particles are more limited in number. The second key point is that the interaction length is shorter since the drift velocities scale like $(a/r)^3$ and not like $(a/r)^2$ like in the two previous cases. Because of these two key characteristics of the drift interactions for these 2 cases, we could expect in regime 4 that the clusters have smaller sizes (with respect to regime 2). But also, we could expect that after many particles have found a stable position in clusters, some particles would not be able to find stable positions in the clusters leading to the gas-like population in the regime.

Regime 4, where many clusters coexist with a gas-like phase very dynamically, is the regime that better resembles the well-known living clusters reported in experiments [13, 14]. In both cases (simulation and experiments), there is particle exchange between the cluster and the gas-like phase and clusters that evolve in time (both increasing or decreasing their sizes). These 2 cases are also congruent with the results reported by [144, 149], where the authors of the second reference called *arrested clusters* for repulsive suspensions when the particles are dipolar dominant. The only difference is that in our simulations, there is a relatively small population of free particles.

We have considered the top and bottom cases in the central columns of figure 4.17 (.a) and .b)), and now it is more natural to check what is happening in the middle. For these cases, we are interested in the activity ratio $\overline{\alpha}/\alpha^* = -0.1$, for which both monopolar and dipolar chemical contributions to the chemical field are relevant. We check some orders of magnitude considering both kind of terms, considering together equations 4.22 and 4.31 and normalizing the equation

with respect to the self induced velocity ($U_n^i = -\overline{M}\alpha^*/2$), we get:

$$\frac{\mathbf{U}_n^a}{U_n^i} = \mathbf{p}_n - 2\sum_j^{j\neq n} \frac{\overline{\alpha}}{\alpha^*}\Big(\frac{a}{r_{jn}}\Big)^2 \mathbf{r}_{jn} - 2\sum_j^{j\neq n} (\mathbf{p}_j \cdot \mathbf{r}_{jn})\Big(\frac{a}{r_{jn}}\Big)^3 \mathbf{r}_{jn}. \tag{4.25}$$

Given the used volume fraction, we could assume that from the start, we would have small temporal clusters as in regime 1, from which bigger clusters could grow. The relative importance of the dipolar terms with respect to the monopolar ones could be quantified through their coefficients ratio which is $\lambda = \frac{\mathbf{p}_j \cdot \mathbf{r}_{jn}}{\overline{\alpha}/\alpha^*}\big(\frac{a}{r_{jn}}\big)$ which for a typical inter-particle distance of $d/a = 2.2$ gives $\lambda = \frac{50}{11}\ (\mathbf{p}_j \cdot \mathbf{r}_{jn})$, meaning that both terms are significant and that depending the relative orientation between particles one term or the other rules, and given the number of particles in the model, we will have all the possible combinations. Then we could expect an intermediate regime between the two extremes in each case. For figure 4.17.a) (phoretic attraction), the suspensions are in regime 2 (big persistent cluster) in the central column and top rows and regime 4 (coexistence of many clusters with gas-like) in the central column and bottom row. Considering that in regime 4, $S_{maxi}$ fluctuates a lot, but it reaches high values ($S_{maxi} \in [100, 350]$), it is not surprising that the transition regime for this case is regime 5 (having one big cluster and gas-like). In the case of figure 4.17.b) (phoretic repulsion), the suspensions are in regime 1 (gas-like) in the central column and top rows and regime 4 (coexistence of many clusters with gas-like) in the central column and bottom row, making the resulting transition the regime 4, something reasonable as a transition between both.

### 4.4.2 Chemotactic and anti-chemotactic particles

Once we see what regimes emerge in the simplest case of the particles without chemotaxis, and once we have some clues why they emerge, the next step is to consider the chemotaxis in the particles and include their capability to re-orient under the presence of an external gradient of concentration. This is done by giving a nonzero mobility contrast $M^*$ to the particle and changing the suspensions' dynamics, as we can see in the results of the phase diagrams (figure 4.17). Considering here the equation for the phoretic rotation (Eq. 4.15) and including in it the simplified description for the polarity (Eq. 4.21), we got:

$$\mathbf{\Omega}_n^a = \mathbf{\Omega}_n^d = \sum_j^{j\neq n} \frac{9aM_n^*\bar{\alpha}}{8r_{jn}^2}\mathbf{p}_n \times \mathbf{r}_{jn}, \tag{4.26}$$

and again since we consider only net sources (or zero production, $\overline{\alpha} \geq 0$), the rotation tends to align $\mathbf{p}_n$ towards the external chemical gradient (opposite to $\mathbf{r}_{jn}$) if the mobility contrast is negative ($M^* < 0$) and against the external gradient if $M^* > 0$. If the particle's intrinsic velocity $\mathbf{U}_n^i$ is parallel to their orientation $\mathbf{p}_n$, it implies that in the first case the particle experiences chemotaxis (swims towards the external gradient, i.e. effective attraction) and anti-chemotaxis in the second case (swims against the external gradient, i.e. effective repulsion), this is precisely the case of figure 4.17.b) in our results. However, this condition could be inverted if the intrinsic velocity $\mathbf{U}_n^i$ is anti-parallel to their orientation $\mathbf{p}_n$, and this is the case of figure 4.17.a).

Considering phoretic attractive particles (figure 4.17.a)), we will have chemotaxis in the case of negative mobility ratios (left side of the table). This will reinforce the attractive tendency present in the central column of the table; for example, for $\overline{\alpha}/\alpha^* = -1$ in which the starting regime for the central column is 2 (big cluster), we kept this regime in the two columns to the left, which make sense given the double attractive effect between particles. The case of $\overline{\alpha}/\alpha^* = -0.1$

is much instructive since we see how the system changes from regime 5 to regime 2, reducing significantly the gas-phase present in the suspension, an indicative of the increasing attractive tendency.

On the right-hand side of figure 4.17.a), for positive mobility ratios, we will have anti-chemotaxis. This should weaken the attractive tendency observed in the central column of the table as we move to the right (higher $M^*$ values). This is especially evident in the case where $\overline{\alpha}/\alpha^* = -0.1$ where the initial regime is 5 (big cluster with gas-like), moving one column to the right, the suspension changes to regime 4 (many clusters with gas-like) and moving another column to the right it changes to regime 1 (gas-like) eliminating the tendency to form clusters in the suspension. Similarly, in figure 4.17.b), where $\overline{\alpha}/\alpha^* = -0.1$, this transition *regime 5* $\rightarrow$ *regime 4* $\rightarrow$ *regime 1* is also observed along the entire row.

Now we will consider three illustrative cases of suspensions with chemotaxis in the case of phoretic attraction (figure 4.17.a)), and since the particles experience attractive drift, it is not surprising that the dominant tendency in this diagram are fully clustered regimes (Regimes 2 and 3). In this sense, maybe the most interesting and unexpected result here is the presence of suspensions in gas-like regime, so we will consider this first.

Particularly, for the case with $\overline{\alpha}/\alpha^* = -0.1$ and $M^*/\overline{M} = +1.0$ (Regime 1), we see that the particles in suspension are mostly dipolar and that they experience negative chemotaxis. If we compare the relative importance of the drift velocity respect to the intrinsic (self-induced) velocity (from Eq. 4.22),

$$\frac{U^{d_1}}{|U^i|} = \frac{\overline{M}\overline{\alpha}(a/d')^2}{\overline{M}\alpha^*/2} = 2\Big(\frac{\overline{\alpha}}{\alpha^*}\Big)\Big(\frac{a}{d'}\Big)^2 \ll 1, \tag{4.27}$$

where $d'$ is the center-to-center inter-particle distance and $d'/a \geq 2$. We see that phoretic drift is small (or mostly negligible) respect to the intrinsic velocity, so that the phoretic attraction is small in this case, leaving the anti-chemotactic interactions (effective repulsion) as dominant in this case. We could illustrate schematically this situation with the three particles configuration (in a plane) shown in figure 4.19.a), where for the given particles' activity ratio the concentration field is shown in figure 4.19.b). Since the particles are mostly dipolar, their perturbation on the other particles decay fast with distance (as can be seen in the $c$ field) making the associated drift small (Eq. 4.27) and so the particles essentially swim independently and when their paths makes them collide (and once they become closer), they reorient away each other avoiding the collision and the clustering of particles (see figure 4.20 for the schematics and detailed explanation).

On the other hand, on the cases with chemotaxis is simpler to understand how the clusters are formed. For instance, consider the suspensions in Regime 2. Comparing again the relative importance of the drift velocity respect to the intrinsic velocity,

$$\frac{U^{d_1}}{|U^i|} = \frac{\overline{M}\overline{\alpha}(a/d')^2}{\overline{M}\alpha^*/2} = 2\Big(\frac{\overline{\alpha}}{\alpha^*}\Big)\Big(\frac{a}{d'}\Big)^2 \lesssim 1, \tag{4.28}$$

is clear how the two velocities have similar magnitudes (considering $\overline{\alpha}/\alpha^* \in [-5, -1]$ and the average length $d'/a \approx 3$ for the current volume fraction $\phi$ and length ratio $L/a$). Let's consider in particular the suspensions with phoretic properties $\overline{\alpha}/\alpha^* = -1.0$ and $M^*/\overline{M} = -1.0$, here the particles are mostly monopolar and they experience positive chemotaxis, and the relative intensity between both velocities can be understood as well by checking the chemical field produced in the schematic three particles configuration (figure 4.19.a)) shown in figure 4.19.c)

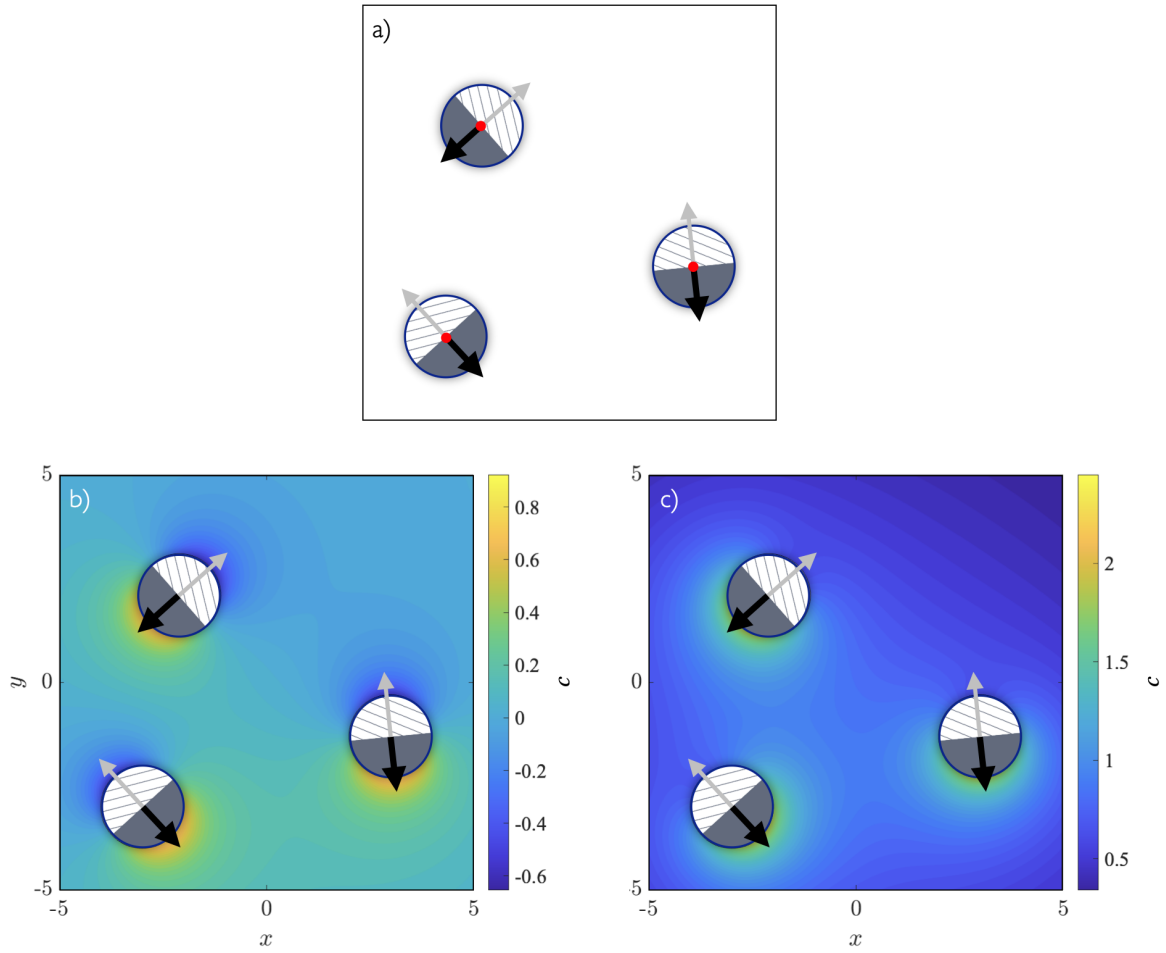


Figure 4.19: Configuration of three particles to consider first three regimes under phoretic attraction with some type of chemotaxis: a) positions and orientations, b) concentration field for $\overline{\alpha}/\alpha^* = -0.1$, c) concentration field for $\overline{\alpha}/\alpha^* = -1.0$. In both cases the highest concentration values are on the back (gray) hemisphere of the particles in first place and in the region between particles in the second place, this is specially evident in the second case (c) where the differences respect to the background field ($c = 0$) are higher. The gray arrows represent the particle orientations, while the black ones the intrinsic particle velocities.

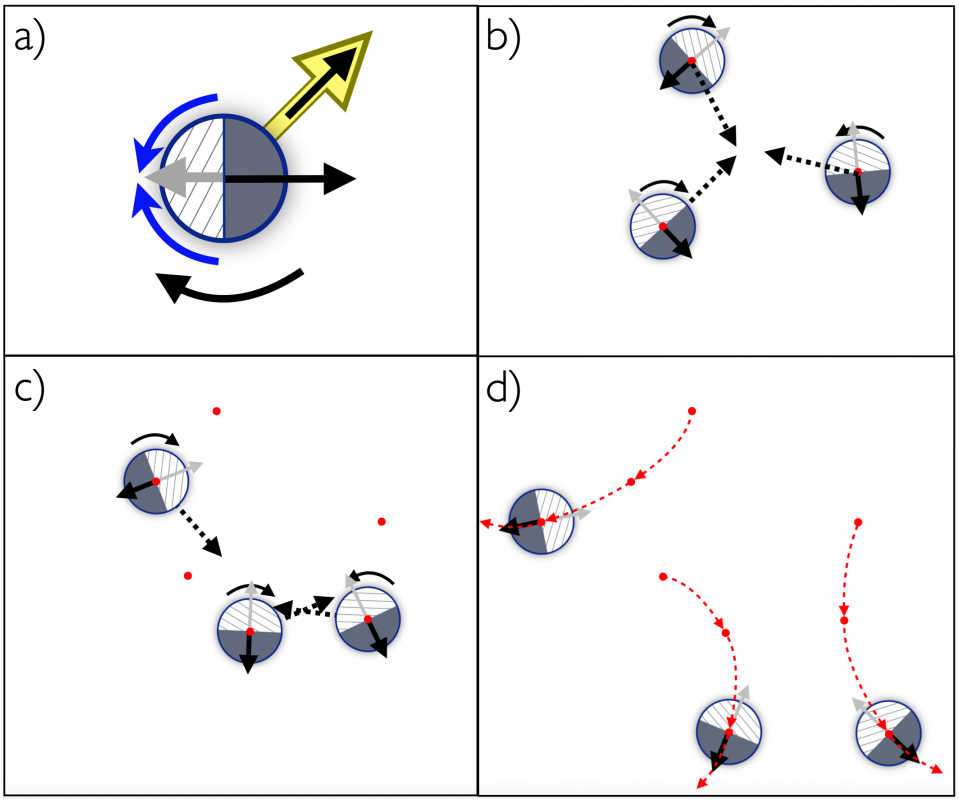


Figure 4.20: Schematic of phoretically attractive and anti-chemotactic suspension in Regime 1: a) Janus particle with its active consuming cap (white) and its active emitting cap (gray) acting as a pusher (if isolated), b) first stage: the particles swim mostly with their intrinsic velocity (having weak interactions), c) second stage: while the upper particle continues their path, the bottom particles have a convergent trajectories that forces them to interact strongly and making them rotate away each other, d) third stage: finally the particles avoid each other having divergent trajectories. The red points represents the particles centroid position, the red dashed lines each particle trajectory and as previously the black arrows the particles velocities and the gray arrow the particles orientation.

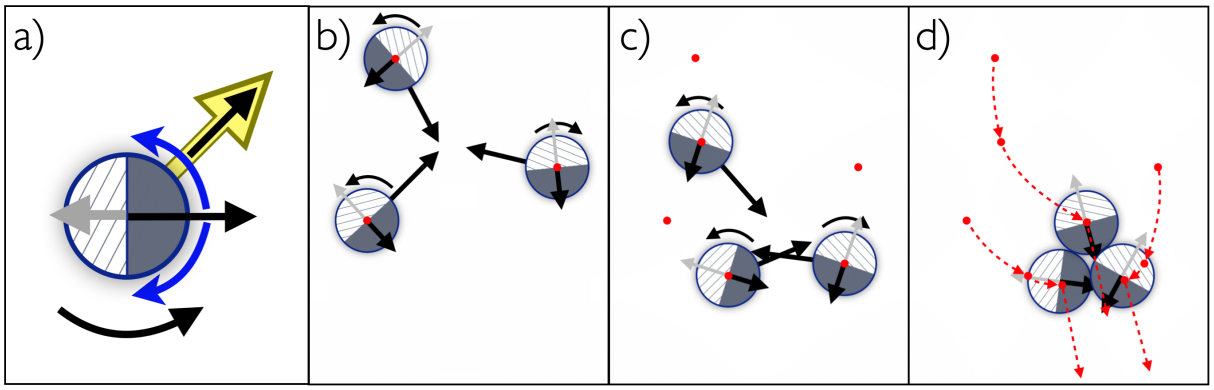


Figure 4.21: Schematic of phoretically attractive and chemotactic suspension in Regime 2: a) Janus particle with its passive cap (white) and its active emitting cap (gray) acting as a puller (if isolated), b) first stage: each particle experiences significant drift and rotation towards the central zone (higher concentration) inducing clustering, c) second stage: the particles become closer accelerating the clustering, d) third stage: full collapse into a cluster having directed motion (dependent on its initial conditions). The red points represents the particles centroid, the red dashed lines each particle trajectory and as previously the black arrows the particles velocities and the gray arrow the particles orientation.

in which the concentration field decays relatively slowly and so the phoretic drift produced by the other particles will be much significant than in the previous case in Regime 1. Considering the mobility parameters, we could understand how this three-particles system evolves in time (figure 4.21): starting from the initial configuration, each particles have a significant attractive drift towards the central area (highest concentration zone) at the same time that the particles rotates towards towards this zone and swims in direction of its intrinsic velocity. This makes the particles become closer increasing their attractive interactions accelerating the final collapse of the particles in the small cluster. Afterwards, external particles could join the cluster and depending on their initial configuration, the cluster can developed some directed translation motion, as in figure 4.21.d).

### 4.4.3 Suspensions in regime 3

The only regime non discussed yet in figure 4.17 is regime 3 (many small persistent clusters with chaotic motion); for this purpose, I will analyze in detail the particular case of attractive particles (figure 4.17.a)) with positive chemotaxis (effectively attractive). In this case, the Janus particle has the following phoretic properties $(\alpha_F, \alpha_B) = (0, 2)$ and $(M_F, M_B) = (9, -11)$, indicating that the front cap is inert, while the back cap is active (generation of solute). Considering this particle isolated, this induces a tangential chemical gradient towards the back cap (same direction for the particle polarity). Since the front cap has positive mobility, the slip velocity will be parallel to local polarity. Still, since the back cap has a (bigger) negative mobility, the slip velocity in the back cap will be opposite to the local polarity, inducing a net slip velocity towards the front cap. The net effect is that the particle velocity is opposite to the particle orientation (as seen at the entire figure 4.17.a), valid for all the particles on it). Finally we have a particle that is phoretically attractive with a strong chemotactic behavior ($M^*/\overline{M} = -10$), that swims (if isolated) like a puller (figure 4.22.a)).

Considering the schematic three particles configuration (figure 4.19.a)), the concentration

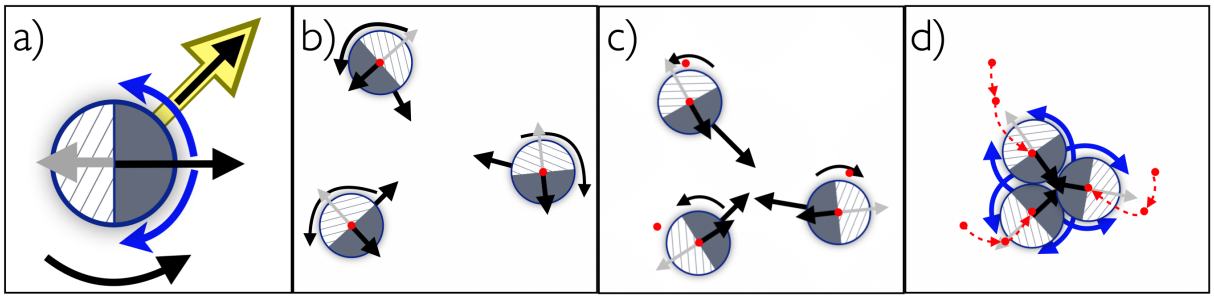


Figure 4.22: Schematic of suspension in Regime 3, in detail the phoretically attractive and strongly-chemotactic case: a) Janus particle with its inert cap (white) and its active emitting cap (gray), b) first stage: reorientation against local group centroid, c) second stage: swimming towards the closest group of particles, d) third stage: local clusters formation. The red points represents the particles centroid, the red dashed lines each particle trajectory and as previously the black arrows the particles velocities and the gray arrow the particles orientation. Particularly, here the slip velocity is displayed when the cluster is fully formed.

field in this case is identical to the previous one in Regime 2 (figure 4.19.c)) and the intrinsic and drift velocity are of the same order (Eq. 4.28 is still valid), and so, where does the differences between regime 2 and 3 arise? Remembering that initially, the particles are randomly distributed in the domain, and since all of them are effective sources, the formation of the small clusters in regime 3 could be explained as follow. Since the particles have a strong chemotactic nature, their rotation (drift) time will be much shorter than the translation (drift) time:

$$\frac{T_\Omega^d}{T_U^d} = \frac{1/\Omega^d}{a/U^{d_1}} = \frac{8d'^2/9aM^*\overline{\alpha}}{d'^2/a\overline{M}\overline{\alpha}} \approx \left(\frac{M^*}{\overline{M}}\right)^{-1} \ll 1, \tag{4.29}$$

Then, the particles will rotate quickly towards the closest particle or small group of particles (figure 4.22.b)). Then the particles will swim in this direction because of their intrinsic velocity and the drift velocity (figure 4.22.c)). Finally, the particle will collapse into a small local cluster (figure 4.22.d)), which is very stable since the centroid of the cluster have a high concentration of solute because the local production and the confinement inducing a) particles drift towards this zone, b) particles reorientation towards this zone of highest concentration (direction of intrinsic velocity). The cluster is also stable considering the hydrodynamics of these particles: (isolated), they act as pullers pumping fluid from their axis towards their equatorial plane, inducing a low-pressure zone at the cluster's centroid. If some particles are still free, they will eventually be attracted and captured by some cluster. Since the particles are randomly distributed, these small clusters are formed more or less uniformly in the domain. The process described here corresponds to the first stage in the clusters formation corresponding up to $tU/a = 20$ in figure 4.11.b). Once this stage has ended, the clusters start to interact between them. Since the formed clusters have an external surface formed with the front caps of the particles (inert), this external surface is also mostly inert. When two clusters collide, they do it through this inert surface, preventing them from merging. In the case that the clusters are not completely formed, leaving some active zone on their surface, the merging of clusters or the interchange of particles could happen: this is related to the long time needed to reach the permanent state in the simulation (figure 4.11.b)).

However the previous explanation doesn't apply completely for the other suspensions in Regime 3 (in which there is not a double attractive effect (phoretic attraction and positive

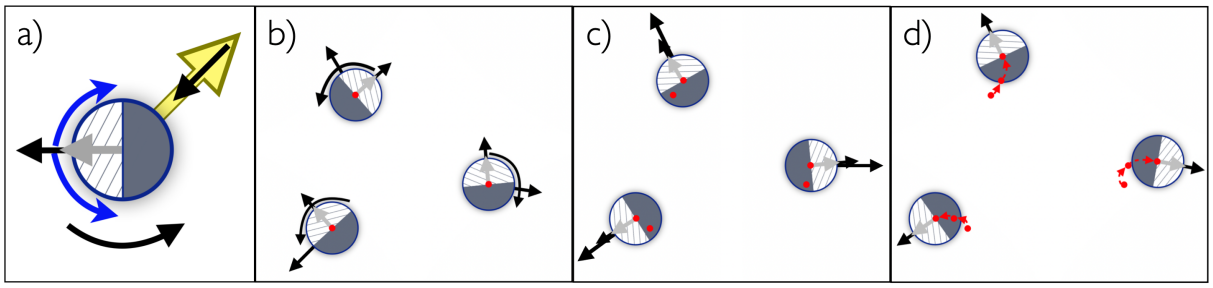


Figure 4.23: Schematic of suspension in Regime 3, in detail the phoretically repulsive and strongly-antichemotactic case: a) Janus particle with its inert cap (white) and its active emitting cap (gray), b) first stage: reorientation against local group centroid, c) second stage: swimming against the closest group of particles, d) third stage: particles avoid effectively each other having divergent trajectories. The red points represents the particles centroid, the red dashed lines each particle trajectory and as previously the black arrows the particles velocities and the gray arrow the particles orientation.

chemotaxis)), specially for the ones with phoretic repulsion (figure 4.17.b)). In this phase diagram, the most critic case is the one with phoretically repulsive particles experiencing negative chemotaxis ($\overline{\alpha}/\alpha^* = -1$ and $M^*\overline{M} = +10$). This double repulsive effect should produce in principle a gas-like state, as can be seen in the figure 4.23, where the particles (in principle) avoid effectively the other particles in suspension. Then, the question here is, how can we understand the emergence of Regime 3 for this extreme case? To do so, we need to re-consider the full expression for the *active* translation velocity (Eq. 3.46) where the presence of terms proportional to the mobility contrast $M^*$ need to be considered. To do so, I will simplify again the expressions considering particles in pairs, and the second moment of concentration $\langle c(\mathbf{nn} - \mathbf{I}/3)\rangle_n$ of the particle $n$ immersed in an external chemical field produced by (a set of) second particles $j$ can be written like:

$$\langle c(\mathbf{nn} - \mathbf{I}/3)\rangle_n = \langle c(\mathbf{nn} - \mathbf{I}/3)\rangle_n^i + \langle c(\mathbf{nn} - \mathbf{I}/3)\rangle_n^{ext} = \mathbf{0} + \sum_j^{j\neq n} \frac{2\overline{\alpha}a^4}{9r_{jn}^3}\mathbf{r}_{jn}\mathbf{r}_{jn}, \tag{4.30}$$

where the *intrinsic* second moment of concentration $\langle c(\mathbf{nn} - \mathbf{I}/3)\rangle_n^i$ is zero given the fact that the Janus particles are exactly hemispheric Janus particles (section 2.2.2). Considering this in the full expression for the *active* translation velocity and the simplifications performed before (Eq. 4.21 for the polarity and Eq. 4.22 for the velocity) we arrive to the following complete expression:

$$\mathbf{U}_n^a = \mathbf{U}_n^i + \sum_j^{j\neq n} \mathbf{U}_{nj}^{d_1} + \sum_j^{j\neq n} \mathbf{U}_{nj}^{d_2} = U_n^i\,\mathbf{p}_n + \sum_j^{j\neq n} \overline{M}\overline{\alpha}\left(\frac{a}{r_{jn}}\right)^2 \mathbf{r}_{jn} + \sum_j^{j\neq n} \left[-M^*\overline{\alpha}\left(\frac{a}{r_{jn}}\right)^3 \left(\frac{5\beta_{jn}}{6}\mathbf{r}_{jn} + \frac{5\beta_{jn}^2}{12}\mathbf{p}_n\right)\right], \tag{4.31}$$

where $\beta_{jn} = \mathbf{p}_n \cdot \mathbf{r}_{jn}$. Then, there is a new term labeled *second contribution* of the drift velocity $\mathbf{U}_{nj}^{d_2}$ proportional to the mobility contrast $M^*$ (which is high for all the cases previously reported in Regime 3 in figure 4.17 implying a strong chemotaxis (either positive or negative)), but also proportional to the second moment of concentration (which is short ranged $r^{-3}$). Their effect in the total drift can be clarified considering a known fact claimed before regarding the strong chemotaxis, in which the (drift) rotation time of the particles is going to be always smaller than the (drift) translation time (Eq 4.29), and so we could draft some general conclusions about the

| | | $M^*/\overline{M} < 0$ | $M^*/\overline{M} > 0$ |
|---|---|---|---|
| Phoretic attraction ($\overline{M} = -1$) | $M^*$ | $> 0$ | $< 0$ |
| | $\beta_{jn}$ | $> 0$ | $< 0$ |
| Phoretic repulsion ($\overline{M} = +1$) | $M^*$ | $< 0$ | $> 0$ |
| | $\beta_{jn}$ | $< 0$ | $> 0$ |

Table 3. Signs for the *second contribution* of the drift velocity $\mathbf{U}_{nj}^{d_2}$.

parameter $\beta_{jn}$ once we give some time to the particles to evolves from its initial condition as follow.

Consider first the attractive and chemotactic case (figure 4.22.a)), in which quickly the orientation $\mathbf{p}_n$ is going to become anti-parallel to the external concentration gradient produced by the particle $j$ (yellow arrow), but since this vector is anti-parallel to the $\mathbf{r}_{jn}$ vector (see figure 4.18 as reference), then $\beta_{jn} > 0$. Still in the phoretically attractive limit (figure 4.17.a)), if we invert the chemotactic tendency, we will have the opposite effect on $\beta_{jn}$. This is reported in the Table 3 in the top part. On the other hand, for repulsive and anti-chemotactic particles (figure 4.23.a)) the orientation $\mathbf{p}_n$ will become anti-parallel to the external concentration gradient produced by the particle $j$ (yellow arrow) and again, since this vector is anti-parallel to the $\mathbf{r}_{jn}$ vector, then $\beta_{jn} > 0$. Similarly, still in the repulsive case, by inverting chemotactic behavior, the resulting sign of $\beta_{jn}$ will change and this is summarized in the bottom part of the Table 3.

The new drift contribution $\mathbf{U}_{nj}^{d_2}$ have two components, one aligned to $\mathbf{r}_{jn}$ and the other to $\mathbf{p}_n$ (here, normalized respect to the intrinsic velocity $U_n^i = |\mathbf{U}_n^i| = |\overline{M}||\alpha^*|/2$):

$$\frac{\mathbf{U}_{nj}^{d_2}}{U_n^i} = -\Big(\frac{M^*}{|\overline{M}|}\Big)\Big(\frac{\overline{\alpha}}{|\alpha^*|}\Big)\Big(\frac{a}{r_{jn}}\Big)^3\Big(\frac{5\beta_{jn}}{3}\mathbf{r}_{jn} + \frac{5\beta_{jn}^2}{6}\mathbf{p}_n\Big), \tag{4.32}$$

and since in general $|\beta_{jn}| \leq 1$, then the first term (aligned to $\mathbf{r}_{jn}$) is going to be dominant and then $\mathbf{U}_{nj}^{d_2}$ is mainly attractive/repulsive along the line that connects the particles. Since we took $\overline{\alpha} \geq 0$, their direction is dictated by the product $M^*\beta_{jn}$, which as can be seen in Table 3 is always positive for the four considered cases in Regime 3, making $\mathbf{U}_{nj}^{d_2}$ parallel to $-\mathbf{r}_{jn}$ and so, this contribution is always attractive (for the strongly chemotactive cases (either positive or negative)). As can be seen in Eq. 4.32, this term is proportional to both the mobility ($M^*/\overline{M}$) and activity ratio ($\overline{\alpha}/\alpha^*$), allowing to understand the emergence of Regime 3 in both sides of the top part of figures 4.17.a) and 4.17.b), regions where precisely these parameters take their maximum values in the considered parameter space.

By comparing the relative intensity of the dominant part of the *second contribution* of the velocity drift respect to the *first contribution*:

$$\frac{U_{nj}^{d_2}}{U_{nj}^{d_1}} = \frac{5M^*\overline{\alpha}\beta_{jn}/6\ (a/d')^3}{\overline{M}\overline{\alpha}\ (a/d')^2} = \frac{5\beta_{jn}}{6}\Big(\frac{M^*}{\overline{M}}\Big)\Big(\frac{a}{d'}\Big) > 1, \tag{4.33}$$

considering $|\frac{M^*}{\overline{M}}| = 10$ and the average length $d'/a \approx 3$ for the current volume fraction $\phi$ and length ratio $L/a$ and so this new attractive drift is always greater than the traditional drift for the strongly chemotactic suspensions in regime 3 consider previously (figure 4.17). Similarly,

by comparing the dominant part of the *second contribution* of the velocity drift respect to the *intrinsic* velocity:

$$\frac{U_{nj}^{d_2}}{U_n^i} = \frac{5M^*\overline{\alpha}\beta_{jn}/6\ (a/d')^3}{\overline{M}\alpha^*/2} = \frac{5\beta_{jn}}{3}\left(\frac{M^*}{\overline{M}}\right)\left(\frac{\overline{\alpha}}{\alpha^*}\right)\left(\frac{a}{d'}\right)^3 \gtrsim 1, \tag{4.34}$$

considering additionally that $\overline{\alpha}/\alpha^* \in [-5, -1]$ and so again this new contribution can be easily similar or greater than the intrinsic velocity. This allows the understanding of how the Regime 3 emerges for the suspensions of repulsive and strongly anti-chemotactic particles described before in the figure 4.23, simply by including as well the *second contribution* of the velocity drift in the balance. Since this is the most critical case with a double repulsive effect (balanced with this second kind of drift), the emergence of Regime 3 in the intermediate cases in which there is one attractive and one repulsive effect (either phoretically attractive and anti-chemotactic, or phoretically repulsive and chemotactic) are now easier to understand.

In a final observation of Regime 3, we could observe some details regarding the shape of the small clusters. In the 2D schematic, the final geometry is an equilateral triangle (figure 4.22.d)). This structure ensures that each particle is oriented toward the highest concentration zone (chemotaxis is strong in this case). If we include a fourth particle in three dimensions, the corresponding structure will be a tetrahedron, and all the particles will be oriented against the cluster centroid. Indeed this always happens in each cluster, which can be observed in figure 4.8.c) (white arrow pointing out the clusters). The strong chemotaxis and the hydrodynamic flows tend to enforce this condition with high symmetry in the clusters. This could explain why the pentagonal base structure (icosahedron) fits better than the hexagonal base structure: it has much more symmetries revealed in the only red triangles' stable locations shown in figure 4.16, with respect to the mix of red triangles and black squares shown in figure 4.15.

## 4.5 Effect of volume fraction

The volume fraction $\phi$ is the third dimensionless parameter in our system. It quantifies the volume occupied by the particles in the system relative to the domain volume. Given the level of truncation in our approximation up to the dipole level both in the chemistry and in the hydrodynamics (Eq. 4.1 and Eq. 4.2) and the good precision of our results up to distances as small as half particle radius (section 3.4) our approach is suitable mainly for semi-dilute suspensions, and that is why previously we use an intermediate value of $\phi = 0.15$.

In general terms, the increase of the volume fraction reduces the average inter-particle distance in the suspension, but also it reduces the 'particles-free' solid angle in the swimming direction of each particle; all this, in principle, should increase the frequency of particles interactions. In this section, I wanted to consider how the volume fraction variation affects five of the reported cases (each one in a different regime) in figure 4.17 ($\phi = 0.15$) and to check how it affects their characteristics. To do this, I considered four possible values reported in Table 4, where for $\phi = 0.15$ are simply the previous reported results. Given the current domain size ($L/a = 24.26$), the corresponding number of particles $N$ will be varied consistently in each case (check Table 4).

| **Parameter** | **Values** |
|---|---|
| $\phi$ | 0.05, 0.10, 0.15, 0.20 |
| $N$ | 172, 344, 515, 687 |

Table 4. Values considered for the volume fraction variation study.

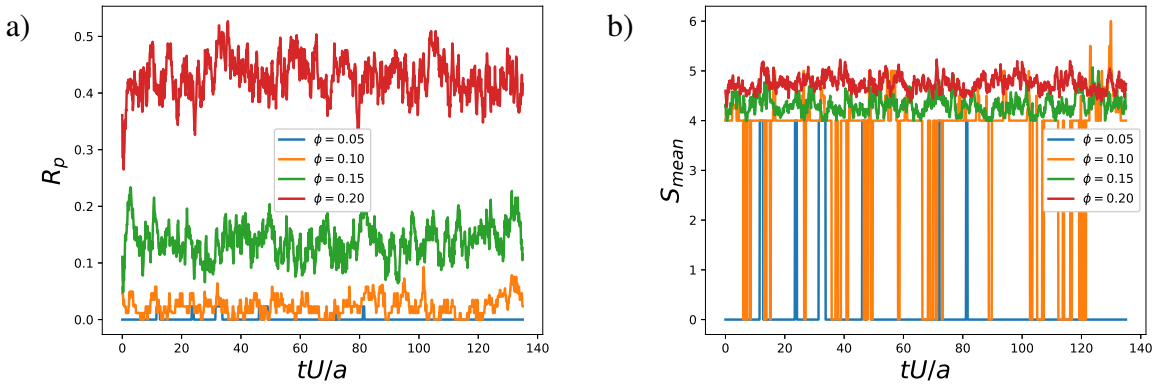


Figure 4.24: Results of variation of volume fraction $\phi$ in case 1: a) ratio of particles in clusters $R_P$ and b) cluster mean size $S_{mean}$.

### 4.5.1 Volume fraction effect on suspension in case 1

For this case, I considered a suspension of particles with properties reported in figure 4.17.b), for $M^*/\overline{M} = 0$ and $\overline{\alpha}/\alpha^* = -1$; this implies chemically repellent particles without chemotaxis and neutral swimmers (if isolated). This suspension is in regime 1 for $\phi = 0.15$; it is characterized by a majority of free particles and some clusters of relatively short persistence in time. As can be seen in figure 4.24, the volume fraction increase directly impacts the ratio of particles that forms clusters showing much higher $R_p$ values than the reference case $\phi = 0.15$. This makes sense since the number of interactions is expected to increase. One significant result is that for the lowest value considered ($\phi = 0.05$), $R_p$ drops to zero most of the time (except for some very short instants). It means that under a given threshold in $\phi$, the particles can adequately avoid the other particles preventing them from clustering. So the dominant interaction between particles is repulsive, and the clusters are formed mainly by the excluded volume effect in this regime.

It is also interesting to note that while $R_p$ increases significantly with $\phi$, the mean cluster size $S_{mean}$ is only minimally modified by its variation, indicating that physically the clusters keep almost the same size (in average) and that the number of clusters $N_c$ also changes significantly with $\phi$ since this three variables are related ($S_{mean}N_c = NR_p$). However, the suspensions formed with this type of particle stay in a gas-like phase (regime 1) regardless of $\phi$, something formally verified with our classification procedure reported in section 4.3.2.

### 4.5.2 Volume fraction effect on suspension in case 2

In this case, the selected suspension is in figure 4.17.a) with $M^*/\overline{M} = -1$ and $\overline{\alpha}/\alpha^* = -1$, which is in regime 2, having a single big cluster with persistent motion. If the particles are isolated, they are chemically attractive, chemotactic, and puller swimmers. It is clear looking in figure 4.25 that the $\phi$ variation doesn't modify this behavior: on the one hand, for all the $\phi$ values, all the particles in the system collapse in the cluster phase; but on the other hand, the number of clusters reduces quickly to 1. The main effect of the increase on $\phi$ is accelerating the system's evolution from its initial condition to the permanent regime, this happens in both $R_p$ and $N_c$ evolutions. Since the attractive interaction is dominant for this regime, the reduction of the inter-particle distance (increase in $\phi$) explains this acceleration. The selected suspension stays in regime 2 (big cluster with persistent motion) no matter the value of $\phi$.

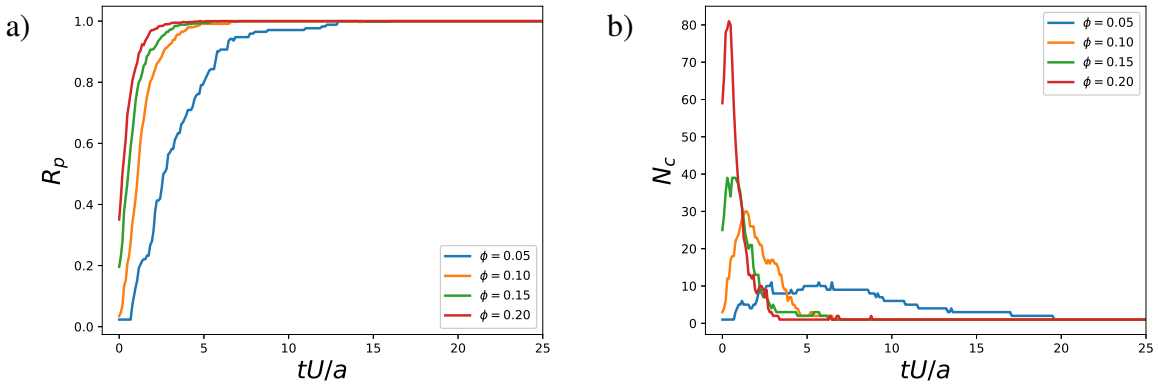


Figure 4.25: Results of variation of volume fraction $\phi$ in case 2: a) ratio of particles in clusters $R_P$ and b) number of clusters $N_c$.

### 4.5.3 Volume fraction effect on suspension in case 3

I selected a suspension with chemically attractive and chemotactic particles that are puller swimmers (if isolated), but this time with a high mobility ratio, in particular the case in figure 4.17.a) with $M^*/\overline{M} = -10$ and $\overline{\alpha}/\alpha^* = -1$. This suspension is in regime 3 for $\phi = 0.15$ (many small clusters with chaotic motion), and this tendency is qualitatively similar for all the volume fractions (see figure 4.26). All the particles become part of some cluster, and this happens for all the volume fractions; similarly, as with Regime 2, the effect of the increase in $\phi$ is the acceleration to reach $R_p = 1$. Because the attractive interaction is dominant in this regime, the reduction of the inter-particle distance is the cause of this acceleration.

On the other hand, the mean cluster size $S_{mean}$ is more sensitive in this case (relative to regime 1), increasing its value as $\phi$ increases. For all the values of $\phi$, there is a rapid increase in the cluster size at the very beginning (corresponding to the first clustering phase in which all the particles collapse into some cluster), followed by a slow increase of $S_{mean}$ corresponding to the time where chaotic motion occurs inducing collision between clusters and some modifications on their structure. Note that while $\phi$ increases, the $S_{mean}$ curve (in this second clustering phase) also becomes more fluctuating, something that indicates that the rate of cluster collision also increases, which make sense given the increase in the number of particles in the same space. Although none of the simulations reach their permanent state for the considered simulation time ($tU/a < 140$), the tendency on $S_{mean}$ is clear for each case, showing a slow convergence to its permanent state value, which increases with the volume fraction. However, the classification procedure can't be formally applied with the information in figure 4.26 since the time series doesn't reach a permanent state.

### 4.5.4 Volume fraction effect on suspension in case 4

The suspension of particles having the following properties ($M^*/\overline{M} = 0.1$ and $\overline{\alpha}/\alpha^* = -0.1$ in figure 4.17.a)) is selected in this case, where the particles are attractive chemically, anti-chemotactic, and puller type (if isolated). Remember that in regime 4, there are many clusters at the same time that free particles around them. In general, the increase in $\phi$, induces an increase in both $R_p$ and $S_{mean}$ as can be seen in figure 4.27. While for high values of $\phi$, $R_p$ presents a rapid increase at the beginning, reaching a plateau (with small fluctuations), $S_{mean}$ presents a bigger fluctuation as $\phi$ increase. It indicates a higher rate of interactions between the clusters

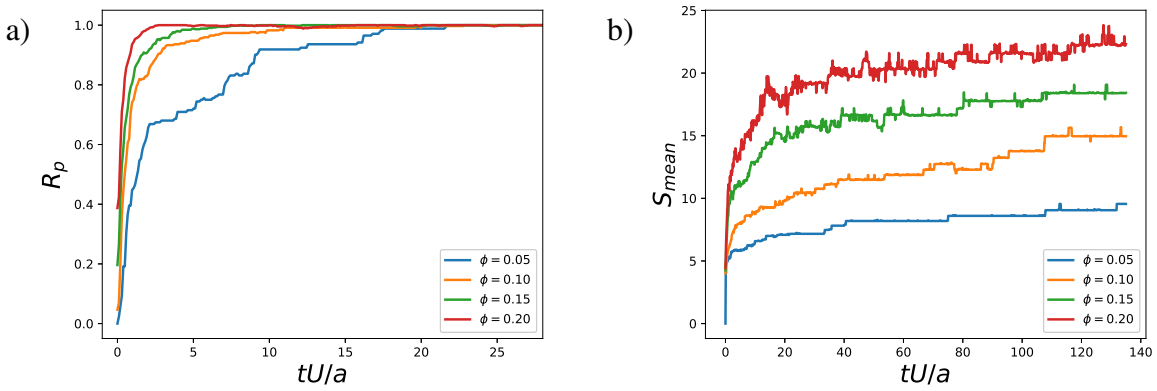


Figure 4.26: Results of variation of volume fraction $\phi$ in case 3: a) ratio of particles in clusters $R_P$ and b) cluster mean size $S_{mean}$. None of them reach the permanent state in the considered simulation time ($tU/a < 140$), but as can be seen in figure 4.11.b) for $\phi = 0.15$, they eventually reach a plateau in a very slowly manner.

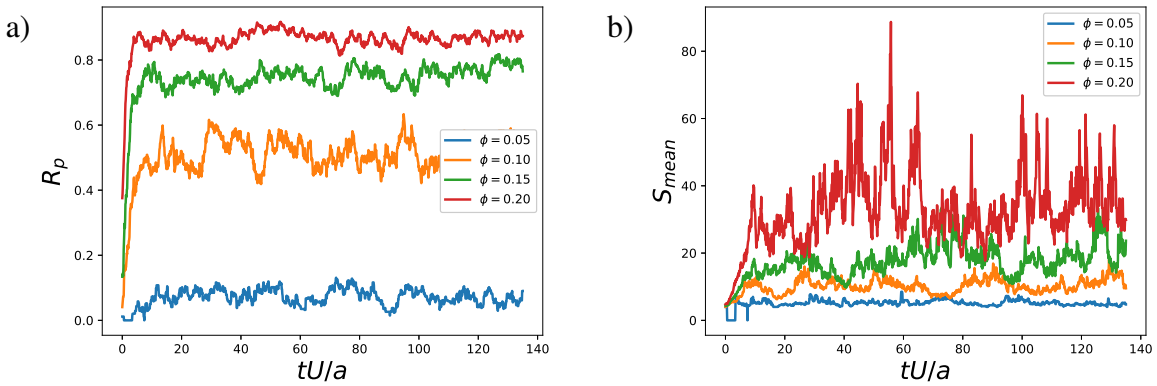


Figure 4.27: Results of variation of volume fraction $\phi$ in case 4: a) ratio of particles in clusters $R_P$ and b) cluster mean size $S_{mean}$.

and the gas-like phase. For high values of volume fraction, the suspension keeps in regime 4.

Something completely different happens for the smallest value ($\phi = 0.05$): it only oscillates at small values both in the ratio of particles in clusters $R_p \approx 0.10$ and in the mean cluster size $S_{mean} \approx 7$. Actually, in this case, it seems that the suspension has a change of regime switching to regime 1 (dominant gas-like with some small nonpersistent clusters), which was confirmed after applying the classification procedure (section 4.3.2). The particles, in this case, are phoretically attractive but have an anti-chemotactic behavior (effectively repulsive). It seems that for small enough $\phi$, the particles have enough time and space to effective avoid other particles, but with the increase in $\phi$, the average inter-particles distance is reduced until the point in which the rate of collision becomes much higher, and the results is the increase in the clustering (switching to regime 4).

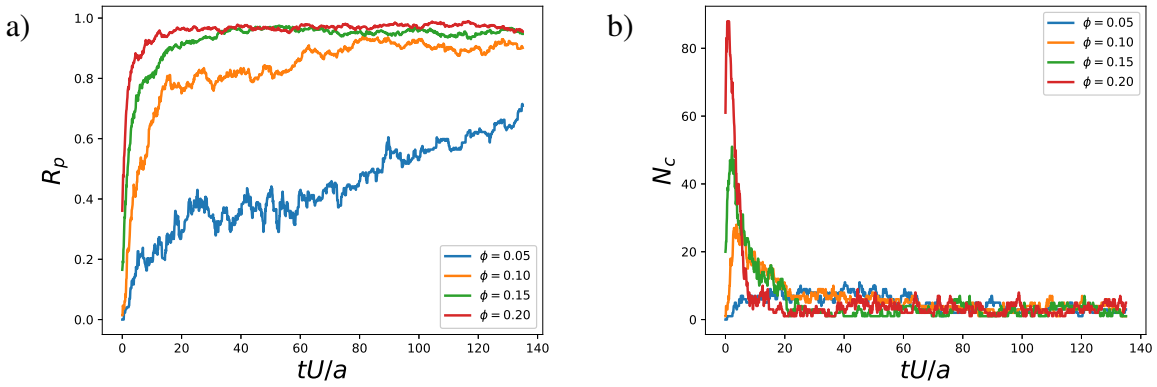


Figure 4.28: Results of variation of volume fraction $\phi$ in case 5: a) ratio of particles in clusters $R_P$ and b) number of clusters $N_c$.

### 4.5.5 Volume fraction effect on suspension in case 5

Finally, for the last case, the particles with properties $M^*/\overline{M} = -0.1$ and $\overline{\alpha}/\alpha^* = 0$ in figure 4.17.a) (chemoattractive, chemotactic and puller swimmer if isolated) are selected to consider the effects of the volume fraction, this suspensions is in regime 5 for $\phi = 0.15$. This regime is characterized by the presence of a dominant big cluster that interacts with a gas-like phase, and sometimes some small clusters detached from the big cluster. The results are presented in figure 4.28.

For high values of the volume fraction, the suspension behaves like in regime 5 with a quick collapse of the majority of particles in the cluster phase, and at the same time, the number of clusters falls quickly to values under 5, being one of them the big dominant cluster in the system. As in previous cases, as $\phi$ increases, there is an acceleration to reach the permanent state. In contrast, the system's dynamics are much slower for the lowest value of $\phi$. It shows only a transient behavior in the considered simulation time, making the recognition of the resulting regime impossible. Since, in this case, the particles are dipolar ($\overline{\alpha} = 0$), their chemical interactions are short-ranged ($(a/r)^{-3}$), and since the suspension is very dilute (for $\phi = 0.05$) is expected that the time evolution is slower. It will take a long time for the particles swimming freely past near the main cluster to become attracted and integrated into it.

## 4.6 Initial conditions sensibility analysis

In this last section, we will check how sensible are the previous results to different initial conditions of the simulation. Remember that until now we have lunched all the simulations starting from random distribution both on the particles' positions and orientations. This is done because in normal conditions we won't have any preferential order in a suspension of particles, but also since under experimental conditions their strict control is hard to achieve and because we are interested in the underlying long term behaviour of the system (if any), independent of the initial conditions.

To check this behaviour, we will check how 4 different realizations of a suspension with the same physical conditions (surface particle's properties ($\alpha$ and $M$) , volume fractions $\phi$ and length ratio $L/a$) evolves starting from different initial conditions ($\mathbf{Y}_n$ and $\mathbf{p}_n$). In particular we have considered 3 different random initial distributions and a very ordered configuration, as

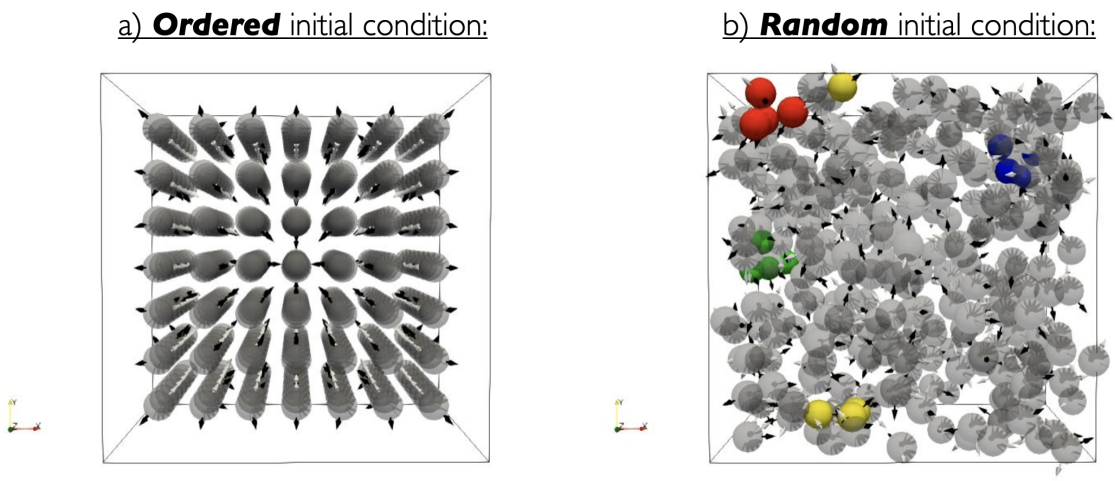


Figure 4.29: Geometric initial conditions to perform the sensibility analysis: a) ordered configuration fully described in Appendix C and b) sample of fully random distribution.

shown in figure 4.29, considering the same cases as in section 4.5 and the results for the volume fraction $\phi = 0.10$. Two critical cases are going to be discussed here in detail, while the other results have been summarized in Appendix D.

Since the ordered distribution is configured so that all the particles tend to swim to the centroid of the box, it enhances a collapse of the particles into a single cluster. This raises the question, for a suspension in principle in Regime 1 (Gas-like), is the repulsive tendency (either by phoretic repulsion, either by anti-chemotaxis or both) strong enough to avoid the collapse into one big cluster? The results are clear and the answer is yes: as can be seen in figure 4.30 the ratio of particles in clusters $R_p$ (as well for the mean cluster size $S_{mean}$) for the ordered configuration reaches a maximum value during a initial phase, after which it is reduced and then it starts to oscillate between the same values for the other three random configurations realizations, meaning that effectively the initial condition enhances the clustering, but it is significant only for an initial transitory time. After applying the classification procedure is confirmed that all the realizations converged to the Gas-like regime.

Consistently, it is expected that this ordered initial configuration should accelerate the convergence to the fully clustering in the cases of clustered states (like regime 2 and 3). The results of the analysis for the case in Regime 2 (Big cluster with persistent motion) precisely confirm this (figure 4.31), however, the sensibility to this initial ordered condition is very weak, and in all the realizations the suspension quickly reaches a single big cluster ($N_C = 1$) with the totality of the particles on it ($R_p = 1$). Again, after applying the classification procedure is confirmed that all the realizations converged to the regime 2.

Similar results were obtained for the other three regimes (3, 4 and 5), as can be checked in Appendix D, clearly indicating that the properties of the suspension system in the permanent regime are only determined by the main four parameters described in section 4.2 (mainly the surface phoretic properties: activity and mobility). They are independent of the initial conditions and not very sensitive to them at the beginning of the simulations.

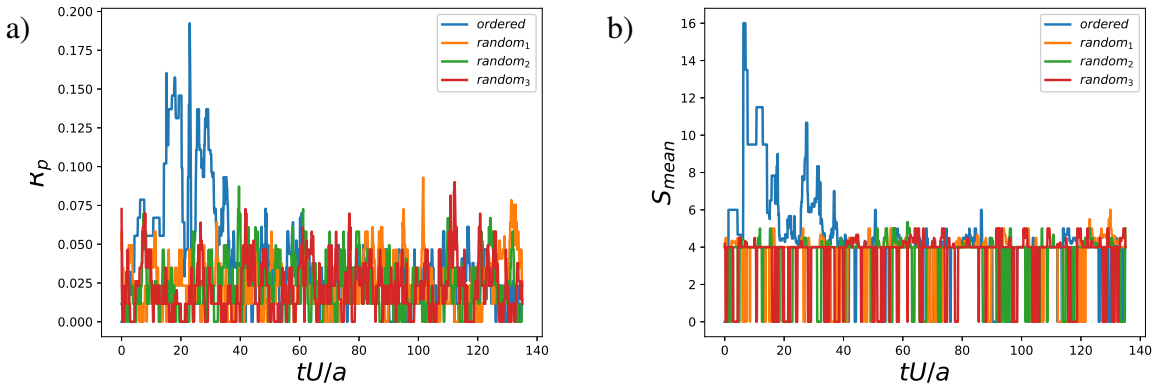


Figure 4.30: Sensibility analysis to different initial conditions for a suspension in regime 1 ($\phi = 0.10$): a) ratio of particles in clusters $R_P$ and b) cluster mean size $S_{mean}$. All the suspension's realizations reach Regime 1, and all these results can be directly compared with the one in figure 4.24.

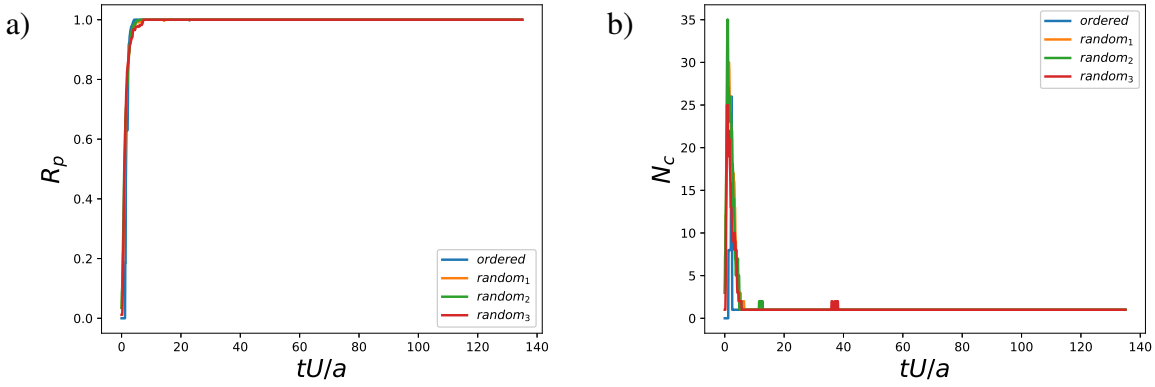


Figure 4.31: Sensibility analysis to different initial conditions for a suspension in regime 2 ($\phi = 0.10$): a) ratio of particles in clusters $R_P$ and b) number of clusters $N_c$. These results can be directly compared with ones in figure 4.25, all the suspension's realizations reach Regime 2.

## 4.7 Discussion

In this chapter, I have used the numerical framework that I developed previously (Chapter 3), and I implemented it in an existing parallel code that solves the hydrodynamics of active particles [106]. This implementation has included the resolution of the chemical problem up to the dipole term (in a regularized multipole expansion), its coupling with the hydrodynamics, and the validation of the new code recovering the previously known solutions (section 3.4).

Once the code was fully validated, I used it in the physical study of suspensions of identical Janus particles considering three dimensionless parameters that characterized the system. Two of the parameters are related to the properties of the particles; in the first place, the activity ratio $\overline{\alpha}/\alpha^*$ which brings the relative importance between the monopolar (symmetric) and the dipolar (front-back asymmetric) generation of chemical solute in the particle surface. In the second place, the mobility ratio $M^*/\overline{M}$ contains information about the particles' attractive (or repulsive) phoretic nature and details of their chemotactic behavior. Finally, the third parameter, called volume fraction $\phi$, relates the particles and the domain through their volumetric ratio.

Considering the first two parameters, a large set of cases were studied, emerging many types of coherent structures, including persistent large clusters, persistent self-limiting size clusters, and small clusters with a short-lived existence as reported in experiments [12, 13, 14] or numerical studies [136, 144, 148, 149]. Additionally, large sets of free particles were observed alone or in combination with the different clusters' types. Similarly, other collective motions were observed, including ballistic and chaotic motion in the case of the fully clustered regimes. To introduce some order in this large set of possibilities, a classification based on the statistics of the resulting structures and motions is proposed. I finally defined five regimes in this classification, including structural and motile characteristics.

Regime 1, called gas-like, is characterized by a significant population of particles that swims freely, except by the formation of short-lived clusters caused mainly by local blocking of particles given the excluded volume effect. This regime's time signals present many small fluctuations given the active local dynamics. The particles are statistically equally distributed in space, given some long-ranged repulsive interaction (either phoretic repulsion or negative chemotaxis) consistent with results reported by [149].

Regime 2 and 3 presents some similarities since the cluster phase is highly persistent in both cases: once the particles switch to this phase, they keep on indefinitely. But also, once the clusters' micro-structure is defined, the particles tend to keep in this configuration leading essentially to rigid body clusters. In regime 2, the final result is a single big cluster (consistent with results reported by [136, 149]) that performs ballistic motion with a constant translation velocity and a minimal (if any) rotation velocity, this is the results of a dominant long-ranged phoretic attraction drift between particles. In regime 3, the particles assemble in many small clusters of self-limiting size with chaotic motion combining translation and rotation that fluctuates continuously in time. Although the phoretic drift (proportional to the first moment of concentration) and the self-propulsion have an influence on the formation of the clusters in this regime, the combination of the strong chemotaxis (which induces a very fast particle reorientation, first) and the second phoretic drift (proportional to the second moment of concentration, which always induces short-ranged attractive interactions, second) the dominant effect that triggers the emergence of these self-limiting size clusters in the general case. The microstructure pattern for this regime has been identified, particularly a 3D pentagonal arrangement (icosahedron). Although the existence of clusters of self-limiting size for chemotactic particles (chemorepulsive active colloids in the continuum limit) have been reported before [130]. This case has similarities with one particular of the reported here in Regime 3, our understanding of this regime is more

general, including suspensions of both phoretically attractive and repulsive particles with both positive and negative chemotaxis, all of them as manifestations of the same phenomena, and because this I recognize this Regime 3 as a new regime for reactive suspensions.

The last two regimes also have some similarities; in regimes 4 and 5, there is a cluster phase that coexists with a gas-like phase. In the case of regime 4, many clusters coexist with free particles during all the simulation, presenting lots of fluctuations in all the time series. Indeed, this is the case that shows more similarities with the well-known living clusters system [13, 14], since the clusters grow, break, merge and separate continuously. Results in regime 4 are also consistent with numerical studies [144, 149]. Finally, regime 5 is characterized by a dominant big cluster that coexists with free particles and intermittent small clusters. This regime shares some similarities with the dry systems of self-propelled rods previously reported [166], in which one big cluster (aggregate in their terms) coexist with a disordered gas-phase but with large fluctuations in its size, like the ones reported for this regime in the results where the presence of the intermittent small clusters creates the fluctuations in the size of the big cluster (figure 4.13.b) for $S_{max}$). However, the nature of the interactions as well as the root of the clustering and alignment mechanism of the particles in both cases are very different.

The variation in the volume fraction has proven to have different effects in the considered suspensions. Since it is proportionally related to the number of particles in a given volume, it modulates the rate of collisions (or, more generally, the rate of interactions) between the particles. The increase of this variable reduces the average inter-particle distances, making some long-ranged interactions act faster $(a/r)^2$ or that some short-ranged interactions become relevant $(a/r)^3$. In the simplest considered case (suspensions in regime 1), the effect of the volume fraction has shown that in this regime, the origin of the small nonpersistent clusters is due only caused by the effect of the excluded volume between particles since under specific $\phi$ value the clustering is no more present. On the other hand, by considering the same low volume fractions in suspensions originally in regimes 2 and 3, we observe that the emerging patterns are unaltered, having one big cluster and many small clusters as previously. In these cases, only an acceleration to achieve the permanent state is observed with the increase of the volume fraction. Finally, specific realizations of suspensions originally in regime 4 and 5 ($\phi = 0.15$), stays in the same regime when $\phi$ increase, but when it is reduced some change of regime is observed.

The reported results have shown to be independent of the initial conditions of the simulations. Once they achieve the permanent state, their behavior depends only on the dimensionless parameters of the system: activity ratio, mobility ratio, and volume fraction.

Finally, it is important to mention some of the limitations of the current results regarding their connection with experimental results in which three aspects can be considered, a) The absence of Brownian effects given the scales of the active colloids; it is important to mention here that the original focus of the research was only to investigate the coupled effects of the hydro-chemical interactions on reactive suspensions (in a deterministic approach), but that the Brownian motion can be incorporated in properly in our code [167, 168]. b) The suspensions simulations were performed in bulk (fully 3D), while experimentally, they are constrained by a horizontal plane since the phoretic particles are not neutrally buoyant and they settle (quasi-2D). This is true, but still, some of the current conclusions should be qualitative valid when gravity rules. Given the increasing interest in space exploration, the current results become relevant. They are valid for conditions of low gravity and microgravity, something of interest for studying active matter in these conditions with relevance both on fundamental and applied level [169]. c) The absence of lubrication forces between the particles in the simulations, something relevant given the existence of clusters and particles in contact; regarding this point, it is important to mention that the inclusion of these effects could be easily included in our code [154], but since

the main interactions between colloids (chemical and hydrodynamical) are long-ranged the same clustered regimes results are expected, only with a slowest convergence in the final stage of the clustering (once the inter-particles distances are small).

# Chapter 5

# Conclusions and perspectives

In this final chapter, I will summarize the results achieved in this thesis. I will bring some future research lines that could take advantage of the current development to contribute to the understanding or applications of reactive suspensions.

## 5.1 Summary and conclusions

My thesis's research objective is to study the collective motion, and the coherent structures that emerge in systems of suspended auto-phoretic particles in fluids interacting through chemical and hydrodynamical fields called reactive suspensions. To do this, I model as accurately as possible, using a particle approach, their hydrodynamics, and chemistry for large sets of particles. The fact is that an analytical solution to this kind of system is not possible and that the most similar level of accuracy could only be achieved by performing full numerical simulations. For example, using the Boundary Element Method (BEM), however, it has a computational cost that increases quadratically with the number of particles. Thus developing an efficient and accurate method capable of handling reactive suspensions with a large number of particles to predict their dynamics was my first objective.

Correspondingly, the development of the Diffusiophoretic Force Coupling Method (DFCM) aims to be a step forward in addressing the numerical modeling of reactive suspensions. First, because of the formal inclusion of the chemical and hydrodynamical interactions, at least approximately until the dipole level in regularized multipole expansion, which implies an improvement over other approaches [43, 125, 128]. Second and given its linear scalability with the number of particles, because of the reduction of the required computational resources with respect to the default quadratic scalability of some methods [138, 149, 150, 121], and even compared with other methods that have improved this default scalability [134, 136]. Some modeling was required to simplify the problem enough. In the case of the standard Force Coupling Method, it is done by removing the particles' surface and enforcing a weak boundary condition form using volumetric averages (something analogous happens with DFCM), as detailed in Chapter 3.

The validation results of DFCM have shown the importance of the correct resolution of higher-order hydro-chemical multipolar signatures (including both the induced polarities for the chemistry and rigidity stresslets for the hydrodynamics) to capture the hydro-chemical interactions between particles accurately. Consistently with our level of approximation, DFCM is not able to resolve the details of the chemical and hydrodynamic fields in the gap between the surface of the particles when they are close to each other ($d \leq 0.5$) because it does not include lubrication forces and it is truncated until the dipole level, as well because it can not represent exactly position of the surface. However, this numerical approach brings significant improvements in capturing such complex effects in comparison with simpler analytical or numerical models (like the far-field method), but at the same time provides a substantial reduction in complexity in comparison with full numerical simulations such as BEM, something that opens considerable opportunities for numerical analysis of larger number of particles in suspensions and this move us to the second big part of my thesis.

My thesis's second objective is to characterize the emerging coherent structures and collective motions present in reactive suspensions using the new DFCM. In particular, to check which dynamical patterns emerge by formally including the hydrodynamic and chemical interactions with respect to simpler models. Moreover, once they are identified, describe them and relate their dynamical characteristic with the corresponding system properties.

The chapter 4 is entirely dedicated to this objective; in which I implement and validate the DFCM in a new parallel code with good scalability for a large number of particles, by using high performance computing tools. Then, I move to the physical study of these reactive suspensions.

Here, by considering several activity and mobility ratios, many types of coherent structures have emerged as in another studies [13, 136, 144, 149], including small clusters with a short-lived existence, persistent self-limiting size clusters, and persistent large clusters. Large populations of free particles were also observed, and in some cases, they coexist with the different clusters mentioned before.

A classification method was required to introduce some order and structure in all the studied cases. It was based on the resulting microstructures of the suspensions, and on the observed types of collective motions in the permanent state of the simulations. All this is fully described in section 4.3.2 and the obtained phase diagrams are reported in figure 4.17. The reported results are independent of the initial conditions, and after the suspensions reach the permanent state (or stationary state) the results depend only on the dimensionless parameter of the system: activity ratio, mobility ratio and volume fraction.

One of the predicted regimes with DFCM simulations (regime 4) resembles the well-known living clusters system [13, 14] reported before since the observed clusters grow, break, merge and separate continuously in a very dynamic suspension. There is another case (regime 5) that is very dynamic, but in this case, it only contains one big cluster interacting with free particles and some small clusters around them.

Another previously reported type of suspension was observed in our simulations, including a gas-like phase characterized by a big population of particles that swims freely, with some short-lived clusters from time to time (regime 1). It has been observed in suspensions of particles chemotactically neutral and phoretically repulsive in concordance with previous studies [149]. But also with monopolar dominantly repulsive particles (both chemotactive and anti-chemotactive, central and top part of figure 4.17.b)), as well in the case of attractive and anti-chemotactic particles (figure 4.17.a)).

Regimes 2 and 3 present cluster phases extremely persistent in terms of the number of particles in their microstructure, leading to essentially rigid body clusters. In regime 2, the final result is a single big cluster that performs ballistic motion as previously reported [136, 149] for monopolar dominantly attractive particles (both chemotactive and anti-chemotactive, central and top part of figure 4.17.a)).

In Regime 3, which is a new regime for reactive suspensions, the particles assemble in many small clusters of self-limiting size exhibiting chaotic motion with significant translation and rotation velocities, in this case the particles in suspensions are monopolar dominantly (both attractive or repulsive) and with a strong chemotactic behavior (both positive or negative), top-lateral regions in figure 4.17.a) and b). In this case, the combination of the strong chemotaxis, inducing a very fast particle reorientation, and the second phoretic drift (proportional to the second moment of concentration), which always causes a short-ranged attractive interactions, is the key effect that triggers the existence of these self-limiting size clusters in the general case.

The effect of the volume fraction was studied for five specific cases of interest, each one originally in a different regime for $\phi = 0.15$. Since the main effect of this variable is to modify the average distance between particles, it modulates the rate of interactions between them. Its variation induces some change of regime, in the case where opposite effects are present (case 4, with attractive and anti-chemotactic particles) while in others, the regime doesn't change but an acceleration of the suspension to reach the permanent state is induced (cases 2 and 3, with chemotactic and attractive particles).

## 5.2 Future perspectives

The focus of the current research has been to consider as precise as possible the coupled effects of the hydrodynamics and the chemistry through the successive solution of the Laplace and Stokes problems. However, the relative importance of the hydrodynamic and the chemical interactions in auto-phoretic suspensions has been a matter of active discussion and research [128, 148]. In the current DFCM framework, it is possible to isolate these contributions to investigate their individual effects on the system's dynamics. Remembering the contributions for the total particles' velocities:

$$\boldsymbol{U}_n = \boldsymbol{U}_n^a - \boldsymbol{W}_n + \int_{V_F} \boldsymbol{u}\, \Delta(\boldsymbol{r}_n) \mathrm{d}V, \tag{5.1}$$

$$\boldsymbol{\Omega}_n = \boldsymbol{\Omega}_n^a + \frac{1}{2} \int_{V_F} [\nabla \times \boldsymbol{u}] \Delta^*(\boldsymbol{r}_n) \mathrm{d}V. \tag{5.2}$$

So, to answer the question: which is the dominant interaction in reactive suspensions? we have two options: on the one hand, we could focus on the chemical interactions by only solving the modified Laplace equation 4.1 and only calculating the first terms in the previous two equations for the particles' velocities ($\boldsymbol{U}_n^a$ and $\boldsymbol{\Omega}_n^a$). On the other hand, we could focus only on the hydrodynamic interactions by solving first the modified Laplace equation 4.1 to calculate the active hydrodynamic forcing $\boldsymbol{S}_n^a$ and $\boldsymbol{H}_n^a$. Then to solve the modified Stokes equation 4.2, and finally, only calculating the second and third terms in equation 5.1 for translation, as well as only the second term in equation 5.2 for rotation. In this second case, it is important to include manually in each particle the self-propulsion velocity provided by equation 2.59. By doing so, it is possible to isolate the interactions in specific cases of interest to determine their effect in the dynamical system and compare to the full simulation (current results). Similar procedures were performed by other researchers to disentangle the effects of the different interactions of the particles in suspensions [148, 170].

The study of the change of the effective rheological and transport properties of the suspending fluid caused by the active stresses exerted by the active particles is of interest from a practical and theoretical point of view because: (i) the self-assembly observed in these systems open the possibility of the creation of a new class of materials called "active materials" [34] with tunable properties, which needs to be studied, understood and characterized before being used in practical applications. (ii) these artificial systems could mimic the behavior of suspensions of micro-swimmers in biological processes with similar physicochemical properties facilitating the study, and the understanding of these natural systems [43].

It is well known that the addition of passive spherical particles in a Newtonian fluid increases its effective viscosity without altering its Newtonian properties (for very small volume fractions) [171]. On the other hand, adding biological microswimmers can increase (for pullers) or decrease (for pushers) the fluid's viscosity [41], depending on the swimmers' properties, as demonstrated experimentally [172, 173]. Analogously the addition of synthetic phoretic particles, which share active properties with their biological counterparts, has similar effects [174]. For example, Stokesian Dynamics simulations were performed with spherical squirmers to study the rheology of active suspensions [175], obtaining non-Newtonian rheology in the case of bottom-heavy squirmers.

Although in the DFCM approach, the squirmer model is included to model active swimmers, we could expect differences in the results since DFCM consider not only the hydrodynamical interactions but also the chemical interactions, i.e., chemical drift and rotation induced by the

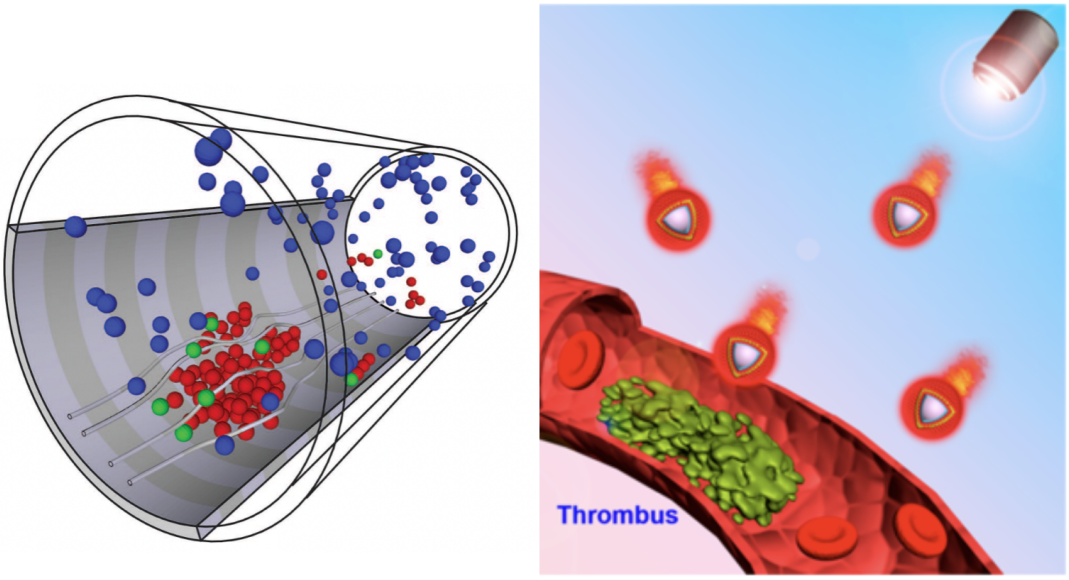


Figure 5.1: Medical application in which the current DFCM framework can be used to complement experimental results including: a) thrombus formation (blue, green and red spheres represent passive, triggered and activated platelets respectively, where the big red aggregate is the formed thrombus in the wall), b) thrombus destruction (where the green aggregate represents the thrombus and the Janus particles are represented as the anisotropic red/yellow particles). In both cases, the blood vessel is represented by the external cylinder. Figures adapted from [19, 9] respectively.

concentration field created by other particles, which is not the case for the squirmer alone. By introducing the Lees-Edwards boundary conditions [176, 177] in the current scalable DFCM implementation, a numerical study could be performed to determine the relationship between the effective viscosity of the suspension and the system properties: activity and mobility ratio as well as its volume fraction, but also a new one related to the shear flow intensity.

Additionally, the current DFCM framework can be used to complement experimental results in real applications by considering different particle designs not tested yet or providing information not available experimentally. For instance, let's consider a medical application regarding the problem of thrombus in blood vessels. While previously, the Force Coupling Method has been used to explore the *thrombus formation* [19] by modeling the transport and aggregation of platelets as passive particles in blood vessels with the background flow in figure 5.1.a); the *thrombus destruction* was explored experimentally [9], through the use of (thermophoretic) active particles that perform directed motion inducing their mechanical ablation. After the inclusion of some small details, the current DFCM code would allow performing a full simulation of both processes (formation and destruction), including a mixture of passive particles (platelets experiencing aggregation forces) and active particles (Janus particles experiencing thermophoresis). Different Janus particle designs can be considered in the thrombus creation/destruction process allowing the performance evaluation of each case, including variables like phoretic properties, volume fraction, background flow, and aggregation characteristics of the platelets.

Despite its specific focus on the modeling of hydrochemical interactions within phoretic suspensions, the present analysis demonstrates how the fundamental idea of the original Force

Coupling Method can be extended and applied to other fields of physics. In such an approach, the elliptic Stokes equations are solved over the entire domain (instead of the multiply-connected fluid domain outside the particles) by introducing regularized forcings whose support is calibrated to account for the finite particle size and whose intensity is determined to account for a weak form of the boundary condition.

For the chemical diffusion problem considered here, this amounts to (i) replacing a Laplace problem with a Poisson equation, (ii) calibrating the support of the spreading operators to match benchmark properties for a single particle, and (iii) determining the forcing intensity by projecting the Neumann-type boundary condition on the particle surface onto a localized support function of appropriate shape (e.g., Gaussian or annular). This approach can readily be adapted for solving diffusion problems with more general (Dirichlet or mixed) boundary conditions, as encountered for more detailed chemical activity of reactive particles [158, 178] or in bubble growth/dissolution problems [179], but also to other physical phenomena driven by elliptic equations, such as electromagnetic interactions of particles [180].

# Appendix A

# Determining the source intensities

We consider here a single active particle bounded by a surface $S$. The concentration field outside $S$ (in the fluid) satisfies Laplace's equation, and its value anywhere in the fluid domain can therefore be obtained in terms of its value and normal flux on $S$ as

$$c(\boldsymbol{r}) = \frac{1}{4\pi}\int_S \left[c(\boldsymbol{s})\boldsymbol{n}\cdot\frac{(\boldsymbol{r}-\boldsymbol{s})}{|\boldsymbol{r}-\boldsymbol{s}|^3} + \left(-\frac{\partial c(\boldsymbol{s})}{\partial n}\right)\frac{1}{|\boldsymbol{r}-\boldsymbol{s}|}\right]\mathrm{d}S. \tag{A.1}$$

where $\boldsymbol{s} = a\boldsymbol{n}$, is a vector of the surface of the particle. Far from the particle (i.e. $|\boldsymbol{r}| \gg |\boldsymbol{s}|$), and using the following Taylor expansion for $|\boldsymbol{r}-\boldsymbol{s}|^{-n}$,

$$\frac{1}{|\boldsymbol{r}-\boldsymbol{s}|^n} \approx \frac{1}{r^n}\left[1 + n\left(\frac{\boldsymbol{s}\cdot\boldsymbol{r}}{r^2}\right) + n\left(\frac{n}{2}+1\right)\left(\frac{\boldsymbol{s}\cdot\boldsymbol{r}}{r^2}\right)^2 + ...\right], \tag{A.2}$$

the concentration field can be expanded in terms of a series of singular multipoles, namely a monopole of intensity $q^M$, a dipole of intensity $\boldsymbol{q}^D$, (and up to the desired order of approximation):

$$c(\boldsymbol{r}) = \frac{q^M}{4\pi r} + \frac{\boldsymbol{q}^D\cdot\boldsymbol{r}}{4\pi r^3} + \dots \tag{A.3}$$

where the intensities are obtained as:

$$q^M = \int\left(-\frac{\partial c(\boldsymbol{s})}{\partial n}\right)\mathrm{d}S, \tag{A.4}$$

$$\boldsymbol{q}^D = a\int\left(-\frac{\partial c(\boldsymbol{s})}{\partial n}\boldsymbol{n}\right)\mathrm{d}S + \int c(\boldsymbol{s})\boldsymbol{n}\,\mathrm{d}S. \tag{A.5}$$

Substitution of the boundary condition Eq. (2.48) leads to the result in Eq. (3.12).

# Appendix B

# Intrinsic phoretic velocities and stresslet

The intrinsic phoretic velocity of a particle (i.e. its swimming speed in the absence of any hydrodynamic interactions or outer flow) is defined in Eq. (2.54). Using the slip velocity definition in Eq. (2.50) and the mobility distribution as in Eq. (2.56), we obtain:

$$\boldsymbol{U}_n^a \;=\; -\langle \boldsymbol{u}_s \rangle_n \;= -\overline{M}_n \langle \nabla_{\parallel} c \rangle_n - M_n^* \langle \mathrm{sign}(\boldsymbol{p}\cdot\boldsymbol{n})\, \nabla_{\parallel} c \rangle_n. \tag{B.1}$$

Integrating by parts the surface averaging operators, we arrive to:

$$\boldsymbol{U}_n^a = -\frac{2\overline{M}_n}{a}\langle c\boldsymbol{n}\rangle_n + \frac{M_n^*\boldsymbol{p}_n}{a}\langle c\rangle_n^{\mathrm{eq}} - \frac{M_n^*}{a}\Big(\langle c\boldsymbol{n}\rangle_n^{+} - \langle c\boldsymbol{n}\rangle_n^{-}\Big), \tag{B.2}$$

where the operators $\langle ... \rangle_n^{\pm}$ refer to the mean value over the front and back caps of particle $n$, respectively, and $\langle \ldots \rangle_n^{\mathrm{eq}}$ is the line average over the equator of particle $n$. To compute these particular averages, we expand the surface concentration $c(\boldsymbol{n})$ in terms of its surface moments and truncate the expansion to the first three terms:

$$c(\boldsymbol{n}) = \langle c\rangle_n + 3\langle c\boldsymbol{n}\rangle_n \cdot\; \boldsymbol{n} + \frac{15}{2}\langle c(\boldsymbol{nn} - \boldsymbol{I}/3)\rangle_n \;:\boldsymbol{nn}. \tag{B.3}$$

Substitution in Eq. (B.1) then finally provides

$$\boldsymbol{U}_n^a = -\frac{2\overline{M}_n}{a}\langle c\boldsymbol{n}\rangle_n - \frac{15M_n^*}{8a}\langle c(\boldsymbol{nn} - \boldsymbol{I}/3)\rangle_n \;:\Big[\boldsymbol{p}_n\boldsymbol{I} + (\boldsymbol{p}_n\boldsymbol{I})^{\mathrm{T}_{12}} + \boldsymbol{p}_n\boldsymbol{p}_n\boldsymbol{p}_n\Big], \tag{B.4}$$

which can be simplified into Eq. (3.46) using the symmetry and traceless property of $\boldsymbol{nn} - \boldsymbol{I}/3$.

Following a similar procedure, the intrinsic phoretic angular velocity can be expanded from Eqs. (2.50), (2.54) and (2.56) as

$$\boldsymbol{\Omega}_n^a = -\frac{3}{2a}\langle \boldsymbol{n}\times M\nabla_{\parallel} c\rangle_n = -\frac{3}{2a}\overline{M}_n\langle \boldsymbol{n}\times\nabla_{\parallel} c\rangle_n - \frac{3}{2a}M_n^*\langle \mathrm{sign}(\boldsymbol{p}\cdot\boldsymbol{n})\, \boldsymbol{n}\times\nabla_{\parallel} c\rangle_n, \tag{B.5}$$

and after integration by parts simplifies to:

$$\boldsymbol{\Omega}_n^a = -\frac{3M_n^*}{2a^2}\left(\boldsymbol{p}_n \times \langle c\boldsymbol{n}\rangle_n^{\mathrm{eq}}\right). \tag{B.6}$$

Substitution of Eq. (B.3) provides the desired expression, Eq. (3.49).

The same method can also be applied to determine the intrinsic phoretic stresslet $\boldsymbol{S}_n^a$. From its definition in Eq. (2.55) and using Eqs. (2.50) and (2.56), we obtain:

$$\boldsymbol{S}_n^a = -10\pi a^2\overline{M}_n\langle(\boldsymbol{n}\nabla_{\parallel} c + (\nabla_{\parallel} c)\,\boldsymbol{n})\rangle_n - 10\pi a^2 M_n^*\langle \mathrm{sign}(\boldsymbol{p}\cdot\boldsymbol{n})(\boldsymbol{n}\nabla_{\parallel} c + (\nabla_{\parallel} c)\,\boldsymbol{n})\rangle_n \tag{B.7}$$

Integrating by parts the surface averaging operators provides

$$\begin{aligned}\boldsymbol{S}_n^a =& -60\pi a\overline{M}_n\langle c(\boldsymbol{nn}-\boldsymbol{I}/3)\rangle_n \\ &+10\pi aM_n^*\left[\langle c\boldsymbol{n}\rangle_n^{\mathrm{eq}}\boldsymbol{p}_n+\boldsymbol{p}_n\langle c\boldsymbol{n}\rangle_n^{\mathrm{eq}}-3\left(\langle c(\boldsymbol{nn}-\boldsymbol{I}/3)\rangle_n^+-\langle c(\boldsymbol{nn}-\boldsymbol{I}/3)\rangle_n^-\right)\right]\end{aligned} \tag{B.8}$$

Subsitution of Eq. (B.3) provides finally

$$\boldsymbol{S}_n^a=-60\pi a\overline{M}_n\langle c(\boldsymbol{nn}-\boldsymbol{I}/3)\rangle_n+\frac{15}{2}\pi aM_n^*\left[\left(\langle c\boldsymbol{n}\rangle_n\cdot\boldsymbol{p}_n\right)(\boldsymbol{I}-\boldsymbol{p}_n\boldsymbol{p}_n)-\langle c\boldsymbol{n}\rangle_n\boldsymbol{p}_n-\boldsymbol{p}_n\langle c\boldsymbol{n}\rangle_n\right]. \tag{B.9}$$

# Appendix C

# Reference velocity $U_R$ determination for time step calculation

Considering the phoretic properties of the particles (activity and mobility) and the number of particles in the system of interest $N$, I designed a critical case so that an instantaneous calculation with our DFCM framework could bring $U_R$ for the time step calculation (Eq. 4.4): consider a compact cubic array of these particles (all of them in contact, i.e., $r/a = 2.0$ where $r$ is the inter-particle distance), oriented such that all them swim to the centroid of the system, without including the repulsive force that model the contact forces, see figure C.1 as reference. In these cluster conditions, the collapse of the particles is inevitable, leading to velocities in the order of magnitude similar to the ones observed in the non-physical simulations when the time step was too large. Then $U_R$ is defined as the maximum velocity obtained in the instantaneous simulation.

Figure C.2 summarizes the calculations performed for attractive particles with phoretic parameters $(\alpha_F, \alpha_B) = (0, 1)$ and $(M_F, M_B) = (0, -1)$ up to $N = 16^3 = 4096$ particles, while Table C.1 present the corresponding calculated velocities in 2 ways: absolute value and relative value respect to the intrinsic velocity as reference. In the calculation two options of grid points number in each direction $N_x$ was considered and reported (where $N_y = N_z = N_x$).

As can be seen in Table C.1, the reference velocity $U_R$ can be much greater than the intrinsic velocity $U^i$. Using these velocities in estimating the time step $\triangle t$, non-physical velocities and particles overlap were effectively avoided in the cases in which big clusters are formed. This calculation depends on the type of particles in consideration so that it will be different in principle in each case. The particle number of interest needs to be rounded to the biggest particle number in these cubic arrays; for example, if we want to consider 970 particles, the nearest possible number will be $1000 = 10^3$.

| **Number of particles** | **Box size 1** | **Box size 2** |
|---|---|---|
| $N = 4^3 = 64$ | $U_R = 1.10 = 8.8U^i$ | $U_R = 1.31 = 10.5U^i$ |
| $N = 5^3 = 125$ | $U_R = 1.77 = 14.2U^i$ | $U_R = 2.75 = 22.0U^i$ |
| $N = 8^3 = 512$ | $U_R = 4.80 = 38.4U^i$ | $U_R = 6.12 = 49.0U^i$ |
| $N = 12^3 = 1728$ | $U_R = 12.81 = 102.5U^i \quad (N_x = 160)$ | |
| $N = 16^3 = 4096$ | $U_R = 18.01 = 144.1U^i$ | $U_R = 24.05 = 192.4U^i$ |

Table C.1. Corresponding reference velocities calculated for figure C.2.

Maybe it seems a little weird that the predicted reference velocity $U_R$ between the two boxes is different. Still, after checking the images in figure C.2 (and the corresponding volume fractions

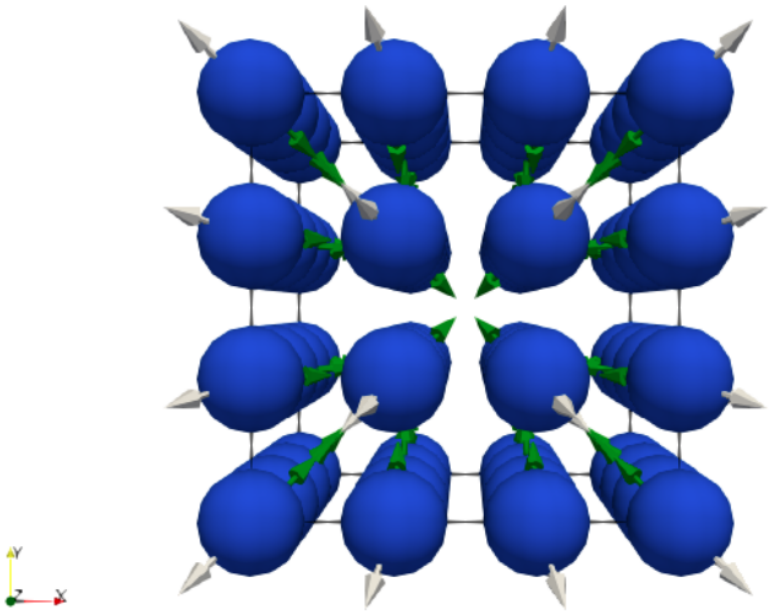

Figure C.1: Cubic array considered for the calculation of the reference velocity $U_R$. Here, particularly $N = 4^3 = 64$ Janus particles, all of them in contact with their neighbors trying to swim to the centroid of the system. The gray arrows represented the orientation, the green arrows the velocity and the particles are scaled by a reducing factor of 0.75 so that, more details can be seen in the figure.

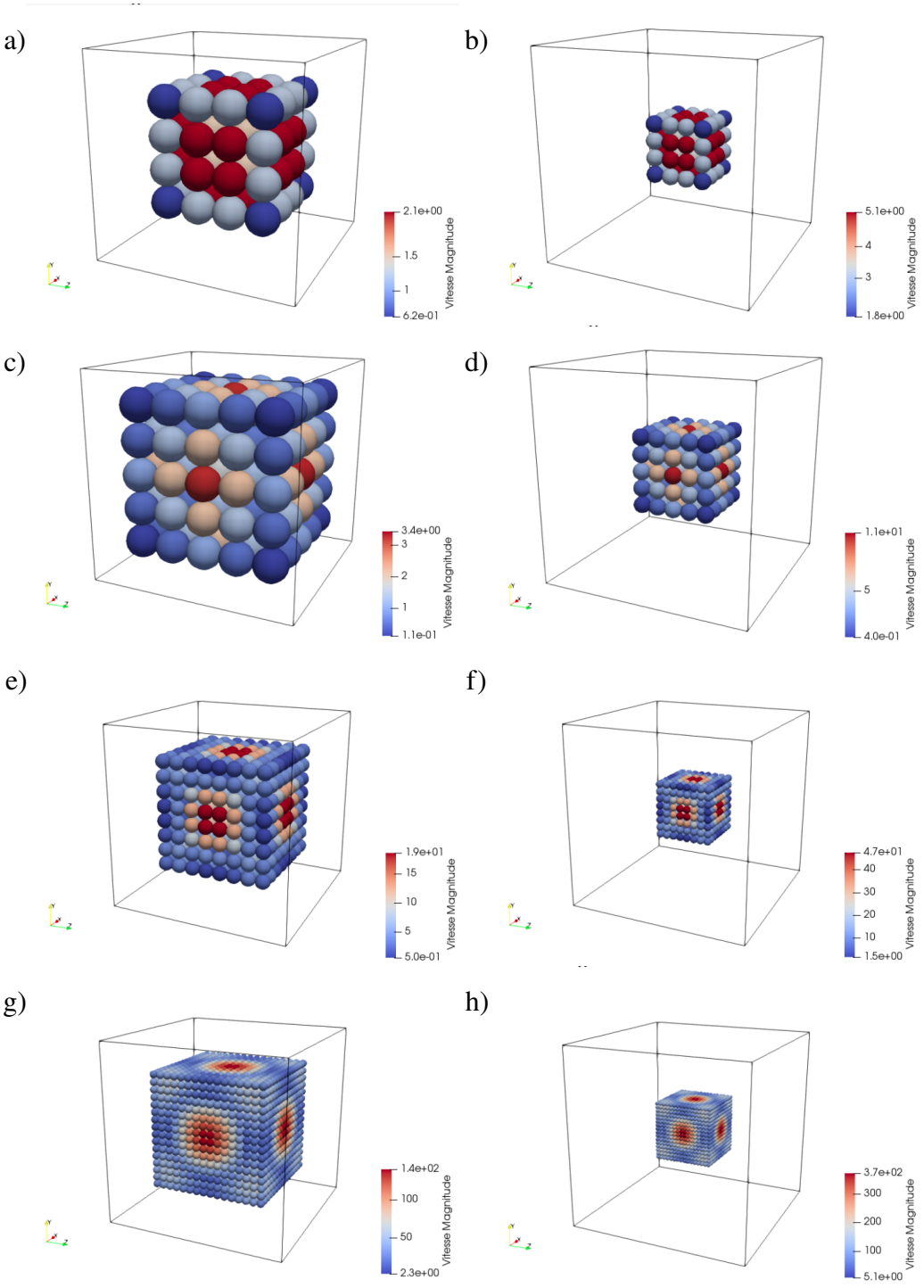


Figure C.2: Some configurations for which the reference velocity $U_R$ was calculated: a) $N = 4^3 = 64$, $N_x = 40$, b) $N = 4^3 = 64$, $N_x = 80$, c) $N = 5^3 = 125$, $N_x = 40$, d) $N = 5^3 = 125$, $N_x = 80$, e) $N = 8^3 = 512$, $N_x = 80$, f) $N = 8^3 = 512$, $N_x = 160$, g) $N = 16^3 = 4096$, $N_x = 160$ and h) $N = 16^3 = 4096$, $N_x = 320$. The particles color represents its instantaneous velocities and the maximum value will be taken as $U_R$. The particles number $N$ and the grid points in each direction $N_x$ are reported (where $N_y = N_z = N_x$).

of $\phi = 0.15$ and $\phi = 0.018$ for $N = 64$ particles), it is evident that the finite size of the domain has a non-negligible effect. To check this, I calculated for the $N = 64$ case the corresponding velocities for larger boxes sizes obtaining the following results: $U_R = 1.3358 = 10.69U^i$ for $N_x = 160$ and $U_R = 1.3392 = 10.71U^i$ for $N_x = 320$ showing a converging behavior consistent with the reduction of the border effect in the calculation

# Appendix D

# Initial conditions sensibility analysis (other regimes)

The sensibility analysis to the different initial conditions for all the found regimes has been performed, while the results for cases in regimes 1 and 2 are presented and discussed in section 4.6, here the analogous results for regimes 3, 4 and 5 are reported in the next figures.

The results for the case in regime 3, having many small clusters with chaotic motion (figure D.1) are very consistent with the clustered state in regime 2 that has been shown before (figure 4.31). The particles in suspension quickly reach the clustered phase ($R_p = 1$), happening much faster for the ordered initial configuration. Although the mean cluster size for the considered time ($tU/a < 140$) differs for the 4 realizations, their difference is small and it is expected that this difference will be reduced after reach the permanent state.

All the realizations for the considered case in regime 4 (coexistence of many cluster with gas-like, figure D.2), have very similar behaviours, with big fluctuations in $R_p$, but all of them in the same numeric range. The biggest difference in the case of the ordered initial condition are observed in $S_{mean}$, where clearly there are several peaks of relative high values (respect to the random cases) but again, after a bigger clustering permanent time, the difference between the four realizations are negligible.

In the last case, suspension in regime 5 (coexistence of big cluster with gas-like, figure D.3), the differences between the four realizations are essentially insignificant and the results are really analogous with the ones of the regime 2 (figure 4.31), in which the biggest difference are in the fastest decay of $N_c$ to the permanent state values for the ordered initial condition.

Finally, after applying the classification procedure in each of the previous cases, it is confirmed that all the realizations in each case/regime converged to the expected result without change of regime, confirming the independence of the permanent state properties of the suspensions respect to the initial conditions.

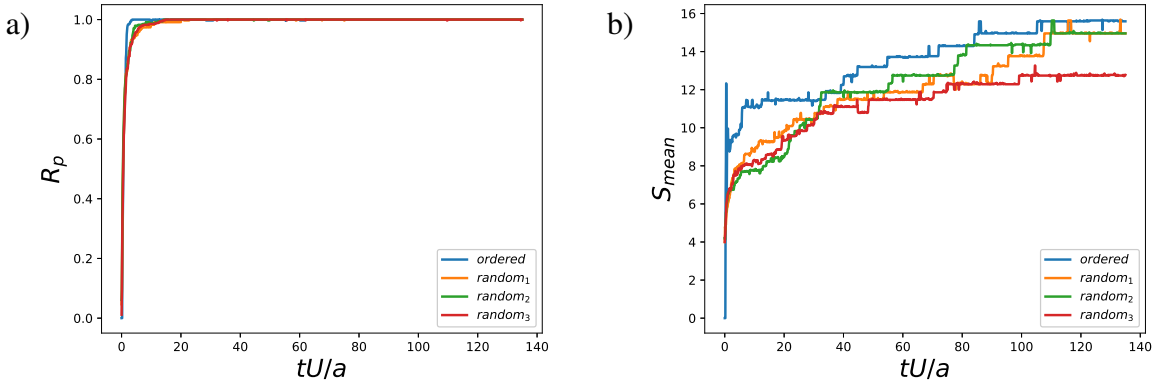


Figure D.1: Sensibility analysis to different initial conditions for a suspension in regime 3 ($\phi = 0.10$): a) ratio of particles in clusters $R_P$ and b) cluster mean size $S_{mean}$. These results can be directly compared with the ones presented in figure 4.26, all the suspension's realizations reach Regime 3.

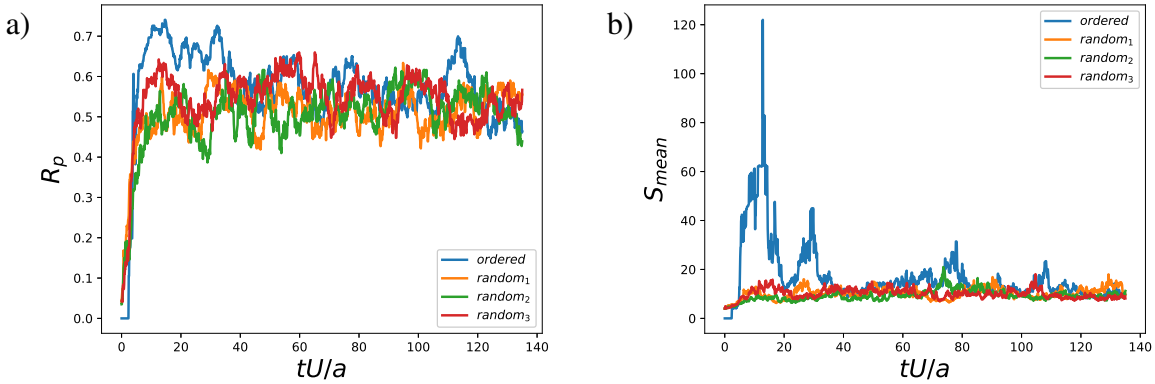


Figure D.2: Sensibility analysis to different initial conditions for a suspension in regime 4 ($\phi = 0.10$): a) ratio of particles in clusters $R_P$ and b) cluster mean size $S_{mean}$. All the suspension's realizations reach Regime 4, and these results can be directly compared with results in figure 4.27.

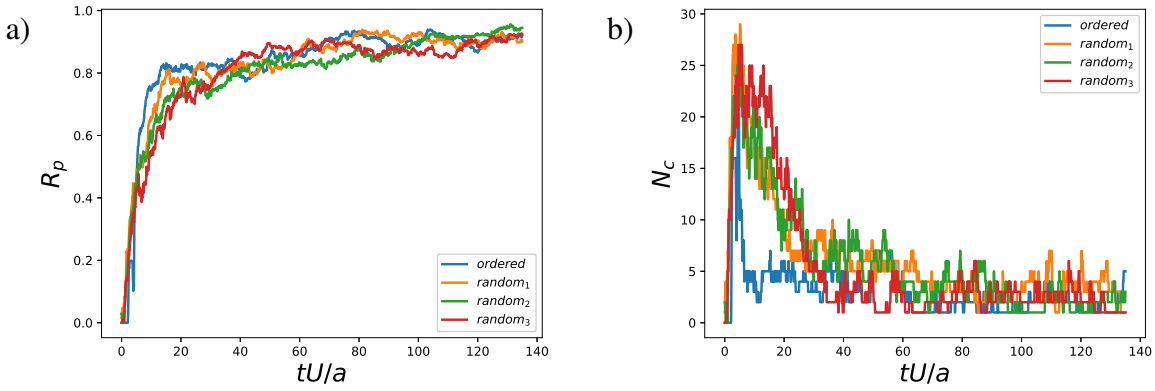


Figure D.3: Sensibility analysis to different initial conditions for a suspension in regime 5 ($\phi = 0.10$): a) ratio of particles in clusters $R_P$ and b) number of clusters $N_c$. These results can be directly compared with the shown in figure 4.28, here all the suspension's realizations reach Regime 5.

# Bibliography


[1] Juliane Adrian, Armin Seyfried, and Anna Sieben. Crowds in front of bottlenecks at entrances from the perspective of physics and social psychology. *Journal of The Royal Society Interface*, 17(165):20190871, 2020.

[2] Dmitri Volfson, Scott Cookson, Jeff Hasty, and Lev S. Tsimring. Biomechanical ordering of dense cell populations. *Proceedings of the National Academy of Sciences*, 105(40):15346–15351, 2008.

[3] Christopher Dombrowski, Luis Cisneros, Sunita Chatkaew, Raymond E. Goldstein, and John O. Kessler. Self-concentration and large-scale coherence in bacterial dynamics. *Phys. Rev. Lett.*, 93:098103, Aug 2004.

[4] S. F. Schoeller, W. V. Holt, and E. Keaveny. Collective dynamics of sperm cells. *Philosophical transactions of the Royal Society B*, 2020.

[5] Yingzi Yang, Jens Elgeti, and Gerhard Gompper. Cooperation of sperm in two dimensions: Synchronization, attraction, and aggregation through hydrodynamic interactions. *Phys. Rev. E*, 78:061903, Dec 2008.

[6] Jing Yan, Ming Han, Jie Zhang, Cong Xu, Erik Luijten, and Steve Granick. Reconfiguring active particles by electrostatic imbalance. *Nature materials*, 15:1095–1099, 2016.

[7] Soichiro Tottori, Li Zhang, Kathrin E. Peyer, and Bradley J. Nelson. Assembly, disassembly, and anomalous propulsion of microscopic helices. *Nano Letters*, 13:4263–4268, 2013.

[8] Jinxing Li, Tianlong Li, Tailin Xu, Melek Kiristi, Wenjuan Liu, Zhiguang Wu, and Joseph Wang. Magneto–acoustic hybrid nanomotor. *Nature Letters*, 15:4814–4821, 2015.

[9] J. Shao, M. Abdelghani, G. Shen, S. Cao, D. S. Williams, and J. C. M. van Hest. Erythrocyte membrane modified janus polymeric motors for thrombus therapy. *ACS Nano*, 12(5):4877–4885, 2018. PMID: 29733578.

[10] J. Li, O. E. Shklyaev, T. Li, W. Liu, H. Shum, I. Rozen, A. C. Balazs, and J. Wang. Self-propelled nanomotors autonomously seek and repair cracks. *Nano Lett.*, 15(10):7077–7085, 2015.

[11] Beatriz Jurado-Sanchez, Sirilak Sattayasamitsathit, Wei Gao, Luis Santos, Yuri Fedorak, Virendra V. Singh, Jahir Orozco, Michael Galarnyk, and Joseph Wang. Self-propelled activated carbon janus micromotors for efficient water purification. *Small*, 11(4):499–506, 2015.

[12] Ivo Buttinoni, Julian Bialké, Felix Kümmel, Hartmut Löwen, Clemens Bechinger, and Thomas Speck. Dynamical clustering and phase separation in suspensions of self-propelled colloidal particles. *Phys. Rev. Lett.*, 110:238301, Jun 2013.

[13] I. Theurkauff, C. Cottin-Bizonne, J. Palacci, C. Ybert, and L. Bocquet. Dynamic clustering in active colloidal suspensions with chemical signaling. *Phys. Rev. Lett.*, 108:268303, Jun 2012.

[14] Jeremie Palacci, Stefano Sacanna, Asher Preska Steinberg, David J. Pine, and Paul M. Chaikin. Living crystals of light-activated colloidal surfers. *Science*, 339(6122):936–940, 2013.

[15] O. S. Pak and E. Lauga. Theoretical models in low-reynolds-number locomotion. *arXiv: Fluid Dynamics*, 2014.

[16] A. Zöttl and H. Stark. Simulating squirmers with multiparticle collision dynamics. *The European Physical Journal E*, 41(5), May 2018.

[17] A. Varma, T. D. Montenegro-Johnson, and S. Michelin. Clustering-induced self-propulsion of isotropic autophoretic particles. *Soft Matter*, 14:7155–7173, 2018.

[18] F. Ginot, I. Theurkauff, F. Detcheverry, C. Ybert, and C. Cottin-Bizonne. Aggregation-fragmentation and individual dynamics of active clusters. *Nat. Comm.*, 9:696, 2018.

[19] Igor V. Pivkin, Peter D. Richardson, and George Karniadakis. Blood flow velocity effects and role of activation delay time on growth and form of platelet thrombi. *Proceedings of the National Academy of Sciences*, 103(46):17164–17169, 2006.

[20] Michele Ballerini, Nicola Cabibbo, Raphael Candelier, Andrea Cavagna, Evaristo Cisbani, Irene Giardina, Alberto Orlandi, Giorgio Parisi, Andrea Procaccini, Massimiliano Viale, and Vladimir Zdravkovic. Empirical investigation of starling flocks: a benchmark study in collective animal behaviour. *Animal Behaviour*, 76(1):201–215, 2008.

[21] Máté Nagy, Zsuzsa Ákos, Dora Biro, and Tamás Vicsek. Hierarchical group dynamics in pigeon flocks. *Nature*, 464:890–893, 2010.

[22] F. Gill. *Ornithology*. New York : W.H. Freeman, 2007.

[23] Tamás Vicsek and Anna Zafeiris. Collective motion. *Physics Reports*, 517(3):71–140, 2012. Collective motion.

[24] James E. Herbert-Read, Andrea Perna, Richard P. Mann, Timothy M. Schaerf, David J. T. Sumpter, and Ashley J. W. Ward. Inferring the rules of interaction of shoaling fish. *Proceedings of the National Academy of Sciences*, 108(46):18726–18731, 2011.

[25] Yael Katz, Kolbjørn Tunstrøm, Christos C. Ioannou, Cristián Huepe, and Iain D. Couzin. Inferring the structure and dynamics of interactions in schooling fish. *Proceedings of the National Academy of Sciences*, 108(46):18720–18725, 2011.

[26] David J.T. Sumpter, Jens Krause, Richard James, Iain D. Couzin, and Ashley J.W. Ward. Consensus decision making by fish. *Current Biology*, 2008.

[27] Matz Larsson. Why do fish school? *Current Zoology*, 58(1):116–128, 02 2012.

[28] Caleb Anderson and Alberto Fernandez-Nieves. Social interactions lead to motility-induced phase separation in fire ants. *Nature Communications*, 13, 2022.

[29] James G. Puckett, Douglas H. Kelley, and Nicholas T. Ouellette. Searching for effective forces in laboratory insect swarms. *Scientific Reports*, 4, 2014.

[30] Andy M. Reynolds. Understanding the thermodynamic properties of insect swarms. *Scientific Reports*, 11, 2021.

[31] Amandine Ramseyer, Alain Boissy, Bertrand Dumont, and Bernard Thierry. Decision making in group departures of sheep is a continuous process. *Animal Behaviour*, 78(1):71–78, 2009.

[32] Francesco Ginelli, Fernando Peruani, Marie-Helène Pillot, Hugues Chaté, Guy Theraulaz, and Richard Bon. Intermittent collective dynamics emerge from conflicting imperatives in sheep herds. *Proceedings of the National Academy of Sciences*, 112(41):12729–12734, 2015.

[33] A. Garcimartin, I. Zuriguel, J.M. Pastor, C. Martin-Gomez, and D.R. Parisi. Experimental evidence of the "faster is slower" effect. *Transportation Research Procedia*, 2014.

[34] M. C. Marchetti, J. F. Joanny, S. Ramaswamy, T. B. Liverpool, J. Prost, Madan Rao, and R. Aditi Simha. Hydrodynamics of soft active matter. *Rev. Mod. Phys.*, 85:1143–1189, Jul 2013.

[35] C. Bechinger, R. Di Leonardo, H. Löwen, C. Reichhardt, G. Volpe, and G. Volpe. Active particles in complex and crowded environments. *Rev. Modern Phys.*, 88:045006, 2016.

[36] H C Berg. Chemotaxis in bacteria. *Annual Review of Biophysics and Bioengineering*, 4(1):119–136, 1975. PMID: 1098551.

[37] Howard C. Berg. *E.coli in Motion*. NewYork:Springer, 2004.

[38] S. S. Suarez and A. A. Pacey. Sperm transport in the female reproductive tract. *Hum Reprod Update*, 2006.

[39] E. M. Purcell. Life at low Reynolds number. *American Journal of Physics*, 45(1):3–11, January 1977.

[40] E. Lauga and T. R Powers. The hydrodynamics of swimming microorganisms. *Rep. Prog. Phys.*, 72(9):096601, aug 2009.

[41] J. Elgeti, R. G. Winkler, and G. Gompper. Physics of microswimmers–single particle motion and collective behavior: a review. *Rep. Prog. Phys.*, 78(5):056601, 2015.

[42] T. J. Pedley and J. O. Kessler. Hydrodynamics phenomena in suspensions of swimming microorganisms. *Annu. Rev. Fluid Mech.*, 24:313–358, 1992.

[43] A. Zöttl and H. Stark. Emergent behavior in active colloids. *Journal of Physics: Condensed Matter*, 28(25):253001, may 2016.

[44] D. Saintillan and M. J. Shelley. Active suspensions and their nonlinear models. *Comptes Rendus Physique*, 14(6):497 – 517, 2013. Living fluids / Fluides vivants.

[45] D. Saintillan. Rheology of active fluids. *Annual Review of Fluid Mechanics*, 50:563–592, 2018.

[46] C. Brennen and H. Winet. Fluid mechanics of propulsion by cilia and flagella. *Annu. Rev. Fluid Mech.*, 9:339–398, 1977.

[47] E. Lauga. Bacterial hydrodynamics. *Annu. Rev. Fluid Mech.*, 48:105–130, 2016.

[48] L. Fauci and R. Dillon. Biofluidmechanics of reproduction. *Annu. Rev. Fluid Mech.*, 38:371–394, 2006.

[49] J. S. Guasto, R. Rusconi, and R. Stocker. Fluid mechanics of planktonic microorganisms. *Annu. Rev. Fluid Mech.*, 44:373–400, 2012.

[50] S. J. Ebbens and J. R. Howse. In pursuit of propulsion at the nanoscale. *Soft Matter*, 6:726–738, 2010.

[51] R. Dreyfus, J. Baudry, M. L. Roper, M. Fermigier, H. A. Stone, and J. Bibette. Microscopic artificial swimmers. *Nature*, 473:862–865, 2005.

[52] L. Zhang, J. J. Abbott, L. Dong, B. E. Kratochvil, D. Bell, and B. J. Nelson. Artificial bacterial flagella: fabrication and magnetic control. *Appl. Phys. Lett.*, 94:064107, 2009.

[53] A. Babataheri, M. Roper, M. Fermigier, and O. du Roure. Tethered flexibmags as artificial cilia. *J. Fluid Mech.*, 678:5–13, 2011.

[54] Brian J. Williams, Sandeep V. Anand, Jagannathan Rajagopalan, and M. Taher A. Saif. A self-propelled biohybrid swimmer at low reynolds number. *Nature communications*, 5:3081, 2014.

[55] C. Wyatt Shields and Orlin D. Velev. The evolution of active particles: Toward externally powered self-propelling and self-reconfiguring particle systems. *Chem*, 3(4):539–559, 2017.

[56] Sumit Gangwal, Olivier J. Cayre, Martin Z. Bazant, and Orlin D. Velev. Induced-charge electrophoresis of metallodielectric particles. *Phys. Rev. Lett.*, 100:058302, Feb 2008.

[57] A. Perro, S. Reculusa, S. Ravaine, E. Bourgeat-Lami, and E. Duguet. Design and synthesis of janus micro- and nanoparticles. *Journal of Material Chemistry*, 15:3745–3760, 2005.

[58] V. Yadav, W. Duan, P. J. Butler, and A. Sen. Anatomy of nanoscale propulsion. *Annu. Rev. Biophys.*, 44:77–100, 2015.

[59] J. L. Moran and J. D. Posner. Phoretic self-propulsion. *Annu. Rev. Fluid Mech.*, 49:511–540, 2017.

[60] W. F. Paxton, K. C. Kistler, C. C. Olmeda, A. Sen, S. K. St. Angelo, Y. Cao, T. E.Mallouk, P. E. Lammert, and V. H. Crespi. Catalytic nanomotors: autonomous movement of striped nanorods. *Journal of the American Chemical Society*, 126(41):13424–1343, 2004.

[61] J. R. Howse, R. A. L. Jones, A. J. Ryan, T. Gough, R. Vafabakhsh, and R. Golestanian. Self-motile colloidal particles: From directed propulsion to random walk. *Phys. Rev. Lett.*, 99:048102, Jul 2007.

[62] M. E. Cates and J. Tailleur. Motility-induced phase separation. *Annu. Rev. Cond. Matter Phys.*, 6:219–244, 2015.

[63] R Golestanian, T B Liverpool, and A Ajdari. Designing phoretic micro- and nano-swimmers. *N. J. Phys.*, 9(5):126–126, may 2007.

[64] J L Anderson. Colloid transport by interfacial forces. *Annu. Rev. Fluid Mech.*, 21(1):61–99, 1989.

[65] Y. Wang, R. M. Hernandez, D. J. Bartlett Jr., J. M. Bingham, T. R. Kline, A. Sen, and T. E. Mallouk. Bipolar electrochemical mechanism for the propulsion of catalytic nanomotors in hydrogene peroxide solutions. *Langmuir*, 22:10451–10456, 2006.

[66] A. P. Bregulla and F. Cichos. Size dependent efficiency of photophoretic swimmers. *Faraday Discuss.*, 184:381, 2015.

[67] C. C. Maass, C. Krüger, S. Herminghaus, and C. Bahr. Swimming droplets. *Annu. Rev. Condens. Matter Phys.*, 7:171–193, 2016.

[68] I. Buttinoni, G. Volpe, F. Kümmel, G. Volpe, and C. Bechinger. Active Brownian motion tunable by light. *J. Phys.: Condens. Matter*, 24:284129, 2012.

[69] Ubaldo M. Córdova-Figueroa and John F. Brady. Osmotic propulsion: The osmotic motor. *Phys. Rev. Lett.*, 100:158303, Apr 2008.

[70] J.F. Brady. Particle motion driven by solute gradients with application to autonomous motion: continuum and colloidal perspectives. *Journal of Fluid Mechanics*, 667:216–259, 2011.

[71] R. Soto and R. Golestanian. Self-assembly of catalytically active colloidal molecules: Tailoring activity through surface chemistry. *Phys. Rev. Lett.*, 112:068301, Feb 2014.

[72] Rodrigo Soto and Ramin Golestanian. Self-assembly of active colloidal molecules with dynamic function. *Phys. Rev. E*, 91:052304, May 2015.

[73] F. Schmidt, B. Liebchen, H. Löwen, and G. Volpe. Light-controlled assembly of active colloidal molecules. *The Journal of Chemical Physics*, 150(9):094905, 2019.

[74] F. Kümmel, B. ten Hagen, R. Wittkowski, I. Buttinoni, R. Eichhorn, G. Volpe, H. Löwen, and C. Bechinger. Circular motion of asymmetric self-propelling particles. *Phys. Rev. Lett.*, 110:198302, 2013.

[75] S. Michelin and E. Lauga. Autophoretic locomotion from geometric asymmetry. *Eur. Phys. J. E*, 38(7), 2015.

[76] S. Michelin, E. Lauga, and D. Bartolo. Spontaneous autophoretic motion of isotropic particles. *Physics of Fluids*, 25(6):061701, 2013.

[77] Z. Izri, M. N. van der Linden, S. Michelin, and O. Dauchot. Self-propulsion of pure water droplets by spontaneous marangoni-stress-driven motion. *Phys. Rev. Lett.*, 113:248302, Dec 2014.

[78] Aidan T. Brown and Wilson C K Poon. Ionic effects in self-propelled pt-coated janus swimmers. *Soft matter*, 10 22:4016–27, 2014.

[79] TC Le, J Zhai, WH Chiu, PA Tran, and N. Tran. Janus particles: recent advances in the biomedical applications. *Int J Nanomedicine*, 2019.

[80] D. Kagan, R. Laocharoensuk, M. Zimmerman, C. Clawson, S. Balasubramanian, D. Kang, D. Bishop, S. Sattayasamitsathit, L. Zhang, and J. Wang. Rapid delivery of drug carriers propelled and navigated by catalytic nanoshuttles. *Small*, 6(23):2741–2747, 2010.

[81] Javier Reguera, Dorleta Jimenez de Aberasturi, Malou Henriksen-Lacey, Judith Langer, Ana Espinosa, Boguslaw Szczupak, Claire Wilhelm, and Luis M. Liz-Marzan. Janus plasmonic–magnetic gold–iron oxide nanoparticles as contrast agents for multimodal imaging. *Nanoscale*, 9:9467–9480, 2017.

[82] Y. Yi, L. Sanchez, Y. Gao, and Y. Yu. Janus particles for biological imaging and sensing. *The Analyst*, 141(12):3526—3539, June 2016.

[83] S. Sundararajan, P. E. Lammert, A. W. Zudans, V. H. Crespi, and A. Sen. Catalytic motors for transport of colloidal cargo. *Nano letters*, 8(5):1271–1276, 2008.

[84] W. Duan, W. Wang, S. Das, V. Yadav, T. E. Mallouk, and A. Sen. Synthetic nano- and micro-machines in analytical chemistry: sensing, migration, capture, delivery, and separation. *Annu. Rev. Anal. Chem.*, 8:311–333, 2015.

[85] Wei Wang, Wentao Duan, Suzanne Ahmed, Thomas E. Mallouk, and Ayusman Sen. Small power: Autonomous nano- and micromotors propelled by self-generated gradients. *Nano Today*, 8(5):531–554, 2013.

[86] Lluis Soler, Veronika Magdanz, Vladimir M. Fomin, Samuel Sanchez, and Oliver G. Schmidt. Self-propelled micromotors for cleaning polluted water. *ACS Nano*, 7(11):9611–9620, 2013. PMID: 24180623.

[87] Diana Vilela, Jemish Parmar, Yongfei Zeng, Yanli Zhao, and Samuel Sanchez. Graphene-based microbots for toxic heavy metal removal and recovery from water. *Nano Letters*, 16(4):2860–2866, 2016. PMID: 26998896.

[88] Ramin Golestanian, Tanniemola B. Liverpool, and Armand Ajdari. Propulsion of a molecular machine by asymmetric distribution of reaction products. *Phys. Rev. Lett.*, 94:220801, Jun 2005.

[89] S.J. Ebbens. Active colloids: Progress and challenges towards realising autonomous applications. *Current Opinion in Colloid & Interface Science*, 21:14–23, 2016.

[90] W. E. Uspal, M. N. Popescu, S. Dietrich, and M. Tasinkevych. Guiding catalytically active particles with chemically patterned surfaces. *Phys. Rev. Lett.*, 117:048002, Jul 2016.

[91] M N Popescu, W E Uspal, and S Dietrich. Chemically active colloids near osmotic-responsive walls with surface-chemistry gradients. *Journal of Physics: Condensed Matter*, 29(13):134001, feb 2017.

[92] Mojdeh Heidari, Andreas Bregulla, Santiago Muinos Landin, Frank Cichos, and Regine von Klitzing. Self-propulsion of janus particles near a brush-functionalized substrate. *Langmuir*, (36):7775–7780, 2020.

[93] J. Schwarz-Linek, C. Valeriani, A. Cacciuto, M. E. Cates, D. Marenduzzo, A. N. Morozov, and W. C. K. Poon. Phase separation and rotor self-assembly in active particle suspensions. *Proceedings of the National Academy of Sciences*, 109(11):4052–4057, 2012.

[94] Xiao Chen, Xiang Yang, Mingcheng Yang, and H. P. Zhang. Dynamic clustering in suspension of motile bacteria. *EPL (Europhysics Letters)*, 111(5):54002, sep 2015.

[95] Alexander P. Petroff, Xiao-Lun Wu, and Albert Libchaber. Fast-moving bacteria self-organize into active two-dimensional crystals of rotating cells. *Phys. Rev. Lett.*, 114:158102, Apr 2015.

[96] E. Guazelli and J. F. Morris. *A Physical Introduction to Suspension Dynamics*. Cambridge University Press, 2012.

[97] P. G. Saffman. On the settling speed of free and fixed suspensions. *Studies in Applied Mathematics*, 52(2):115–127, 1973.

[98] C. Pozrikidis. *Boundary Integral and Singularity Methods for Linearized Viscous Flow*. Cambridge Texts in Applied Mathematics. Cambridge University Press, 1992.

[99] Kim S. and Karrilla S.J. *Microhydrodynamics: Principles and Selected Applications*. Butterworth-Heinemann, 2013.

[100] G. I. Taylor. Analysis of the swimming of microscopic organisms. *Proceedings of the Royal Society of London, Series A: Mathematical and Physical Sciences*, 1951.

[101] G. I. Taylor. The action of waving cylindrical tails in propelling microscopic organisms. *Proceedings of the Royal Society of London. Series A. Mathematical and Physical Sciences*, 211(1105):225–239, 1952.

[102] T. J. Pedley, D. R. Brumley, and R. E. Goldstein. Squirmers with swirl: a model for volvox swimming. *Journal of Fluid Mechanics*, 798:165–186, 2016.

[103] H. A. Stone and A. D. T. Samuel. Propulsion of microorganisms by surface distortions. *Phys. Rev. Lett.*, 77:4102, 1996.

[104] M. J. Lighthill. On the squirming motion of nearly spherical deformable bodies through liquids at very small reynolds numbers. *Communications on Pure and Applied Mathematics*, 1952.

[105] J. R. Blake. A spherical envelope approach to ciliary propulsion. *J. Fluid Mech.*, 46(1):199–208, 1971.

[106] B. Delmotte, E. E. Keaveny, F. Plouraboué, and E. Climent. Large-scale simulation of steady and time-dependent active suspensions with the force-coupling method. *J. Comput. Phys.*, 302:524–547, December 2015.

[107] Knut Drescher, Jörn Dunkel, Luis H. Cisneros, Sujoy Ganguly, and Raymond E. Goldstein. Fluid dynamics and noise in bacterial cell-cell and cell-surface scattering. *Proceedings of the National Academy of Sciences*, 108(27):10940–10945, 2011.

[108] Takuji Ishikawa and Masateru Hota. Interaction of two swimming Paramecia. *Journal of Experimental Biology*, 209(22):4452–4463, 11 2006.

[109] Knut Drescher, Raymond E. Goldstein, Nicolas Michel, Marco Polin, and Idan Tuval. Direct measurement of the flow field around swimming microorganisms. *Phys. Rev. Lett.*, 105:168101, Oct 2010.

[110] T. Ishikawa, M.P. Simmonds, and T. J. Pedley. Hydrodynamic interaction of two swimming model micro-organisms. *Journal of Fluid Mechanics*, 568:119–160, 2006.

[111] T. Ishikawa, T.J. Pedley, and T. Yamaguchi. Orientational relaxation time of bottom-heavy squirmers in a semi-dilute suspension. *Journal of Theoretical Biology*, 249(2):296–306, 2007.

[112] Takuji Ishikawa, J. T. Locsei, and T. J. Pedley. Fluid particle diffusion in a semidilute suspension of model micro-organisms. *Phys. Rev. E*, 82:021408, Aug 2010.

[113] Takuji Ishikawa. Vertical dispersion of model microorganisms in horizontal shear flow. *Journal of Fluid Mechanics*, 705:98–119, 2012.

[114] Ignacio Pagonabarraga and Isaac Llopis. The structure and rheology of sheared model swimmer suspensions. *Soft Matter*, 9:7174–7184, 2013.

[115] B. Derjaguin, G. Sidorenkov, E. Zubashchenkov, and E. Kiseleva. Kinetic phenomena in boundary films of liquids. *Kolloidn. zh*, 9:4263–4268, 1947.

[116] J. L. Anderson, M. E. Lowell, and D. C. Prieve. Motion of a particle generated by chemical gradients part 1. non-electrolytes. *Journal of Fluid Mechanics*, 117:107–121, 1982.

[117] John L. Anderson and Dennis C. Prieve. Diffusiophoresis: Migration of colloidal particles in gradients of solute concentration. *Separation and Purification Methods*, 13(1):67–103, 1984.

[118] G. K. Batchelor. The stress system in a suspension of force-free particles. *J. Fluid Mech.*, 41:545–570, 1970.

[119] E. Lauga and S. Michelin. Stresslets induced by active swimmers. *Phys. Rev. Lett.*, 117:148001, Sep 2016.

[120] B. Nasouri and R. Golestanian. Exact phoretic interaction of two chemically active particles. *Phys. Rev. Lett.*, 124:168003, Apr 2020.

[121] A. Varma and S. Michelin. Modeling chemo-hydrodynamic interactions of phoretic particles: A unified framework. *Phys. Rev. Fluids*, 4:124204, Dec 2019.

[122] B. Nasouri and R. Golestanian. Exact axisymmetric interaction of phoretically active janus particles. *J. Fluid Mech.*, 905:A13, 2020.

[123] N. Sharifi-Mood, A. Mozzafari, and U. M. Córdova-Figueroa. Pair interaction of catalytically active colloids: from assembly to escape. *J. Fluid Mech.*, 798:910–954, 2016.

[124] Benno Liebchen, Davide Marenduzzo, and Michael E. Cates. Phoretic interactions generically induce dynamic clusters and wave patterns in active colloids. *Phys. Rev. Lett.*, 118:268001, Jun 2017.

[125] J. Sturmer, M. Seyrich, and H. Stark. Chemotaxis in a binary mixture of active and passive particles. *J. Chem. Phys.*, 150,:214901, 2019.

[126] S. Saha, R. Golestanian, and S. Ramaswamy. Clusters, asters, and collective oscillations in chemotactic colloids. *Phys. Rev. E*, 89:062316, Jun 2014.

[127] E. Kanso and S. Michelin. Phoretic and hydrodynamic interactions of weakly confined autophoretic particles. *J. Chem. Phys.*, 150:044902, 2019.

[128] B. Liebchen and H. Löwen. Which interactions dominate in active colloids? *J. Chem. Phys.*, 150:061102, 2019.

[129] S. Thutupalli, D. Geyer, R. Singh, R. Adhikari, and H. A. Stone. Flow-induced phase separation of active particles is controlled by boundary conditions. *Proc. Natl. Ac. Sci. USA*, 115:5403–5408, 2018.

[130] B. Liebchen, D. Marenduzzo, I. Pagonabarraga, and M. E. Cates. Clustering and pattern formation in chemicorepulsive active colloids. *Phys. Rev. Lett.*, 115:258301, 2015.

[131] T. Traverso and S. Michelin. Hydrochemical interactions in dilute phoretic suspensions: from individual particle properties to collective organization. *Phys. Rev. Fluids*, 5:104203, 2020.

[132] J F Brady and G Bossis. Stokesian dynamics. *Annu. Rev. Fluid Mech.*, 20(1):111–157, 1988.

[133] J. W. Swan, J. F. Brady, and R. S. Moore. Modeling hydrodynamic self-propulsion with stokesian dynamics. or teaching stokesian dynamics to swim. *Physics of Fluids*, 23(7):071901, 2011.

[134] A. Sierou and J. F. Brady. Accelerated stokesian dynamics simulations. *Journal of Fluid Mechanics*, 448:115–146, 2001.

[135] A. M. Fiore and J. W. Swan. Fast stokesian dynamics. *J. Fluid Mech.*, 878:544–597, 2019.

[136] W. Yan and J. F. Brady. The behavior of active diffusiophoretic suspensions: An accelerated laplacian dynamics study. *The Journal of Chemical Physics*, 145(13):134902, 2016.

[137] W. E. Uspal, M. N. Popescu, S. Dietrich, and M. Tasinkevych. Self-propulsion of a catalytically active particle near a planar wall: from reflection to sliding and hovering. *Soft Matter*, 11:434–438, 2015.

[138] T. D. Montenegro-Johnson, S. Michelin, and E. Lauga. A regularised singularity approach to phoretic problems. *The European Physical Journal E*, 38(12):139, 2015.

[139] Enkeleida Lushi and Charles S. Peskin. Modeling and simulation of active suspensions containing large numbers of interacting micro-swimmers. *Comp. Struct.*, 122:239–248, 2013.

[140] RA Lambert, F Picano, WP Breugem, and L Brandt. Active suspensions in thin films: nutrient uptake and swimmer motion. *J. Fluid Mech.*, 733:528–557, 2013. harvest.

[141] A. P. S. Bhalla, B. E. Griffith, N. A. Patankar, and A. Donev. A minimally-resolved immersed boundary model for reaction-diffusion problems. *The Journal of Chemical Physics*, 139(21):214112, 2013.

[142] F. Alarcón and I. Pagonabarraga. Spontaneous aggregation and global polar ordering in squirmer suspensions. *J. of Mol. Liq.*, 185:56 – 61, 2013.

[143] A. J. C. Ladd and R. Verberg. Lattice-boltzmann simulations of particle-fluid suspensions. *J. Stat. Phys.*, 104(5):1191, 2001.

[144] Andrea Scagliarini and Ignacio Pagonabarraga. Unravelling the role of phoretic and hydrodynamic interactions in active colloidal suspensions. *Soft Matter*, 16:8893–8903, 2020.

[145] Andreas Zöttl and Holger Stark. Hydrodynamics determines collective motion and phase behavior of active colloids in quasi-two-dimensional confinement. *Phys. Rev. Lett.*, 112:118101, Mar 2014.

[146] M. Yang, A. Wysocki, and M. Ripoll. Hydrodynamic simulations of self-phoretic microswimmers. *Soft Matter*, 10:6208–6218, 2014.

[147] P. H. Colberg and R. Kapral. Many-body dynamics of chemically propelled nanomotors. *J. Chem. Phys.*, 147(6):064910, 2017.

[148] Mu-Jie Huang, Jeremy Schofield, and Raymond Kapral. Chemotactic and hydrodynamic effects on collective dynamics of self-diffusiophoretic janus motors. *New Journal of Physics*, 19(12):125003, dec 2017.

[149] Rajesh Singh, R. Adhikari, and M. E. Cates. Competing chemical and hydrodynamic interactions in autophoretic colloidal suspensions. *The Journal of Chemical Physics*, 151(4):044901, 2019.

[150] Rajesh Singh and Ronojoy Adhikari. Pystokes: phoresis and stokesian hydrodynamics in python. *J. Open Source Softw.*, 5(55):2318, 2020.

[151] M. Maxey and B. K. Patel. Localized force representations for particles sedimenting in stokes flow. *Int. J. Multiph. Flow*, 27:1603–1626, 2001.

[152] S. Lomholt and M. R. Maxey. Force-coupling method for particulate two-phase flow: Stokes flow. *J. Comput. Phys.*, 184(2):381–405, January 2003.

[153] J. Xu, M. R. Maxey, and G. E.M. Karniadakis. Numerical simulation of turbulent drag reduction using micro-bubbles. *Journal of Fluid Mechanics*, 468:271–281, 2002.

[154] S.L. Dance and M.R. Maxey. Incorporation of lubrication effects into the force-coupling method for particulate two-phase flow. *J. Comp. Phys.*, 189(1):212 – 238, 2003.

[155] D. Liu, E.E. Keaveny, M.R. Maxey, and G.E. Karniadakis. Force-coupling method for flows with ellipsoidal particles. *J. Comp. Phys.*, 228(10):3559 – 3581, 2009.

[156] K. Yeo and M. R. Maxey. Simulation of concentrated suspensions using the force-coupling method. *J. Comp. Phys.*, 229:2401–2421, 2010.

[157] O. S. Pak and E. Lauga. Generalized squirming motion of a sphere. *J. Eng. Math.*, 88:1–28, 2014.

[158] S. Michelin and E. Lauga. Phoretic self-propulsion at finite péclet numbers. *J. Fluid Mech.*, 747:572–604, 2014.

[159] Z. Liang, Z. Gimbutas, L. Greengard, J. Huang, and S. Jiang. A fast multipole method for the rotne-prager-yamakawa tensor and its applications. *J. Comp. Phys.*, 234:133–139, 2013.

[160] W. Yan and R. Blackwell. Kernel aggregated fast multipole method: Efficient summation of laplace and stokes kernel functions. *arXiv preprint arXiv:2010.15155*, 2020.

[161] S. L. Dance, E. Climent, and M. R. Maxey. Collision barrier effects on the bulk flow in a random suspension. *Physics of Fluids*, 16(3):828–831, 2004.

[162] Cristián Huepe and Maximino Aldana. Intermittency and clustering in a system of self-driven particles. *Phys. Rev. Lett.*, 92:168701, Apr 2004.

[163] B. M. Mognetti, A. Šarić, S. Angioletti-Uberti, A. Cacciuto, C. Valeriani, and D. Frenkel. Living clusters and crystals from low-density suspensions of active colloids. *Phys. Rev. Lett.*, 111:245702, Dec 2013.

[164] Gabriel S. Redner, Caleb G. Wagner, Aparna Baskaran, and Michael F. Hagan. Classical nucleation theory description of active colloid assembly. *Phys. Rev. Lett.*, 117:148002, Sep 2016.

[165] Fergal Reid, Aaron McDaid, and Neil Hurley. Percolation computation in complex networks. In *2012 IEEE/ACM International Conference on Advances in Social Networks Analysis and Mining*, pages 274–281, 2012.

[166] Sebastian Weitz, Andreas Deutsch, and Fernando Peruani. Self-propelled rods exhibit a phase-separated state characterized by the presence of active stresses and the ejection of polar clusters. *Phys. Rev. E*, 92:012322, Jul 2015.

[167] Eric E. Keaveny. Fluctuating force-coupling method for simulations of colloidal suspensions. *Journal of Computational Physics*, 269:61–79, 2014.

[168] Blaise Delmotte and Eric E. Keaveny. Simulating brownian suspensions with fluctuating hydrodynamics. *The Journal of Chemical Physics*, 143(24):244109, 2015.

[169] Giorgio Volpe, Clemens Bechinger, Frank Cichos, Ramin Golestanian, Hartmut Lowen, Matthias Sperl, and Giovanni Volpe. Active matter in space. *npj Microgravity*, 8(54), 2022.

[170] Sergi Roca-Bonet, Martin Wagner, and Marisol Ripoll. Clustering of self-thermophilic asymmetric dimers: the relevance of hydrodynamics. *Soft Matter*, 18:7741–7751, 2022.

[171] A. J. Hughes. The einstein relation between relative viscosity and volume concentration of suspensions of spheres. *Nature*, (173):1089, 1954.

[172] Salima Rafaï, Levan Jibuti, and Philippe Peyla. Effective viscosity of microswimmer suspensions. *Phys. Rev. Lett.*, 104:098102, Mar 2010.

[173] Andrey Sokolov and Igor S. Aranson. Reduction of viscosity in suspension of swimming bacteria. *Phys. Rev. Lett.*, 103:148101, Sep 2009.

[174] T. Traverso and S. Michelin. Collective dynamics and rheology of confined phoretic suspensions. *Journal of Fluid Mechanics*, 943:A21, 2022.

[175] T. Ishikawa and T. J. Pedley. The rheology of a semi-dilute suspension of swimming model micro-organisms. *J. Fluid Mech.*, 588:399–435, 2007.

[176] A. Lees and S. Edwards. The computer study of transport process under extreme condition. *Journal of Physics C: Solid State Physics*, (5):1921–1928, 1972.

[177] N. Verdon, A. Lefebvre-Lepot, P Laure, and L Lobry. Modified lees–edwards boundary conditions and viscous contact for numerical simulations of particles in a shear flow. *European Journal of Computational Mechanics*, (3-6 / Special Issue: French Conference on Computational Mechanics 2011: selected contributions):397–406, 2012.

[178] M. Tatulea-Codrean and E. Lauga. Artificial chemotaxis of phoretic swimmers: instantaneous and long-time behaviour. *J. Fluid Mech.*, 856:921–957, 2018.

[179] S. Michelin, E. Guérin, and E. Lauga. Collective dissolution of microbubbles. *Phys. Rev. Fluids*, 3:043601, 2019.

[180] E. E. Keaveny and M. R. Maxey. Modeling the magnetic interactions between paramagnetic beads in magnetorheological fluids. *J. Comp. Phys.*, 227:9554–9571, 2008.

ECOLE DOCTORALE

**Titre :** Mouvement collectif en suspensions réactives

**Mots clés :** Suspensions réactives, matière active, particules phorétiques, mouvement colectif, CFD, FCM

**Résumé :**
Le mouvement collectif comprend de nombreuses échelles allant des volées d'oiseaux et de poissons aux colonies de micro-organismes. Récemment, des particules microscopiques synthétiques autopropulsées (suspendues dans des fluides) ont été développées pour modéliser de tels systèmes et effectuer des applications d'ingénierie, biomédicales, environnementales et autres. Les interactions hydrodynamiques et chimiques entre ces particules conduisent à l'émergence de dynamiques riches et de structures cohérentes.
Leur modélisation numérique reste difficile compte tenu du couplage des problèmes hydrodynamiques et chimiques et de l'augmentation rapide des ressources de calcul requises pour les grands ensembles de particules. Étant donné que les particules ont généralement des tailles micrométriques avec des vitesses relativement faibles (quelques longueurs de corps par seconde), les effets d'inertie et d'advection sont négligeables dans la suspension, et le problème est régi par les équations de Stokes et Laplace.
Dans cette thèse, un nouveau cadre numérique appelé Diffusio-phoretic Force Coupling Method (DFCM) est proposé, qui est basé sur une expansion multipolaire régularisée pour les solutions hydrodynamiques et chimiques, capable de traiter efficacement le problème couplé pour un grand nombre de particules. Il remplace la représentation exacte de la surface par un forçage volumétrique équivalent. Après sa validation, il a été implémenté dans un solveur parallèle efficace pour modéliser le mouvement collectif des suspensions formées avec des grands ensembles de particules Janus.
L'influence des propriétés des particules, de leurs interactions hydro-chimiques, de la taille du système et de leur densité sur les motifs émergents est systématiquement étudiée dans nos simulations. Cinq régimes différents ont été identifiés et classés, montrant des phases gazeuses, des agrégates et leurs mélanges, ayant un mouvement ordonné ou chaotique de particules libres et des agrégates formées. Les transitions entre les différents régimes ont été principalement rationalisées en fonction des interactions chimiques. Enfin, un nouveau régime clusterisé est rapporté et largement caractérisé.

**Title :** Collective motion in reactive suspensions

**Keywords :** Reactive suspensions, active matter, phoretic particles, collective motion, CFD, FCM

**Abstract :**
Collective motion comprises many scales sweeping from flocks of birds and fish to colonies of microorganisms. Recently, synthetic self-propelled microscopic particles (suspended in fluids) have been developed to model such systems and perform engineering, biomedical, environmental, and other applications. The hydrodynamic and chemical interactions between these particles lead to the emergence of rich dynamics and coherent structures.
Their numerical modeling remains challenging given the coupling of the hydrodynamic and chemical problems and the rapid increase in the required computational resources for large particle ensembles. Since the particles typically have micro-metrical sizes with relatively small velocities (some body lengths per second), the inertial and advective effects are negligible in the suspension, and the problem is governed by the Stokes and Laplace equations.
In this thesis, a new numerical framework called Diffusio-phoretic Force Coupling Method (DFCM) is proposed, which is based on a regularized multipole expansion for the hydrodynamical and chemical solutions, able to handle the coupled problem efficiently for a large number of particles. It replaces the exact surface representation with an equivalent volumetric forcing. After its validation, it was implemented in an efficient parallel solver to model the collective motion of suspensions formed with large ensembles of Janus particles.
The influence of the particle properties, their hydrochemical interactions, the system size, and their density on the emerging patterns is systematically studied in our simulations. Five different regimes have been identified and classified, showing gas-like, clustered phases and mixtures of them, having ordered or chaotic motion of free particles and formed clusters. The transitions between the different regimes were primarily rationalized based on chemical interactions. Finally, a new clustered regime is reported and widely characterized.

**Institut Polytechnique de Paris**
91120 Palaiseau, France